



A Sensitive and Label-Free Electrochemical Impedance Immunosensor for CDH 22 Biomarker Detection Based on Organo-Functional Silane Modified ITO Electrode

Organo-Fonksiyonel Silan ile Modifiye Edilmiş ITO Elektrot Temelli CDH 22 Biyobelirteç Tespiti için Hassas ve Etiketsiz Bir Elektrokimyasal İmpedans İmmünosensörü

Elif Burcu AYDIN*

Tekirdağ Namık Kemal University, Scientific and Technological Research Center, Tekirdağ, Turkey.

ABSTRACT

In this work, a novel electrochemical label free immunosensor was fabricated for Cadherin-like protein 22 (CDH 22) biomarker detection based on specific immunoreaction between anti-CDH 22 antibody and CDH 22 antigen. The developed immunosensor was constructed through the immobilization of anti-CDH 22 antibodies on 3-cyanopropyltrimethoxysilane (CPTMS) modified ITO substrate. The effective binding of the anti-CDH 22 antibodies on the CPTMS silanization agent was investigated by using morphological characterization (Scanning Electron Microscopy (SEM), Atomic Force Microscopy (AFM)) and electrochemical characterization (Electrochemical Impedance Spectroscopy (EIS), Cyclic Voltammetry (CV)). Under optimum experimental conditions, the ITO/CPTMS modified electrode was a good linker for anti-CDH 22 antibody anchoring. In addition, CPTMS modified electrode offered an efficient surface to CDH 22 antigen detection. The immunosensor had a wide linear detection range (0.03-3 pg/mL) with low detection limit (9 fg/mL). Also, it had good reproducibility, excellent repeatability and long storage stability. In addition, the practical applicability of the proposed immunosensor was investigated by utilizing human serum samples. The human serum samples recovery results (99.16% - 101.94%) illustrated the accuracy of the suggested biosensor. Consequently, CPTMS can be a promising platform for biosensor construction and this suggested immunosensor can be applicable for real human serum analysis.

Key Words

Cadherin-like protein 22, electrochemical impedance spectroscopy, disposable electrode.

ÖZ

Bu çalışmada, anti-CDH 22 antikorunu ve CDH 22 antijeni arasındaki spesifik immüno-reaksiyona dayanan, kadherin benzeri protein (CDH 22) biyobelirtecini tespiti için yeni bir elektrokimyasal etiketsiz immünosensör üretilmiştir. Geliştirilen immünosensör, anti-CDH 22 antikorlarının 3-siyanopropiltrimetoksilsilan (CPTMS) ile modifiye edilmiş ITO substratı üzerinde immobilizasyonu ile oluşturulmuştur. Anti-CDH 22 antikorlarının CPTMS silanizasyon ajanına etkili bağlanması, morfolojik karakterizasyon (Taramalı Elektron Mikroskobu (SEM), Atomik Kuvvet Mikroskobu (AFM)) ve elektrokimyasal karakterizasyon (Elektrokimyasal İmpedans Spektroskopisi (EIS), Siklik Voltammetri (CV)) kullanılarak incelendi. Optimum deney koşulları altında, ITO / CPTMS ile modifiye edilmiş elektrot, anti-CDH 22 antikor bağlanması için iyi bir bağlayıcıdır. Ek olarak, CPTMS modifiye elektrot CDH 22 antijen tespiti için etkili bir yüzey sunmuştur. İmmünosensör, geniş bir lineer tespit aralığı (0.03-3 pg/mL) ile düşük tespit limiti (9 fg/mL) ile sahipti. Ayrıca, iyi tekrarlanabilirlik, mükemmel tekrarlanabilirlik ve uzun depolama kararlılığına sahipti. Ek olarak, önerilen immünosensörün pratik uygulanabilirliği, insan serum numuneleri kullanılarak araştırıldı. İnsan serum numuneleri geri kazanım sonuçları (% 99.16 -% 101.94) önerilen biyosensörün doğruluğunu göstermektedir. Sonuç olarak, CPTMS, biyosensör yapımı için umut verici bir platform olabilir ve bu önerilen immünosensör gerçek insan serum analizi için uygulanabilir.

Anahtar Kelimeler

Kadherin benzeri protein, elektrokimyasal impedans spektroskopisi, tek kullanımlık elektrot.

Article History: Received: Jan 21, 2019; Revised: Mar 15, 2019; Accepted: May 28, 2019; Available Online: Nov 1, 2019.

DOI: <https://doi.org/10.15671/hjbc.515739>

Correspondence to: E.B. Aydın, Tekirdağ Namık Kemal University, Scientific and Technological Research Center, Tekirdağ, Tukey.

E-Mail: ebbahadir@nku.edu.tr

INTRODUCTION

Cancer threatens the human health and in the diagnosis of cancer, immunohistochemistry and fluorescence methods are usually utilized [1, 2]. These methods require a lot of steps for cancer diagnosis and therefore, the analysis duration of these methods is long [3]. Biosensors are new devices for detection of biomolecules and specific biorecognition feature makes them reliable and rapid tools for medical applications. In biosensor designing different detection strategies have been utilized [4]. Electrochemical detection is mostly preferred due to high specificity and sensitivity. Biomarkers are biomolecules, which are found in human fluids and utilized for early detection of cancer. A lot of studies have been performed for biomarker detection by utilizing biosensors [4, 5].

Cadherin-like protein 22 (CDH22) is a transmembrane glycoprotein. It is known as PB-cadherin and belongs to cadherin superfamily [6]. It has role in cell-cell adhesion and metastasis. CDH22 hypermethylation is an independent prognostic biomarker in breast cancer [7, 8]. It is produced in the pituitary gland and brain. It helps to form tissue in neural and nonneural cells [6]. Over-expression of CDH22 results in colorectal cancer [6-8], breast cancer [7] and metastatic melanoma [8]. In addition, Cadherin-22 is a prognostic marker in advanced cancer stages and a potential factor in cancer metastasis or spread. The hindering of CDH 22 biomarker decreases the adhesion and invasion rate of breast and brain cancer cells. Because of this, it has gained interest in diagnosis of breast cancer [9]. The detection of CDH22 biomarker is often carried out by utilizing ELISA kit. The linear range and detection limit of the ELISA kit are 15.6-500 ng/mL and 2 ng/mL, respectively [9].

Indium tin oxide (ITO) is an excellent transparent semi-conductive substrate in different applications such as photovoltaic cell, optoelectronic devices and sensors. In sensor applications, it is utilized as a transducer owing to its unique optical transparency, broad working potential, stable electrochemical and physical features [10, 11]. The selection of electrode for electrochemical immunosensing is important to develop sensitive immunosensor. Therefore, ITO is a favorable electrode material and has been employed as a working electrode in electrochemical sensors and biosensors. The effective anchoring of the biomolecules on the ITO substrate surface is a significant point to develop a successful

biosensor. Therefore, several modification strategies such as physical adsorption [12], electrophoretic deposition [13-15], electrochemical deposition [16, 17], silanization [18, 19], self-assembled monolayer formation [20] and electro-polymerization [21-23] have been employed to develop ITO based biosensor. ITO substrates have been modified with different silane agents such as 3-isocyanatopropyl triethoxysilane (IPTES) [24], 3-aminopropyltriethoxy silane (APTES) [25-27], 11-cyanoundecyltrimethoxysilane (11-CUTMS) [28], (3-glycidoxypropyl)trimethoxysilane [29], N-(2-aminoethyl)-3-aminopropyltrimethoxysilane [18], 3-mercaptopropyl trimethoxysilane (3-MPTMS) [30], 3-glycidoxy propyl dimethoxysilane [19], 11-(triethoxysilyl)undecanal (TESU) [31], carboxyethylsilanetriol (CTES) [32]. Silane agents form layers with terminal amino, epoxy or chloro groups. These groups are utilized for immobilization of biorecognition molecules. The basic principle of this technique is based on self-assembled monolayer (SAM) construction on the ITO substrate with hydroxyl ends. In this modification method, siloxane bonds are formed between hydroxylated ITO sheet surface and silane agent. Silane based SAMs provide a stable, reusable, reproducible and well-controlled surfaces for biomolecule attaching. In addition, the preparation of these layer is simple, and this layer prevents possible denaturation and non-specific adsorption. Cyanopropylsiloxanes are organosilane molecules and they have both polar and polarizable properties. Moreover, they have low surface tension, thus, they increase good surface wetting and the adhesion between dissimilar materials. They form interactions between the monolayer and the substrate which are used as binding platforms. The CPTMS silane agent includes a head group, an alkyl chain and an end group. The head group, trimethoxy- provides the attaching of the silane agent onto the platform. The alkyl chain increases the stability of the single layer owing to van der Waals interactions. The terminal group provides chemical groups to bind biomolecules [33, 34].

Electrochemical impedance spectroscopy (EIS) is a sensitive and an old electrochemical method utilized in biosensor characterization. It has gained interest due to informative features. This method is often employed to investigate the variations formed on the electrode surface due to antibody-antigen immune-interaction, probe DNA-target DNA interactions or enzyme-substrate reactions. The changes in electrode-electrolyte interface give information about the biosensing system. Additionally, impedance analyses are utilized in several

electrochemical applications such as analysis of electrochemical kinetics of electrodes, batteries and sensors/biosensors [35-37]. It is also a successful way to characterize of modifications formed on the electrodes. By using this way, the detection of some analytes from small ions to large proteins is possible [38, 39]. Because of this, this method has been utilized for several analytes detection. In the impedance analysis, the biosensing system includes three electrodes; a working electrode (modified to investigate the target analyte), a counter electrode (for applying the electric current) and a reference electrode (for providing a reference value) [40]. This measurement way is sensitive and simple compared to other redox labelled electrochemical methods such as cyclic voltammetry (CV), differential pulse voltammetry (DPV) and square wave voltammetry (SWV) [41]. Electrochemically inert molecules can be measured by using EIS technique, during the analysis is carried out in the presence of redox couple (ferricyanide/ferricyanide). In this technique, the oxidation and reduction reactions are formed at the electrode surface [42].

The goal of this work was a specific, sensitive and reproducible ITO based biosensor development for determination of CDH 22 cancer marker. In the first step of the immunosensor fabrication, ITO sheet modified with CPTMS to form immobilization points for anti-CDH 22 antibodies. CPTMS was used for a self-assembled monolayer formation and it served as a link between ITO sheet and the biomolecule (anti-CDH 22 antibody). The variations formed on the immunosensor surface were investigated via cyclic voltammetry (CV) and EIS methods. The optimal experimental parameters were determined by performing a lot of experiments. The immunosensor analytical characterizations were performed under optimum experimental conditions. The repeatability, reproducibility and storage stability of the proposed immunosensor were also analyzed and discussed. This fabricated biosensor had a wide linear detection range (0.03-3 pg/mL) and low LOD (9 fg/mL). In addition, the practical applicability of the proposed immunosensor was investigated by utilizing human serum samples. The human serum samples results illustrated the accuracy of the suggested biosensor. The EIS responses indicated that CDH 22 antigens could be detected simply and sensitively by this new biosensor. Moreover, the immunosensor responses demonstrated that the fabricated biosensor could be employed to detect CDH 22 antigen in human serum samples.

MATERIALS and METHODS

Reagents

ITO coated Polyethylene Terephthalate (PET) films (resistance and thickness are 60 Ω /square and 150 nm), 3-cyanopropyltrimethoxysilane (CPTMS), toluene, Monoclonal anti-CDH 22 antibody, CDH 22 antigen and BSA were supplied by Sigma-Aldrich. Dilutions of anti-CDH 22 antibodies and CDH 22 antigens were prepared with PBS buffer (pH 7.4, 50 mM) before use. Ferri-ferro solution was utilized as a redox couple and prepared by utilizing 5 mM $K_4[Fe(CN)_6]/K_3[Fe(CN)_6]$.

Apparatus

Electrochemical analyses were recorded with Gamry 1000 Potentiostat/Galvanostat. Disposable ITO sheet (2*20 mm), Ag/AgCl electrode, and platinum wire were utilized as working, reference and counter electrode, respectively. Two different electrochemical methods were employed: EIS and CV. All the analyses were carried out at room conditions using a 5 mM redox couple solution of $K_3Fe(CN)_6/K_4Fe(CN)_6$. In the EIS experiments the frequency range was from 0.05 to 50 KHz. The working conditions for CV analyses were as follows; scan rate: 100 mVs⁻¹ and step size 10 mV. The surface topography during biosensor fabrication steps was investigated by using FEI-Quanta FEG 250 Model SEM microscope at an operating voltage 5 kV. AFM images were recorded utilizing a NanoMagnetics Instruments-AFM Plus Model. All AFM images were taken in tapping mode with a tapping silicon tip and the tip radius was <10 nm. In order to follow the side groups formed on the ITO electrode, FTIR (Bruker Vertex 70 ATR Model) and Raman Spectroscopy (Thermo DXR Raman spectrometer equipped with a 780-nm excitation laser) was employed.

Modification of ITO Electrodes for CDH 22 Antigen Detection

Before the modification of ITO electrodes, they were cleaned in ultrasonic bath with ethanol, soap solution and ultrapure water, respectively. After cleaning, they were immersed in a mix solution of $H_2O_2/NH_4OH/H_2O$ (1:1:5) for 90 min at room conditions to form hydroxyl end on the ITO electrode surfaces. Then, they were washed with ultrapure water and were dried under argon gas. The silanization of ITO sheets were performed by immersing in 0.5% CPTMS solution (prepared

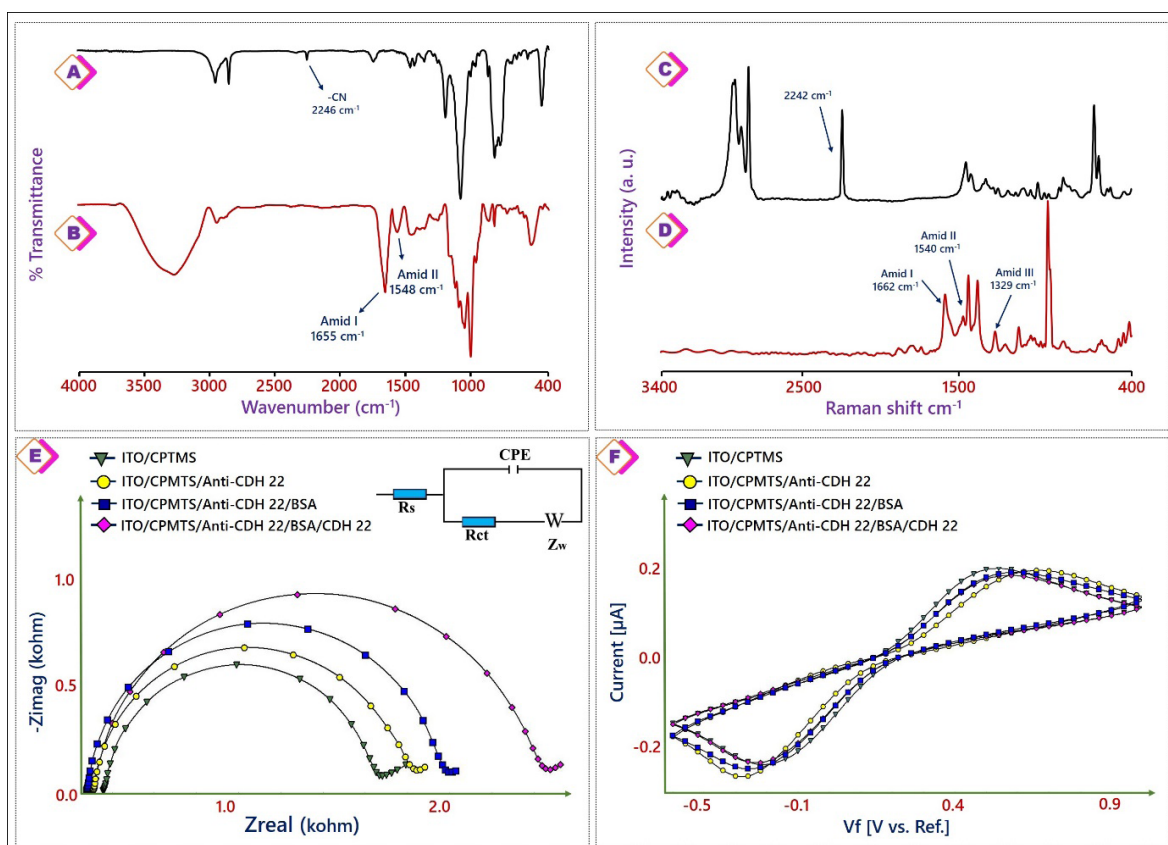


Figure 1. FTIR spectra and Raman spectra of CPTMS functionalized ITO substrate (A and C) and after anti-CDH 22 anchoring on the working electrode (B and D), Nyquist plots (E) and CVs (F) of the CDH 22 biosensor of the immune-electrode construction stage; Randle's equivalent circuit (inset).

by using toluene) for overnight. After CPTMS layer formation on the ITO sheets, they were washed with toluene and ultrapure water to eliminate the nonattached silane molecules and dried under argon gas. Afterwards, anti-CDH 22 antibody immobilization was performed by incubation in anti-CDH 22 antibody solution (2 ng/mL). The nonattached antibody molecules removed by washing ultrapure water. Finally, the remaining cyano groups of CPTMS were blocked by utilizing BSA protein. After these steps, ITO electrodes could be used for CDH 22 antigen detection.

Human Serum Sample Measurements

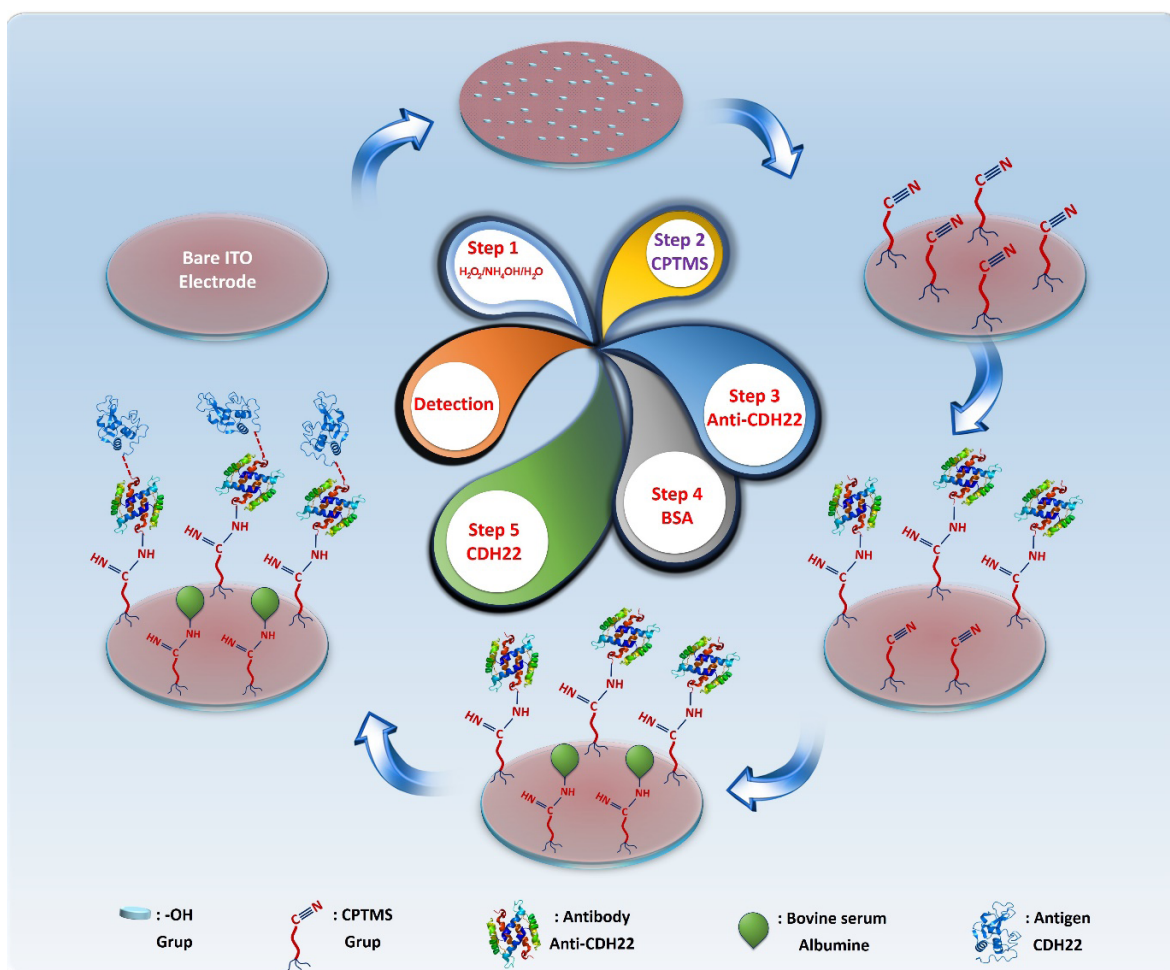
Human serum samples were supplied by the Tekirdağ Namık Kemal University Faculty of Medicine. CDH 22 antigen measurements were performed after a 100000 fold dilution with phosphate buffer (50 mM, pH 7.4). The success of the suggested biosensor was investigated by addition of CDH 22 antigen to the diluted human serum samples.

RESULTS and DISCUSSION

Chemical Characterization of the Immunosensor

In this work, the FTIR and Raman Spectrometers were utilized to investigate the chemical bonds between cyano groups of CPTMS present on the ITO substrate and amino ends of anti-CDH 22 antibodies. The FTIR spectra of CPTMS functionalized ITO substrate and anti-CDH 22 antibody attached ITO substrate are displayed in Figure 1A and Figure 1B, respectively.

The FTIR spectra of CPTMS functionalized ITO substrate (Figure 1A) showed the characteristic absorption peak at 2246 cm^{-1} ($\text{C}\equiv\text{N}$), that proved the CPTMS SAMs were formed completely [43–45]. As seen Figure 1B, the FTIR spectrum illustrated that the amino ends were introduced on the CPTMS functionalized ITO substrate. The peak at 1655 cm^{-1} and 1548 cm^{-1} in the FTIR spectrum of anti-CDH 22 antibody immobilized disposable ITO substrate proved that amino ends were present on the working electrode [28]. In addition to FTIR analysis, Ra-



Scheme 1. Schematic illustration of biosensor fabrication steps and electrochemical detection of CDH 22 antigen.

man spectrometer was utilized for the chemical characterization. Raman spectroscopy is a useful technique to investigate of chemical binding of proteins, nucleic acids, large molecules. In the FTIR spectra of proteins and nucleic acids are complicated and many bands are overlapped. The Raman spectra of CPTMS functionalized ITO substrate and anti-CDH 22 antibody attached ITO substrate are displayed in Figure 1C and Figure 1D, respectively. As seen in Figure 1C, the cyano group of CPTMS was observed at 2242 cm^{-1} . Amide I, II and III regions are usually observed between $1650\text{--}1680\text{ cm}^{-1}$, $1480\text{--}1570\text{ cm}^{-1}$ and $1235\text{--}1300\text{ cm}^{-1}$, respectively. As shown in Figure 1D, amide I, amide II and amide III bonds were observed at 1662 , 1540 and 1329 cm^{-1} , respectively.

Electrochemical Characterization of the Fabrication Procedure

The CDH 22 immunosensor fabrication stages are illustrated in Scheme 1. ITO electrode surface was hydroxy-

lated by $\text{H}_2\text{O}_2/\text{NH}_4\text{OH}/\text{H}_2\text{O}$ solution and CPTMS linked to hydroxyl ends on the ITO electrode surface via siloxane bonds. In this way, a biomolecule immobilization matrix was formed on the disposable ITO sheet. CPTMS provided free cyano ends on the ITO sheet surface allowing the covalent binding of NH_2 groups of anti-CDH 22 antibodies. After antibodies binding on the modified ITO electrode, the free cyano groups blocked by BSA. After that, the immunosensor was utilized for CDH 22 antigen detection.

The modification steps of the CDH 22 biosensor was investigated by EIS and CV analyses. EIS is a powerful method for investigation of the electrode interface properties. $[\text{Fe}(\text{CN})_6]^{3-/4-}$ was a redox active couple and utilized for monitoring electrochemical features of the proposed immunosensor [43]. Figure 1E shows the Nyquist plots after modification steps. Nyquist plots of the modified ITO electrodes contain a semicircle portion and a linear portion. A semicircle part and a linear part are

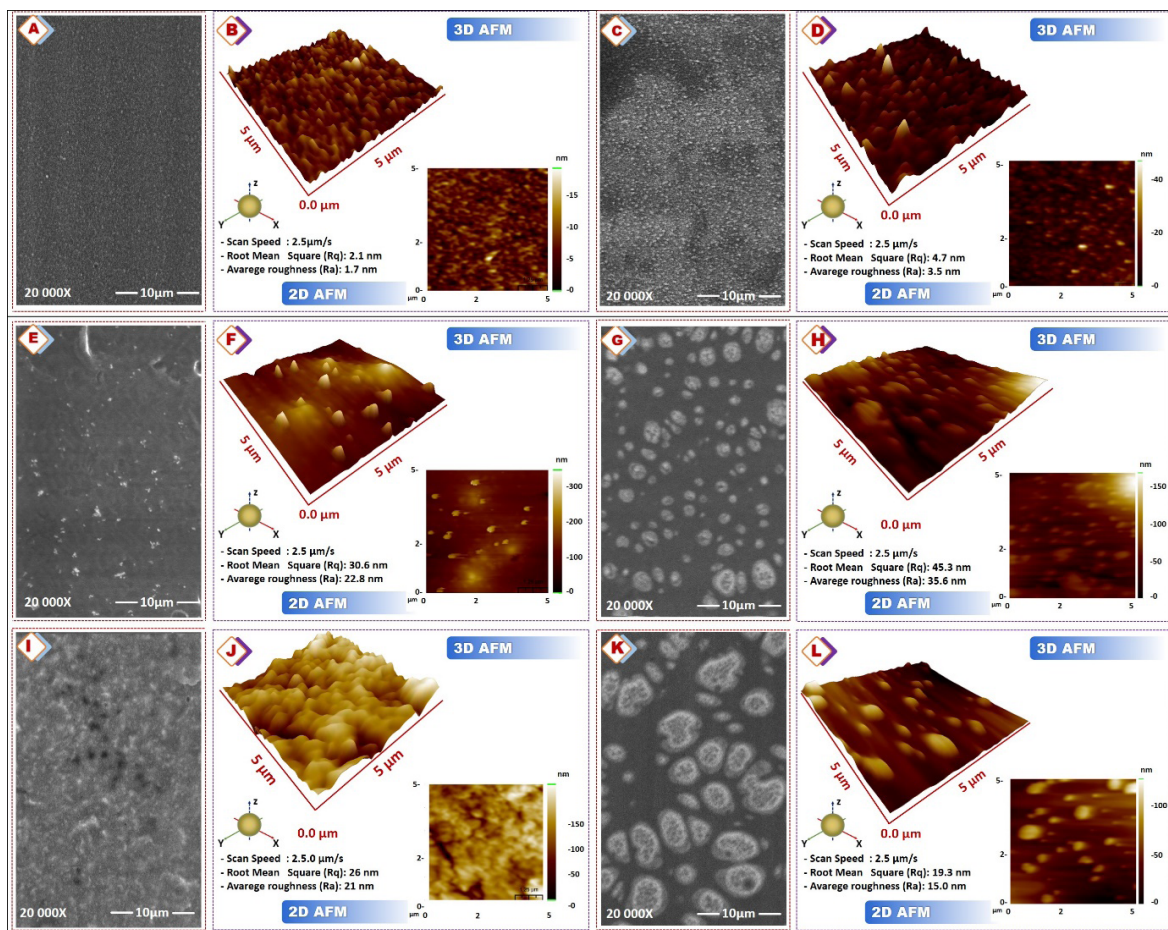


Figure 2. SEM and AFM images of bare ITO (A and B), ITO/OH (C and D), ITO/CPTMS (E, and F), ITO/CPTMS/anti-CDH 22 (G and H), ITO/CPTMS/anti-CDH 22/BSA (I and J), ITO/CPTMS/anti-CDH 22/BSA/CDH 22 (K and L).

obtained at higher frequencies and at lower frequencies, respectively. The semicircle part and the linear part are related to electron transfer and diffusion processes, respectively. The semicircle diameter is responsible for the electron transfer resistance (R_{ct}). The variations in R_{ct} value is associated with the blocking effect of the step-by-step fabrication process of the immunosensor. The impedance responses are fitted to the Randle's equivalent circuit. It contains the ohmic resistance of the electrolyte solution (R_s), constant phase element (CPE), Warburg impedance (Z_w) and charge transfer resistance (R_{ct}) (Figure 1E inset). Under ideal conditions, Z_w and R_s illustrate the properties of the electrolyte solution and diffusion of the redox couple, therefore to they are not affected from electrode modification steps. Additionally, CPE and R_{ct} display the dielectric and insulating features at the electrode/electrolyte interface and the variations occurred on the electrode surfaces affects them [44, 45].

Electrochemical characterizations with CV and EIS methods are useful to evaluate the electrochemical process on the modified surfaces. The CVs and EIS spectra were shown in Figure 1 to illustrate the electrochemical behavior of the ITO surface during the immunosensor fabrication. As shown in Figure 1E, ITO/CPTMS electrode had small semicircle diameter that indicated easy electron transfer between electrode surface and electrolyte solution. After anti-CDH 22 antibody immobilization on the CPTMS modified ITO substrate, an increase was seen in semicircle diameter. The immobilization of antibodies caused a layer formation on the ITO substrate surface. Thus, the electron transfer rate was decreased. In the BSA blockage step, electron transfer was obstructed, and an increase was seen in semicircle diameter. The specific immuno-reaction between anti-CDH 22 antibody and CDH 22 antigen formed a immunocomplex and a large semicircle diameter was seen. Compared

to hydroxylated ITO surface, the CPTMS modified ITO electrode surface had lower peak currents (Figure 1F). This result confirmed the CPTMS SAMs on the ITO substrate surface. After anti-CDH22 antibody, BSA and CDH 22 antigen immobilization, peak currents were decreased due to nonconductive layers formation on the electrode surface. These layers prevented the electron transfer between ITO electrode surface and electrolyte solution. In other words, these layers illustrated hindrance effects to electron transfer.

Morphological Characterization of the Fabrication Steps

The morphological characterization of the proposed immunosensor was performed AFM and SEM imaging. Figure 2 illustrates images of the proposed immunosensor surfaces during the fabrication. After cleaning of ITO sheet, a smooth surface was obtained (Figure 2A and Figure 2B). In this step, the average roughness (Ra) was measured as 1.7 nm on a 5×5 μm scale. The hydroxylation of clean ITO sheet increased the roughness of ITO surface (Figure 2D). As seen in figure 2C, this process changed the electrode surface. After hydroxylation, the average roughness (Ra) was measured as 3.5 nm on

a 5×5 μm scale. As mentioned above, Self-assembled monolayer formation technique was utilized for biorecognition molecule immobilization. In this study, CPTMS was used as linker for anti-CDH 22 antibody anchoring, The SEM and AFM images illustrated that a uniform CPTMS SAMs formation on the ITO electrode in Figure 2E and Figure 2F, respectively. The average roughness (Ra) was measured as 22.8 nm on a 5×5 μm scale. The variations on the ITO substrate surface after anti-CDH 22 antibody attaching are displayed in Figure 2G and Figure 2H. It can be clearly seen that the anti-CDH 22 antibodies were linked on the substrate and they looked like granules. In this step, the Ra value was measured as 88 nm on a 5×5 μm scale. At the BSA blockage step, the surface morphology of the ITO substrate was changed as observed in Figure 2I and Figure 2J. After BSA immobilization, the Ra value was measured as 21 nm on 5×5 μm scale. Figure 2K and Figure 2L display the SEM and AFM images of specific immuno-reaction between anti-CDH 22 antibodies and CDH 22 antigens. As seen in SEM image (Figure 2K), the surface was changed and it was in accord with AFM observation. The Ra value was measured as 126 nm on 5×5 μm scale (Figure 2L).

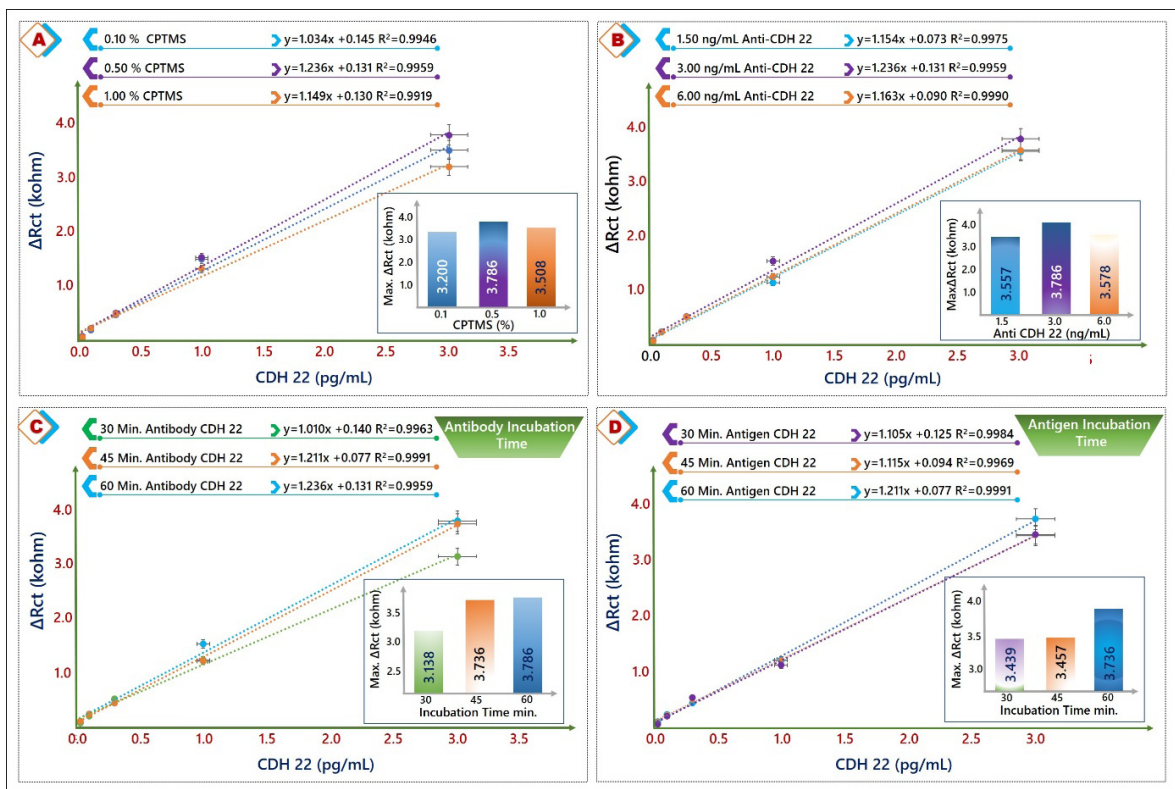


Figure 3. Optimization results (A) CPTMS quantity, (B) anti-CDH 22 antibody level, (C) anti-CDH 22 antibody incubation duration, (D) CDH 22 antigen incubation duration.

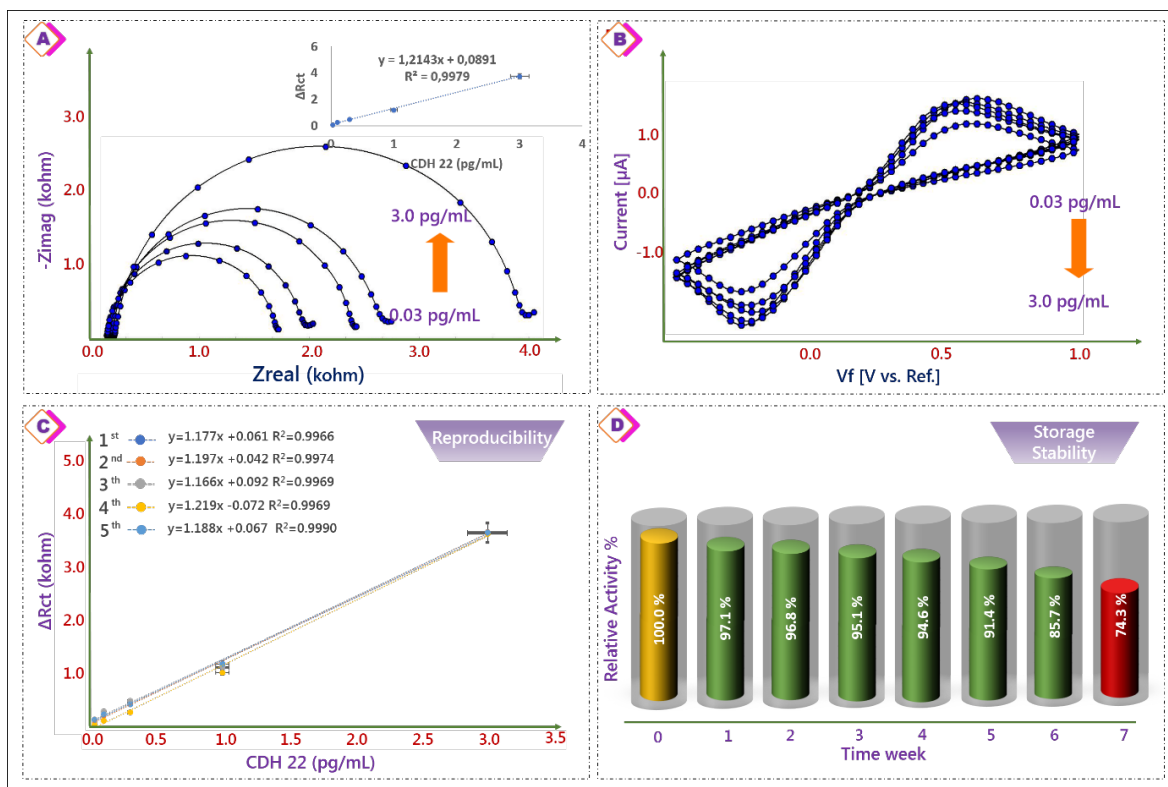


Figure 4. EIS (A) and CV (B) results of the biosensor for the determination of CDH 22 biomarker (from 0.03 to 3 pg/mL), calibration plot (inset). Reproducibility (C), Storage stability (D) of the biosensor.

Optimization of Experimental Conditions

In order to determine optimal experimental conditions, a variety of experiments were performed. The optimization of these parameters provided a sensitive and stable biosensor fabrication. In this work, CPTMS concentration, anti-CDH 22 antibody level, anti-CDH 22 antibody incubation duration and CDH 22 antigen incubation duration were optimized. These analyses were performed at room conditions and these parameters were followed by EIS and CV.

In the first stage of the experimental conditions optimization, the utilized CPTMS concentration was optimized. This stage had a significant role in the binding of adequate amount of anti-CDH 22 antibodies. Because of this, three different amounts (0.1%; 0.5%; 1% w/w) were studied. Silane ends of CPTMS bound to hydroxyl group of hydroxylated ITO electrode. The low CPTMS level caused low immunosensor response because, a stable SAMs was not formed. The high CPTMS levels (0.5% and 1%) caused similar immunosensor signals. The highest signal was achieved after utilizing 0.5% concentration of CPTMS. The responses of the immunosensors that obtained after usage of these levels were utilized to draw

of the linear curves. These linear curves are illustrated in Figure 3A. Then, anti-CDH 22 antibody level was optimized. This stage had a significant role in analytical performance of the proposed immunosensor. In order to select optimal anti-CDH 22 antibody level, 1.5 ng/mL, 3 ng/mL and 6 ng/mL anti-CDH 22 antibody concentrations were tried. The highest ΔR_{ct} value was found at 3 ng/mL anti-CDH 22 concentration. Because of this, 3 ng/mL anti-CDH 22 level was selected optimal antibody level. The calibration plots of these levels are displayed in Figure 3B. To determine the optimal CDH 22 antibody incubation time, CPTMS functionalized ITO sheets incubated in anti-CDH 22 antibody solution for 30, 45 and 60 min. The highest response was found after 60 min incubation, but the response at 45 min incubation time was nearly same. Therefore, 45 min was selected as the optimal incubation time for antibody anchoring. The short preparation period of the immunoelectrode provides a short fabrication process of the proposed immunosensor. The calibration plots of the different incubation times are displayed in Figure 3C. Lastly, the immunoreaction period between anti-CDH22 antibody and CDH 22 antigen was optimized. At this step, the prepared immunoelectrodes were immersed in CDH

22 antigen solution for three different times (30 min, 45 min, 60 min). The maximum immunosensor response was obtained after 60 min incubation. The other signals were nearly same and low. Because of this, 60 min was optimum incubation time (Figure 3D).

Electrochemical Detection of CDH 22 Antigen

Electrochemical detection of CDH 22 antigen was achieved by CV and EIS analyses in the presence of redox system. Figure 4 illustrates the EIS and CV responses of the immunosensor at the increasing concentration of CDH 22 antigens. The increasing concentration of CDH 22 antigens caused gradual increases in impedance responses (Figure 4A) and gradual decreases in CVs (Figure 4B). Also, these responses showed that these antigens formed a blocking wall, and lead to higher electrochemical resistances and lower peak currents. Also, an increase in R_{ct} value was observed as the concentration of CDH 22 antigen concentration increased from 0.03 pg/mL to 3 pg/mL (Figure 4A inset). The limit of detection (LOD) was estimated to be 9 fg/mL based on the 3σ rule. The limit of quantification (LOQ) was calculated to be 30 fg/mL based on the 10σ rule.

Repeatability, Reproducibility and Stability

The repeatability of the proposed immunosensor was evaluated by measuring CDH 22 concentration (0.3 pg/mL) with 10 different bioelectrodes prepared under identical conditions. The relative standard deviation (RSD) was measured as 2.17%. The reproducibility of the suggested immunosensor was investigated by measuring CDH 22 concentration with 5 different biosensing system. Under the identical experimental conditions, the RSD was measured as 1.50% (Figure 4C). These obtained results indicated an excellent precision and good reproducibility of the prepared immunosensor.

The stability of the CDH 22 immunosensor was also investigated. The immunosensor was stored at 4°C for 10 weeks. During the storage period, a gradually decrease was seen in the impedance response. After 7 weeks of storage, the impedance response of the CDH 22 immunosensor decreased 74.3% of its initial activity, showing that the immunosensor could keep its activity for a long time (Figure 4D).

Analysis of Real Human Serum Samples

In order to verify the applicability of suggested immunosensor, the prepared immunoelectrodes were utilized for human serum sample analysis and the accuracy of the proposed biosensor was examined by utilizing the standard addition technique. The CDH 22 protein is present in human serum at ng/mL. Therefore, the human serum samples were diluted 100000 times by using PBS buffer. As observed in Table 1, the recovery ranges were from 99.16 to 101.94%, that confirmed the applicability of the biosensor for CDH 22 antigen determination.

Conclusion

In this study, an impedimetric immunosensor was successfully introduced by using disposable ITO sheet for CDH 22 biomarker detection. This sensitive and specific immunosensor was developed by immobilizing anti-CDH 22 antibody onto CPTMS modified ITO electrode. Step-by-step modification process and the immunosensing process was followed by using electrochemical (CV, EIS) and morphological (SEM and AFM) techniques. Under optimum experimental conditions, the developed immunosensor displayed a selective detection of CDH 22 cancer biomarker. In addition, our proposed method exhibited a highly sensitive and selective determination of CDH 22 antigen with a detection limit of 9

Table 1. Results of human serum samples.

Sample	Found by the biosensor (pg/mL)	Added CDH 22 amount (pg/mL)	Total found	% Recovery	% Relative difference
Human Serum 1	0.50	0.2	0.72	101.94	1.94
Human Serum 2	0.68	0.2	0.88	100.57	0.57
Human Serum 3	0.82	0.2	1.03	101.41	1.41
Human Serum 4	0.83	0.2	1.04	101.00	1.00
Human Serum 5	0.52	0.2	0.72	99.16	-0.84

fg/mL and a linear range from 0.03 pg/mL to 3 pg/mL. The success of the proposed biosensor in human serum samples analysis illustrated that this biosensor was a simple, cost-effective, selective and sensitive platform for determination of biomarkers. This proposed immunosensor provided simple tool for biomarker detection in clinical applications.

References

- J. Duraiyan, R. Govindarajan, K. Kaliyappan, M. Palanisamy, Applications of immunohistochemistry, *J. Pharm. BioAllied Sci.*, 4 (2012) S307.
- D. Shin, N. Vigneswaran, A. Gillenwater, R. Richards-Kortum, Advances in fluorescence imaging techniques to detect oral cancer and its precursors, *Future Oncol.*, 6 (2010) 1143-1154.
- A. Gündoğdu, E.B. Aydın, M.K. Sezgintürk, A novel electrochemical immunosensor based on ITO modified by carboxyl-ended silane agent for ultrasensitive detection of MAGE-1 in human serum, *Anal. Biochem.*, 537 (2017) 84-92.
- E.B. Aydın, M. Aydın, M.K. Sezgintürk, Highly sensitive electrochemical immunosensor based on polythiophene polymer with densely populated carboxyl groups as immobilization matrix for detection of interleukin 1β in human serum and saliva, *Sens. Actuator. B*, 270 (2018) 18-27.
- E.B. Aydın, M. Aydın, M.K. Sezgintürk, Electrochemical immunosensor based on chitosan/conductive carbon black composite modified disposable ITO electrode: An analytical platform for p53 detection, *Biosens. Bioelectron.*, 121 (2018) 80-89.
- J. Zhou, J. Li, J. Chen, Y. Liu, W. Gao, Y. Ding, Over-expression of CDH22 is associated with tumor progression in colorectal cancer, *Tumor Biol.*, 30 (2009) 130-140.
- E. Martín-Sánchez, S. Mendaza, A. Ulazia-Garmendia, I. Monreal-Santesteban, A. Córdoba, F. Vicente-García, I. Blanco-Luquin, S. De La Cruz, A. Aramendia, D. Guerrero-Setas, CDH22 hypermethylation is an independent prognostic biomarker in breast cancer, *Clin. Epigenet.*, 9 (2017) 7.
- B. Piche, S. Khosravi, M. Martinka, V. Ho, G. Li, CDH22 expression is reduced in metastatic melanoma, *Am. J. Cancer Res.*, 1 (2011) 233.
- M. Aydın, E.B. Aydın, M.K. Sezgintürk, Electrochemical immunosensor for CDH22 biomarker based on benzaldehyde substituted poly (phosphazene) modified disposable ITO electrode: A new fabrication strategy for biosensors, *Biosens. Bioelectron.*, 126 (2019) 230-239.
- X.R. Cheng, B.Y. Hau, T. Endo, K. Kerman, Au nanoparticle-modified DNA sensor based on simultaneous electrochemical impedance spectroscopy and localized surface plasmon resonance, *Biosens. Bioelectron.*, 53 (2014) 513-518.
- E.B. Aydın, M.K. Sezgintürk, Indium Tin Oxide (ITO): A promising material in biosensing technology, *TrAC, Trends Anal. Chem.*, 97 (2017) 309-315.
- C.M. Pandey, S. Dewan, S. Chawla, B.K. Yadav, G. Sumana, B.D. Malhotra, Controlled deposition of functionalized silica coated zinc oxide nano-assemblies at the air/water interface for blood cancer detection, *Anal. Chim. Acta*, 937 (2016) 29-38.
- S. Kumar, S. Kumar, S. Tiwari, S. Augustine, S. Srivastava, B.K. Yadav, B.D. Malhotra, Highly sensitive protein functionalized nanostructured hafnium oxide based biosensing platform for non-invasive oral cancer detection, *Sens. Actuators, B*, 235 (2016) 1-10.
- I. Tiwari, M. Singh, C.M. Pandey, G. Sumana, Electrochemical genosensor based on graphene oxide modified iron oxide-chitosan hybrid nanocomposite for pathogen detection, *Sens. Actuators, B*, 206 (2015) 276-283.
- A. Sharma, D. Baral, H. Bohidar, P.R. Solanki, Oxalic acid capped iron oxide nanorods as a sensing platform, *Chem.-Biol. Interact.*, 238 (2015) 129-137.
- A. Singh, M. Choudhary, M. Singh, H. Verma, S.P. Singh, K. Arora, DNA functionalized direct electro-deposited gold nanoaggregates for efficient detection of *Salmonella typhi*, *Bioelectrochemistry*, 105 (2015) 7-15.
- A.K. Yagati, J.C. Pyun, J. Min, S. Cho, Label-free and direct detection of C-reactive protein using reduced graphene oxide-nanoparticle hybrid impedimetric sensor, *Bioelectrochemistry*, 107 (2016) 37-44.
- L. Yang, Y. Li, AFM and impedance spectroscopy characterization of the immobilization of antibodies on indium-tin oxide electrode through self-assembled monolayer of epoxysilane and their capture of *Escherichia coli* O157: H7, *Biosens. Bioelectron.*, 20 (2005) 1407-1416.
- M.B. dos Santos, S. Azevedo, J. Aguil, B. Prieto-Simon, C. Sporer, E. Torrents, A. Juárez, V. Teixeira, J. Samitier, Label-free ITO-based immunosensor for the detection of very low concentrations of pathogenic bacteria, *Bioelectrochemistry*, 101 (2015) 146-152.
- E.B. Aydın, M. Aydın, M.K. Sezgintürk, A highly sensitive immunosensor based on ITO thin films covered by a new semi-conductive conjugated polymer for the determination of TNF α in human saliva and serum samples, *Biosens. Bioelectron.*, 97 (2017) 169-176.
- S. Komathi, A.I. Gopalan, K.P. Lee, Fabrication of a novel layer-by-layer film based glucose biosensor with compact arrangement of multi-components and glucose oxidase, *Biosens. Bioelectron.*, 24 (2009) 3131-3134.
- W. Chu, Q. Zhou, S. Li, W. Zhao, N. Li, J. Zheng, Oxidation and sensing of ascorbic acid and dopamine on self-assembled gold nanoparticles incorporated within polyaniline film, *Appl. Surf. Sci.*, 353 (2015) 425-432.
- N. Prabhakar, Z. Matharu, B. Malhotra, Polyaniline Langmuir-Blodgett film based aptasensor for ochratoxin A detection, *Biosens. Bioelectron.*, 26 (2011) 4006-4011.
- M. Ozmen, K. Can, M. Ersoz, Immobilization of albumin on indium-tin oxide (ITO) surface via isocyanate linkage, *J. Electroanal. Chem.*, 633 (2009) 228-234.
- M.Ç. Canbaz, M.K. Sezgintürk, Fabrication of a highly sensitive disposable immunosensor based on indium tin oxide substrates for cancer biomarker detection, *Anal. Biochem.*, 446 (2014) 9-18.
- M. Khan, X. Liu, J. Zhu, F. Ma, W. Hu, X. Liu, Electrochemical detection of tyramine with ITO/APTES/ErGO electrode and its application in real sample analysis, *Biosens. Bioelectron.*, 108 (2018) 76-81.
- M.Z.H. Khan, Effect of ITO surface properties on SAM modification: A review toward biosensor application, *Cogent Engineering*, 3 (2016) 1170097.
- H. Törer, E.B. Aydın, M.K. Sezgintürk, A label-free electrochemical biosensor for direct detection of RACK 1 by using disposable, low-cost and reproducible ITO based electrode, *Anal. Chim. Acta*, 1024 (2018) 65-72.

29. D. Guo, M. Zhuo, X. Zhang, C. Xu, J. Jiang, F. Gao, Q. Wan, Q. Li, T. Wang, Indium-tin-oxide thin film transistor biosensors for label-free detection of avian influenza virus H5N1, *Anal. Chim. Acta*, 773 (2013) 83-88.
30. A.K. Yagati, T. Lee, J. Min, J.-W. Choi, Electrochemical performance of gold nanoparticle–cytochrome c hybrid interface for H₂O₂ detection, *Colloids Surf. B*, 92 (2012) 161-167.
31. E. Bahadır, M. Sezgintürk, Label-free, ITO-based immunosensor for the detection of a cancer biomarker: Receptor for Activated C Kinase 1, *Analyst*, 141 (2016) 5618-5626.
32. E.B. Aydın, M.K. Sezgintürk, A sensitive and disposable electrochemical immunosensor for detection of SOX2, a biomarker of cancer, *Talanta*, 172 (2017) 162-170.
33. M.N.S. Karaboğa, M.K. Sezgintürk, A novel silanization agent based single used biosensing system: Detection of C-reactive protein as a potential Alzheimer's disease blood biomarker, *J. Pharm. Biomed. Anal.*, 154 (2018) 227-235.
34. C. Haensch, S. Hoepfner, U.S. Schubert, Chemical modification of self-assembled silane based monolayers by surface reactions, *Chem. Soc. Rev.*, 39 (2010) 2323-2334.
35. J. Muñoz, R. Montes, M. Baeza, Trends in electrochemical impedance spectroscopy involving nanocomposite transducers: Characterization, architecture surface and biosensing, *TrAC, Trends Anal. Chem.*, 97 (2017) 201-215.
36. E.B. Aydın, M.K. Sezgintürk, A disposable and ultrasensitive ITO based biosensor modified by 6-phosphonohexanoic acid for electrochemical sensing of IL-1 β in human serum and saliva, *Anal. Chim. Acta*, 1039 (2018) 41-50.
37. M. Aydın, E.B. Aydın, M.K. Sezgintürk, A Disposable Immunosensor Using ITO Based Electrode Modified by a Star-Shaped Polymer for Analysis of Tumor Suppressor Protein p53 In Human Serum, *Biosens. Bioelectron.*, 107 (2018) 1-9.
38. X.Y. Zhang, L.Y. Zhou, H.Q. Luo, N.B. Li, A sensitive and label-free impedimetric biosensor based on an adjunct probe, *Anal. Chim. Acta*, 776 (2013) 11-16.
39. M. Labib, S. Martić, P.O. Shipman, H.B. Kraatz, Electrochemical analysis of HIV-1 reverse transcriptase serum level: Exploiting protein binding to a functionalized nanostructured surface, *Talanta*, 85 (2011) 770-778.
40. A.S. Bandarenka, Exploring the interfaces between metal electrodes and aqueous electrolytes with electrochemical impedance spectroscopy, *Analyst*, 138 (2013) 5540-5554.
41. M. Labib, P.O. Shipman, S. Martić, H.B. Kraatz, Towards an early diagnosis of HIV infection: an electrochemical approach for detection of HIV-1 reverse transcriptase enzyme, *Analyst*, 136 (2011) 708-715.
42. M. Behpour, S.M. Ghoreishi, E. Honarmand, M. Salavati-Niasari, Comparative electrochemical study of new self-assembled monolayers of 2-[[[(Z)-1-(3-furyl) methylidene] amino]-1-benzenethiol and 2-[[[(2-sulfanylphenyl) imino] methyl] phenol for determination of dopamine in the presence of high concentration of ascorbic acid and uric acid, *Analyst*, 136 (2011) 1979-1986.
43. S. Wang, Y. Zhang, J. Yu, X. Song, S. Ge, M. Yan, Application of indium tin oxide device in gold-coated magnetic iron solid support enhanced electrochemiluminescent immunosensor for determination of carcinoma embryonic antigen, *Sens. Actuators B*, 171-172 (2012) 891-898.
44. L. Alfonta, A. Bardea, O. Khersonsky, E. Katz, I. Willner, Chronopotentiometry and Faradaic impedance spectroscopy as signal transduction methods for the biocatalytic precipitation of an insoluble product on electrode supports: routes for enzyme sensors, immunosensors and DNA sensors, *Biosens. Bioelectron.*, 16 (2001) 675-687.
45. Y. Huang, M.C. Bell, I.I. Suni, Impedance biosensor for peanut protein Ara h 1, *Anal. Chem.*, 80 (2008) 9157-9161.



Plasmonic Zr-Based Metal–Organic Frameworks for Accelerated De-Colorization of Methylene Blue Under LED Light Irradiation

LED Işık Işınımı Altında Metilen Mavisinin Hızlandırılmış Renksizleştirilmesi için Plazmonik Zr-esaslı Metal–Organik Çerçeveseler

Kouroush Salimi[®]

Department of Chemical Engineering, Ankara Yıldırım Beyazıt University, Etlik, Ankara, Turkey.

ABSTRACT

Well-defined photocatalyst with 3D morphologies have attracted the attention of scientists due to the more accessible reactive surfaces, easy to recover from reaction medium, and low aggregation. Within this scope, photocatalysis based on plasmonic metal-organic frameworks (MOFs) were synthesized and utilized as an alternative reactive platform for visible-light degradation of methylene blue (MB) under green LED irradiation for the first time. In order to reduce the recombination between electron-hole pairs, a stable oxidant, namely sodium persulfate (PS) was employed to accelerate the photocatalytic decolorization of MB. These feasible strategies demonstrated that a bleaching degree of 91% (i.e., in the presence of PS) within 120 min was achieved compared to the bare Au@UiO-66@Pdop NPs (bleaching degree 31%). The obtained results from this study highlighted the superior properties of the newly synthesized core-shell Au@UiO-66@Pdop photocatalysts and clearly declared the great potential of the photo-responsive MOFs for organic pollutant degradations as well.

Key Words

Plasmonic metal organic frameworks (MOFs), visible LED light, photocatalytic decolorization.

ÖZ

3 boyutlu morfolojiye sahip iyi tanımlanmış fotokatalizörler, daha erişilebilir reaktif yüzeyler, reaksiyon ortamından kolay bir şekilde elde edilebilmeleri ve düşük agregasyona sahip olmalarından dolayı bilim adamlarının dikkatini çekmiştir. Bu kapsamda, plazmonik metal organik çerçeve (MOF'ler) esaslı fotokatalizör sentezlendi ve ilk kez yeşil LED ışık ışınımı aracılığıyla metilen mavisinin (MB) görünür ışık altındaki degradasyonu için alternatif bir reaktif platform olarak kullanılmıştır. Elektron-boşluk çiftleri arasındaki rekombinasyonu azaltarak MB'nin fotokatalitik renksizleştirilmesini hızlandırmak için istikrarlı bir oksidan olan sodyum persülfat (PS) kullanılmıştır. Uygulanan stratejiler aracılığıyla çıplak Au@UiO-66@Pdop NP'lere kıyasla (yıkım derecesi %31) PS kullanılarak 120 dakika içinde %91'lik bir degradasyon derecesinin eldesi gösterilmiştir. Bu çalışmadan elde edilen sonuçlar, yeni sentezlenmiş çekirdek kabuk (core-shell) yapısındaki Au@UiO-66@Pdop fotokatalizörünün üstün özelliklerini vurgulamış ve ışık duyarlı MOF'lerin organik kirleticilerin degradasyonu için de mükemmel potansiyelini açık şekilde ortaya koymuştur.

Anahtar Kelimeler

Plazmonik metal–organik çerçeveseler (MOF'ler), görünür LED ışık, fotokatalitik renksizleştirme.

Article History: Received: Sep 11, 2019; Revised: Oct 9, 2019; Accepted: Oct 16, 2019; Available Online: Oct 30, 2019.

DOI: <https://doi.org/10.15671/hjbc.618668>

Correspondence to: K. Salimi; Department of Chemical Engineering, Ankara Yıldırım Beyazıt University, Etlik, Ankara, Turkey..

E-Mail: kouroushsalimi@gmail.com

INTRODUCTION

Recently, visible light sensitive photocatalysts (i.e., GaP, WO_3 , CdS, ZnS, and etc.) have attracted the attention of related communities due to their narrow band gap compared to conventional UV-light responsive TiO_2 based materials [1-3]. However, this inorganic photocatalysts showed some drawbacks like low light conversion efficiency, hard desorption/separation from reaction media, as well as strong tendency for agglomeration [4]. This issue places the demand for the fabrication of a new class of photocatalysts with potential application in organic pollutant degradations.

Metal-organic frameworks (MOFs) are a class of porous coordination polymers constructed by strong chemical bonding of metal nodes and organic linkers [5, 6]. The unique chemical composition and diverse structural and functional features (i.e., large surface area, easy in-pore and surface functionalization) make them an extraordinary material for various applications including carbon dioxide capture, catalyst, separation science, sensing, biomedical, and analytical sciences [7-12]. Owing to the absorption of the irradiated light, MOFs were carried out as a significant photocatalyst for environmental fi-

elds [4, 13]. Xamena et al. reported the application of MOF-5 in photocatalytic degradation of phenols under UV-light irradiation [14]. Das et al. investigated a Zn_2O -containing doubly interpenetrated MOF for photocatalytic degradation of methyl orange using UV or visible light source [15]. More recently, reduced energy demand of photocatalytic degradation processes and optimizing of the photocatalytic parameters increased the use of LED photoreactors [16]. These photoreactors provided high energy efficiency, long lifespan, as well as low power consumption compared to the conventional light sources [16]. In this context, MIL-53 (Fe) was developed for accelerated photocatalytic degradation of acid Orange 7 (AO7) using visible LED light irradiation [16]. They provided an accelerated photocatalytic performance by reducing the charge carrier recombination using persulfate as an oxidant [16].

In this study, plasmonic zirconium-based metal-organic frameworks (Au@UiO-66@Pdop) were utilized for de-colorization of methylene blue (MB) under green LED light irradiation for the first time in the literature. Plasmonic photo-responsive catalyst was synthesized using polydopamine nanoparticles (Pdop NPs) as starting template. Thanks to the catechol groups of the

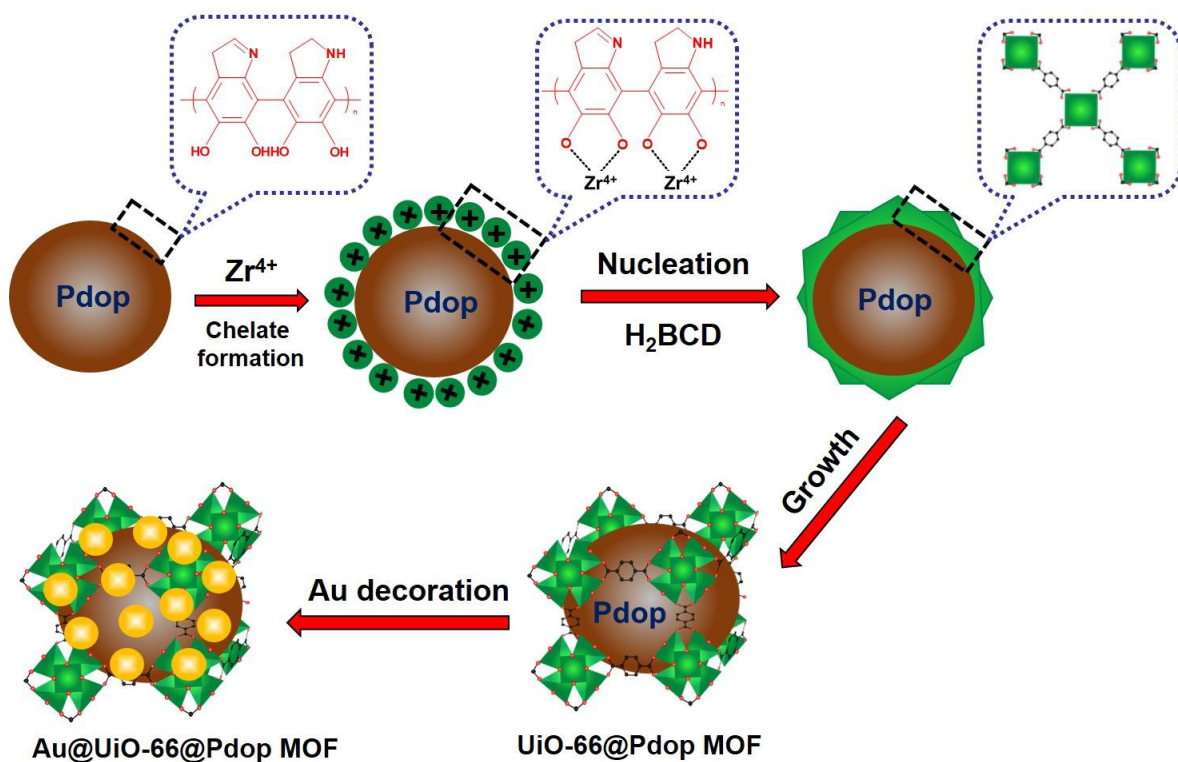


Figure 1. Schematic illustration of the synthetic pathway of Au@UiO-66@Pdop MOFs.

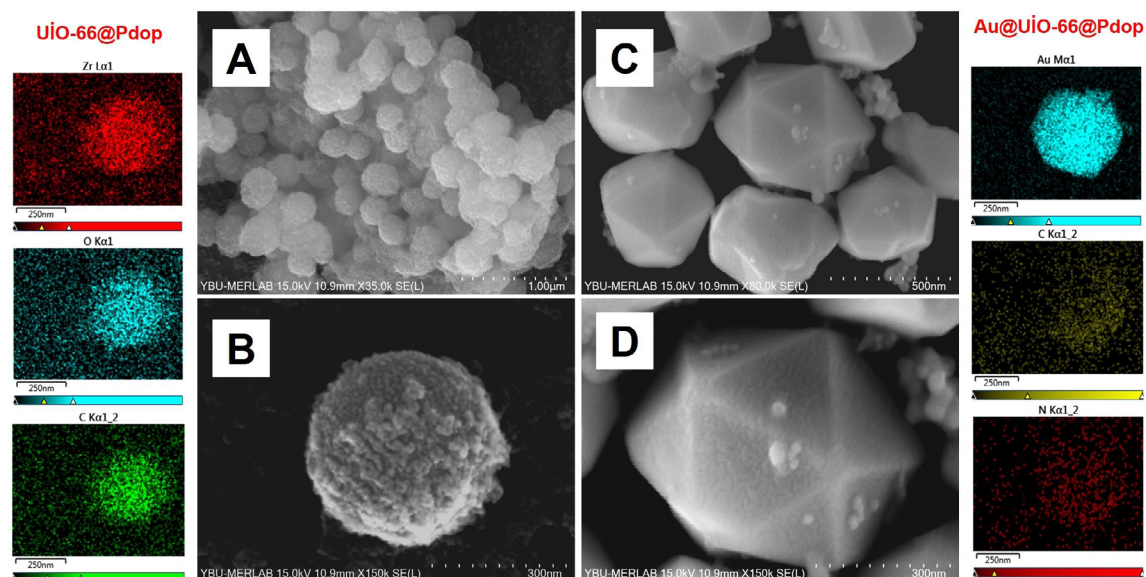


Figure 2. SEM and EDX analysis of A-B) UiO-66@Pdop, and C-D) Au@UiO-66@Pdop NPs.

Pdop, quite stable core-shell catalyst NPs with desired spherical morphologies and good localized surface plasmon resonance (LSPR) properties were obtained. Additionally, a home-made green LED light source was employed to investigate the performance of the photo-responsive Au@UiO-66@Pdop NPs for an efficient decolorization of organic pollutant. An excellent photocatalytic performance was recorded using sodium persulfate (PS) with important reduction in the charge carrier recombination. Finally, the effect of different reaction conditions on the variation of MB concentration (C/C_0) and reaction time were reported.

MATERIALS and METHODS

Synthesis Methods

Polydopamine nanoparticles (Pdop NPs) were synthesized according to the literature with some modifications [17]. Briefly, an aqueous solution containing ammonia (3.5 mL, 2.5 %), ethanol (2 mL), and DDI water (6 mL) were stirred at room temperature for 5 min followed by the addition of dopamine hydrochloride (1 mg in 1 mL DDI water). The resulting dispersion was stirred at room temperature for 8 h. Finally, Pdop NPs were centrifuged and washed with DDI water several times.

A well-defined core shell structure between Pdop NPs and Zr-based MOFs (UiO-66) was achieved in the presence of metal nodes and organic building blocks [18]. Typically, Pdop NPs (1 mg) were dispersed into N-N,dimethylformamide (DMF, 10 mL) and ultraso-

nicated for 10 min using an ice-bath. Then, zirconium chloride ($ZrCl_4$, 1 mg) and 1,4-benzenedicarboxylic acid (H2BDC, 10 mg) were introduced into the as-prepared solution and stirred at 140°C for 100 min. MOF shell coated Pdop NPs (UiO-66@Pdop) were isolated from reaction media and washed with methanol and DDI water, respectively.

For the synthesis of plasmonic Zr-based MOFs (Au@UiO-66@Pdop), MOF coated Pdop NPs were dispersed into an aqueous solution of chloroauric acid (30 mg, 50 mL) and vigorously mixed at 50°C for 2 h. Then, the solution was heated to boiling and the boiling was continued for 5 min. Subsequently, an aqueous solution of tri-sodium citrate (2 mL, 0.035 g) was introduced into the as-prepared solution and the boiling was further continued for 30 min. The resulting nanostructures were cooled down to room temperature and finally washed with DDI water for three times using centrifugation method. Finally, Au NPs embedded Zr-based MOFs (Au@UiO-66@Pdop) were kept in DDI water for further usage.

Characterization of Au@UiO-66@Pdop MOFs

The surface morphology and size distribution of nanostructures were determined by a scanning electron microscope (Hitachi, SU5000, Japan) which is equipped with an Energy Dispersive X-Ray spectrometry (EDX). The surface chemistry of plasmonic MOFs were analyzed using X-ray photoelectron spectroscopy (XPS, Thermo-K-Alpha-Monochromatic high-performance

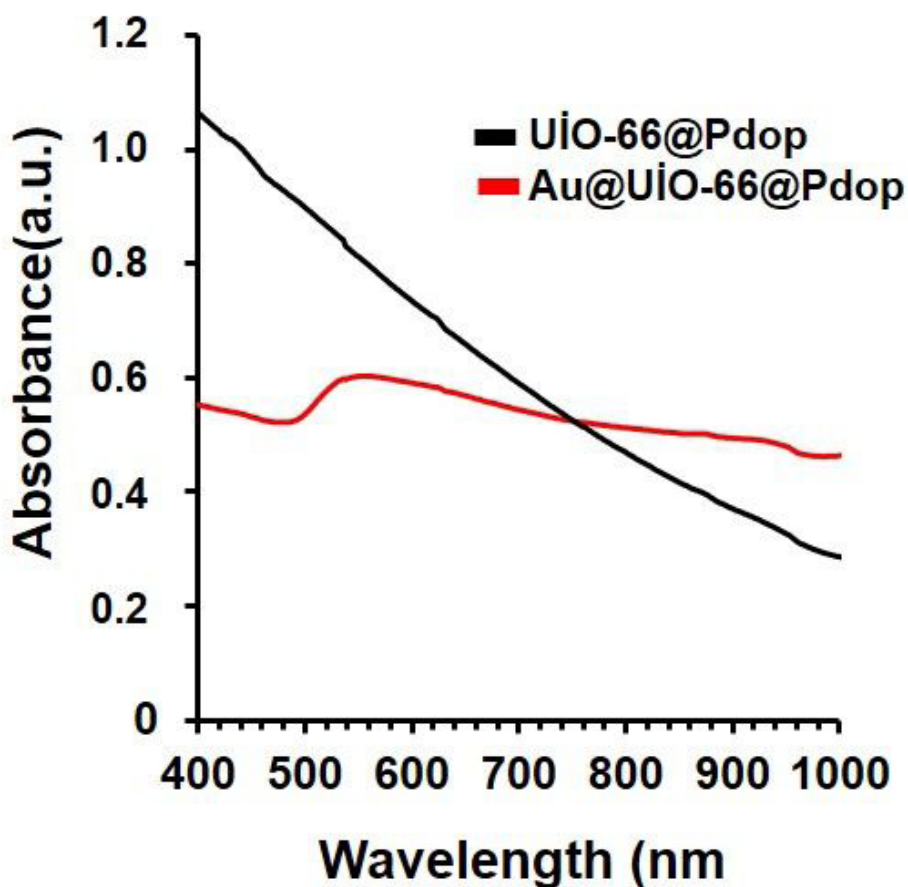


Figure 3. UV-vis spectra of the aqueous solution of UiO-66@Pdop and Au@UiO-66@Pdop NPs.

XPS Spectrometer, source gun: Al K-Alpha at 1.4 kV focus voltage, beam current: 6 mA). The UV-vis measurement of devices was performed by Shimadzu 3600 spectrophotometer.

Photocatalytic Activity Tests

The photocatalytic degradation of methylene blue (MB) was carried out using a home-made green-LED photo-reactor equipped with a cylinder type aluminium which containing 237 LED lamps. Typically, 20 mL of dye solution (3.125×10^{-5} M) containing 20 mg of plasmonic photocatalyst was magnetically stirred in the dark for 30 min in order to reach an adsorption-desorption equilibrium as well. Then, the light was irradiated onto the solution in which the sampling was carried out in specific time intervals. For this purpose, 2.0 mL of sample solution was taken from the reactor and centrifuged at 5000 rpm for 5 min. The real-time concentration of MB molecules in the supernatant was measured at 610 nm using the UV-vis spectrometer. The same procedure was repeated when the PS (2.0 mM) was introduced in the reaction medium.

RESULTS and DISCUSSION

The synthetic pathway for the fabrication of plasmonic core-shell Au@UiO-66@Pdop MOFs is represented in Figure 1. Firstly, Pdop NPs were synthesized by polymerization of dopamine in alkaline medium using ammonia, ethanol, and DDI water. After that, the one-pot synthesis of well-defined Zr-based MOF shell onto Pdop NPs was carried out using DMF, H₂BCD, and ZrCl₄. The presence of strong diol groups (-OH) onto Pdop NPs led to the enrichment of Zr⁴⁺ ions as well as chelate formation while the organic building blocks (H₂BCD) initiated the nucleation of UiO-66 MOF. This technique prevented the independent formation of MOFs in the reaction medium. Additionally, once the nucleation of MOF onto Pdop NPs was started, the layer-by-layer shell growth realized without free MOF particles in the reaction medium. Finally, Au@UiO-66@Pdop MOFs were achieved using a simple solution impregnation method, in which Au NPs were successfully embedded into the pores of MOF shell as well.

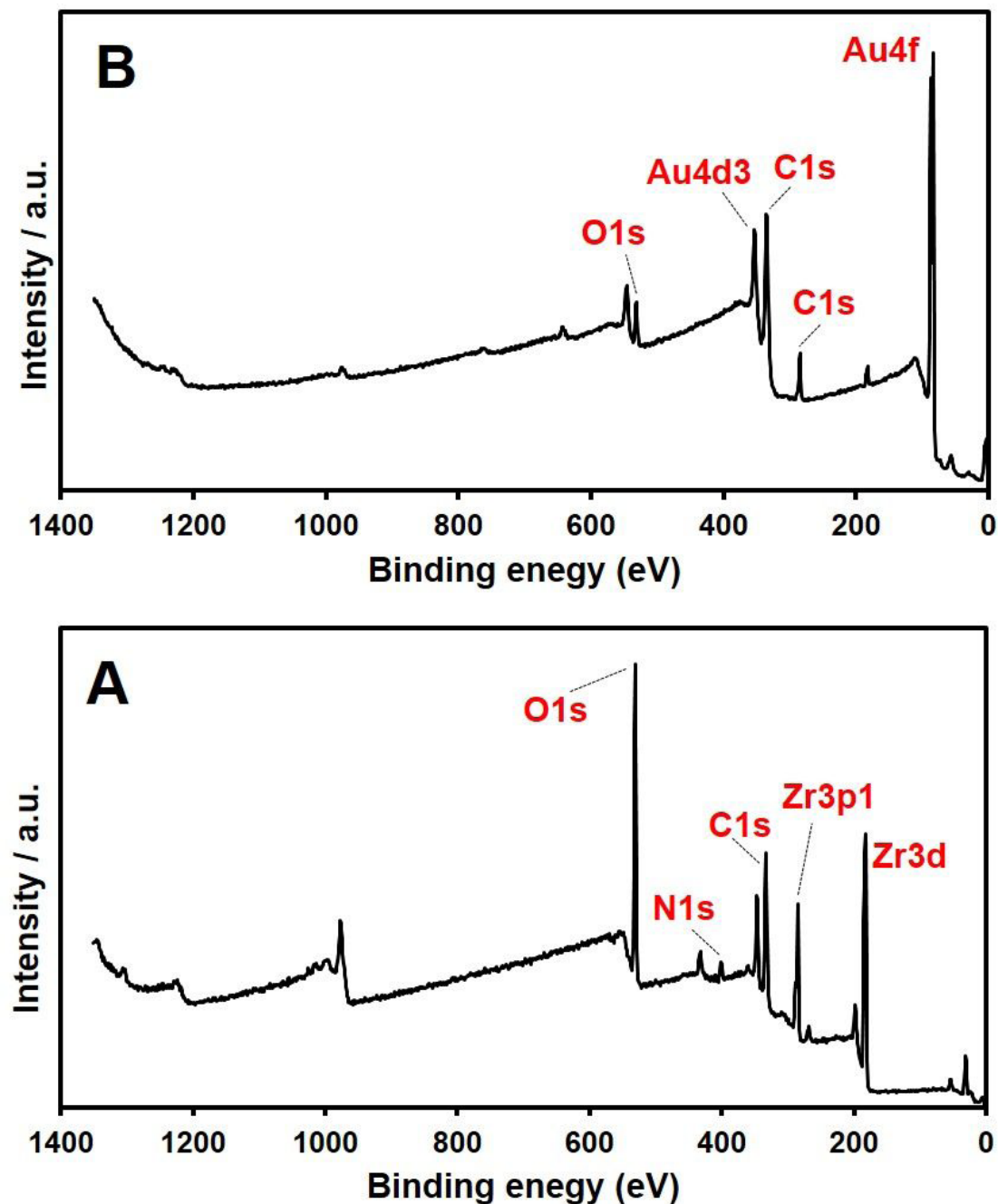


Figure 4. XPS spectra of A) UiO-66@Pdop and B) Au@UiO-66@Pdop NPs.

The SEM images and EDX analysis of the UiO-66@Pdop and Au@UiO-66@Pdop NPs are presented in Figure 2. As seen here, all of the NPs were demonstrated narrow size distribution with no significant change in the spherical morphology of the starting Pdop nanoparticles (Figure 2A and 2B). Additionally, Zr-based MOFs were successfully coated onto the Pdop templates without free MOF aggregates (Figure 2 A, B). Furthermore, the SEM images and EDX mapping of the Au@UiO-66@Pdop

NPs clearly showed that the solution impregnation of Au as well as Au NPs embedding were also successfully synthesized. Moreover, from the EDX analysis, Zr L α 1 (17.5 Wt%), O K α 1 (38.9 Wt%), C K α 1 (43.6 Wt%), and Au M α 1 (53.5 Wt%), C K α 1 (42.2 Wt%), N K α 1 (4.3 Wt%) elemental compositions related to the UiO-66@Pdop and Au@UiO-66@Pdop NPs were achieved with quite clear photographs, respectively.

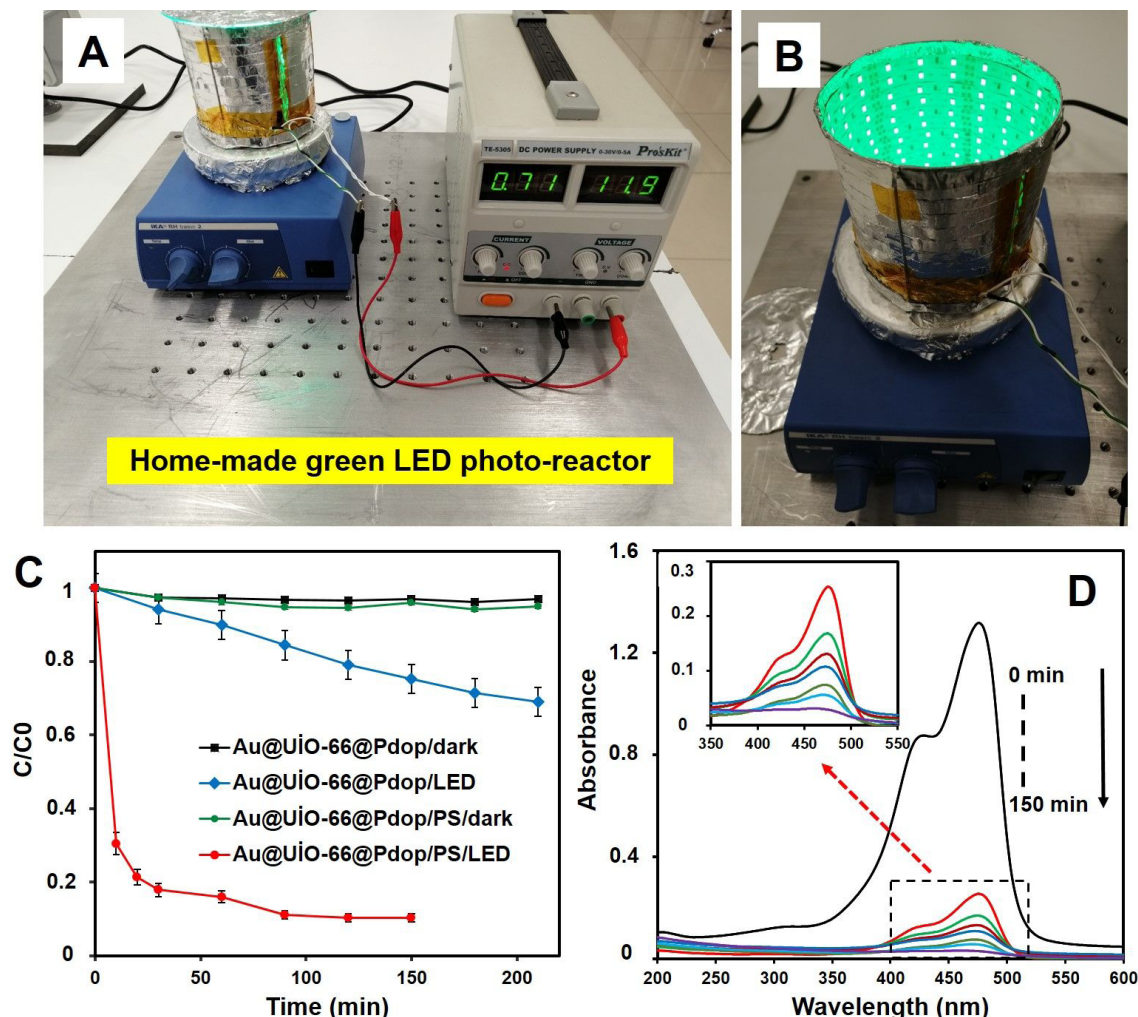


Figure 5. A, B) photographs of the designed home-made green LED photo-reactor, C) The variation of MB concentration (C/C_0) and reaction time at different catalytic conditions (Reaction parameters: MB initial concentration: 3.125×10^{-5} M; Au@UiO-66@Pdop: 20 mg; PS: 2.0 mM), and D) The changes in the UV-vis spectra of MB during the decolorization process using plasmonic catalyst (Reaction parameters: MB initial concentration: 3.125×10^{-5} M; Au@UiO-66@Pdop: 20 mg; PS: 2.0 mM).

Figure 3 showed the UV-vis spectra of the aqueous solution of UiO-66@Pdop and Au@UiO-66@Pdop NPs. As seen here, appearance of a new peak around 554 nm obviously demonstrated the embedding of the Au NPs into the pores of UiO-66@Pdop NPs as well. This peak indicated the localized surface plasmon resonance (LSPR) properties of Au NPs in which no peak was observed around 500-600 nm in the case of UiO-66@Pdop NPs. Moreover, the related LSPR peak are in good agreement with the obtained EDX results in which the dense elemental composition of the Au NPs were successfully identified.

To recognize the chemical states of the UiO-66@Pdop and Au@UiO-66@Pdop NPs, the XPS analysis technique were employed (Figure 4). As seen here, five main

peaks (i.e., O 1s, N 1s, C1s, Zr 3p1, and Zr 3d) related to the binding energies of the UiO-66@Pdop NPs were observed with good intensities (Figure 4A). In Figure 4B, Au 4d3 and Au 4f binding energies were supported the presence of Au NPs into the pores of UiO-66@Pdop nanostructures which are in good agreement with EDX and UV-vis results. Note that, embedding of Au NPs via solution impregnation method significantly influenced the XPS results that identified the successful fabrication of the plasmonic Au@UiO-66@Pdop NPs (Figure 4B).

The photocatalytic decolorization of MB was performed to study the photocatalytic performance of Au@UiO-66@Pdop NPs under green LED light irradiation (Figure 5A, B). For this purpose, the aerobic degradation of MB was carried out in an aqueous solution (20 mL) containing 20 mg

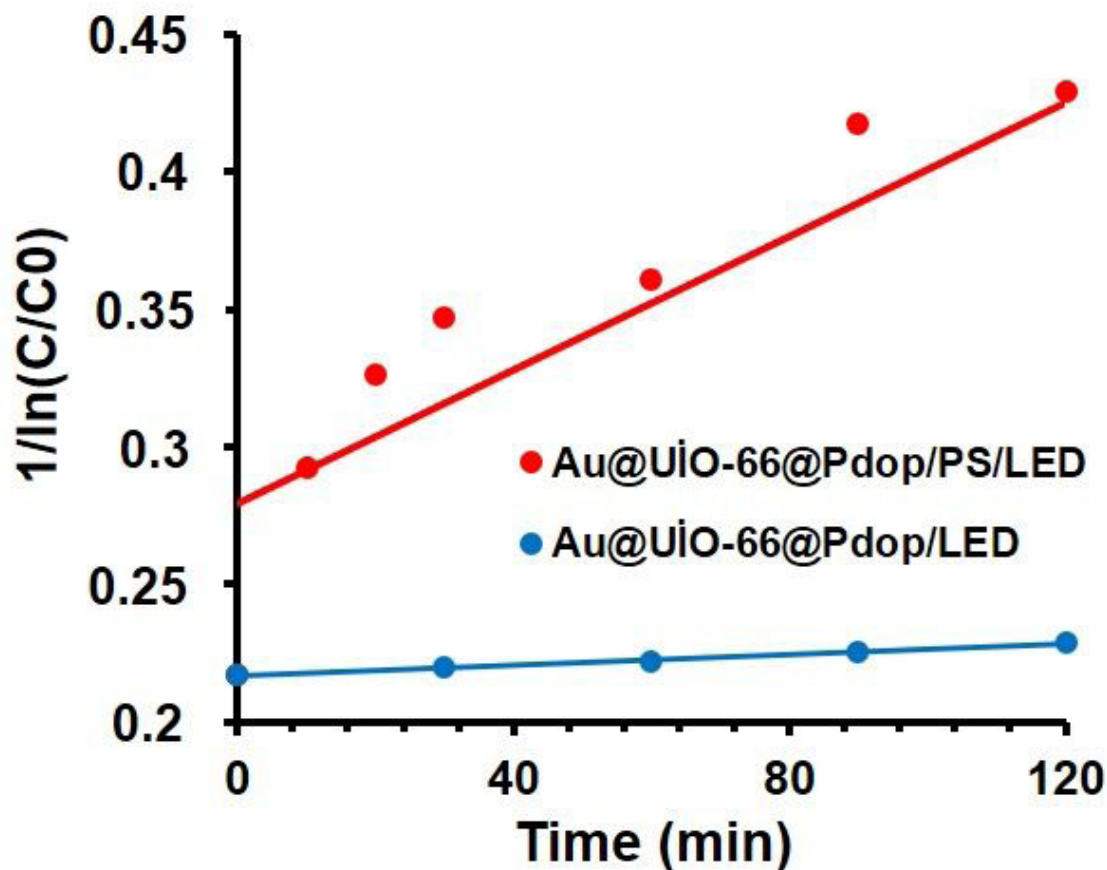


Figure 6. The plots of pseudo-second-order kinetic model for the photocatalytic degradation of MB.

of plasmonic catalyst. Different catalytic conditions were employed to investigate the variations of the MB concentration (C/C_0)/reaction time functions (Figure 5C). As seen here, without light irradiation, no significant degradation was achieved for 210 min, demonstrated that MB was very stable toward Au@UiO-66@Pdop/dark or Au@UiO-66@Pdop/PS/dark conditions. These two important results clearly showed that plasmonic Au@UiO-66@Pdop NPs neither decolorized the MB solution nor activated the PS and reactive charge carriers in dark reaction medium. While in the case of Au@UiO-66@Pdop/LED, a moderate 31% bleaching degree was recorded. This value might be attributed to the compatibility between green LED and plasmonic Au@UiO-66@Pdop absorption wavelength (see Figure 3). In order to achieve a reasonable bleaching degree, the fast recombination between photogenerated electron (e^-) and hole (h^+) pairs must be minimized [16, 19]. The introduction of PS into photocatalytic reaction medium either increased the performance of Au@UiO-66@Pdop NPs directly or generated reactive charge carriers in which 91% decolorization of MB was recorded within 120 min (Figure 5C). Furthermore, PS (i.e., an electron acceptor) inhibited the recombination between photogenerated

electron (e^-) (i.e., generated electron from Au@UiO-66@Pdop catalyst) and hole (h^+) pairs as well as accelerated the decolorization of MB under LED light irradiation.

The photocatalytic performance of Au@UiO-66@Pdop NPS as well as real-time concentration of MB molecules in the supernatant were measured using the UV-vis spectrometer (Figure 5D). As seen here, the concentration of the MB was sharply decreased under green LED irradiation. After 120 min, approximately 91% of the MB was bleached which corresponds to the structural changes in the chromophoric groups of the dye molecules [20]. Furthermore, the pseudo-second-order reaction kinetics of the photocatalysts were calculated and the obtained results were reported in Figure 6. The reaction rate constants related to the bare (Au@UiO-66@Pdop/LED) and oxidant containing catalyst (Au@UiO-66@Pdop/PS/LED) are obtained to be 0.0001 and 0.0012 min^{-1} , respectively. These results clearly demonstrated the higher catalytic activity of oxidant containing reaction medium compared to the bare one.

CONCLUSION

In summary, plasmonic Au@UiO-66@Pdop NPs were synthesized for efficient decolorization of MB under green LED light irradiation. The catechol groups of the Pdop NPs initiated the Zr (IV) chelate formation in which the organic building blocks started the nucleation of the MOF layer. The physico-chemical analysis of the NPs clearly revealed that stable plasmonic photocatalyst with desired morphology was obtained. A superior and satisfied bleaching degree was achieved thanks to the wavelength compatibility between the irradiated light source as well as good dispersion of the Au@UiO-66@Pdop NPs in reaction medium. Moreover, the introduction of PS accelerated the decolorization via reducing the charge recombination. The combination between the Au@UiO-66@Pdop NPs and green LED light for visible light degradation of such an organic pollutant could provide the wide range application of the plasmonic MOFs.

Acknowledgments

This study was partially supported by Ankara Yildirim Beyazit University Scientific Research Unit (Grant No. 4875 and 4736). I would like to thank Mustafa Yasir Aydin for his help with some of the measurements.

References

- S. Cao, C.J. Wang, X.J. Lv, Y. Chen, W.F. Fu, A highly efficient photocatalytic H₂ evolution system using colloidal CdS nanorods and nickel nanoparticles in water under visible light irradiation, *Appl. Catal. B: Environ.*, 162 (2015) 381–391.
- T. Baran, S. Wojtyła, A. Dibenedetto, M. Aresta, W. Macyk, Zinc sulfide functionalized with ruthenium nanoparticles for photocatalytic reduction of CO₂, *Appl. Catal. B: Environ.*, 178 (2015) 170–176.
- K. Villa, S. Murcia-López, T. Andreu, J.R. Morante, Mesoporous WO₃ photocatalyst for the partial oxidation of methane to methanol using electron scavengers, *Appl. Catal. B: Environ.*, 163(2015) 150–155.
- C.C. Wang, J.R. Li, X.L. Lv, Y.Q. Zhang, G. Guo, Photocatalytic organic pollutants degradation in metal–organic frameworks, *Energy Environ. Sci.*, 7 (2014) 2831–2867.
- S. Yuan, L. Feng, K. Wang, J. Pang, M. Bosch, C. Lollar, Y. Sun, J. Qin, X. Yang, P. Zhang, Q. Wang, L. Zou, Y. Zhang, L. Zhang, Y. Fang, J. Li, H.C. Zhou, Stable metal–organic frameworks: design, synthesis, and applications, *Adv. Mater.*, 30 (2018) 1704303.
- C. Yu, S. Bourrelly, C. Martineau, F. Saidi, E. Bloch, H. Lavrard, F. Taulelle, P. Horcajada, C. Serre, P. L. Llewellyn, E. Magnier, T. Devic, Functionalization of Zr-based MOFs with alkyl and perfluoroalkyl groups: the effect on the water sorption behavior, *Dalton Trans.*, 44 (2015) 19687–19692.
- C. Wang, G.L. Guo, P. Wang, Synthesis, structure, and luminescent properties of three silver(I) complexes with organic carboxylic acid and 4,4'-bipyridine-like ligands, *Transition Met. Chem.*, 38 (2013) 455–462.
- C.Y. Sun, S.X. Liu, D.D. Liang, K.Z. Shao, Y.H. Ren, Z.M. Su, Highly stable crystalline catalysts based on a microporous metal–organic framework and polyoxometalates, *J. Am. Chem. Soc.*, 131 (2009) 1883–1888.
- J.R. Li, J. Sculley, H.C. Zhou, Metal–organic frameworks for separations, *Chem. Rev.*, 112 (2011) 869–932.
- N.L. Rosi, J. Eckert, M. Eddaoudi, D.T. Vodak, J. Kim, M. O’Keeffe, O. M. Yaghi, Hydrogen storage in microporous metal–organic frameworks, *Science*, 300 (2003) 1127–1129.
- A.R. Millward, O.M. Yaghi, Metal–organic frameworks with exceptionally high capacity for storage of carbon dioxide at room temperature, *J. Am. Chem. Soc.*, 127 (2005) 17998–17999.
- C. Wang, P. Wang, L. Feng, Influence of organic carboxylic acids on self-assembly of silver(I) complexes containing 1,2-bis(4-pyridyl) ethane ligands, *Transition Met. Chem.*, 37 (2012) 225–234.
- C.G. Silva, A. Corma, H. Garcia, Metal–organic frameworks as semiconductors, *J. Mater. Chem.*, 20 (2010) 3141,3156.
- F.X. Llabrés i Xamena, A. Corma, H. Garcia, Applications for metal–organic frameworks (MOFs) as quantum dot semiconductors, *J. Phys. Chem.*, C 111 (2007) 80–85.
- M.C. Das, H. Xu, Z. Wang, G. Srinivas, W. Zhou, Y.F. Yue, V.N. Nesterov, G. Qian, B. Chen, A Zn₂O-containing doubly interpenetrated porous metal–organic framework for photocatalytic decomposition of methyl orange, *Chem. Commun.*, 47 (2011) 11715–11717.
- Y. Gao, S. Li, Y. Li, L. Yao, H. Zhang, Accelerated photocatalytic degradation of organic pollutant overmetal-organic framework MIL-53(Fe) under visible LED lightmediated by persulfate, *Appl. Catal. B Environ.*, 202 (2017) 165–174.
- K. Ai, Y. Liu, C. Ruan, L. Lu, G. Lu, Sp² C-Dominant N-Doped Carbon Submicrometer Spheres with Tunable Size: A Versatile Platform for Highly Efficient Oxygen Reduction Catalysts, *J. Adv. Mater.*, 25 (2013) 998–1003.
- M. Zhao, C. Deng, X. Zhang, The design and synthesis of a hydrophilic core– shell–shell structured magnetic metal–organic framework as a novel immobilized metal ion affinity platform for phosphoproteome research, *Chem. Commun.*, 50 (2014) 6228–6231.
- J.J. Du, Y.P. Yuan, J.X. Sun, F.M. Peng, X. Jiang, L.G. Qiu, A.J. Xie, Y.H. Shen, J.F. Zhu, New photocatalysts based on MIL-53 metal–organic frameworks for the decolorization of methylene blue dye, *J. Hazard. Mater.*, 190 (2011) 945–951.
- B. Paul, B. Bhuyan, D.D. Purkayastha, M. Dey, S.S. Dhar, Green synthesis of gold nanoparticles using Pogestemon benghalensis (B) O. Ktz. leaf extract and studies of their photocatalytic activity in degradation of methylene blue, *Mater. Lett.*, 148 (2015) 37–40.



Assessment of The Spatio-Temporal Distribution and Habitat Preferences of Ostracoda (Crustacea) Related to Certain Environmental Factors in Kapıdağ Peninsula (The Sea of Marmara, Turkey)

Kapıdağ Yarımadası'ndaki (Marmara Denizi, Türkiye) Ostrakodların (Crustacea) Çevresel Faktörlere Bağlı Olarak Spatio-Temporal Dağılımı ve Habitat Tercihleri

Ferda Perçin Paçal¹, Selçuk Altınışaçlı², Saltuk Buğra Arısal³, Hüsamettin Balkıs⁴

¹Istanbul University, Aziz Sancar Institute of Experimental Medicine, Department of Genetics, Şehremini, Istanbul, Turkey.

²Merdivenköy Mahallesi, Ortabahar Sok. No: 20/4, Kadıköy, İstanbul, Turkey.

³Nişantaşı University, Vocational School, Medical Laboratory Techniques, Bayrampaşa, İstanbul, Turkey.

⁴Istanbul University, Faculty of Science, Department of Biology, Vezneçiler, İstanbul, Turkey.

ABSTRACT

The Sea of Marmara is exposed to pollutants in excess from the coastal industrial facilities and intensive urbanization, and because of that, the ecosystem is affected negatively. The aim of this study was to determine the environmental factors and ecological parameters on the species distribution and abundance of Ostracoda in Kapıdağ Peninsula coastline. At four seasons (April, July, October 2011 and January 2012), samples were collected from 21 stations (total of 84 samples) and 36 Ostracoda species were identified. The most distributed ostracod species were *Carinocythereis antiquata*, *Aurila convexa*, *Loxococoncha gibberosa*, *Paradoxostoma fuscum*, *Cushmanidea elongata*, and *Xestoleberis decipiens*. The highest numbers of individuals observed were *Loxococoncha rhomboidea* and *Xestoleberis aurantia*. During the study, water temperature varied between 7.5 and 30°C, salinity varied between 12.1 and 29.2‰, pH varied between 6.6 and 8.7, and dissolved oxygen varied between 1.2 and 15.3 mgL⁻¹ in the stations across the four seasons. Depth, mud percentage and the transparency of the water were the most effective factors on the living ostracod species of Kapıdağ Peninsula coastline according to spearman correlations.

Key Words

Kapıdağ Peninsula, ostracoda, ecology, distribution.

ÖZ

Marmara Denizi, kıyısında yer alan yoğun sanayileşme ve kentleşmeden dolayı kirliliğe maruz kalmakta, bu nedenle de ekosistemi olumsuz yönde etkilenmektedir. Bu çalışmada Kapıdağ Yarımadası kıyısındaki Ostracoda türlerinin dağılımı ve bolluğuna etki eden çevresel faktörlerin ve ekolojik parametrelerin belirlenmesi hedeflenmiştir. Dört mevsim boyunca (Nisan, Temmuz, Ekim 2011 ve Ocak 2012) 21 istasyonda (toplam 84 adet) örnek toplanmış ve 36 Ostracoda türü belirlenmiştir. En geniş dağılım gösteren türlerin *Carinocythereis antiquata*, *Aurila convexa*, *Loxococoncha gibberosa*, *Paradoxostoma fuscum*, *Cushmanidea elongata*, ve *Xestoleberis decipiens* olduğu görülmüştür. En fazla birey sayısı *Loxococoncha rhomboidea* ve *Xestoleberis aurantia* türlerinde saptanmıştır. Çalışmada dört mevsim boyunca sıcaklık 7.5-30°C, tuzluluk ‰12.1-29.2, pH 6.6-8.7, ve çözünmüş oksijen 1.2-15.3 mgL⁻¹ aralıklarında belirlenmiştir. Spearman korelasyon analizine göre derinlik, çamur yüzdesi ve görünürlüğün Kapıdağ Yarımadası kıyılarında yaşayan ostrakod türleri üzerinde en etkili faktörler olduğu belirlenmiştir.

Anahtar Kelimeler

Kapıdağ Yarımadası, ostrakod, ekoloji, dağılım.

Article History: Received: Feb 25, 2019; Revised: May 18, 2019; Accepted: Jun 25, 2019; Available Online: Nov 1, 2019.

DOI: <https://doi.org/10.15671/hjbc.531987>

Correspondence to: F. Perçin-Paçal, Aziz Sancar Institute of Experimental Medicine, ¹Istanbul University, Şehremini, Istanbul, Turkey.

E-Mail: ferda.pacal@istanbul.edu.tr

INTRODUCTION

The small bivalved crustaceans, ostracods, have laterally compressed bodies and two calcified valves. These crustaceans are diverse at very different environmental conditions [1, 2], including estuaries, seas, oceans, lagoons, lakes, ponds, streams, springs, rivers, peatlands, caves [3] and groundwaters from deep seas [4] to coastal and also terrestrial environments [5]. Fossils and living ostracods have been used as important indicator organisms for recent paleoecological studies because of their great potential for ecological monitoring [6,7]. The ostracod species, widely distributed in aquatic areas, are important for ecological balance in terms of the separation of detritus and the nutrition of fish. Ostracods are also an important food source for invertebrates [5] and fish [8]. In both polluted and clean aquatic environments, ostracods are indicators of changes in marine habitats [9], which can be more reliable and more economic for environmental monitoring than long-term chemical analyses. Their composition, density, and diversity of assemblages are controlled by environmental parameters (salinity, temperature, pH, oxygen, hydrodynamic conditions with the type of substratum) and also related to anthropogenic pollution (e.g. nutrient and heavy metal content) [2,6,10]. They are sensitive to anthropogenic pollution [11,12] and can be used as indicators in marine, brackish, and freshwater environments [13-17].

The Sea of Marmara, which divides the Asian and European parts of Turkey, is a transitional waterway bet-

ween the Black Sea and the Mediterranean Sea in the Turkish Strait System (TSS). This inner sea connects the Black Sea and the Aegean Sea with the Bosphorus in the north and the Dardanelles in the south [18]. The Sea of Marmara which covers a surface area of 11,350 km² is under pressure of pollution from large industrial establishments as well as the high population density and its domestic waste [19].

To date, 210 benthic ostracod species have been determined from the Sea of Marmara [20]. Also, 382 ostracod species have been reported in Turkish seas (326 from marine and 56 from coastal brackish waters) [21]. Perçin-Paçal and Balkis, (2012) [22] reported 112 ostracod species (including most of the ostracod species identified in this study) together with their SEM photographs from Bandırma Bay and Erdek Bay, which compose the east end west side of Kapıdağ Peninsula. Our new data of the ecological parameters and species compositions are compared with the above-mentioned study by Perçin-Paçal and Balkis, (2012) [22] and other studies [23, 24].

The present study aims to investigate the relationships of the recent ostracod species with different physicochemical parameters, a determination of spatio-temporal distributions, and habitat preferences of the species living between a depth of 0.5 and 30 m on the Kapıdağ Peninsula coastline. The secondary objective of this paper is to analyze the spatial and seasonal change of physicochemical and biological parameters considered to be caused by anthropogenic activities.

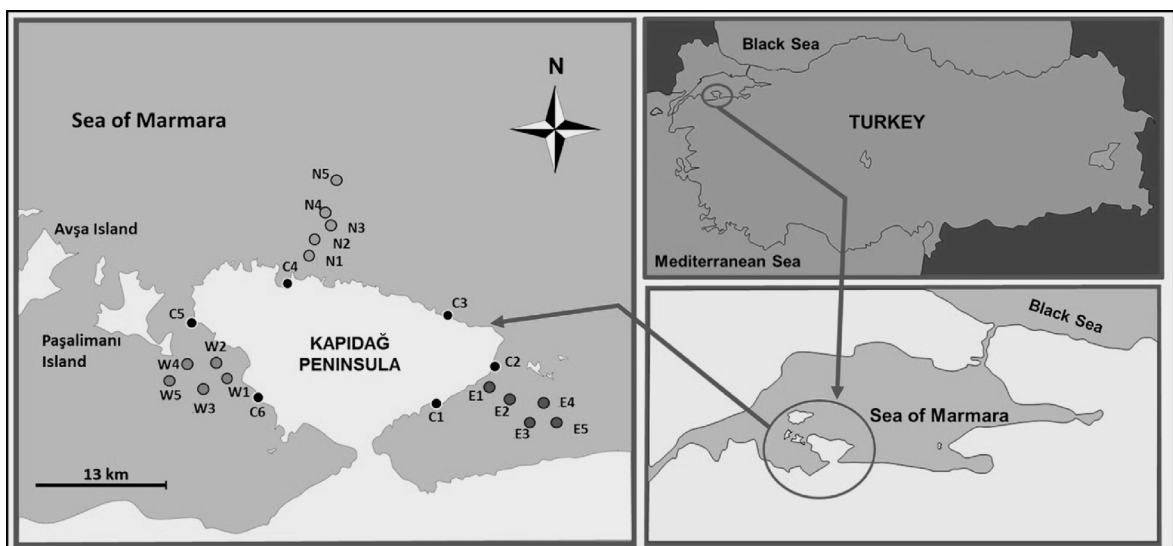


Figure 1. Locations of the sampling stations.

MATERIALS and METHODS

Study Area

Kapıdağ Peninsula is located between Bandırma Bay (in the southeast) and Erdek Bay (in the southwest) on the southern coast of the Sea of Marmara (Figure 1). The area of the peninsula is approximately 290 km². It is generally covered with bushes and, in some areas, forests, too. Tourism and fishing are widespread in the region. Erdek, covered with olive groves, fruit gardens, and vineyards, is a popular tourist center in the region. Bandırma Bay has a higher population density and industrial activities compared with Erdek Bay, meaning it is threatened by pollution from industrial and domestic waste as a result of industrial facilities surrounding it and population growth.

Bandırma is a developing industrial region and a major contributor to the regional economy and population growth with an organized industrial zone, founded in 1997 and located over an area of 150 hectares [25]. With the acceleration of industrialization, an additional area of 200 hectares was set aside to contribute to the development of trade. Bandırma Port is the second

largest port in the Sea of Marmara after Istanbul Port [25]. In the future, Bandırma Port will become bigger, which will create negative environmental effects on the Sea of Marmara, which has already received most of Bandırma's pollution. Therefore, there is a strong possibility that the data from this study will contain valuable information for the future of the region.

The oceanographic characteristics of the coastline of Kapıdağ Peninsula are similar to the Sea of Marmara, and the water column has a two-layer structure. The surface water (the brackish Black Sea water) of the Sea of Marmara has a salinity of 17.6‰ and flows through the Bosphorus to the Sea of Marmara. The waters of the Mediterranean originate with a salinity of about 38 ‰ and flow through the Dardanelles to the Sea of Marmara in a lower layer. According to the density differences between the two water layers, there is an intermediate (Halocline zone) salinity mass 25 m deep [19].

Sampling Procedure

The sampling was carried out from 21 stations at depths of 0.5, 1, 5, 10, 20, and 30 m out from the southeast, southwest, and north sides of the peninsula in April, July,

Table 1. Results of human serum samples.

Stations	Coordinates	Depth	Sediment type	Sampling equipment
N1	40°30'48.1"N-27°48'14.1"E	1	Sand	Van Veen Grab
N2	40°30'51.7"N-27°48'15.8"E	5		
N3	40°30'55.8"N-27°48'21.4"E	10		
N4	40°30'59.4"N-27°48'21.3"E	20		
N5	40°31'10.9"N-27°48'27.4"E	30		
W1	40°26'08.2"N-27°44'55.0"E	1	Sand and mud	
W2	40°26'08.4"N-27°44'54.2"E	5		
W3	40°26'08.5"N-27°44'53.2"E	10		
W4	40°26'11.4"N-27°44'48.3"E	20		
W5	40°26'11.0"N-27°44'46.1"E	30		
E1	40°26'38.7"N-28°00'32.2"E	1	Mud	
E2	40°26'39.1"N-28°00'32.5"E	5		
E3	40°26'37.2"N-28°00'33.4"E	10		
E4	40°26'35.5"N-28°00'31.6"E	20		
E5	40°26'32.5"N-28°00'30.8"E	30		
C1	40°25'22.7"N-27°57'17.7"E	0.5	Mytilus galloprovincialis, photophilic algae	hand net (mesh size 50 µm)
C2	40°27'35.9"N-28°01'23.7"E	0.5		
C3	40°29'33.7"N-27°57'52.9"E	0.5		
C4	40°30'24.1"N-27°47'30.9"E	0.5		
C5	40°29'38.9"N-27°40'59.5"E	0.5		
C6	40°26'04.0"N-27°44'53.3"E	0.5		

October 2011, and January 2012 (Figure 1). The coordinates for each sampling site were determined using a hand-held GPS. Coordinates and other characteristics of each sampling site are given in Table 1.

The Ostracoda samples were collected with a hand net (mesh size 50 μm) from six stations (from shallow waters not exceeding 50 cm in depth) which has 0.1 m² sampling area. For other stations, a Van Veen Grab sampler was used to perform vertical cross-section sampling at depths of 1, 5, 10, 20, and 30 m which has 0.1 m² sampling field. Two replicates were collected in each station. The 200 gr of the uppermost sediments was fixed in 70% ethanol in situ. Also 200 gr sediments were gathered and stored for the sediment analysis. For distinguish the ostracod species, the sediment was washed off under pressurized tap water and separated into four grain-size fractions by using standardized sieves (2, 1.5, 0.5, 0.25, and 0.125 mm mesh size). Ostracods were sorted under a stereomicroscope and fixed again in 70% ethanol. Subsequently, the washed specimens were preserved in 70% ethanol, and the retained material transferred to a petri dish to be picked out of the sediment under a stereo zoom microscope, and the soft body parts were dissected in lactophenol solution for taxonomic identification. The number of adult individuals belonging to each identified ostracod species was detected. The ostracods were handpicked and identified using the keys developed by Mordukhai and Boltovskoi (1969) [26], Schornikov (1969) [27], Barbeito-Gonzales (1971) [28], Hartmann and Puri (1974) [29], Bonaduce et al. (1975) [30], Athersuch et al. (1989) [31], Yassini (1979) [32], and Stambolidis (1985) [33]. The current taxonomy and classification of ostracod species were checked using the WoRMS (2018) [34] (<http://www.marinespecies.org/aphia.php?p=taxdetails&id=1078>).

Analytical Procedure

The sea water was collected by 3L Ruttner water sampler with marked rope at 5m intervals from five different depths (1, 5, 10, 20 and 30m) for the physico-chemical analyses. The sea temperature ($^{\circ}\text{C}$) at the water sampling depth was measured by means of a thermometer fixed to the Ruttner water sampler. The Winkler method [35] was used to measure dissolved oxygen (DO) (mgL^{-1}) and the Mohr-Knudsen method [36] for the salinity (Sal.) (‰). The Orion multiparameter device was used to measure the pH and ORP value of the seawater in situ. The transparency of the water was determined by using a 25 cm diameter Secchi disc. Mud percentage analyses

of the sediments were defined according to Folk (1974) [37] methods and classification, sand fraction is composed by grains whose diameter varies from 63 to 2000 mm, silt fraction consists of grains with diameter ranging between 4 and 63 μm , and clay fraction constitutes very fine material, whose diameter is less than 4 μm . Total organic carbon (TOC) was analyzed using the Walkley-Blake method, which involves titration after a wet combustion of the samples [38,39]. The total calcium carbonate contents of the sediments were determined using the gasometric-volumetric method [39].

Statistical Analyses

Bray-Curtis similarity index was used to detect the species similarity among the 21 sampling stations. The degree of similarities were expressed as dendrograms. Bray-Curtis similarity index were estimated using Biodiversity Pro software package 2.0 [40]. Also this software package was used to examine seasonal distributional differences in ostracod species and to calculate the Shannon–Weaver diversity index (H') Pielou's evenness (J') and Margalef richness (D') for each site across four seasons. [40]. These calculation indexes were based on the 36 ostracod species found at the sites.

The frequency of ostracod species was calculated by using the formula $F = N_{ax}100/N_n$. F is the frequency of the species, N_a is the number of sampling stations containing the species, and N_n is the total number of sampling stations [41, 42].

The two-tailed Spearman rank correlation test [43] was applied to evaluate the levels of correlations between the environmental variables (temperature, salinity, pH, dissolved oxygen, total organic carbon, total calcium carbonate, transparency of the water, oxidation-reduction potential, and depth), and 36 ostracod species.

Canonical correspondence analysis (CCA) was also used to evaluate the species–environment relationships and to identify environmental factors potentially influencing ostracod assemblages [44]. Data were analyzed using the Multi-Variate Statistical Package (MVSP), version 3.22 [45].

RESULTS

Species Assemblages

In this study, 36 ostracod species belonging to 12 families were determined from the 21 stations sampled over the four seasons (Table 2). A total of 5841 individuals were counted. The highest number of individuals observed were: *L. rhomboidea* (Fischer, 1855) (369 individuals) and *X. aurantia* (Baird, 1838) (351 individuals) species. The greatest numbers of species and individuals were observed from the genera of *Loxoconcha* (5 species and 1614 individuals), *Xestoleberis* (4 species and 1185 individuals), and *Paradoxostoma* (4 species and 834 individuals).

Carinocythereis antiquata, *A. convexa*, *L. gibberosa*, *P. fuscum*, *P. maculatum*, *C. elongata*, and *X. decipiens* were the most distributed species on the Kapıdağ Peninsula coastline (see Table 2). The most frequent species were *L. gibberosa* (78.6%), *X. decipiens* (78.6%), and *A. convexa* (77.4 %); the least frequent species were *B. dentata* (3.6%), *P. jonesii* (3.6%), and *P. ceratoptera* (4.8%) (see Table 2).

Water Quality

During the study, water temperature varied between 7.5°C and 30°C, salinity varied between 12.5 and 29.2 ‰, pH varied between 6.6 and 8.7, ORP varied between -104.1 and 672.3 and DO varied between 1.2 and 15.3 mg L⁻¹. Total organic carbon content of the sediment varied between 0.02% and 3.5%, total calcium carbonate varied between 0.3% and 85.9%, and mud percentages were highest in the deeper stations compared with the coastal sampling stations (Table 3).

Species Tolerance and Environment Correlation

Species such as *L. rhomboidea*, *L. stellifera*, *L. tumida*, *L. minima*, *X. aurantia*, *X. communis*, and *A. prasina* are dominant species because these species are highly tolerant to various ecological variables (see Table 3). Some habitat variables and ostracod species observed on the coastline of Kapıdağ Peninsula are shown in Table 3.

According to the Shannon–Weaver diversity index values, the highest species diversity was determined at sampling stations W-2 and W-3 in spring and the lowest in fall at the sampling station N-4. Pielou's evenness (*J'*) results were highest at sampling stations N-3, N-4, and

E-4 in fall, E-3, E-4, E-5, and C-5 in winter, and were the lowest at the sampling station E-3 in spring. According to Margalef richness (*D'*) results, the highest value was determined at sampling station N-4 in fall, while the lowest value was at station W-3 in summer (Table 4).

Bray-Curtis similarity index illustrates eight clustering groups of species (Figure 3 A). Groups 7 and 8 have sub-clusters grouped by similarity of ostracod assemblages. Most ostracods determined in this study have been found in the continental shelf of the Sea of Marmara. Therefore most of them are high tolerant and abundant species and they grouped together with in the seventh clustering group (Table 3). Bray-Curtis similarity index illustrates five clustering groups of stations (Figure 3 B). The level of similarity among station with a cluster is highly related to habitat type and depth as seen in Figure 3 B (Table 1). Because C-1, C-2, C-3, C-4, C-5, C-6 are coastal stations and grouped together with. Also W-1, W-2, W-3, W-4, W-5 stations grouped together with in the west side of the Kapıdağ peninsula.

The significant correlations among the 36 species and 10 environmental variables according to the results of the Spearman correlation analysis are shown in Table 5. Depth, mud percentage, and transparency of the water were the most effective ecological parameters on the ostracod species according to Spearman correlations on the Kapıdağ Peninsula coastline.

While there was no significant relationship between the number of species and physicochemical parameters at the stations, a positive correlation was found between the number of individuals and total calcium carbonate and species numbers (Table 6).

The relationship between the physicochemical variables and species composition on the Kapıdağ Peninsula coastline is illustrated by the CCA biplot in Figure 4. The lengths of the arrows on the CCA graph show the strong effect of environmental variables on the distribution of ostracods (Figure 4). According to the results of the CCA, mud percentage and TCC content were the factors most affecting ostracod species on the Kapıdağ Peninsula coastline. Also species composed groups coherent with Bray-Curtis dendrograms (Figure 3) that shown with dashes in Figure 4.

Table 3. Determined environmental variables in habitats of living ostracod species on the coasts of Kapıdağ Peninsula. (Abbreviations: Sal= salinity, DO = dissolved oxygen; T = temperature; TOC = total organic carbon; TCC = total calcium carbonate; ORP = oxidation-reduction potential; SD = Secchi depth; MP = mud percentage; TNI = total number of individuals).

Species Code	Depth (m)	Sal. (‰)	DO (mgL ⁻¹)	pH	T (°C)	TOC (%)	TCC (%)	MP (%)	ORP	SD (m)	TNI
Achx	0-30	17.7-27.9	1.2-14.6	7.4-8.7	7.5-27	0.29-2.41	0.7-85.85	0.3-70.8	(-85);610.3	0.5-10.5	129
Acon	0-30	12.5-29.2	1.2-14.7	6.6-8.7	7.5-30	0.02-2.89	0.3-85.85	0.3-94.2	(-104.1);672.3	0.5-13	291
Apra	0-30	12.5-29.2	1.2-14.7	6.6-8.7	7.5-30	0.02-2.89	0.3-85.85	0.3-94.2	(-85);672.3	0.5-12	312
Bber	1-30	17.1-28.2	1.2-15.3	6.6-8.7	7.5-27	0.02-3.5	0.7-85.9	2.4-74.1	(-85);623.6	1-11.0	120
Bden	5-10	19-24.7	1.6-14.3	7.6-8.2	7.5-16.5	0.52-2.1	4.6-22.1	10.6-13.4	35.4;610.3	2.7-10.0	9
Bsub	1-30	19-27.5	1.2-14.3	7.4-8.2	8.0-17.0	0.59-2.89	0.4-22.1	2.2-70.8	(-85);610.6	1.0-12.0	72
Cant	0-30	12.7-29.2	1.2-15.3	6.6-8.7	7.5-27	0.02-2.41	0.3-85.9	0.3-94.2	(-85);672.3	0.5-12.0	225
Cbat	1-30	17.7-29.2	2.0-9.9	7.4-8.2	8.0-18.0	0.5-2.1	0.7-22.1	2.4-94.2	(-38.4);364.8	1.0-12.0	48
Ccar	0-30	17.7-29.2	1.2-15.3	6.6-8.7	7.5-27	0.02-2.3	0.3-85.85	0.4-94.2	(-84.3);599.5	0.5-12.0	117
Cdif	0-30	16.8-25.9	2.0-13.2	7.2-8.7	8.0-27.0	0.5-2.1	0.3-22.1	0.4-94.2	54.5-592	0.5-10	36
Cedw	0-30	21.2-25.9	2.0-10.5	7.0-8.2	8.0-27.0	0.47-2.1	0.3-17.98	0.4-94.2	54.5-672.3	0.5-10	42
Celo	0-30	12.5-29.2	1.2-14.6	6.6-8.7	7.5-30.0	0.02-2.89	0.3-85.9	0.3-94.2	(-85);672.3	0.5-12	207
Cqua	0-10	17.7-25.4	2.0-13.2	7.6-8.7	8.0-28.0	0.29-2.1	0.6-22.1	0.3-13.4	54.5-413.1	0.5-10	39
Ctor	0-20	12.5-25.4	1.3-13.2	7.4-8.7	10.7-29	0.06-1.7	0.6-5.8	0.3-0.6	50-643.3	0.50	30
Cvar	10-20	18.3-25	1.2-14.3	7.6-8.2	7.7-27	0.64-2.1	0.4-85.9	0.9-13.4	(-40.6);389.4	2.7-10.5	36
Halb	0-1	12.5-23.7	2.7-15.3	7-8.5	7.5-27	0.02-1.7	1.2-4.06	0.4-58.3	62.3-620.9	0.5-1	24
Lgib	0-30	12.5-28.4	1.2-15.3	7.1-8.7	7.5-30	0.02-3.5	0.3-85.9	0.3-94.2	(-104.1);643.3	0.5-13	318
Llac	0-30	17.1-28.4	1.2-15.3	7.0-8.7	7.5-27	0.42-3.5	0.3-85.85	0.3-94.2	(-104.1);610.3	0.5-13	105
Lmin	0-30	17.1-28.4	1.2-15.3	6.6-8.7	7.5-30	0.02-3.5	0.3-85.9	0.3-94.2	(-85);623.6	0.5-12	315
Lrom	0-30	12.7-29.2	1.2-15.3	6.6-8.7	7.5-30	0.02-3.5	0.3-85.9	0.3-94.2	(-104.1);623.6	0.5-13	369
Lste	0-30	12.7-28.4	1.2-15.3	6.6-8.7	7.5-30	0.02-3.5	0.3-85.9	0.3-94.2	(-84.3);672.3	0.5-12	312
Ltum	0-30	17.1-28.4	1.2-15.3	6.6-8.7	7.5-30	0.02-3.5	0.3-85.9	0.3-94.2	(-104.1);672.3	0.5-13	300
Nmed	0-20	17.1-25.4	1.3-15.3	6.6-8.7	7.5-30	0.02-2.89	0.3-8.2	0.4-74.1	(-57.6);643.3	0.5-12	129

Table 3. Determined environmental variables in habitats of living ostracod species on the coasts of Kapıdağ Peninsula. (Abbreviations: Sal= salinity, DO = dissolved oxygen; T = temperature; TOC = total organic carbon; TCC = total calcium carbonate; ORP = oxidation-reduction potential; SD = Secchi depth; MP = mud percentage; TNI = total number of individuals). Continued.

Species Code	Depth (m)	Sal. (‰)	DO (mgL ⁻¹)	pH	T (°C)	TOC (%)	TCC (%)	MP (%)	ORP	SD (m)	TNI
Pcer	10-30	18.3-25.9	2.0-12.0	7.4-8.1	7.7-15	0.76-1.9	0.4-5.22	0.9-94.2	(-40.6);389.4	7.5-10	12
Pfus	0-30	12.5-29.2	1.2-14.7	6.6-8.7	7.5-30	0.02-2.89	0.3-85.9	0.3-94.2	(-85);672.3	0.5-12	180
Pint	0-30	12.7-29.2	1.2-14.7	6.6-8.7	7.5-30	0.02-2.89	0.3-85.9	0.3-74.1	(-85);672.3	0.5-12	216
Pjon	10	22.6-29.2	1.8-12.0	7.6-7.9	9.5-18.0	0.64-1.41	0.4-7.31	0.9	182.5-599.5	7.5-10	9
Pmac	0-30	17.5-29.2	1.2-14.7	6.6-8.7	7.5-30	0.02-2.89	0.3-85.9	0.3-94.2	(-85);672.3	0.5-12	237
Ppar	0-30	12.5-29.2	1.2-14.7	6.6-8.7	7.5-30	0.02-2.89	0.3-14.5	0.3-94.2	(-104.1);672.3	0.5-13	171
Psim	0-30	12.5-29.2	1.2-14.7	6.6-8.7	7.5-30	0.02-2.89	0.3-85.9	0.3-74.1	(-85);672.3	0.5-12	201
Sacu	1-30	17.7-25.9	1.6-7.3	7.6-8.0	7.5-26.5	0.29-1.3	2.7-8.2	4.3-19.8	62.3-610.3	1-10.5	18
Umar	5-30	21.9-27.5	1.2-9.6	7.6-8.1	7.5-26	0.7-2.58	2.32-9.3	10.6-70.8	(-85.0);610.3	4-10.5	27
Xaur	0-30	12.5-28.2	1.2-15.3	7.0-8.7	7.5-30	0.02-3.5	0.3-85.9	0.3-94.2	(-85);672.3	0.5-10.5	351
Xcom	0-30	17.1-28.4	1.2-15.3	6.6-8.7	7.5-30	0.02-3.5	0.3-85.9	0.3-94.2	(-85);672.3	0.5-12	315
Xdec	0-30	12.5-29.2	1.2-15.3	7.0-8.7	7.5-30	0.02-3.5	0.3-85.9	0.3-94.2	(-104.1);672.3	0.5-13	234
Xdis	0-30	17.1-28.4	1.2-15.3	6.6-8.7	7.5-30	0.02-3.5	0.3-85.9	0.3-94.2	(-104.1);672.3	0.5-13	285

It has been determined that the salinity tolerance ranges of ostracod species on the Kapıdağ Peninsula coastline were between mesohaline to polyhaline. Salinity ranges of the identified ostracod species are shown in Figure 5. Seven ostracod species (*B. berchoni*, *B. dentata*, *C. diffusa*, *C. variabilis*, *P. ceratoptera*, *P. jonesii*, and *U. margaritifera*) were observed only in polyhaline conditions.

DISCUSSION

The number of ostracod species (36 ostracod species and 5841 individuals) obtained from the Kapıdağ Peninsula coastline was considerably lower than that obtained from Bandırma Bay and Erdek Bay (112 ostracod species and 37550 individuals) [22] (Figure 6). The information obtained from the current study's results indicates that increasing the number of samples will not always provide the expected increase in the number of species and individuals.

The species diversity rate is higher in the spring (26 species) and summer (24 species) seasons compared with the fall (20 species) and winter (20 species) seasons. However, according to the Spearman correlation analysis, no significant relationship was found between the number of species and the ecological parameters. Also, a positive correlation was detected between species of *L. gibberosa*, *B. berchoni*, *B. dentata*, and *X. aurantia* and the amount of total calcium carbonate (TCC) in sediments. The effect of the TCC was supported by the CCA results as shown in Figure 4. Similarly, a positive correlation has previously been found between species numbers and TCC in studies performed on Bandırma Bay and Erdek Bay [23,24].

In addition to ecological parameters, the distribution of ostracod species is also affected by the composition of vegetation, predation pressure, sediment structure,

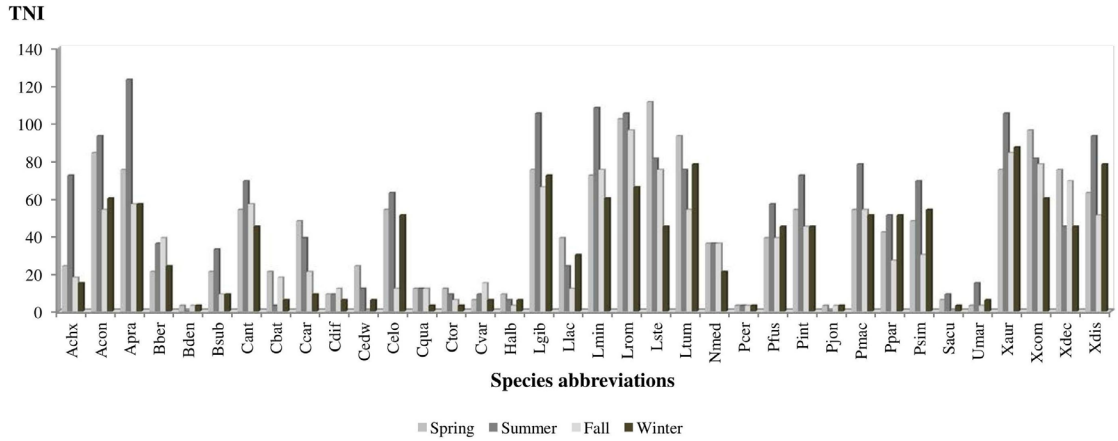


Figure 2. Total number of individuals (TNI) for each species according to season.

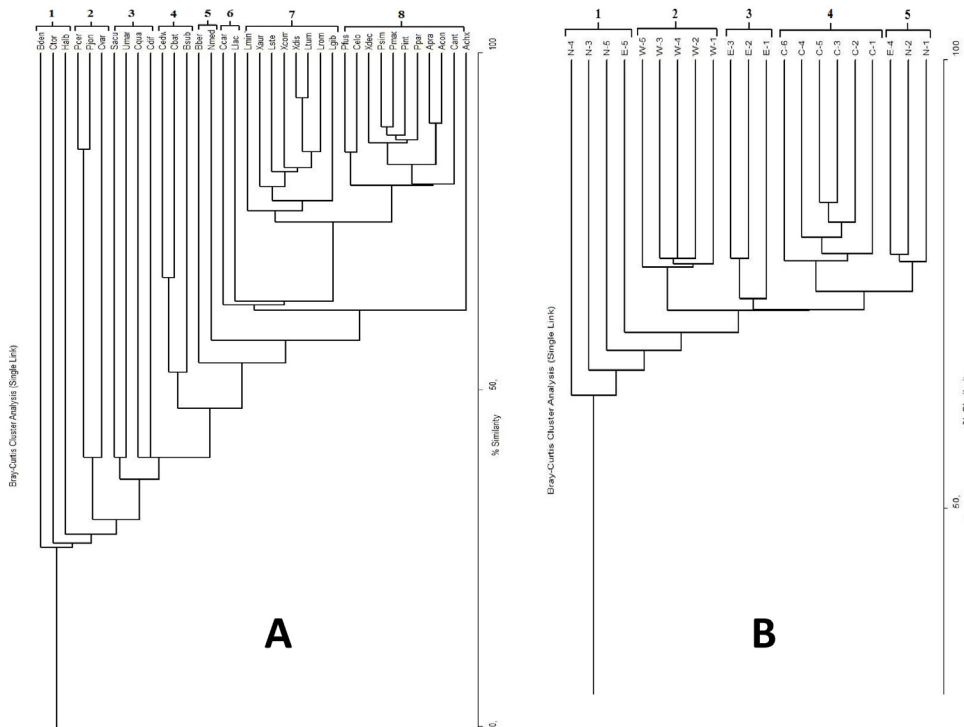


Figure 3. Dendrogram built by Bray-Curtis cluster analysis for the 36 ostracod species determined from 21 sampling stations. A. similarity of ostracod species; B. similarity of stations.

Table 5. Significant correlations between species abundance and environmental parameters according to the Spearman correlation coefficients. (Abbreviations are the same as Table 2-3: **p<0.01, *p<0.05).

	Spring	Achx	Nmed	Bber	Cant	Ccar	Cqua	Bden	Cvar	Bsub	Cbat	Cedw	Acon	Apra	Umar	Pjon	Pcer	Cdif	Celo
Depth		-,323**	-,315**	ns	ns	ns	ns	ns	,240*	,269*	,216*	ns	ns	ns	ns	ns	ns	ns	ns
Sal	ns	ns	ns	ns	,226*	ns	ns	ns	ns	ns	ns	ns	ns	ns	,253*	ns	ns	ns	ns
DO	ns	ns	ns	ns	ns	ns	ns	ns	ns	ns	ns	ns	ns	ns	ns	ns	ns	ns	ns
pH	ns	ns	ns	ns	ns	ns	ns	ns	ns	ns	ns	ns	ns	ns	ns	ns	ns	ns	ns
T	,285**	ns	ns	ns	ns	ns	ns	ns	ns	ns	ns	ns	ns	ns	ns	ns	ns	ns	-,296**
TCC	ns	ns	,326**	ns	ns	ns	ns	,220*	ns	ns	ns	ns	ns	ns	ns	ns	ns	ns	ns
TOC	ns	ns	ns	ns	ns	ns	ns	ns	,285**	ns	ns	ns	ns	ns	ns	ns	ns	ns	ns
MUD	-,316**	ns	,371**	ns	ns	ns	ns	ns	ns	ns	ns	ns	-,294**	-,375**	ns	ns	ns	ns	ns
ORP	ns	ns	ns	ns	ns	ns	ns	ns	ns	ns	ns	ns	ns	ns	ns	ns	ns	ns	ns
SECCI	-,276*	-,265*	ns	ns	ns	ns	ns	ns	,296**	,252*	ns	ns	ns	ns	ns	ns	ns	ns	ns
	Llac	Halb	Sacu	Lgib	Lmin	Lrom	Lste	Ltum	Ppar	Pfus	Pint	Pmac	Psim	Xaur	Xcom	Xdis	Xdec	Ctor	
Depth	,227*	-,286**	ns	ns	ns	ns	ns	ns	-,230*	ns	ns	-,231*	-,254*	ns	ns	ns	-,338**	-,380**	
Sal	,276*	-,350**	ns	ns	ns	ns	ns	ns	ns	ns	ns	ns	ns	ns	ns	ns	ns	ns	ns
DO	ns	ns	ns	ns	ns	ns	,247*	ns	ns	ns	ns	ns	ns	ns	ns	ns	ns	,342**	ns
pH	ns	ns	ns	ns	ns	ns	ns	ns	ns	ns	ns	ns	ns	ns	ns	ns	ns	ns	ns
T	ns	ns	ns	ns	ns	ns	ns	ns	ns	ns	ns	ns	ns	ns	ns	ns	ns	ns	ns
TCC	ns	ns	ns	,389**	ns	ns	ns	ns	-,360**	ns	ns	ns	ns	ns	,381**	ns	ns	ns	ns
TOC	,252*	ns	ns	ns	ns	ns	ns	ns	ns	ns	ns	ns	ns	ns	ns	ns	ns	ns	ns
MUD	,414**	ns	ns	ns	,288**	ns	ns	ns	-,227*	ns	ns	-,261*	-,293**	ns	ns	ns	ns	-,321**	-,374**
ORP	ns	ns	ns	ns	ns	ns	ns	ns	,232*	ns	ns	ns	,285**	ns	ns	ns	ns	ns	ns
SECCI	,290**	-,285**	ns	ns	ns	ns	ns	ns	-,288**	ns	-,241*	-,296**	-,338**	ns	ns	ns	ns	-,338**	-,378**

Table 6. Spearman correlation matrix between ecological parameters with number of species and individuals. (Abbreviations are the same as Table 3: NS = number of species; NI = number of individuals; **P<0.01, *P<0.05).

Ecological Parameters	Depth	Sal	DO	pH	T	TCC	TOC	MP	ORP	SD	NS	NI
Depth	1,000											
Sal	,623**	1,000										
DO	-,226*	-,239*	1,000									
pH	ns	ns	,616**	1,000								
T	ns	ns	ns	ns	1,000							
TCC	,478**	,277*	-,273*	ns	ns	1,000						
TOC	,584**	,541**	ns	ns	-,314**	,291**	1,000					
MUD	,776**	,492**	ns	ns	ns	,370**	,434**	1,000				
ORP	-,274*	-,081	-,477**	-,622**	-,229*	-,229*	-,055	-,147	1,000			
SD	,924**	,554**	-,273*	ns	ns	,433**	,488**	,691**	-,256*	1,000		
NS	ns	ns	ns	ns	ns	ns	ns	ns	ns	ns	1,000	

chemical material residues in the sediment, and wave motion in the water, as are other living organisms living in the aquatic environment [46]. For this reason, the species diversity may have differed among the different stations due to the influence of the above-mentioned factors.

Aurila convexa, *C. antiquata*, *C. elongata*, *L. gibberosa*, *P. fuscum*, and *X. decipiens* were shown to have a wide distribution in this study. *Loxoconcha rhomboidea* (369 individuals), *X. aurantia* (351 individuals) *L. gibberosa* (318 individuals), *L. minima* (315 individuals), *X. communis* (315 individuals), *A. prasina* (312 individuals), and *L. stellifera* (312 individuals) were the most abundant species on the Kapıdağ Peninsula coastline.

Aurila convexa is known to be a cosmopolitan Mediterranean species [30]. It is also common in the Sea of Marmara and has been recorded in northern parts of the Aegean Sea [33], as well as in the Black Sea in brackish water systems as a polyhaline species [27]. It is widely distributed in the littoral and sublittoral zones of most Turkish coastlines [21]. *Aurila convexa* was observed at all the stations in the present study at high frequency (77.4%), with a wide range of ecological parameters and at higher numbers than other species, showing a significant negative correlation with mud percentage.

Aurila prasina is a typical near-shore species and has been reported in a variety of marine habitats in the Aegean Sea, the Black Sea, as well as lagoon environments

[21]. In accordance with other studies, we determined a high number of individuals of this species from 20 stations (excepting E-3 station), in mesohaline to polyhaline conditions at depths ranging from 0.5 to 30 m. Its frequency was 70.2 %, and it showed a significant negative correlation with mud percentage, similar to *A. convexa*. *Carinocythereis antiquata* occurs in all types of bottom sediments, from shallow water to 71 m depths in the Adriatic Sea [30]. It is also a common species in the Mediterranean Sea [30]. Concordantly, we observed this species at all stations from 0.5 m to 30 m, in a variety of ecological environments at 66.7% frequency. No correlation detected between this species and ecological parameters.

Cushmanidea elongata is a common species in the Mediterranean Sea and the Aegean Sea [21]. We observed this species at all stations in mesohaline to polyhaline conditions, although the number of individuals was not high, at 65.5% frequency. It showed a significant negative correlation with pH.

Loxoconcha gibberosa has been identified in the Aegean Sea and the Sea of Marmara [21]. We determined this species at all the stations on the Kapıdağ Peninsula coastline, from mesohaline to polyhaline salinity conditions, with a high number of individuals and at 78.6% frequency. A significant positive correction was detected between TCC and this species.

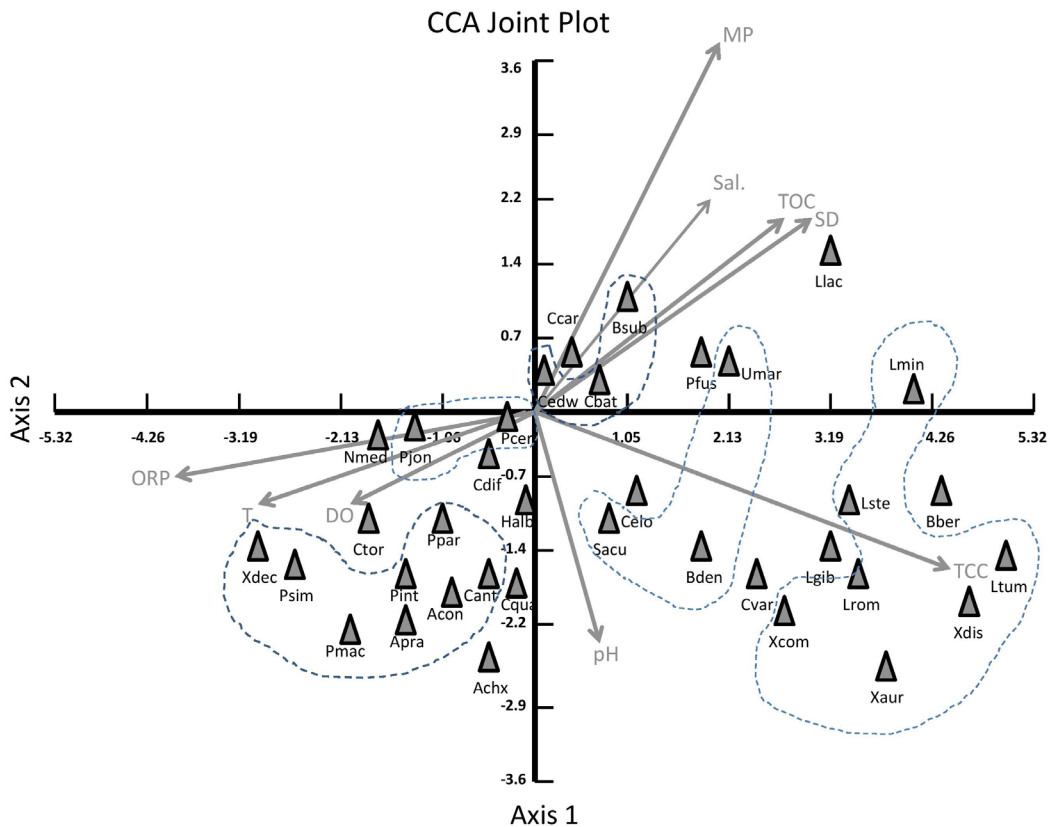


Figure 4. Canonical correspondence analysis (CCA) plot showing relationships between environmental variables and the 36 species. Eigenvalues 0.121-axis 1; 0.089-axis 2; percentage 23.945-axis 1; 17.543-axis 2; Cumulative Percentage 23.945-axis 1; 41.488-axis 2; Cumulative Constr. Percentage 23.945-axis1; 41.488-axis 2; Species-environment correlations 1-axis 1; 1-axis 2. (The dashes show the species groups that composed compatible with Bray-Curtis dendrograms)

Loxoconcha minima prefer a near-shore environment with sandy, silt, and pelite substrates [30]. We observed this species abundantly at 19 stations (excepting N-4 and N-5) at a frequency of 70.2% (Table 2). It has previously been identified on the coasts of the Mediterranean Sea and the Sea of Marmara [21]. This species showed a significant positive correlation with mud percentage. *Xestoleberis aurantia* has been found as a euryhaline species in northeast England [46]. This species is known as a marine brackish littoral species, but has also been reported in freshwater and oligohaline shallow-water environments [47]. We observed *X. aurantia* from mesohaline to polyhaline environments at 18 stations. It was observed in the present study with a wide range of ecological parameters at high numbers, at a frequency of 66.7%. A positive correlation was detected with TCC. *Xestoleberis communis* was observed at 18 stations (excepting N-3, N-4, N-5) with a wide range of ecological parameters but particularly in polyhaline conditions, and at a frequency of 73.8%. This species has been identified

as a dominant species and is widely distributed in the Mediterranean Sea [28,48]. No correlation was detected between this species and the studied ecological parameters.

We determined *X. decipiens* at all the stations in mesohaline to polyhaline conditions. The number of individuals was not high but the species was widely distributed in different ecological environments at a frequency of 78.6%. It has been identified on most Turkish coastlines in recent studies [21]. This species showed negative correlations with depth, mud percentage, and Secchi depth, and a positive correlation with dissolved oxygen. *Loxoconcha rhomboidea* was observed as the most abundant species on the Kapıdağ Peninsula coastline, with the highest individual numbers and at a frequency of 75.0%. It was found in mesohaline to polyhaline conditions at 19 stations (excepting N-3 and N-4). This is a very common species, widely found in littoral and sublittoral zones of most Turkish coasts [21]. It has been reported at 1–57 m depths in the Mediterranean Sea

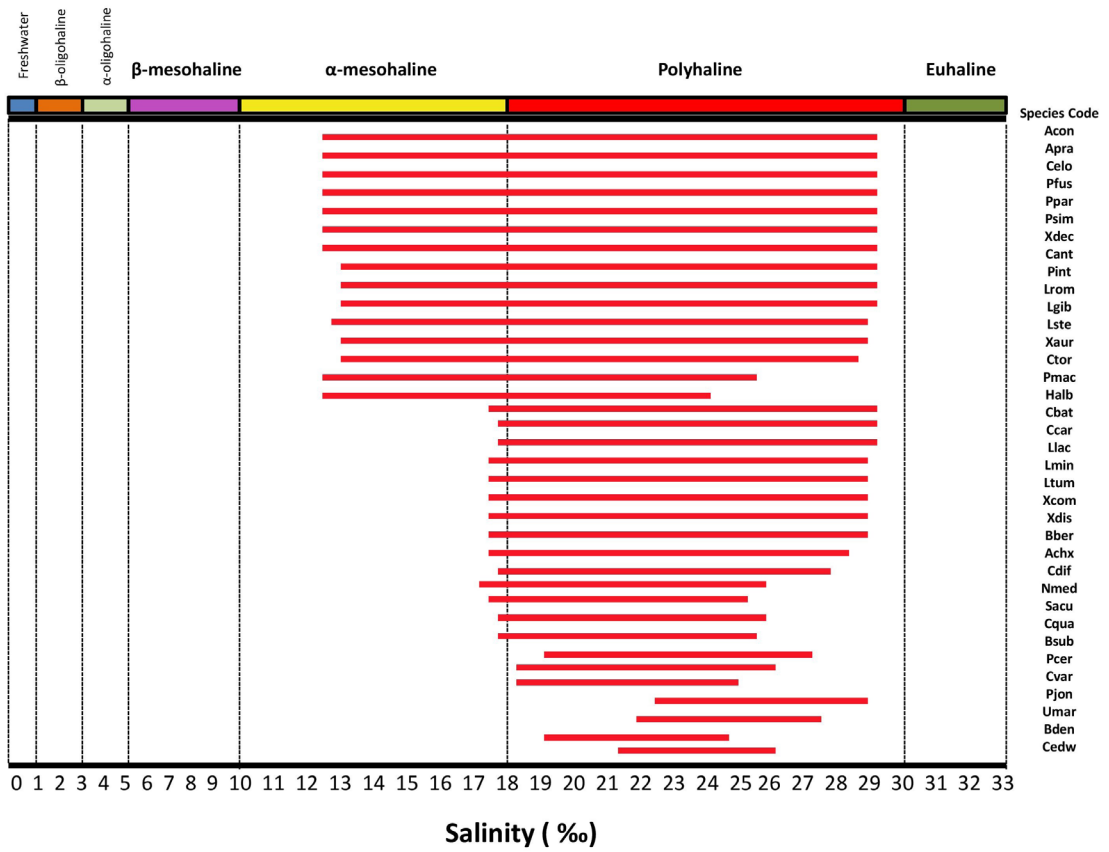


Figure 5. The ostracod species and their salinity records from Kapıdağ Peninsula.

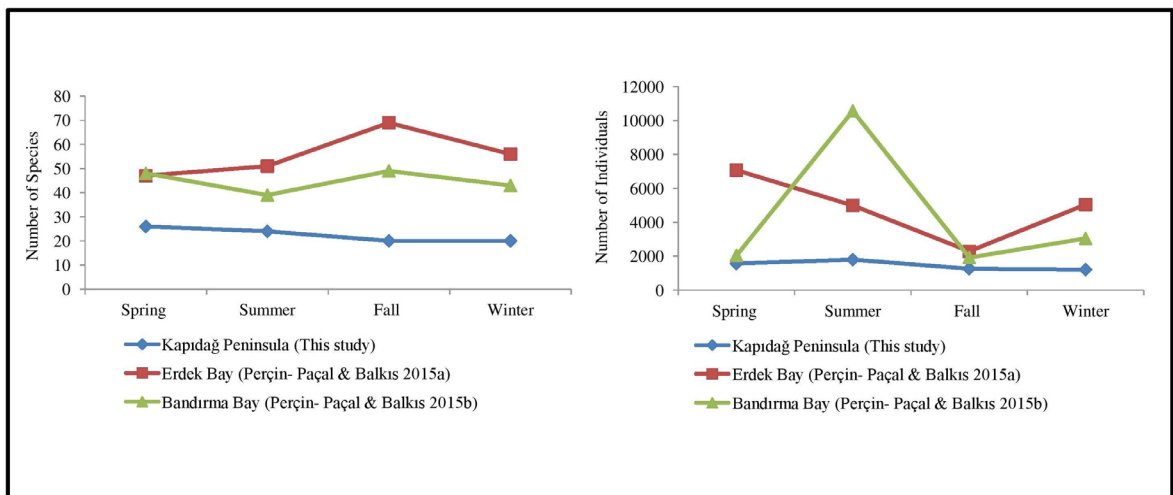


Figure 6. Seasonal numbers of ostracod species and numbers of individuals determined in the current study compared to other studies.

[28,33]. No correlation was detected between this species and our ecological parameters.

Loxococoncha stellifera was observed at 0.5-30 m depths in this study, in high numbers and at a frequency of 75.0%, from mesohaline to polyhaline conditions. The species has been observed at 3.5-33 m on muddy and sandy sediments in the Aegean Sea [28,33]. It also lives in the littoral and sublittoral zones of most Turkish coasts [21]. A positive correlation was observed between this species and dissolved oxygen.

Although *Paradoxostoma fuscum* is not found widely on Turkish coastlines [21], we observed this species at all the stations, from mesohaline to polyhaline conditions at 64.3% frequency. No correlation was detected between this species and the ecological parameters.

A greater number of ostracod species and individuals were observed in the Bandırma and Erdek bays at the same depths in the years of 2006-2007 [23,24]. When the current study's findings on habitat variables are compared with the studies mentioned above, it was noted that DO, salinity, and temperature were lower in the current study (Table 7).

In 2008, an environmental problem occurred due to the formation of mucilage formed by the proliferation of diatoms together with bacteria throughout the Sea of Marmara. Some studies stated that because of this, living creatures in the Sea of Marmara were adversely affected [49,50]. This could explain the decrease in ostracod species and the number of individuals and changes in ecological parameters since the previous research on Kapıdağ Peninsula. [22-24].

Although the measured average DO was at appropriate survival levels in this study, it decreased to 1.2 mgL^{-1} at W-3 and W-4 stations, especially during winter. It has been observed in general that DO significantly decreases with depth in all seasons. In previous studies, although the measured DO was higher, the decrease of DO with depth has been observed in Bandırma Bay and Erdek Bay [23,24]. It is well known that the DO in surface waters is higher due to photosynthetic activities and DO reduces with depth. Increase of phytoplankton biomass in response to excessive inputs of nutrients and higher organic loads in eutrophic systems lead to an increase in bacterial activity and a decrease in DO levels [51]. When the DO level falls below 5 mgL^{-1} , oxygen-sensitive inver-

tebrate and fish species are negatively affected [52]. The amount of the DO measured in the current study was lower than in previous studies [23,24]; therefore, the adverse effects of low DO on organisms that live in the study area of the Kapıdağ Peninsula are inevitable.

Secchi disk visibility in oligotrophic waters is 20–40 m, in mesotrophic waters 10–20 m, and in eutrophic waters, less than 10 m [53]. Secchi depths ranged between 0.5 and 13 m in the current study. These values show that the study area is in the mesotrophic water category. The Secchi depth measurements from this study are very similar to previous ones: 3–13 m in the Bandırma and Erdek bays in the years of 2006-2007 [23-24].

Erdek Bay and Bandırma Bay are affected by heavy pollutants coming from numerous industrial facilities and human settlements [50]. The northeastern part of Kapıdağ Peninsula contains higher levels of phosphates than other regions [50]. Waters from Susurluk River and Kara River spill into Bandırma Bay and pollute the surface waters [50]. The presence of a white-meat processing plant and a fertilizer factory also causes intense pollution in this region [54]. According to the Integrated Coastal Area Plan of Bursa Province (2015) [55], the Sea of Marmara is less polluted, but Bandırma Bay and Gemlik Bay are at a mid-level stage polluted and were found to be prone to intense pollution. As can be inferred from the results of the current study, the decrease in the number of ostracod species and individuals and the decrease in the quality of the environmental variables (DO, salinity, and temperature) suggest that negative changes in the water quality of Kapıdağ Peninsula's coastline are because of pollution. These polluted environments allow for the advance of cosmopolitan species with wide ecological tolerance through the elimination of low-tolerance species. Already, the existence of environmental tolerant species *L. stellifera* [56,57], *A. prasina* [57], *L. rhomboidea* [56,57], and *X. aurantia* [57] and the reduction of the number of ostracod species are suggested by our findings.

Although the results of this study have not been thoroughly evaluated in terms of pollutants on the surface waters, the results show that the Kapıdağ Peninsula coastline has an ecosystem that requires measurement in terms of pollutants.

The present study establishes a sharp decline in ostracod species numbers. This evident decline can be attri-

Table 7. Comparative ecology of the Kapıdağ Peninsula coastline (this study 2011-2012) and the Erdek and Bandırma bays in the years of 2006-2007 [23,24].

Depth	Ecological Parameters	Kapıdağ Peninsula This study (2011-2012) (Mean values)	Erdek Bay [23] (2006-2007) (Mean values)	Bandırma Bay [24] (2006-2007) (Mean values)
0-0.5 m	Salinity (‰)	20.3	24.8	24.5
	Dissolved oxygen (mg/l)	6.9	10	9.6
	Temperature (°C)	16.4	17.7	17.4
	Total organic carbon (%)	0.8	0.4	0.4
	Total calcium carbonate (%)	2.8	4.8	4.1
	Mud percentage (%)	0.5	0.39	1.09
1 m	Salinity (‰)	20.7	24.7	24.2
	Dissolved oxygen (mg/l)	6.8	8.9	9.1
	Temperature (°C)	15.2	16.9	17.5
	Total organic carbon (%)	0.7	0.5	0.5
	Total calcium carbonate (%)	2.7	2.6	1
	Mud percentage (%)	21.7	4.96	1
5 m	Salinity (‰)	21.4	25	24.9
	Dissolved oxygen (mg/l)	6.3	8.1	8.4
	Temperature (°C)	14.9	16.2	16.1
	Total organic carbon (%)	0.8	0.7	0.4
	Total calcium carbonate (%)	3	62.8	1.3
	Mud percentage (%)	19.9	15.82	1.5
10 m	Salinity (‰)	21.8	25.2	25.7
	Dissolved oxygen (mg/l)	6.7	7.6	8.1
	Temperature (°C)	14.3	15.8	16.5
	Total organic carbon (%)	1.1	1.3	1.6
	Total calcium carbonate (%)	7	71.1	17.1
	Mud percentage (%)	29.5	37.24	31
20 m	Salinity (‰)	24.1	30.2	27.7
	Dissolved oxygen (mg/l)	5	7.2	7.8
	Temperature (°C)	12	14.1	13.5
	Total organic carbon (%)	1.7	0.8	1.2
	Total calcium carbonate (%)	30.8	48.7	57.9
	Mud percentage (%)	24.4	47.07	48.03
30 m	Salinity (‰)	27.5	36	35.5
	Dissolved oxygen (mg/l)	4.5	6	6.3
	Temperature (°C)	14.1	15.5	15.4
	Total organic carbon (%)	2.1	1.5	2.4
	Total calcium carbonate (%)	7.2	14.1	11.9
	Mud percentage (%)	31.6	91.02	85.99

buted to low dissolved oxygen levels at depth, which is evidence of the adverse effects of anthropogenic activities on the marine ecosystem on the Kapıdağ Peninsula coastline.

References

- D.J. Horne, A. Cohen, K. Martens, Taxonomy, morphology and biology of Quaternary and living Ostracoda. In: *The Ostracoda: Applications in Quaternary Research* (J.A. Holmes and A.R. Chivas, Eds.), American Geophysical Union, Washington, DC. (2002) 5-36.
- T. Salel, H. Bruneton, D. Lefèvre, Ostracods and environmental variability in lagoons and deltas along the north-western Mediterranean coast (Gulf of Lions, France and Ebro delta, Spain), *Review of Micropaléontology*. 59 (2016) 425-444.
- W.T.R. Chiu, M. Yasuhara, H. Iwatani, A. Kitamura, K. Fujita, Response of subtropical submarine-cave ecosystem to Holocene cave development and Asian monsoon variability, *Paleobiology*, 43 (2017) 425-434.
- M. Yasuhara, T.M. Cronin, Climatic influences on deep sea ostracode (Crustacea) diversity for the last three million years, *Ecology*, 89 (2008) 52-65.
- C. Meisc, Freshwater Ostracoda of Western and Central Europe.-In J Schwoerbel and P. Zwick, Editors: *Süßwasserfauna von Mitteleuropa* 8/3. Spektrum Akademischer Verlag, Heidelberg, Berlin. (2000) 522 pp.
- P. Frenzel, I. Boomer, The use of ostracods from marginal marine, brackish waters as bioindicators of modern and Quaternary environmental change. *Palaeogeography, Palaeoclimatology, Palaeoecology*, 225 (2005) 68-92.
- F. Mesquita-Joanes, A.J. Smith, F.A. Viehberg, The ecology of Ostracoda across levels of biological organisation from individual to ecosystem: a review of recent developments and future potential. In: *Ostracoda as Proxies for Quaternary Climate Change* (D.J. Horne, J. Holmes, J. Rodriguez-Lazaro and F.A. Viehberg, eds.), (2012). pp. 15-35. Elsevier, Amsterdam.
- J.W. Neale, Some factors influencing the distribution of Recent. *British Ostracoda*. *Publ. Staz. Zool. Napoli* 33 (Suppl.) (1964) 247-296.
- F. Ruiz, M. Abad, A.M. Bodergat, P. Carbonel, J. Rodríguez-Lázaro, M.L. González-Regalado, A. Toscano, E.X. García, J. Prenda, Freshwater ostracods as environmental tracers, *I. J. Environ. Sci. Technol.*, 10 (2013) 1115-1125.
- Y. Hong, M. Yasuhara, H. Iwatani, Seto K., Yokoyama Y., Yoshioka K.B. Mamo, Freshwater reservoir construction by damming a marine inlet in Hong Kong: Paleocological evidence of local community change, *Marine Micropaleontology*, 132 (2017) 53-59.
- F. Ruiz, M. Abad, A.M. Bodergat, P. Carbonel, J. Rodríguez-Lázaro, M. Yasuhara Marine and brackish-water ostracods as sentinels of anthropogenic impacts, *Earth-Sci. Rev.*, 72 (2005) 89-111.
- M. Yasuhara, H. Yamazaki A. Tsujimoto, K. Hirose, The effect of long-term spatiotemporal variations in urbanization-induced eutrophication on a benthic ecosystem, *Osaka Bay, Japan, Limnol. Oceanogr.*, 52 (2007) 1633-1644.
- A.M. Bodergat, M. Rio, N. Ikeya, Tide versus eutrophication, impact on ostracods populations structure of Mikawa Bay (Japan), *Revue de Micropalé'ontlogie*, 40 (1997) 3-13.
- F. Mezquita, R. Hernandez, J. Rueda, Ecology and distribution of ostracods in polluted Mediterranean River, *Palaeogeography, Palaeoclimatology, Palaeoecology* 148 (1999) 87-103.
- F. Ruiz, M.L. González-Regalado, J.M. Muñoz, Multivariate analysis applied to total and living fauna: seasonal ecology of recent Ostracoda off the North Cadiz Gulf coast (southwestern Spain), *Marine Micropaleontology*, 31 (1997) 183-203.
- F. Ruiz, M.L. González-Regalado, J.I. Baceta, J.M. Muñoz, Comparative ecological analysis of the ostracod faunas from low- and high-polluted southwestern Spanish estuaries: a multivariate approach, *Marine Micropaleontology*, 40 (2000) 345-76.
- M. Yasuhara, H. Yamazaki, T. Irizuki, S. Yoshikawa, Temporal changes of ostracode assemblages and anthropogenic pollution during the last 100 years, in sediment cores from Hiroshima Bay, Japan. *Holocene*, 13 (2003) 527-536.
- Ş.T. Beşiktepe, H.İ. Sur, E. Özsoy, M.A. Abdullatif, T. Oğuz, Ü. Ünlüata, The circulation and hydrography of the Marmara Sea, *Progress in Oceanography*, 34 (1994) 285-334.
- H. Yüce, A. Türker, Marmara Denizi'nin fiziksel oşinografik özellikleri ve Akdeniz suyunun Karadeniz'e girişi, *Uluslararası Çevre Sorunları Sempozyumu Tebliğleri, İstanbul Marmara Rotary Kulübü, İstanbul*, (1991) 284-303.
- F. Perçin-Paçal, S. Altınışaılı, H. Balkis "Recent Ostracoda Species of the Sea of Marmara with Çanakkale (Dardanelles) and İstanbul Strait (Bosphorus): A Review", *The Sea of Marmara: Marine Biodiversity, fisheries, conservation and governance*, E. Özsoy, M.N. Çağatay, N. Balkis, N. Balkis, B. Öztürk, Ed., TUDAV, İstanbul, (2016) 454-467.
- F. Perçin-Paçal, S. Altınışaılı, H. Balkis An updated checklist of recent marine and coastal brackish water ostracods (Crustacea Ostracoda) in Turkey., *J. Entomology and Zoology Studies*, 3 (2015) 20-33.
- F. Perçin-Paçal, H. Balkis, Seasonal Distribution of Ostracoda in Bandırma Bay and Erdek Bay, Sea of Marmara, Turkey, *Crustaceana*, 85 (2012) 847-875.
- F. Perçin-Paçal, H. Balkis, The Ecology of Ostracoda (Crustacea) Species Obtained From Erdek Bay (The Marmara Sea, Turkey) *International Journal of Environmental Research*. 9 (2015 a) 1245-1258.
- F. Perçin-Paçal, H. Balkis, Environmental and Ecological Assessment of Ostracods inhabiting in Bandırma Bay, The Marmara Sea, Turkey, *I. J. Fisheries and Aquatic Studies*, 2 (2015) 285-299.
- Strategic Plan, The Bandırma Chamber of Commerce 2018-2021. Strategic Plan was approved by the decision of the board of directors dated 13.03.2018 and numbered (2018) 245.
- D.D. Mordukhai-Boltovskoi, Ostracoda of the Black Sea from determination of the fauna of the Black and Azov Seas (in Russian). *Kiev, Kievskaya Kni/linaya Fabrika*; (1969) 1-82.
- E.I. Schornikov, Ostracoda, *Führer der fauna des. Schwarzen Meers und der Azov Sea*. In *Frielbenden invertebraten* (ed. A.A. Vodyanistskii), *Crustacean. Akademii Nauk. U.S.S.R. Institute. Biology, Naukova. Dumka Kiev*, (1969) 163-260.
- P.J. Barbeito-Gonzalez, Die Ostracoden des Küstenbereiches von Naxos (Griechenland) und ihre Lebensbereiche. *Mitteilungen aus dem von Naxos (Griechenland) und ihre Lebensbereiche, Mitteilungen aus dem Hamburgischen Zoologischen Museum und Institut*. 67 (1971) 255-326.

29. G. Hartmann, S.H. Puri, Summary of neontological and paleontological classification of Ostracoda, *Mitteilungen aus dem Hamburgischen Zoologischen Museum und Institut*, Band, 70 (1974) 7-73.
30. G. Bonaduce, G. Ciampo, M. Masoli, Distribution of Ostracoda in the Adriatic Sea, *Publicazioni Della Stazione Zoologica di Napoli*; 40 (1975) 1-154.
31. J. Athersuch, D.J. Horne, J.E. Whittaker, Marine and brackish water ostracods. In: Kermack D.M. and Barnes R.S.K. (eds.), *Synopses of the British Fauna (New Series)*, No. 43, E.J. Brill, Leiden (for the Linnean Society of London and the Estuarine and Brackish Water Sciences Association), (1989) 361 pp.
32. I. Yassini, The littoral system ostracodes from the Bay of Bou-İsmaïl, Algiers, Algeria Rev. *Revista Espanola Micropaleontology*, 3 (1979) 353-416.
33. A. Stambolidis, Zur Kenntnis Der Ostracodes des Evros-Delta (Nord-Agaisches Meer) Griechenland, *Mitteilungen aus dem Hamburgischen Zoologischen Museum und Institut*, 82 (1985) 155-254.
34. WoRMS, World Register of Marine Species (<http://www.marinespecies.org/aphia.php?p=taxdetails&id=1078>) (2018).
35. L.W. Winkler, The determination of dissolved oxygen in water, *Berichte der Deutschen Chemischen Gesellschaft*, 21 (1888) 2843-2855.
36. A. Ivanoff, *Introduction à l'océanographie*, Tome I. Librairie Vuibert, Paris (1972).
37. L.R. Folk, *Petrology of Sedimentary Rocks*, Hemphill, Tulsa, Oklahoma (1974).
38. H. Gaudette, W. Flight, L. Tanner, D. Folger, An Expensive titration method for the determination of organic carbon in recent sediments, *J. Sedimentary Petrology*, 44 (1974) 249-253.
39. D.H. Loring, R.T.T. Rantala, *Manuel for the Geochemical Analyses of Marine Sediments and Suspended Particulate Matter*. *Earth Science Reviews*, 32 (1992) 235-283.
40. N. McAleece, J.D.G. Gage, P.J.D. Lamshead, G.L.J. Paterson, *BioDiversity Professional Statistics Analysis Software*. Jointly developed by the Scottish Association for Marine Science and the Natural History Museum London, The Natural History Museum and The Scottish Association for Marine Science, Oban (1997).
41. A. Kocataş *Ekoloji ve çevre biyolojisi*. (Ecology and environmental biology) Üçüncü baskı. Ege Üniversitesi, Su Ürünleri Fakültesi Yayınları, No: 20. Ege University Press, Bornova, İzmir (1996).
42. M. Mahajan, S. Fatima, Frequency, Abundance and Density of Plant Species by List Quadrat Method. *Epitome, International Journal of Multidisciplinary Research*, 3 (2017) 7, ISSN: 2395-6968.
43. IBM Corp. Released, *IBM SPSS Statistics for Windows, Version 21.0*. Armonk, NY: IBM Corp. (2012).
44. C.J.F. Ter Braak, Canonical correspondence analysis: A new eigenvector technique for multivariate direct gradient analysis, *Ecology*, 67 (1986) 1167-1179.
45. W. Kovach, *MVSP – A MultiVariate Statistical Package, MVSP Version 3.22*, Kovach Computing Services, Pentraeth, Wales, U.K. (2013).
46. S. Hull, Seasonal changes in diversity and abundance of ostracods on four species of intertidal algae with differing structural complexity, *Marine Ecology Progress Series*, 161 (1997) 71-82.
47. I. Mazzini, P. Anadon, M. Babieri, F. Castorina, L. Ferrelid, E. Gliozzie, M. Molae E.Vittorif, Late Quaternary sea-level changes along the Tyrrhenian coast near Orbetello (Tuscany, central Italy): palaeoenvironmental reconstruction using ostracods, *Marine Micropaleontology*, 37 (1999) 289-311.
48. F. Perçin-Paçal, The ecology of the Ostracoda (Crustacea) species obtained from the coasts of İskenderun Bay (Eastern Mediterranean Sea), *J. Black Sea/Mediterranean Environment*, 17 (2011) 127-144.
49. N. Balkis, H. Atabay, I. Türetgen, S. Albayrak, H. Balkis V. Tüfekçi, Role of single-celled organisms in mucilage formation on the shores of Büyükada Island (the Marmara Sea), *J. Marine Biological Association of the United Kingdom*, 91 (2011) 771-781.
50. N. Balkis, B. Toklu-Alıçlı, M. Balcı, Evaluation of Ecological Quality Status with the Trophic Index (TRIX) Values in the Coastal Waters of the Gulfs of Erdek and Bandırma in the Marmara Sea *Ecological Water Quality-Water Treatment and Reuse*, Dr. Voudouris (Ed.), (2012) ISBN: 978-953-51-0508-4.
51. M. Karydis, Eutrophication assessment of coastal waters based on indicators: a literature review, *Global NEST J.*, 11 (2009) 373-390.
52. J.D. Frodge, G.L. Thomas G.B. Pauley, Effects of canopy formation by floating and submergent aquatic macrophytes on the water quality of two shallow Pacific Northwest lakes. *Aquatic Botany*, 38 (1990) 231-248.
53. I. Ignatiades, D. Georgopoulos, M. Karydis, Description of a phytoplanktonic community of the oligotrophic waters of SE Aegean Sea (Mediterranean), *Marine Ecology*, 16 (1995) 13-26.
54. T. Koç, Bandırma ilçesinde tavukçuluğun çevresel etkisi, *Ekoloji*, 11 (2002) 11-16.
55. Ministry of Environment and Urban, General Directorate of Spatial planning, "Integrated coastal area plan of Bursa province, Plan statement report.", (2015) 1-74 pp.
56. D. Arbulla, N. Pugliese, A. Russo, Ostracods from the National Park of La Maddalena Archipelago (Sardinia, Italy) *Bulletino della Societa Paleontologica Italiana* 43 (2004) 91-99.
57. S. Altınışçılı, F. Perçin-Paçal, S. Altınışçılı, Assessments on diversity, spatiotemporal distribution and ecology of the living ostracod species (Crustacea) in oligo-hypersaline coastal wetland of Bargilya (Milas, Muğla, Turkey), *I. J. Fisheries and Aquatic Studies, IJFAS*, 3 (2015) 357-373.



Biosynthesis of Gold Nanoparticles using *Scytosiphon lomentaria* (Brown algae) and *Spyridia filamentosa* (Red algae) from Kyrenia Region and Evaluation of their Antimicrobial and Antioxidant Activity

Girne Bölgesi'nden *Scytosiphon lomentaria* (Kahverengi algler) ve *Spyridia filamentosa* (Kırmızı algler) kullanarak Altın Nanoparçacıklarının Biyosentezi ve Antimikrobiyal ve Antioksidan Aktivitelerinin Değerlendirilmesi

Doga Kavaz^{1,2,3}, Tariro Zimuto³ and Huzaifa Umar^{1,2,3}

¹Department of Bioengineering, Institute of Graduate Studies and Research, Cyprus International University, Mersin, Turkey.

²Biotechnology Research Center, Cyprus International University, Mersin, Turkey.

³Bioengineering Department, Cyprus International University, Mersin, Turkey.

ABSTRACT

This study was carried out for biosynthesis of gold nanoparticles by using *Scytosiphon lomentaria* (brown algae) and *Spyridia filamentosa* (red algae) and compared. Synthesized gold nanoparticles were characterized using the UV-Vis spectroscopy (UV-Vis), Fourier transform infrared (FTIR) and Master Sizer analysis. Macro algae extract involvement in the stabilization of the gold nanoparticles was confirmed by the presence of UV-Vis peak at 540 nm and is an indication of the presence of the gold nanoparticles (AuNPs). Stretch in peaks of the FTIR showed that the biomolecules present in the seaweed extract reduced the gold ions. Master sizer results for AuNPs were within the range of 15-55 nm. Antioxidant activity carried out using 2,2-diphenyl-1-picrylhydrazyl (DPPH) free radical scavenging activity revealed significant activity for both AuNPs. Biosynthesized AuNPs also showed antimicrobial activity against *S. typhi* and *E. coli*. The *S. lomentaria* AuNPs exhibited inhibition against *E. coli*, whereas *S. filamentosa* gold nanoparticles showed antibacterial activity against *S. typhi*. Synthesized AuNPs using *S. lomentaria* and *S. filamentosa* extracts as stabilizing agents showed convincing antioxidant and antimicrobial activity against gram negative and gram positive bacteria.

Key Words

Nanoparticle preparation, Characterization, *S. filamentosa*, *S. lomentaria*.

ÖZ

Bu çalışma, *Scytosiphon lomentaria* (kahverengi yosun) ve *Spyridia filamentosa* (kırmızı yosun) kullanılarak altın nanopartiküllerinin (AuNPs) sentezi için yürütülmüş ve bu iki türden kullanılarak sentezlenen nanopartiküllerin karşılaştırması yapılmıştır. Altın nanoparçacıklar daha sonra UV-Vis spektrofotometre, FTIR ve Mastersizer kullanılarak karakterize edilmiştir. UV-Vis kullanılarak altın nanopartiküllerin oluşumu 540 nm'de oluşan pik ile görülmektedir. FTIR'daki gerilme, deniz yosunu ekstraktında bulunan biyomoleküllerin altın iyonlarını azalttığını göstermiştir. Mastersizer sonuçları, nanoparçacıkların 15-55 nm aralığında geniş bir dağılım göstermektedir. 2,2-diphenyl-1-picrylhydrazyl (DPPH) serbest radikal yöntemi kullanılarak gerçekleştirilen antioksidan aktivitesi, her iki nanopartikül için de önemli aktiviteler göstermiştir. *S. typhi* ve *E. coli* kullanılarak antimikrobiyal etkileri araştırılmıştır. *S. lomentaria* altın nanoparçacıklar *E. coli*'ye karşı inhibisyon sergilerken, *S. filamentosa* altın nanopartikülleri *S. typhi*'ye karşı inhibisyon göstermiştir. Stabilize edici ajan olarak kullanılan *S. lomentaria* ve *S. filamentosa* özütleri ile sentezlenen altın nanoparçacıklar, hem gram negatif hem de gram pozitif bakterilere karşı ikna edici antioksidan ve antimikrobiyal aktivite göstermiştir.

Anahtar Kelimeler

Nanoparçacık hazırlanması, karakterizasyonu, *S. filamentosa*, *S. lomentaria*.

Article History: Received: Jan 28, 2019; Revised: May 12, 2019; Accepted: Jul 11, 2019; Available Online: Nov 1, 2019.

DOI: <https://doi.org/10.15671/hjbc.518593>

Correspondence to: D. Kavaz, Bioengineering Department, Cyprus International University, Mersin 10, Turkey.

E-Mail: dkavaz@ciu.edu.tr

INTRODUCTION

Nanotechnology is rapidly expanding with it serving the main purpose of manufacturing materials at nanoscale although having the same application as the normal size material. Nanotechnology is defined as a study of techniques of materials manipulation in the range from 1-100nm such as from the size of a single atom up to those of traditional chemistry [1]. It has become an important part of the livelihood of most living organisms. Nanotechnology has led to a huge revolutionary change in science, having great technological achievements and employment of people with great expertise and experience, thus encompassing both practical and theoretical science. The nanoparticles are chosen and synthesized based on their different properties which make them suitable for the purposes they serve [2]. The synthesis of nanoparticles can be achieved by some physical and chemical methods. The traditional and commonly used method for nanoparticles synthesis is wet method. Nanoparticles have become the hope for the future as they are now synthesized and utilized in different ways [3]. The utilization of nanoparticles is increasing due to their increased surface area to volume ratio. Studies have been carried out in different fields to observe the various properties and characteristics of the nanoparticles. During these past few decades, further studies of these nanoparticles has shown their integrated biological properties such as antitumor, antimicrobial and anti-HIV activities [4].

Simultaneously, nanotechnology has evolved as a subdivision of green innovation or eco-innovation technologies, which allows for application in various aspects that support “green growth” and excellent perspectives for social and economic development [5]. With the introduction of biosynthesis of nanoparticles, the high demand of the nanoparticles can now be overcome without any damage being done to the environment. The aim for green innovation is to produce new nanoparticles using various biological entities and eco-friendly recyclable materials. This brings about new production procedures and purchase modalities thus, reduction in work space, work load (because of the one pot synthesis), labor is reduced, and the use of hazardous chemicals [6]. The significantly new methods of synthesis are also aimed at addressing the health and environmental safety of the formation and utilization of the nanoparticles.

Biological entities are being considered and tried for the green synthesis of many nanoparticles with their different applications. Among the different biological entities being investigated for biosynthesis is macro algae which are also called bionanofactories because they synthesize nanoparticles with high stability and eliminate cell maintenance. Algae are naturally available and are a very important source of phytochemicals involved in the synthesis of metallic nanoparticles. Seaweeds have shown a wide spectrum use in the medical field [7]. They are a good source of bioactive compounds which have a wide range of biological applications that include anticoagulant, antifouling and antibacterial activity [8]. Seaweeds have been used since ancient times for medicinal purposes as an anthelmintic and aesthetics. They were used as antibiotics in the treatment of gout, wounds, cough, hypertension and even some venereal diseases. Recent literature has also shown that macro algae can be used in the treatment of hypertension, cancer, allergy, oxidative stress, thrombosis, lipemia and some degenerative diseases [9].

Green synthesis is being adopted by scientists because it has proven to have lesser after effects to human and animals when using the products [10]. It is also reliable because it is simple, easy, environmentally friendly and less laborious. Synthesis gold nanoparticles using this method has a greater advantage and it is a fast one-step biosynthesis method [11]. The biosynthesized nanoparticles also exhibit a unique particle size. Thus, the green synthesis of nanoparticles is dependent on shape, physical, chemical and biological properties [12]. The gold nanoparticles are used for the development of biosensors, DNA labeling and vapor sensing [13-15] and gold nanoparticles also applied to the determination of ct-DNA and used as potential biological labels [16].

In this study, stable and eco-friendly green synthesis of gold nanoparticles using *S. lomentaria* and *S. filamentosa* aqueous extract as a stabilizing agent and their characterization done using various spectroscopic techniques was also reported. Antioxidant activity of the synthesized nanoparticles was carried out DPPH free radical scavenging activity and antimicrobial activity against *E. coli* and *S. typhi* using disc diffusion method.

MATERIALS and METHODS

Chemical Reagents

Potassium tetrachloroaurate (KAuCl_4), Nutrient agar, Nutrient broth, Antibiotics, distilled water, ethanol, barium chloride and sulphuric acid. All chemicals used in the experiment were ACS-reagent grade, produced by Sigma (St. Louis, MO, USA).

Sample Collection

The algal species were collected from the Kyrenia harbour which is along the coastline of the Mediterranean Sea. The samples were collected and stored in polythene bags and taken to the laboratory for classification. The species that were collected were *S. lomentaria* and *S. filamentosa*. The samples were then stored in a cool place until they were used for preparation of the algal extracts.

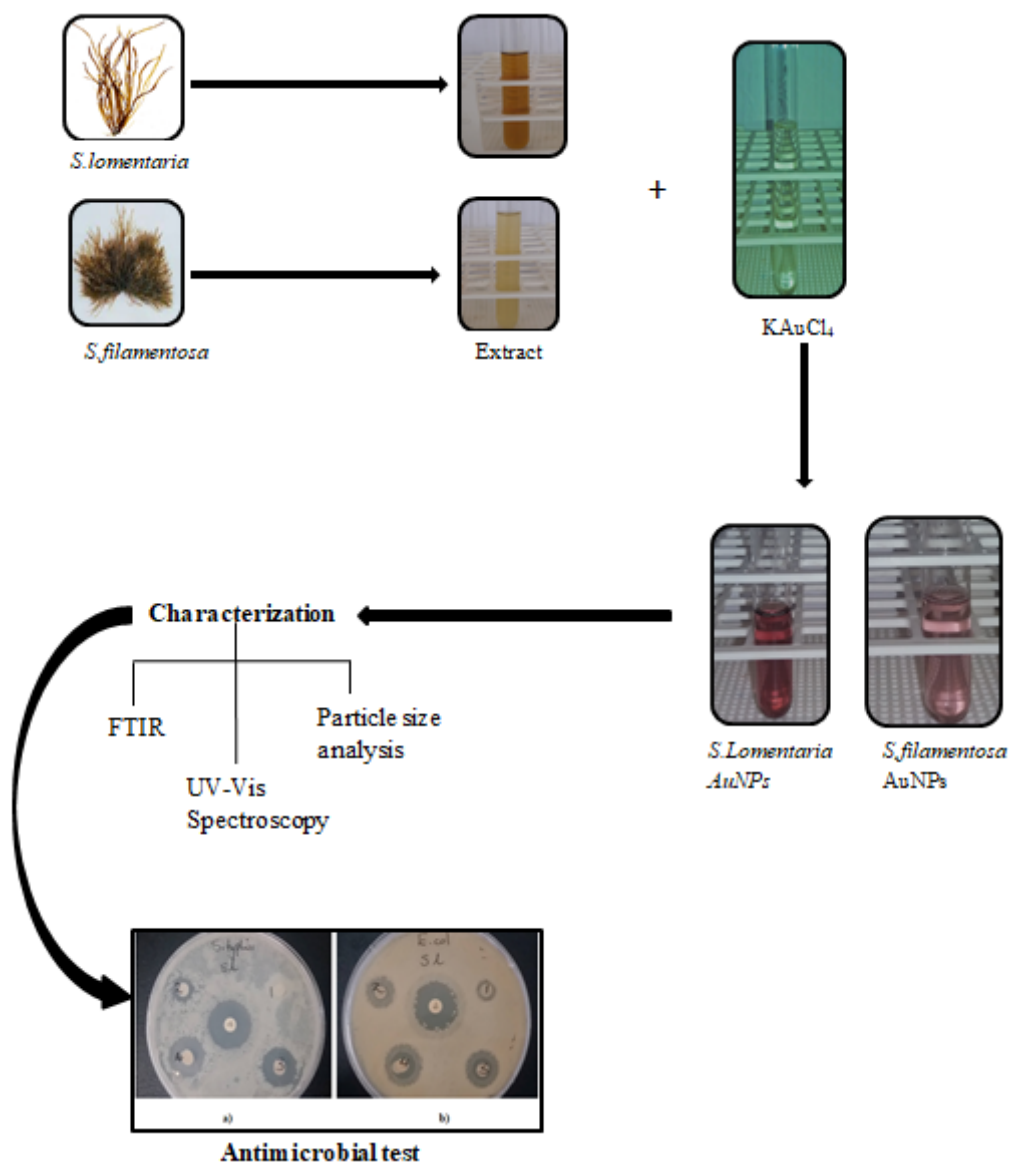


Figure 1. The overview of synthesis, characterization and antibacterial activity of gold nanoparticles using *S. lomentaria* and *S. filamentosa* extract.

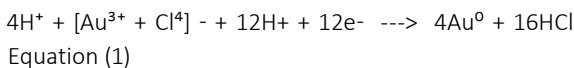
The flow chart shows a summary of the process from the collection of the seaweed and the preparation of the extract solutions. The extract solution are then mixed with the potassium tetrachloroaurate at a certain ratio to produce the nanoparticles and characterization was then done using the FTIR, UV-Vis spectrophotometer and the Mastersizer. The antibacterial test was then done using the disc diffusion method.

Preparation of Extract

The seaweeds were washed with tap water to remove other marine organisms and epiphytes. They were rinsed with distilled water and then placed in the oven to dry at 45°C. The samples are ground into a powder using a pestle and mortar. The algae powder was mixed with ethanol at a ratio of 1:15 (w/v) and poured into the soxhlet apparatus. The extraction process was done at 50°C for 8 hours. After extraction the solvent was then evaporated at a temperature of 40°C using rotary evaporator. The *S. lomentaria* extract was brown in color and the *S. filamentosa* extract is yellowish as shown in Figure 1 is then kept at 4°C in refrigerator for further use.

Synthesis of Gold Nanoparticles

Potassium tetrachloroaurate (KAuCl₄) purchased from Sigma-Aldrich was the source of the Au³⁺. The potassium tetrachloroaurate is dissolved in distilled water to make a solution that is 2.5×10⁻⁴M in concentration. For synthesis as shown in Figure 1, 22.5 ml of potassium tetrachloroaurate is added into a beaker and it is heated to 100°C and stirred vigorously. 7.5 ml of seaweed extract was measured using a graduated syringe and added to the KAuCl₄. The solution is continuously stirred for about 10 minutes and the color change is observed. The synthesis is repeated at different time intervals and temperatures. The UV-Vis spectroscopy is carried out at the different intervals to monitor the progress of the reaction. For time intervals the UV-vis spectrum was recorded at 5 min, 10 min, 15 min, 20 min, 25 and 30 min whereas for temperature intervals, the synthesis is carried out at 25°C, 50°C, 75°C and 100°C. This was done for both seaweed samples. The chemical equation for this reaction is:



Characterization of Synthesized Gold Nanoparticles

The synthesis of the AuNPs and kinetic behavior was monitored by the UV-Vis spectrophotometer by analyzing formation of the surface resonance peaks. The scanning range of the nanoparticles is 400-800 nm at a scanning speed of 480 mm/min. The FT-IR was done to analyze the presence of the phytochemicals in the extracts used in the biosynthesis. Small aliquots of the concentrated reaction mixture are measured after the reaction in the mode at 400-4000cm⁻¹. The spectra were recorded and the analysis was also carried out

after the synthesis of the AuNPs and the spectra are then analyzed. Nanoparticle size was measured using the Malvern Mastersizer 2000 particle size analyzer. Crystalline structure was analyzed using X-ray diffractometer (Rigaku ZSX Primus II).

Antioxidant Activity of the Synthesized Gold Nanoparticles

The effect of extracts on DPPH radical was estimated by DPPH radical scavenging assay using the method of Znati et al. [17] with slight modification. Solution of 0.135 mM DPPH in methanol was prepared and 1.0 ml of this solution was mixed with 1.0 ml (1:1 ratio) of nanoparticles suspension in methanol containing (20, 40, 60, 80, 100 g/ml) of the nanoparticles. After 30 min at 25°C incubated in darkness, the absorbance of each sample is measured at 517 nm. Blank is prepared by mixing 0.5 ml of DPPH solution with 0.5 ml of ethanol. A positive control of Gallic acid is prepared to compare the results of decreased absorption induced by the samples. The following equation is used to calculate the capability to scavenge 50% of DPPH, which is the percentage of inhibition (Equation 2).

DPPH scavenging effect / Inhibition ratio (%) =

$$\left[\frac{(A_{\text{control}} - A_{\text{sample}})}{A_{\text{control}}} \right] \times 100$$

(Equation 2)

All tests are carried out in triplicate. A control stands for the absorbance for all the reagents except the tested sample. A sample stands for the absorbance of the test sample.

Antimicrobial Activity

Minimum Inhibitory Concentration

This technique is done to deduce the minimum amount of AuNPs that can inhibit the growth of bacteria. Different concentrations of gold nanoparticles were prepared (25 µl, 50 µl, 75 µl and 100 µl). The bacteria (*S. typhi* and *E. coli*) were then cultured in the nutrient broth and the AuNPs was also added. Nutrient broth with bacteria only and another without the bacteria served as the controls. The bacterial cultures were then incubated at 37°C for 24 hours and then the results were recorded.

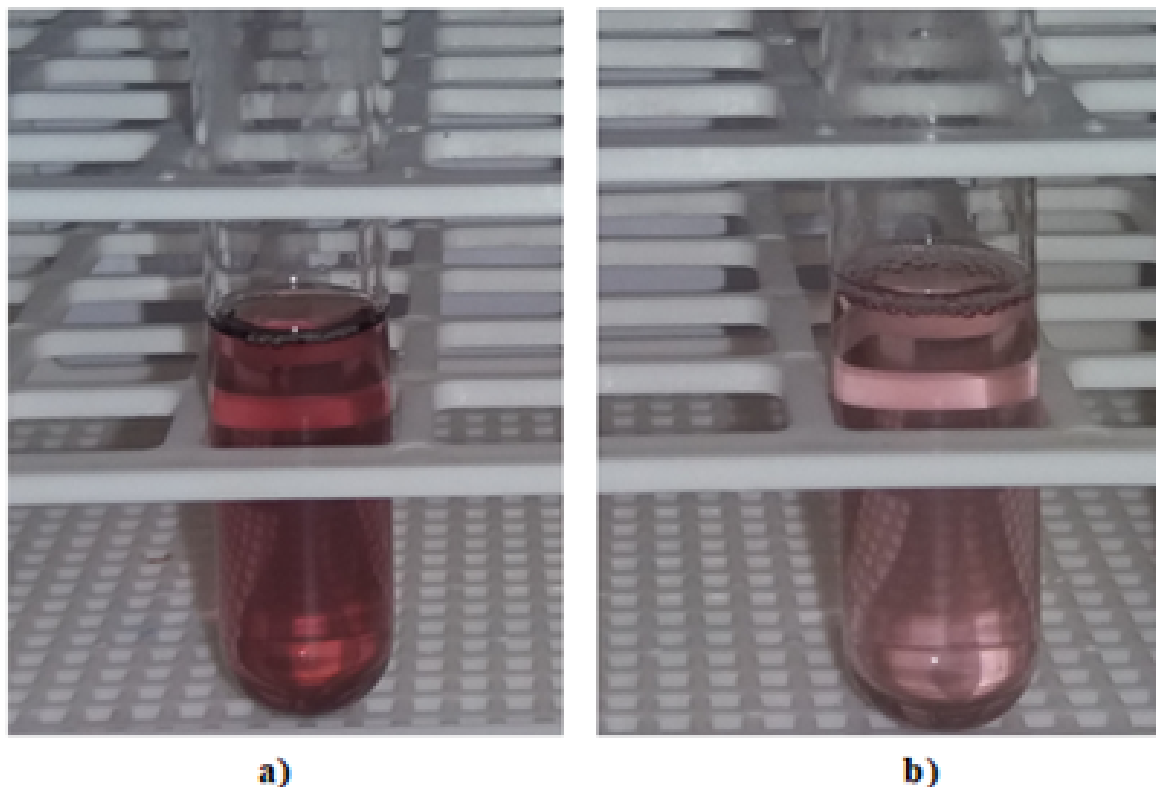


Figure 2. The color of the gold AuNPs synthesized using a) *S. lomentaria* and b) *S. filamentosa*. The solution of the gold nanoparticles synthesized using *S. lomentaria* species showed a ruby red color and that of gold nanoparticles synthesized using *S. filamentosa* species exhibited a pink color.

Zone of Inhibition

Antibacterial activity analysis was carried out using disc diffusion method, in which a loop was used to take the bacterial solution and swab it on the surface of the media. The discs impregnated with the gold nanoparticles (100 μ l per disc in 6mm in diameter) and allowed to dry before they were placed onto the surface of the petri dishes using forceps. The dishes with bacteria were then incubated at 37°C for 24hours. The antibiotics ciprofloxacin were used as the positive control. After 24hours the clear zones around the discs were measured and expressed in millimeters and this is known as the zone of inhibition.

Statistical Analysis

Data were analyzed with one-way analysis of variance (ANOVA). The significant difference among the mean values was examined by Duncan's test ($P \leq 0.05$) with SPSS 13.0 software (SPSS Inc., Chicago, USA).

RESULTS and DISCUSSIONS

Biosynthesis of AuNPs and UV-vis spectroscopy

The formation and presence of bio reduction was confirmed by the color changes that take place within a few minutes after addition of the seaweed extract. Initially on a ratio of 1:1 the color of the solution was purple and the gold nanoparticles formed were relatively large after few adjustments were made to the experimental parameters and the reactants. The color of the solution changed to pink and ruby red following the mixing of extract and the gold at a ratio of 1:4 as shown in Figure 2 for both species *S. filamentosa* (SF) and *S. lomentaria* (SL) respectively, which is a characteristics of AuNPs [18]. Change in the color of the solution to pink and ruby confirmed the synthesis of AuNPs with respect to reaction time and temperature nanoparticles was seen in Figure 2. Increased in the color intensity as well as absorbance increase has to do with reaction time and temperature [19]. AuNPs formation was confirmed by the rapid appearance of red or pink color, which has to do with bio reduction of Au (III) ions due to excitation

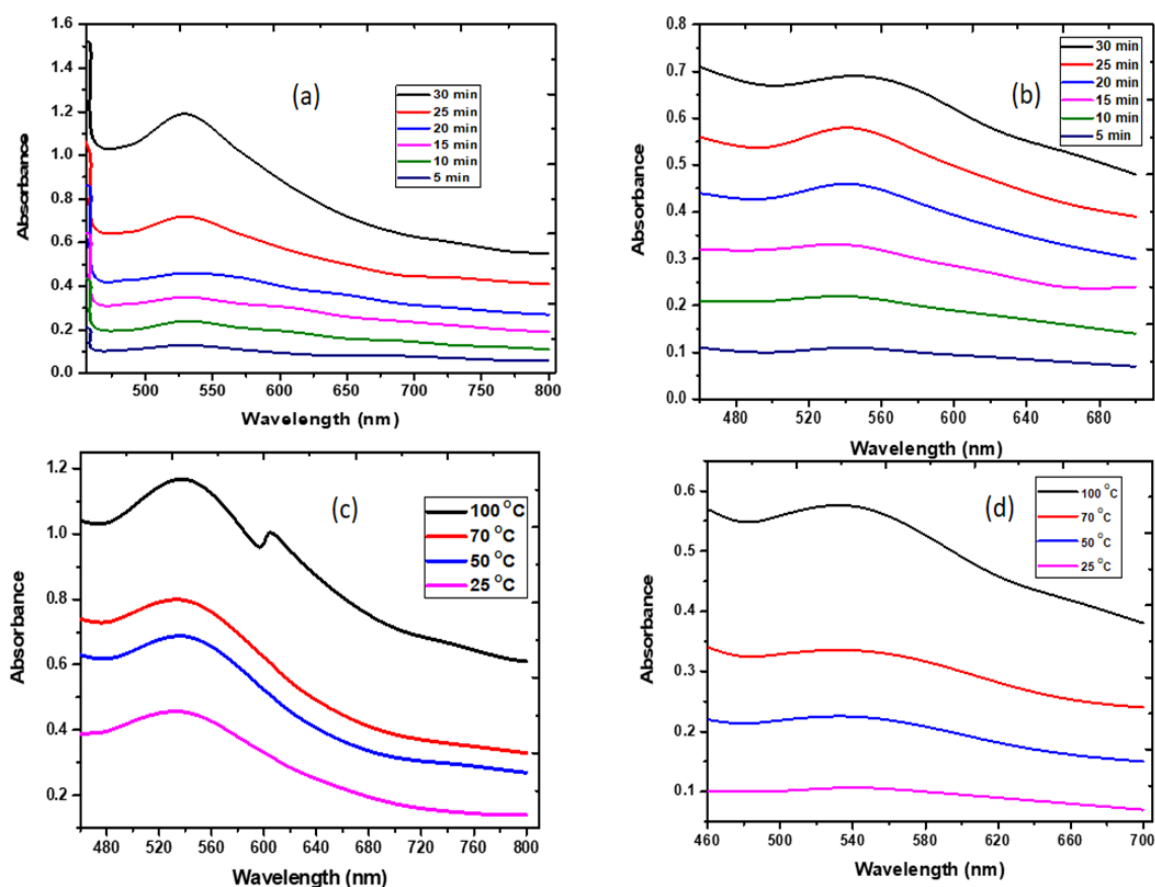


Figure 3. (a) UV-Vis spectrum of gold nanoparticles synthesised using *S. lomentaria* with respect to time. (b) UV-visible spectrum of gold nanoparticles synthesized using *S. filamentosa* with respect to time (c) UV-Vis spectrum of gold nanoparticles synthesized using *S. lomentaria* with respect to time (d) UV-visible spectrum of gold nanoparticles synthesized using *S. filamentosa* with respect to temperature.

of surface plasmon resonance in the gold nanoparticles [19].

The synthesis of AuNPs using *S. lomentaria* and *S. filamentosa* extract was demonstrated by the subsequent color changes that took place in the reaction mixture. The color of the gold nanoparticles synthesized using *S. lomentaria* change from yellow to ruby red and that of the synthesis using *S. filamentosa* changed to pink [20]. The color of the AuNPs change directly from yellow to red or sometimes pink is as a result of surface plasmon resonance excitation in the AuNPs which was observed and confirmed using the UV-Vis spectral evaluation [21].

Shift in SPR of the AuNPs in relation with time interval and temperature change (Figure 3a-d). Absorbance and color intensity values gradually changes with the reaction time which has to do with AuNPs increased as observed, and it also leads to continuous reduction of Au ions

as observed. Characteristic SPR absorption peaks at 532 nm confirms the formation of nanoparticles.

The reaction mixture with an excitation of the surface plasmon resonance recorded of 540 nm at the higher temperatures as shown in Figure 3a-d. The reaction time is prolonged with respect to decrease in temperature, at lower temperature, the reaction time is prolonged and the absorption spectra show a gradual increase of the absorbance shift in the λ_{max} from 550 nm to 540 nm. Additionally, effect of temperature on the stability of *S. lomentaria* AuNPs was investigated by heating the nanoparticles at 80°C for 30 min. Furthermore, increase in temperature would lead to the production of AuNPs that are stable under a wide range of environmental factors and this enabled them to study their potential effectiveness and safe therapy. Thus, the stability of the *S. lomentaria* AuNPs made it easier for the storage of the nanoparticles for use during the antimicrobial test

[22]. Increase in temperature resulted in the shifting of the λ_{max} to longer wavelengths. Thus, at temperature above 50°C leads to further increase in the absorption indicating the formation of smaller nanoparticles. The absorption maximum is attributed by the surface plasmon resonance. There is a smaller change in absorbance when the temperature is increased from 50°C to 70°C which indicates there is a slight change in size of the gold nanoparticles. On the other hand big gaps are visible when the temperature is increased from 25°C to 50°C and from 70°C to 100°C indicating an increased in the reaction speed.

Temperature affects the size of the nanoparticles and the rate of the reaction. The gold nanoparticles produced for both extract at higher temperature are highly stable and can be stored for some days without any change. The maximum absorption of gold nanoparticles with respect to temperature ranges from 536 to 545 nm. Furthermore, there was a slight increase in the absorbance maxima which indicates the production of large nanoparticles at lower temperatures. Thus, at a higher temperature, the reduction was faster and it was observed by the change in color and the mixture with an excitation of the surface plasmon resonance at 536 nm. This can be compared to the synthesis of gold nanoparticles using *P. tetrastromatica* which showed that

smaller nanoparticles where synthesized at high temperature of 80°C and the UV-Vis spectra peaks where in the range of 55-540 nm [23, 24].

Surface plasmon bands of the gold nanoparticles are broad with an absorption tail in the longer wavelength region that extends well into the near infrared region of the colloids synthesized at different temperatures. The absorption maxima for the gold nanoparticles were obtained for the least values (535-543 nm) without any other absorption band in the longitudinal plasmon resonance (Figure 3d). Additionally, significant increase in the intensity of the absorption peak is noted. Initially, at 5 minutes there is slight to no reaction at all and the color solution remains gold the absorption peak is at approximately 540nm. Color starts to change gradually with change in time, and there is a slight shift in the absorption peak at 10minutes. Furthermore, color change was also observed over time as the color change starts taking place after 10 to 15 minutes and the solution starts turning into a pale pink color. Increase revealed some significant peak shifts which is attributed by the surface plasmon resonance band of the gold nanoparticles.

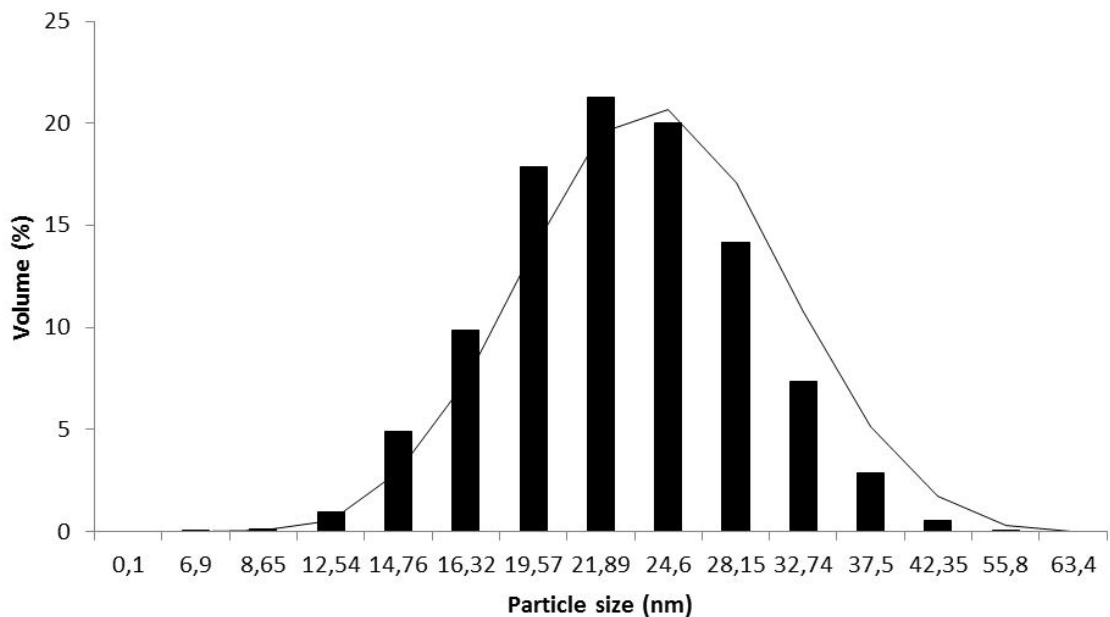


Figure 4a. Mean average particle size distribution of the *S. lomentaria* species. The graph is representation of data as mean values of the particle size and the experiment with n=3 replicates of the experiment. The graph also shows the trend line for the particle size distribution filamentosa with respect to temperature.

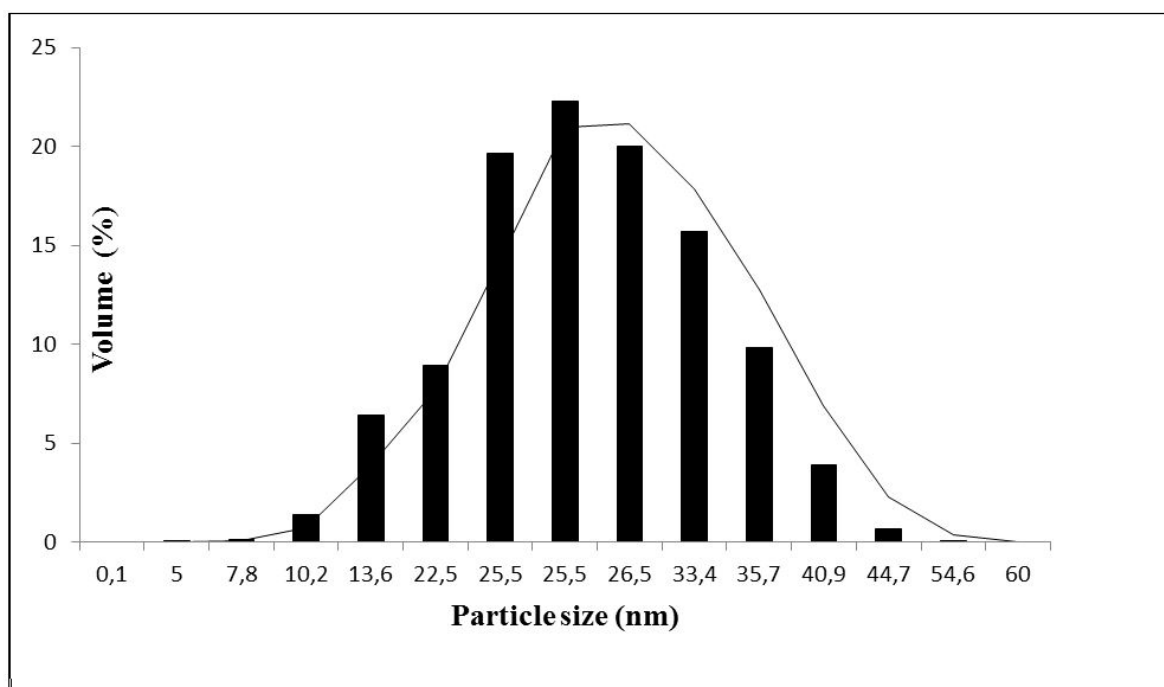


Figure 4b. The average particle size distribution of AuNPs synthesized using *S. filamentosa*. The graph represents data as mean values of the particle size and the experiment with $n=3$ replicates of the experiment. The graph also shows the trend line for the particle size distribution.

Fourier transform infrared (FTIR) Studies

FTIR analysis of AuNPs were carried out at 25°C to identify the type of the biological molecules present in the AuNPs synthesized using *S. Lomentaria* and *S. filamentosa* extracts as reducing agents. The FTIR was analyzed at a range of 500 and 4000 cm^{-1} . Synthesized AuNPs using *S. Lomentaria* and *S. filamentosa* revealed FTIR spectra, which show the composition of the molecules of *S. Lomentaria* and *S. filamentosa* and their distribution on the AuNPs surface.

Stretch of the peak at 3275 cm^{-1} is a characteristic of the O-H bond in *S. Lomentaria* (Figure 5a), which stretches to 3292 after the bio reduction of the gold solution to form gold nanoparticles using *S. Lomentaria* (Figure 5c). This peak has a broad trough and this peak is present in both spectra because the O-H bond is still present even after the bio reduction of the gold solution [18]. The appearance of the peak at 1622 cm^{-1} is characteristic of the C=O bond (carbonyl). The peak at 3275 cm^{-1} represent the presence of organic compounds in the both the extract and the gold nanoparticle solution. This indicates the presence of amide bonds in the extract solution. Presence of the amide bonds after reduction is also shown by the stretch of peaks after reduction at 1630 cm^{-1} and 1900 cm^{-1} . Study has also shown the gold

nanoparticles were synthesized using *Turbinaria conoides*, the FTIR results showed the presence of amines, polyphenolic and carboxylic groups in the algae extract [18]. The groups are responsible for the reduction of the gold ions just like the *S. lomentaria* extract. The strong bands at 1042 cm^{-1} and 1080 cm^{-1} are caused by the vibrations of the C-OH bonds which are single bond absorption that can either be caused by the presence of proteins or certain glucosides. The peak at 2976 cm^{-1} corresponds with presence of C-H bonds. The weak aromatic C-H bonds are also represented by the 876 cm^{-1} and 590 cm^{-1} . Additionally presence of carboxyl groups as identified by FTIR were involved in the gold recovery with the brown alga (*Sargassum polycystum*) and proposed the formation of oxygen bridges between gold and these groups [25].

The FTIR spectrum result shows bands represented by the bond vibrations and stretch caused by the biomolecules present in both *S. lomentaria* and *S. filamentosa*. After bio reduction of the gold solution, FTIR spectrum shows stretch of the functional groups represented by the bands formed as a result of stretch and vibrations after the formation of new bonds. Some of the functional groups represented by the bands are carboxylic acids, hydroxyl, carbonyls and amines.

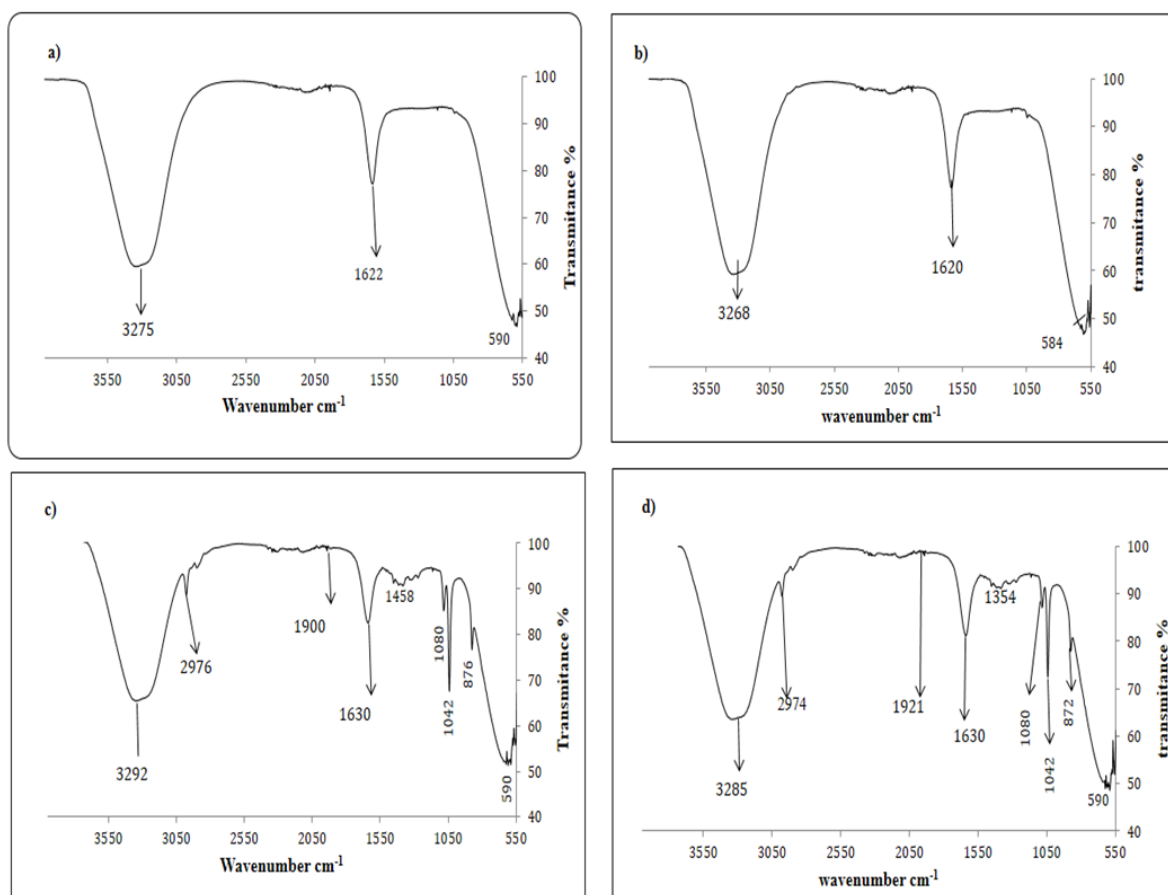


Figure 5. FT-IR spectra showing the bands of (a) *S. lomentaria* extract (b) *S. filamentosa* extract (c) Gold nanoparticles synthesized using *S. lomentaria*. (d) Gold nanoparticles synthesized using *S. filamentosa*. The FTIR spectrum result shows bands represented by the bond vibrations and stretch caused by the biomolecules present in both *S. lomentaria* and *S. filamentosa*. After bio reduction of the gold solution, FTIR spectrum shows stretch of the functional groups represented by the bands formed as a result of stretch and vibrations after the formation of new bonds. Some of the functional groups represented by the bands are carboxylic acids, hydroxyl, carbonyls and amines.

The stretch of the peak at 3268 cm^{-1} is a characteristic of the O-H bond in *S. filamentosa* (Figure 5b), which stretches to 3285 cm^{-1} after the bio reduction of the gold solution to form gold nanoparticles using in *S. filamentosa* (Figure 5d). The stretch at 1630 cm^{-1} and 1921 cm^{-1} give rise to the possible presence of the carbonyl (C=O) group which means there are amide bonds present in both the extract and the gold nanoparticle solution. The peak at 2974 cm^{-1} corresponds with the C-H bonds present in the gold nanoparticle solution. The peaks resemble the presence of flavonoids, phenolics, flavones and terpenoids. There are also the presence of the aromatic carbons that are shown by the bands at 1042 cm^{-1} and 1080.13 cm^{-1} . The bands at 872 and 590 cm^{-1} represent weak aromatic C-H bonds. In a study on the synthesis of gold nanoparticles using *P. tetrastromatica*, the FTIR showed that the extract contained functional group that might relate to some sugar molecules [23].

XRD Results

The result of XRD pattern analysis of AuNPs using Cu K α radiation ($\lambda = 1.54184\text{ \AA}$) in 2θ at a range of 100 to 1000 (scan speed of 30 min^{-1}), which revealed the Bragg's reflections at 2θ values of 39.579 , 46.567 , 64.610 , 77.546 and 79.700 . Similarly, the Bragg's reflections at 2θ values represented [200], [111], [311] and [220] planes respectively, that confirmed the crystalline nature of gold with cubic face centered (FCC) structure of AuNPs (Figure 6a). Presence of those peaks confirm the formation of highly purified AuNPs without any impurity. Additionally, the pattern shows that the AuNPs was obtained from natural sources.

The XRD pattern obtained for gold nanoparticles synthesized using *S. lomentaria* exhibits Bragg reflections, which could be well manifested on the basis of the face centered cubic (FCC) gold nanostructures. The

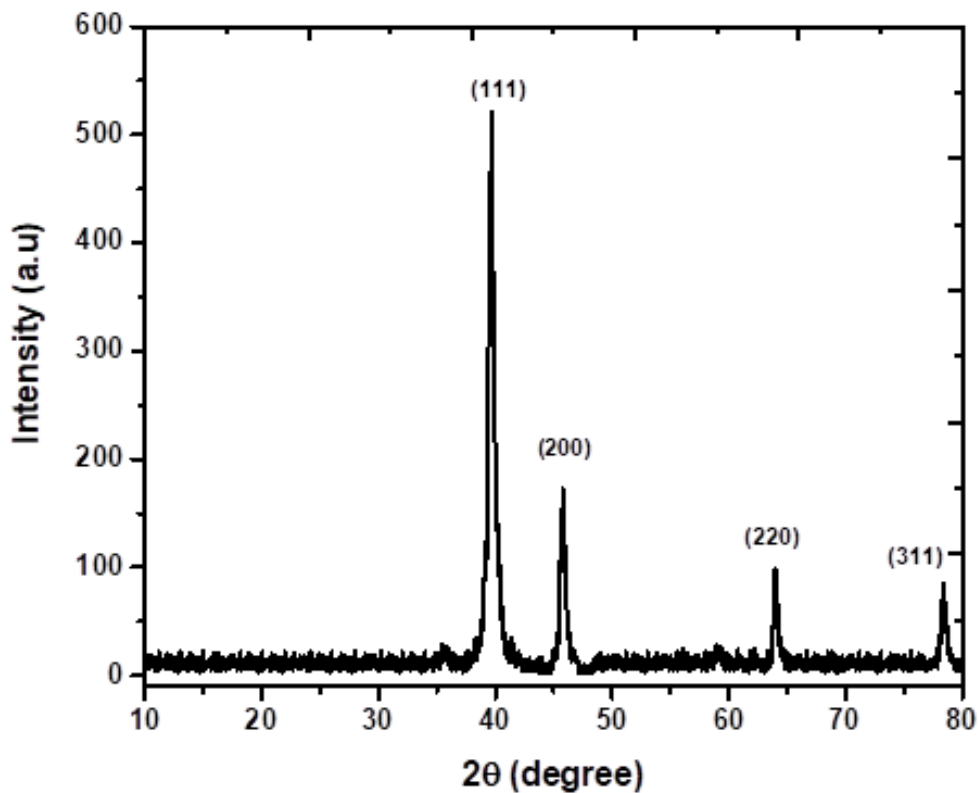


Figure 6a. XRD of gold nanoparticles synthesized using *S. filamentosa*.

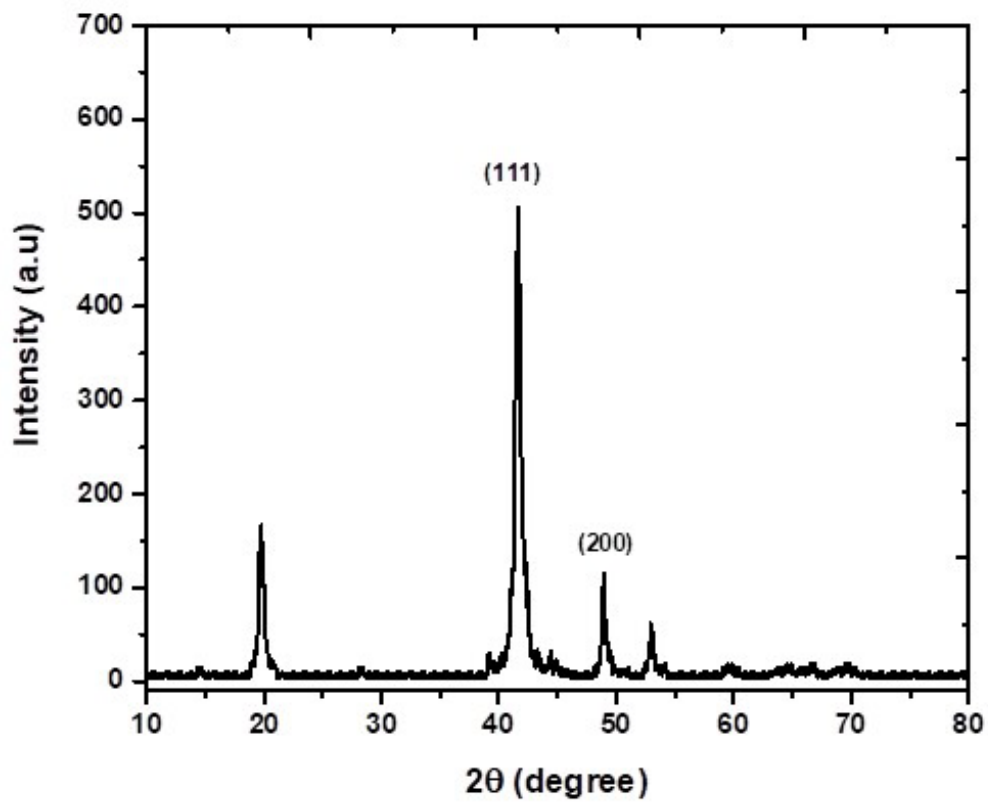


Figure 6b. XRD of gold nanoparticles synthesized using *S. lomentaria* aqueous extract.

Table 1. Minimum inhibitory concentration using different concentration.

	Sample	<i>E. coli</i>	<i>S. typhii</i>
Nutrient Broth	NB	-	-
	NBB	+	+
<i>S. filamentosa</i> AuNPs	25 µl	+	+
	50 µl	+	+
	75 µl	-	+
	100 µl	-	-
<i>S. lomentaria</i> AuNPs	25 µl	+	+
	50 µl	+	+
	75 µl	-	-
	100 µl	-	-

The Minimum inhibitory concentration was done with:- NB: - Nutrient broth only. NBB:-Nutrient broth cultured with bacteria. +:- Stands for bacterial growth. - : stands for no bacterial growth.

The volume of nanoparticles that is put on to the discs was 25 µl, 50 µl, 75 µl, and 100 µl. The minimum amount of gold nanoparticles required to inhibit the growth of bacteria was 75µl.

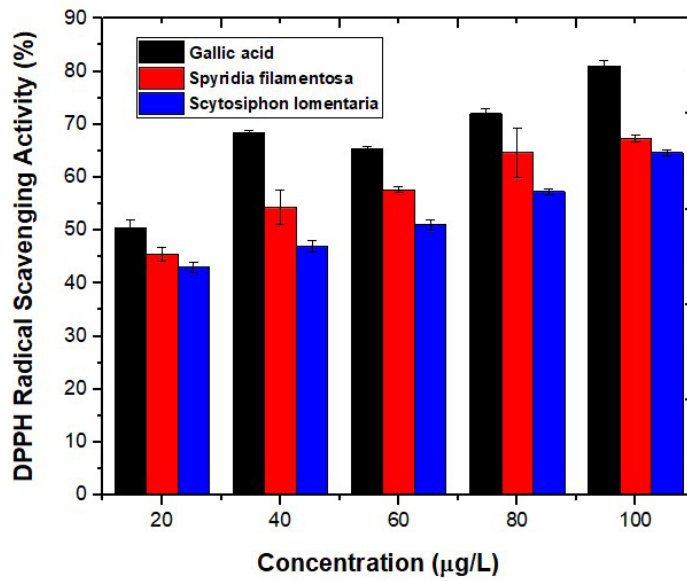


Figure 7. DPPH free radical scavenging activity of biosynthesized AuNPS using *S. filamentosa* and *S. lomentaria*.

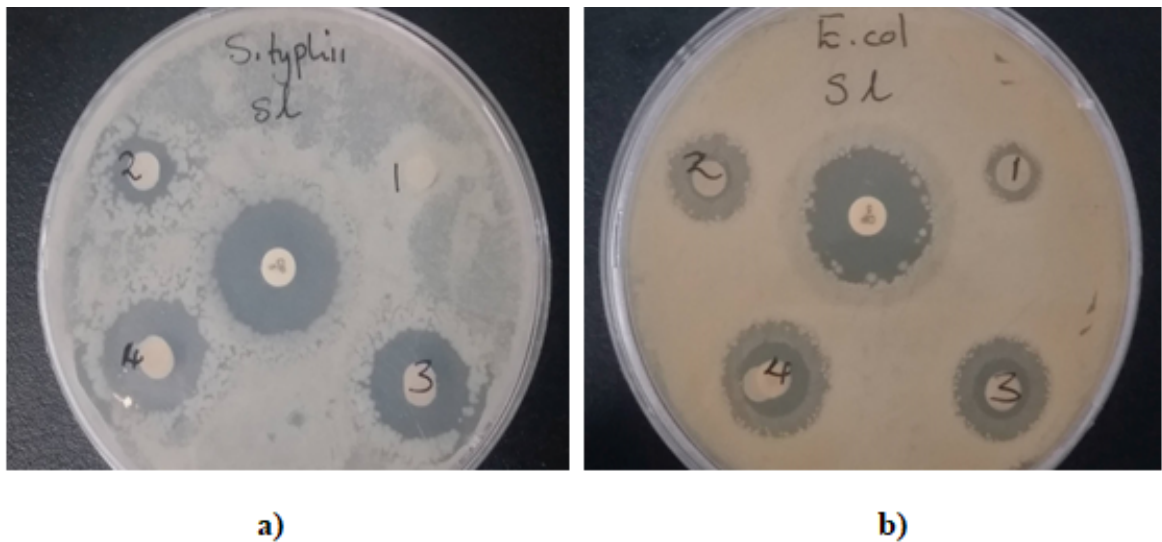


Figure 8a. Diagram showing disc diffusion method for *S. lomentaria* AuNPs against a) *S. typhii* and b) *E. coli*.

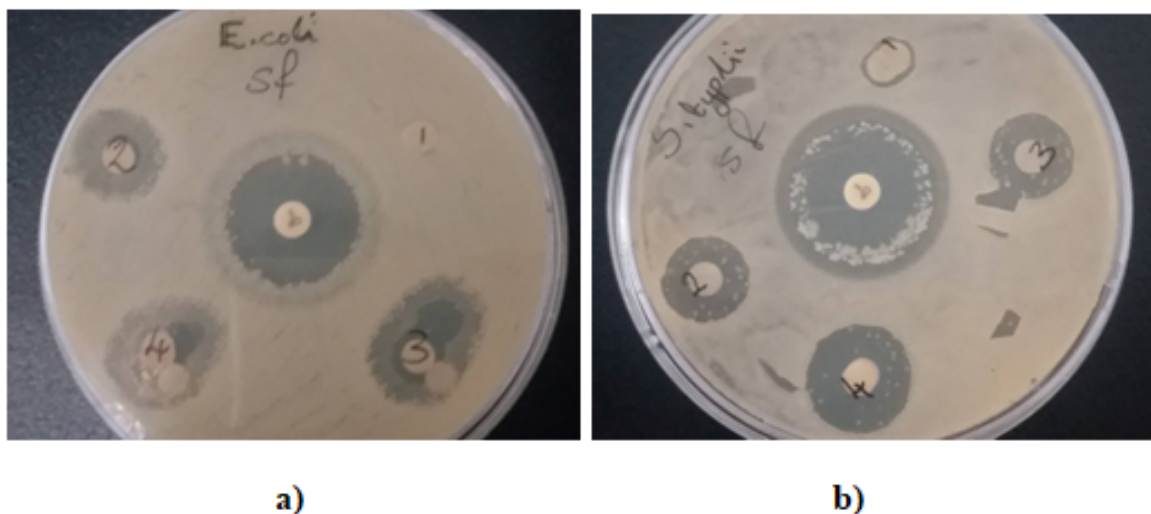


Figure 8b. Diagram showing disc diffusion method for *S. filamentosa* AuNPs against a) *E. coli* and b) *S. typhi*.

The antibacterial activity assay was carried out with the Antibiotics at the center, 1) negative control, 2) Extract, 3) KAuCl₄, 4) AuNPs as shown by figure 20 and 21 respectively. The experiment was carried out in triplicate.

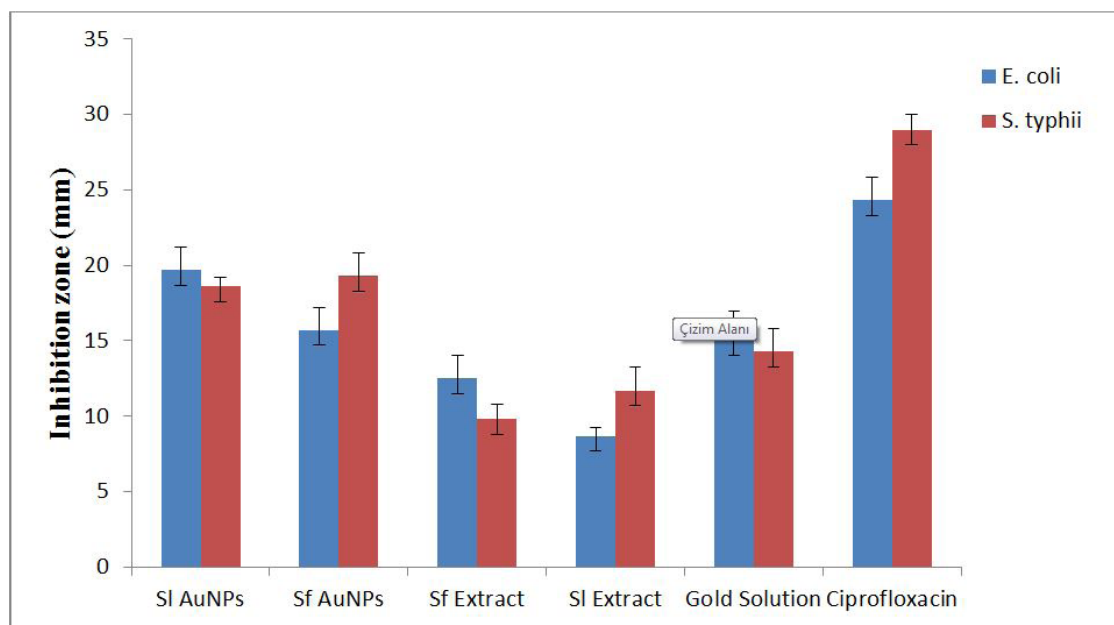


Figure 8c. A graphical representation of the mean zones of inhibition formed during the disc diffusion method of antimicrobial test. The data is represented as the mean \pm standard deviation of the at least n=3 replicates of the experiment.

very strong diffraction peak at 39.512 degrees is considered to be of [111] facet of the face centered cubic structure (Figure 6b), while the diffraction peaks of other gold peaks are found to be much weaker compared to gold nanoparticles synthesized using *S. filamentosa*. It is imperative to note that the ratio of intensity between [200] and [111] peaks, [220] and [111] peaks as well as [311] and [111] peaks are much smaller compared to the intensity ratios of gold nanoparticles synthesized using *S. filamentosa*. Presence of those peaks confirm the development of purified AuNPs without any impurity. Additionally, the pattern shows that the AuNPs was

obtained from natural sources. Results obtained from our study are in agreement with many similar studies and supports the previous findings of Philip [28] that revealed the crystalline nature of gold to be like that of circular rings.

Antioxidant Activity of Gold Nanoparticles

Antioxidant activity of the synthesized AuNPs for both extract were studied using DPPH free radical scavenging activity assay. In addition, the results obtained from the study were shown in Figure 7. Both nanoparticles showed significant activity but *S. filamentosa* AuNPs

Table 2. Comparison of the AuNPs synthesised using *S. filamentosa* and *S. lomentaria*

Algae species	Colour change	UV-Vis spectroscopy	Particle size distribution	Antibacterial activity	References
<i>Turbinaria conoides</i>	Ruby red	538 nm	2-19 nm	No inhibition formed against marine biofilm forming bacteria strains.	Vijayan et al., (2014) [36]
<i>Stoechospermum marginatum</i>	Ruby red	550 nm	<100 nm	Maximum inhibition against <i>E. faecalis</i>	Rajathi et al., (2012) [37]
<i>Galaxaura elongata</i>	Ruby red	536 nm (powder) 535 nm (extract)	2-100 nm	Maximum inhibition against <i>K. pneumoniae</i>	Abdel-Raouf et al., (2017) [38]
<i>Padina tetrastromatica</i>	Ruby red	550 nm	20-90 nm	High zone of inhibition against <i>S. aureus</i> and <i>P. aereginosa</i> .	Kayalvizhi et al., (2014) [39]
<i>Turbanaria ornate</i>	Ruby red	~550 nm	20-90 nm	Maximum zone of inhibition against <i>S. aureus</i>	Kayalvizhi et al., (2014) [39]
<i>Sargassum polycystum</i>	Ruby red	534 nm	50-80 nm	Maximum inhibition zone against <i>E. coli</i>	Dhas et al., (2014) [40]
<i>S. filamentosa</i>	pink	536 nm	<100 nm	Maximum inhibition zone against <i>S. typhi</i>	Present Study

revealed higher antioxidant activity ($IC_{50} = 38.84 \mu\text{g}/\text{mL}$) compared to *S. lomentaria* ($IC_{50} = 32.804 \mu\text{g}/\text{mL}$) and this might be as a result of biomolecules present in the extract. Antioxidant activity that is demonstrated by nanoparticles has to do with organic biomolecules present within the extract used during the nanoparticle synthesis as a chelating agent [29]. Additionally, studies reveal that high surface to volume ration are the reason for free radical scavenging activity of various synthesized nanoparticles [30, 31].

Antimicrobial Activity

Antimicrobial potential of the synthesized AuNPs were investigated using agar well diffusion assay. Minimum inhibition concentration (MIC) and mean zone of inhibition (diameter in mm) were evaluated against *E. coli* and *S. typhi* and the result of the MIC was presented in Table 1 and mean zone of inhibition was represented in Figure 8a-d. The MIC for both was found nanoparticles was found to be SI AuNPs and Sf AuNPs gave the higher zone of inhibition when compared with the plant extract and

gold nanoparticles solution. Sf AuNPs revealed highest zone of inhibition against *S. typhi* when compared with SI AuNPs. Differences in the zone of inhibition between the two nanoparticles could be as a results of the difference in the biomolecules presents in the plants.

The antibacterial properties of the gold nanoparticles synthesised using *S. lomentaria* and *S. filamentosa* was tested against two strains of bacteria that are food borne (*E. coli* and *S. typhi*) and the visual observation showed that there were zones of inhibition formed around the nanoparticle solution and as shown in Figure 8.

Inhibitory action of nanoparticles differs and it has been reported to be based on surface area, size, biomolecule constituents coated on the AuNPs and the species [32]. Both SI AuNPs and Sf AuNPs revealed more inhibition on *S. typhi* than on *E. coli* and this could be as result of differences in the bacterial membrane structure, Gram positive bacteria, peptidoglycan layers are very thick than Gram negative bacteria [33]. Additionally, studi-

es reported that, AuNPs exert its anti-microbial effect through changing the membrane potential and inhibition of F-type ATP synthase, which could lead to decrease in ATP level and decline in the metabolism of microbes [34]. AuNPs can also inhibit ribosomal RNA protein S10 subunit through modification of 4, 6-diaminopyrimidine thiol, which can serve as bacterial tRNA base, and it has the proficiency to inhibit tRNA function which could lead to the loss of protein synthesis [35].

The inhibition zone of the 19.7 mm and 15.7 mm was recorded for *E. coli* against the *S. lomentaria* AuNPs and *S. filamentosa* AuNPs respectively (Figure 8c). Simultaneously 18.6 mm and 19.3 mm was recorded for *S. typhi* against the *S. lomentaria* AuNPs and *S. filamentosa* AuNPs respectively. A similar study done on the synthesis of gold nanoparticles using a *G. elongata* ethanoic extract showed that more of inhibition were formed against *E. coli*, *K. pneumoniae* and multiple antibiotic resistant *S. aureus* with the maximum zones measuring between 17 mm and 16 mm respectively [38]. A report done by Kayalvizhi et al., indicated that capped gold nanoparticles can interact with bacterial cell walls and interrupted the metabolism of the bacterial cell due to the presence of phytochemicals that are present in the in the plant extract. The small size of the nanoparticles allowed them to enter the cell membrane and interact with the mitochondria and other organelles since the nanoparticles do not degrade the cell wall [39]. The *S. lomentaria* gold nanoparticles showed the greatest antibacterial effect against *E. coli*. The gold nanoparticles synthesized using the *S. filamentosa* also showed a great antibacterial effect against *S. typhi*. The p values are $p < 0.05$. Thus, there is a significant difference in the zone of inhibition zone formed by the gold nanoparticles synthesized using *S. lomentaria* and there is no significant difference between the gold solution and the gold nanoparticles synthesized using the *S. filamentosa* as the p value is greater than the critical values.

Comparison of the Gold Nanoparticles

The gold nanoparticles formed using *S. lomentaria* form a ruby red colour whereas the *S. filamentosa* synthesised nanoparticles form a pink colour. This is due to the different surface plasmon resonance which also UV-Vis peaks at 536 and 540 nm. On average the nanoparticles are relatively equal as shown in Table 2. There is no significant difference in the bands shown by the FT-IR spectra showing that there are approximately similar bi-

omolecules. Our study revealed that, the two species of seaweed have antibacterial activity against *S. typhimurium* and *E. coli*. After the synthesis of the nanoparticles, the test showed that there is a significant difference in the inhibition zones formed by extracts and those formed by the nanoparticles. According to literature there is not much variation in the functional groups found in the bioactive compounds of most seaweed compounds, therefore Table 2 shows some of the variations in antibacterial activity, UV-Vis spectroscopy, colour change and particle size of AuNPs synthesised using various seaweed species.

Furthermore, antioxidant study using DPPH free radical scavenging activity revealed *S. filamentosa* to have higher antioxidant activity ($IC_{50} = 38.84 \mu\text{g/mL}$) when compared to *S. lomentaria* ($IC_{50} = 32.804 \mu\text{g/mL}$) and this might be as a result of biomolecules present in the extract.

Conclusion

Overall, AuNPs were synthesized using aqueous extract of *S. filamentosa* and *S. lomentaria* through a constant, and eco-friendly green route. Gold reduction using the two species of seaweeds is effective as the biomolecules required for the reduction of the gold ions are available in the extract solution. The successful synthesis of AuNPs using aqueous extract of *S. filamentosa* and *S. lomentaria* was confirmed using UV-vis, Zeta sizer, FTIR and XRD. The UV-Vis result revealed absorption peak at range of 540 nm. The biosynthesized nanoparticle showed strong antioxidant activity with IC_{50} value of 38.84 and 32.804 $\mu\text{g/mL}$ for *S. filamentosa* and *S. lomentaria* respectively. Additionally, synthesized AuNPs showed significant antimicrobial activity against *E. coli* and *S. typhi*.

References

1. S. Hua, M.B.C. de Matos, J.M. Metselaar, G. Storm, Current Trends and challenges in the clinical translation of nanoparticulate nanomedicines: pathways for translational development and commercialization, *Front Pharmacol.*, 9 (2018) 790.
2. P.K. Jain, X. Huang, I.H. El-Sayed, M.A. El-Sayed, Noble metals on the nanoscale: optical and photothermal properties and applications in imaging, sensing, biology, and medicine, *Acc. Chem. Res.*, 41 (2008) 1578-1586.
3. P. Mohanpuria, N.K. Rana, S.K. Yadav, Biosynthesis of nanoparticles: technological concepts and future applications, *J. Nanopart. Res.*, 10 (2008) 507-517.

4. P. Khandel, R.K. Yadaw, D.K. Soni, L.Kanwar, S.K. Shahi, Biogenesis of metal nanoparticles and their pharmacological applications: present status and application prospects, *J. Nanostructure Chem.*, 8 (2018) 217-254.
5. V.G. Kumar, S.D. Gokavarapu, A. Rajeswari, T.S. Dhas, V. Karthick, Z. Kapadia, T. Shrestha, I.A. Barathy, A. Roy, S. Sinha, Facile green synthesis of gold nanoparticles using leaf extract of antidiabetic potent *Cassia auriculata*, *Colloids Surf. B.*, 87 (2011) 159-163.
6. D. Kavaz, S. Lamido, H. Umar, Antimicrobial activity of silver nanoparticles synthesized via green chemistry, *the Russian Academic Journal*, 34 (2015) 36-44.
7. H.Y. El-Kassas, M.M. El-Sheekh, Induction of the synthesis of bioactive compounds of the marine alga *Tetraselmis tetraele* (West) Butcher grown under salinity stress, *Egypt J. Aquat. Res.*, 42 (2016) 385-391.
8. S. Naraginti, Y. Li, Preliminary investigation of catalytic, antioxidant, anticancer and bactericidal activity of green synthesized silver and gold nanoparticles using *Actinidia deliciosa*, *J. Photochem. Photobiol. B Biol.*, 170 (2017) 225-234.
9. Z. Salari, F. Danafar, S. Dabaghi, S.A. Ataei, Sustainable synthesis of silver nanoparticles using macroalgae *Spirogyra varians* and analysis of their antibacterial activity, *J. Saudi Chem. Soc.*, 20 (2016) 459-464.
10. K.Vijayaraghavan, T. Ashokkumar, Plant-mediated biosynthesis of metallic nanoparticles: A review of literature, factors affecting synthesis, characterization techniques and applications, *J. Environ. Chem. Eng.*, 5 (2017) 4866-4883.
11. A.M. Alkilany, C.J. Murph, Toxicity and cellular uptake of gold nanoparticles: what we have learned so far? *J. Nanopart. Res.*, 12 (2010) 2313-2333.
12. M. Rajan, K. Meena, D. Philip, Shape tailored green synthesis and catalytic properties of gold nanocrystals, *Spectrochim. Acta. Part A: Mol. Biomol. Spectrosc.*, 118 (2014) 793-799.
13. Y. Li, H.J. Schluessener, S. Xu, Gold nanoparticle-based biosensors. *Gold Bull.*, 43 (2010) 29-41.
14. K. Saha, S.S. Agasti, C. Kim, X. Li, V.M. Rotello, Gold nanoparticles in chemical and biological sensing, *Chem Rev.*, 112 (2012) 2739-2779.
15. L. Dykman, N. Khlebtsov, Gold nanoparticles in biomedical applications: recent advances and perspectives, *Chem. Soc. Rev.*, 41 (2012) 2256-2282.
16. P. Sandström, M. Boncheva, B. Åkerman, Nonspecific and thiol-specific binding of DNA to gold nanoparticles. *Langmuir*, 19 (2013) 7537-7543.
17. M. Znati, H.B. Jannet, S. Cazaux, J. Bouajila, Chemical Composition, Biological and Cytotoxic Activities of Plant Extracts and Compounds Isolated from *Ferula lutea*, *Molecules*, 19 (2014) 2733-2747.
18. K. Vijayaraghavan, A. Mahadevan, M. Sathishkumar, S. Pavagadhi, R. Balasubramanian, Biosynthesis of Au (0) from Au(III) via biosorption and bioreduction using brown marine alga *Turbinaria conoides*, *Chem. Eng. J.*, 167 (2011) 223-227.
19. M. Ramakrishna, B.D. Rajesh, G. Robert, S. Chandra, G. Rao, Green synthesis of gold nanoparticles using marine algae and evaluation of their catalytic activity, *J. Nanostructure Chem.*, 6 (2016) 1-13.
20. D. Mubarak Ali, N. Thajuddin, K. Jeganathan,, M. Gunasekaran,, Plant extract mediated synthesis of silver and gold nanoparticles and its antibacterial activity against clinically isolated pathogens, *Colloid Surface B.*, 85 (2011) 360-365.
21. D. Inbakandan, R. Venkatesan, S.A. Khan, Biosynthesis of gold nanoparticles utilizing marine sponge *Acanthella elongate*, *Colloids Surf. B.*, 81 (2010) 634-639.
22. S.A. Aromal, D. Philip, Benincasa hispida seed mediated green synthesis of gold nanoparticles and its optical nonlinearity, *Physica E. Low. Dimens. Syst. Nanostruct.*, 44 (2012) 1329-34.
23. K.F. Princy, A. Gopinath, Optimization of physicochemical parameters in the bio fabrication of gold nanoparticles using marine macro algae *Padina tetrastromatica* and its catalytic efficacy in the degradation of organic dyes, *J. Nanostruct. Chem.*, 8 (2018) 333-342.
24. R. Geetha, T. Ashokkumar, S. Tamilselvan, K. Govindaraju, M. Sadiq, G. Singaravelu, Green synthesis of gold nanoparticles and their anticancer activity, *Cancer Nanotechnol.*, 4 (2013) 91-98.
25. N. Kuyucak, B. Volesky, Accumulation of gold by algal biosorbent, *Biorecovery*, 1 (1989) 189-204.
26. P. Karupaiya, E. Satheeshkumar, W.T. Chao, L.Y. Kao, E.C. Chen, H.S. Tsay, Antimetastatic activity of biologically synthesized gold nanoparticles on human fibrosarcoma cell line HT-1080, *Colloid Surface B.*, 110 (2013) 163-70.
27. C.H. Ramamurthy, M. Padma, I.D. Samadanam, R. Mareeswaran, A. Suyavarana, M.S. Kumar, K. Premkumar, C. Thirunavukkarasu, The extra cellular synthesis of gold and silver nanoparticles and their free radical scavenging and antibacterial properties, *Colloid Surface B.*, 102 (2013) 808-815.
28. D. Philip, Honey mediated green synthesis of gold nanoparticles, *Spectrochim. Acta A*, 73 (2009) 650-653.
29. H. Umar, D. Kavaz, N. Rizaner, Biosynthesis of zinc oxide nanoparticles using *Albizia lebeckstem* bark, and evaluation of its antimicrobial, antioxidant, and cytotoxic activities on human breast cancer cell lines, *Int. J. Nanomed.*, 14 (2019) 87-100.
30. G. Balasubramani, R. Ramkumar, N. Krishnaveni, A. Pazhanimuthu, T. Natarajan, R.Sowmiya, P. Perumal, Structural characterization, antioxidant and anticancer properties of gold nanoparticles synthesized from leaf extract (decoction) of *Antigonon leptopus*, *J. Trace Elem. Med. Biol.*, 30 (2015) 83-89.
31. M.K. Swamy, M.S. Akhtar, S.K. Mohanty, U.R. Sinniah, Synthesis and characterization of silver nanoparticles using fruit extract of *Momordica cymbalaria* and assessment of their in vitro antimicrobial, antioxidant and cytotoxicity activities, *Spectrochim. Acta A*, 151 (2015) 939-944.
32. T.J.I. Edison, M.G. Sethuraman, Instant green synthesis of silver nanoparticles using *Terminalia chebula* fruit extract and evaluation of their catalytic activity on reduction of methylene blue, *Process Biochem.*, 47 (2012) 1351-1357.
33. M.M. Mohamed, S. A. Fouad, H.A. Elshoky, G.M. Mohammed, T.A. Salaheldin, Antibacterial effect of gold nanoparticles against *Corynebacterium pseudotuberculosis*, *Int. J. Vet. Sci. Med.*, 5 (2017) 23-29.
34. S. Prabukumar, C. Rajkuberan, G. Sathishkumar, M. Illaiyaraja, S. Sivaramkrishnan, Biogenic gold nanoparticles synthesized using *Crescentia sujete* L. and evaluation of their different biological activities, *Biocatal. Agric. Biotechnol.*, 11 (2017) 75-82.
35. M. Umadevi, T. Rani, T. Balkrishnan, R. Ramanibai, Antimicrobial activity of silver nanoparticles under an ultrasonic field, *Int. J. Pharm. Sci. Nanotechnol.* 4 (2011) 1491-1496.

36. S.R. Vijayan, P. Santhiyagu, M.S. Singamuthu, N. Kumari, R. Anila, R. Jayaraman, K. Ethiraj, Synthesis and characterization of silver and gold nanoparticles using aqueous seaweed; *Turbinaria conoides* and their antimicrobial activity, *The Scientific World Journal*. 2014 (2014) Article ID 938272. <http://dx.doi.org/10.1155/2014/938272>.
37. F.A.A. Rajathi, C. Parthiban, G.V. Kumar, P. Anantharaman, Biosynthesis of antibacterial gold nanoparticles using brown alga *Stoechospermum marginatum*, *Spectrochim. Acta A.*, 99 (2012) 166-173.
38. N. Abdel-Raouf, N.M. Al-Enazi, I.B.M. Ibraheem, Green biosynthesis of gold nanoparticles using *Galaxaura elongata* and characterization of their antibacterial activity, *Arab. J. Chem.*, 10 (2017) 3029-3039.
39. K. Kayalvizhi, N. Asmathunisha, V. Subramanian, K. Kathiresan, Purification of silver and gold nanoparticles from two species of brown seaweeds (*Padina tetrastromatica* and *Turbinaria ornata*), *J. Med. Plants Stud.*, 2 (2014) 32-37.
40. T.S. Dhas, V.G.Kumar, T. Malyalagan, K. Govindaraju, Biofabrication of Gold Nanoparticles Using *Sargassum polycystum* and their Antibacterial Activity, *Adv. Chem. Lett.*, 2 (2015) 31-35.



Exosome Production, Isolation and Characterization from A549 Epithelial Carcinoma Cells

A549 Epitelyal Karsinom Hücrelerinden Eksozom Üretimi, İzolasyonu ve Karakterizasyonu

Esra Cansever Mutlu^{1,2}, Özge Kaya³, Arzu Birinci Yildirim⁴ and Ayhan Çetinkaya⁵

¹Beykent University, Faculty of Engineering and Architecture, Department of Biomedical Engineering, Istanbul, Turkey.

²Scientific Industrial and Technological Application and Research Center, Bolu Abant İzzet Baysal University, Bolu, Turkey.

³Department of Biology, Faculty of Arts and Sciences, Bolu Abant İzzet Baysal University, Bolu, Turkey.

⁴Department of Field Crops, Faculty of Agricultural and Natural Sciences, Bolu Abant İzzet Baysal University, Bolu, Turkey.

⁵Department of Physiology, Faculty of Medicine, Bolu Abant İzzet Baysal University, Bolu, Turkey.

ABSTRACT

Exosomes are natural nanoparticles that their special features as a natural, homogeneous, nanosized, targeted vesicles (~ 50-100 nm) have started to be used in the treatment of cancer very recently. They have high avidity (many conformational attachment) to attach onto targeted cancer cell surfaces. They are composed of bioactive double-layered lipid layers in which their original nature has the adhesive proteins interacting with the cancer cell membrane easily. In this study, the exosomes of non-small cell lung cancer, A549-epithelial carcinoma cells were investigated for their potential to be the natural or synthetic drug carrier. Firstly, exosomes of A549 cell line were produced using exosome-free media. Immediately after, isolation of their exosomes were performed by using ultracentrifugation procedure. Their SEM image, particle size and zeta potential measurements, exosomal RNA analysis and Protein Content by Bradford assays were performed. Findings (Size: 168 nm; zeta: -16mV) on the properties of A549 cell exosomes proved their potential to be used as the drug carrier for cancer cell therapy.

Key Words

Exosome, ultracentrifugation, A549 cell Line, miRNA.

Öz

Ekzosomlar, kanser tedavisinde doğal, homojen, nano boyutlu, hedeflenmiş veziküller (~ 50 ila 100 nm) olarak özel özelliklerin son yıllarda kullanılmaya başlandığı doğal nanopartiküllerdir. Hedeflenen kanser hücreyi yüzeylerine bağlanmak için yüksek bir aviditeye (birçok konformasyonel tutunmaya) sahiptirler. Özgün doğasında kanser hücreyi membrani ile kolaylıkla etkileşebilen yapışkan proteinlere sahip olan biyoaktif çift-katmanlı lipit tabakalarından oluşurlar. Bu çalışmada, küçük hücreli olmayan A549 epitelyal kanser hücrelerinin ekzosomlarının doğal ya da sentetik ilaç taşıyıcı olabileme potansiyelleri araştırıldı. Öncelikle, ekzosom içermeyen ortamlarda üretilen A549 hücre dizisinin ekzosomları üretildi. Hemen sonrasında, ekzosomlarının izolasyonu ultrasantrifüj prosedürü kullanılarak yapıldı. SEM görüntü, partikül boyutu ve zeta potansiyel ölçümleri, ekzosomal RNA analizleri ve Bradford yöntemi ile protein içeriği analizi gerçekleştirildi. A549 hücrelerinin ekzosomlarının özelliklerine ilişkin bulgular (Boyut: 168 nm; zeta: -16mV), kanser hücreyi terapisi için ilaç taşıyıcı olarak kullanıma potansiyellerini kanıtlamıştır.

Anahtar Kelimeler

Ekzosom, ultrasantrifüj, A549 hücre hattı, miRNA.

Article History: Received: Jan 31, 2019; Revised: Apr 20, 2019; Accepted: Jul 23, 2017; Available Online: Nov 1, 2019.

DOI: <https://doi.org/10.15671/hjbc.520101>

Correspondence to: Cansever Mutlu, Beykent University, Faculty of Engineering and Architecture, Department of Biomedical Engineering, Istanbul, Turkey.

E-Mail: esramutlu@beykent.edu.tr

INTRODUCTION

Exosomes as extracellular vehicles below 100 nm are composed of natural lipid bilayers and they are responsible for cellular functions between cells and their environments. Moreover, they have got many oncological vital functions when they are especially secreted by cancer entitled oncosomes [1, 2]. Not only they can interact cellular membranes easily via adhesive proteins on their surface, but also avoid entrapments of mononuclear phagocytes. This also represents their superior property for enhancing the delivery of incorporated drugs to desired cells by altering therapeutic efficiency. Therefore, exosomes now are one of the new hot topics in the subject of nanomedicine among cancer therapy studies [3, 4].

Lung cancer is one of the major health problems affecting too many people in all around the world. In 2012, the most common cancer type with 13% of occurrence frequency in the world was the lung cancer. At the same time, lung cancer is the most common cause of death, corresponding to 19.4% out of total cancer deaths in the world. Lung cancer is clinically based on the size and appearance of malignant cells; small cell lung (16.8%) and non-small cell lung cancer (80.4%) were divided into two main groups [5, 6].

Recently, it was indicated that the cancer cells secrete their characteristic exosomes which are not present among exosomes of healthy cells. Exosomes from tumor cells play vital role to suppress immune system components [7]. Interestingly, they can be larger (in micron diameters) than ones from normal cells vesicles termed oncosomes. However, they are desired to be obtained in diameters below 200 nm.

In this study, we developed an isolation technique for the exosomes from A549 Epithelial carcinoma cells in order to evaluate their drug carrier potential according to their sizes and stabilities. Their miRNA, total RNA and protein content have been investigated due to the sufficiency of drug loading [3, 4, 8].

MATERIALS and METHODS

Materials

DMEM/F-12 (Dulbecco's Modified Eagle Medium/Nutrient Mixture F-12) is a widely used basal medium for supporting the growth of A549 Lung Cancer Cells, was

purchased as PAN Biotec™. Fetal Bovine Serum (FBS) was obtained as BioSera™. Penicillin-Streptomycin (5000 U/mL), Trypsin-EDTA (0.25% w/phenol red), PBS (phosphate buffered saline w/o Calcium Magnesium Phenol Red) were used Gibco, Thermo Fisher Scientific. Ultracentrifuge tubes were purchased as HITACHI MODEL S303922A™.

Pretreated Solutions

- PBS, ddH₂O, FBS were subjected to ultracentrifugation to obtain ExoFreePBS, ExoFreeWater and ExoFreeFBS.
- After sterilization of ultracentrifuge tubes at 121°C, each has fulfilled using PBS, water and FBS.
- After balance measurements, ultracentrifugation were performed overnight at 120.000 g [9].
- Each tube had a volume of 8 mL. Supernatant was collected gently after ultracentrifugation in order to be used during our further studies.
- Supernatant collected in another 15-mL sterile falcon tubes and DexFreeFBS were kept -20°C again. DexFreePBS and DexFreeWater were kept +4°C.

Production of Exosomes

- A549 Epithelial Lung Carcinoma Cells were obtained from Bolu Abant İzzet Baysal University, Department of Physiology stocks.
- Cells were grown under optimum full growth condition (DMEM-F12 90%, 10% DexFreeFBS, Antibiotic Solution (50 U.mL⁻¹ penicillin, and 50 mg.mL⁻¹ streptomycin), 0.5% Amphotericin in t25 flask).
- After 3 days in a 5% CO₂ humid atmosphere at 37°C, cells were transferred to TPPTM t75 flasks for optimal full growth condition by using Tripsin-EDTA and PBS.
- After 3 passages, 6,23x10³ cells were obtained in each t75 media. Cell Counting were performed by using Bio-Rad's TC20™ Cell Counter.

Isolation of Exosomes

- Cells were transferred into centrifuge tubes. After centrifugation at 300g for 15 min at 4°C, cell pellets were removed.
- Supernatants were transferred into 8-mL ultracentrifuge tubes placed in dry ice. Immediately after ultra-centrifugations were performed at 17.000g to eliminate cell debris completely.
- Supernatants were filtered by sterile syringe through sterile 0.2-µm filters to remove larger particles

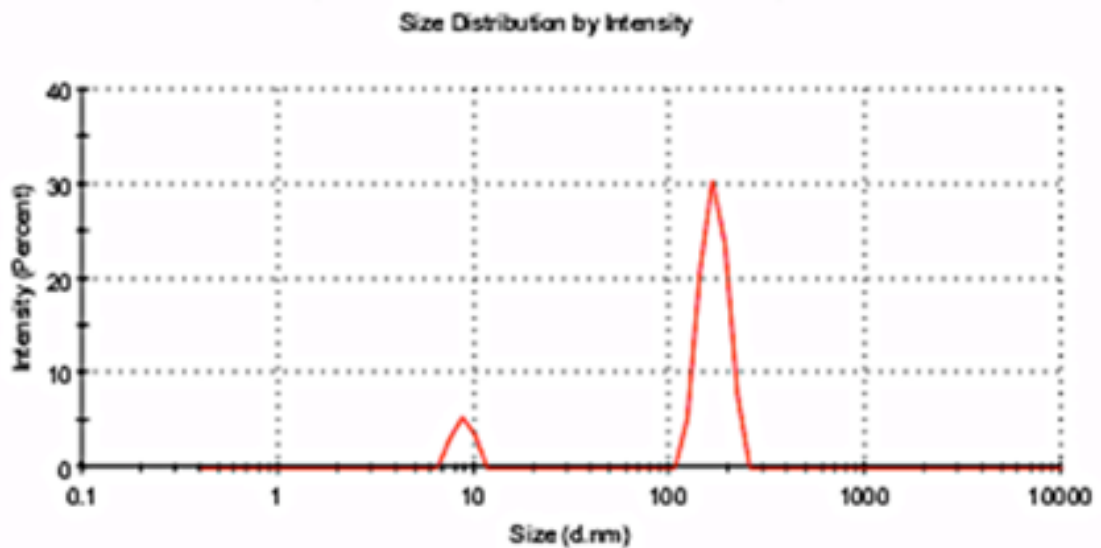


Figure 1. Size distribution of Exosomes from A549 Lung Cancer Cell Line.

more than 200 nm [10].

- Filtered part were transferred to new sterile ultracentrifuge tubes. Ultracentrifugation was performed at 120.000 g for 60 minutes at 4°C.
- Pellet (Exosomes) were resuspended by ExoFree BPS by (3 X 50 μ L) to sterile cryotubes.
- Cryotubes were kept at -80 °C for exosome analysis.

SEM Analysis

Cryotubes containing exosomes were left to melt down at room temperature. A sample from each tube was dropped using sterile Pasteur pipettes onto metal grids with double sided adhesive carbon tape. After they are dried at room temperature, coated with gold to $\sim 500 \times 10^{-8}$ cm in thickness using sputter coater under high vacuum, 0.1 Torr, 1.2 kV, and 50mA at $27 \pm 1^\circ\text{C}$. The surface morphology of coated samples was evaluated by scanning electron microscopy (SEM), Leica™(2)[4].

Zeta/Size Analyses

Cryotubes were left to melt down at room temperature. Each tube was diluted using 2 mL ExoFree PBS and measurements were performed by Malvern Nanosizer/Zetasizer nano-ZS ZEN 3600. Completely disposable dip-cell cuvettes were used during measurements [4].

Extraction and Quantification of Exosomal RNA

In order to evaluate the exosomal RNA content; two column base commercial RNA isolation kits were used namely innuPREP RNA Minianalytik™ (Jena, Germany) for

total RNA extraction and miRNA™ (Omega Bio-tek, Inc, Guangzhou, China) kit for miRNA extraction. 30 μ L of exosome samples suspended in DexFree PBS were mixed with lysis buffer of the each kit and manufacturer's instructions are followed. Isolated RNA molecules were eluted from the columns by centrifuge method as described their procedures by using nuclease-free water. Total RNA and miRNA quantification measurements were carried out by using QuantiFluor® RNA Dye on fluorometry (Quantus™2 Fluorometer, Promega®, Madison, USA) and Thermo Scientific / 2000™Nanodrop. [4, 9] and Nuclease free water used as the control. During the extraction whole working area was cleaned with the "RNase-ExitusPlus" from AppliChem and all the materials used for RNA extraction was nuclease-free in order to prevent RNase contamination.

Analysis of Protein Content

Total protein content of the A549 exosome samples suspended in DexFreePBS were evaluated with Bradford (1976) [11] method by using Pierce™ Coomassie (Bradford) Protein Assay Kit. The amount of total protein was measured colorimetrically at 595 nm using a UV/Vis spectrophotometer (Jasco V-530 UV/Vis spectrophotometer, Jasco International Corporation, Tokyo, Japan) and was quantified as Bovine serum albumin equivalent (BSA) value.

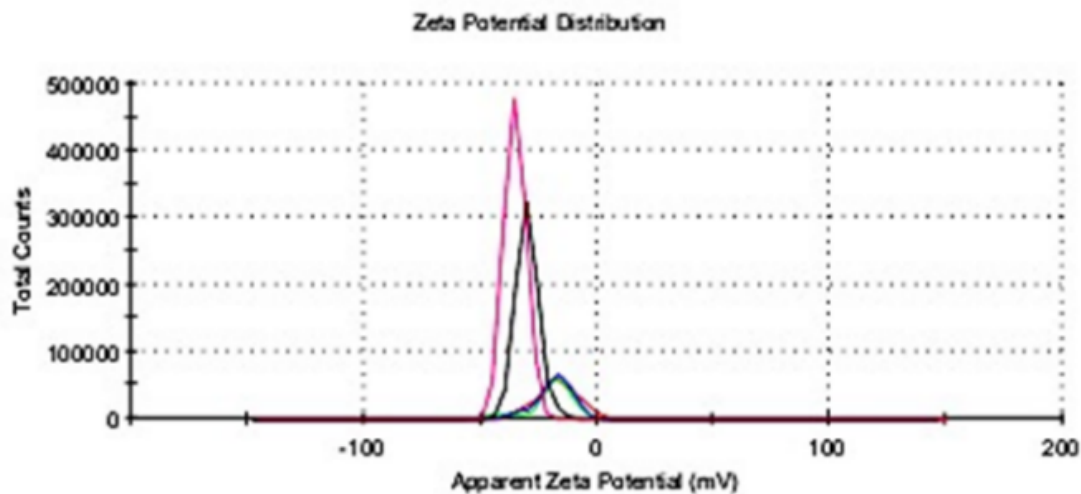


Figure 2. Zeta Potential of Exosomes from A549 Lung Cancer Cell Lines.

RESULTS and DISCUSSION

Size/zeta measurements of exosomes were performed in order to prove its drug delivery potential with respect to their dimensions and stabilities. Size distribution of exosomes displayed bimodal dispersion (Figure 1). The distribution of first peak is 168.3 ± 25.8 nm; second peak is 8.83 ± 0.9 nm. While, intensity of first peak is %87.9; intensity of the second peak is %12.1.

Zeta potential measurement showed that the exosome of A549 Lung Cancer Cell Line was -16 ± 8.72 mV (Figure 2).

SEM images showed that the exosomes of A549 cell lines have the distribution between ~ 50 -150 nm (Figure 3). Images proved that coagulation has poor and the exosomes are highly durable even at 70°C . After 80°C , their spherical structures converted into more rigid structures.

RNA could not be detected in miRNA measurements. In the exosomes samples obtained from A549 cells, 4.5 ng/106 cell total RNA was detected, while RNA was not detected in the control sample with fluorometric measurements. Bradford (1976) [11] method was used to determine the exosomal protein concentration. So, exosome samples of A549 cells were measured protein content equivalent to $13.2 \mu\text{g}/106$ cells of BSA. No protein was detected in the control (DexFreePBS) samples. In this study, the potential of promising usage of exosomes from A549 cell lines were investigated for their

drug loading capacities for probable use in cancer therapy as the next strategy [12, 13]. Thereby, we evaluated all the results to enlighten the material properties of natural nanoparticles, exosomes, of A549 cell line. According to our findings, all exosomes are quite small (≤ 200 nm), (-16 mV) and have lowest amount of RNA content. The prospective challenge would be that they have highly protein content before drug loading.

In fact, even clinical study was performed previously [14]. Although a few studies in the literature were carried out to produce exosomes of A549 cell line from microvesicles (MVs), there is no spotlight exosomal study of this cancer line searching for their sizes, zeta, image analysis and molecular content such as miRNA, totalRNA and protein contents [15].

CONCLUSION

Cancer cell exosomes has the great potential for cancer therapy, this perspective brings with many unknown questions for therapy. Steric stabilization and pH effects of them are of note to change general phenomenon for zeta potential measurements. Our results showed that exosomes of A549 cell line -16 mV. This circumstance showed chemical structure of A549 cell line exosomes should be investigated as the prospective study to enlighten protein content of their surface which may affect zeta potential value. Nonetheless, exosomes of A549 cell line has the great potential for synthetic drug loading by sonication method; for, they are spherically durable even at 70°C . These results, has been displa-

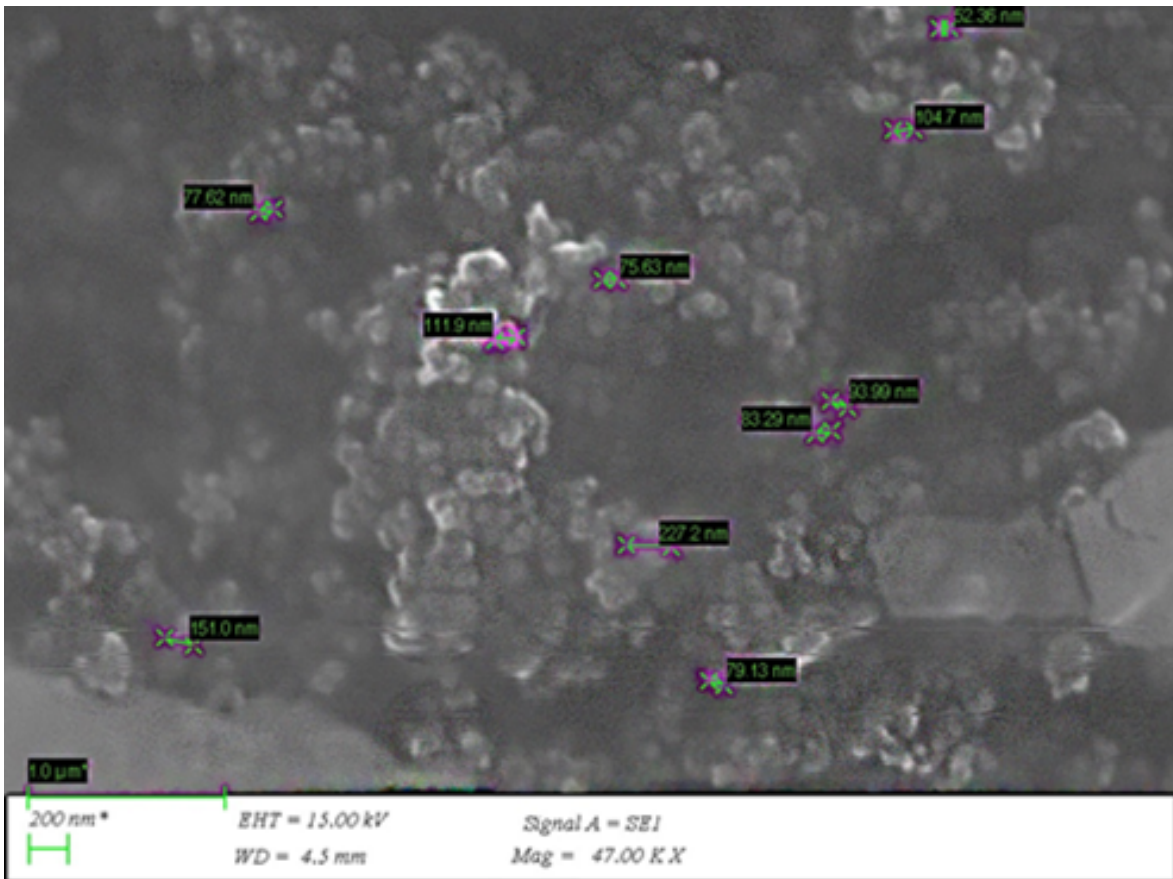


Figure 2. Zeta Potential of Exosomes from A549 Lung Cancer Cell Lines.

yed the new research guide and the method article for A549 cell line exosomes in cancer therapy.

Acknowledgments

Authors thank to Bolu Abant İzzet Baysal University Research Fund through BAP Project 2018.31.01.1359.

References

- G. Mignot, S. Roux, C. Thery, E. Ségura, L. Zitvogel, Prospects for exosomes in immunotherapy of cancer, *J. Cell. Mol. Med.*, 10 (2006) 376-388.
- M. Morello, V. Minciocchi, P. De Candia, J. Yang, E. Posadas, H. Kim, D. Griffiths, N. Bhowmick, L. Chung, P. Gandellini, Large oncosomes mediate intercellular transfer of functional microRNA, *Cell cycle*, 12 (2013) 3526-3536.
- P. Vader, X. O. Breakefield, M. J. Wood, Extracellular vesicles: emerging targets for cancer therapy, *Trends. Mol. Med.*, 20 (2014) 385-393.
- M. S. Kim, M. J. Haney, Y. Zhao, V. Mahajan, I. Deygen, N. L. Klyachko, E. Inskoe, A. Piroyan, M. Sokolsky, O. Okolie, Development of exosome-encapsulated paclitaxel to overcome MDR in cancer cells, *Nanomed-Nanotechnol.*, 12 (2016) 655-664.
- A. Jemal, R. Siegel, E. Ward, Y. Hao, J. Xu, T. Murray, M. J. Thun, *Cancer statistics, 2008*, CA: a cancer journal for clinicians, 58 (2008) 71-96.
- R. Siegel, C. DeSantis, A. Jemal, *Colorectal cancer statistics, 2014*, CA: a cancer journal for clinicians, 64 (2014) 104-117.
- C. Théry, M. Ostrowski, E. Segura, Membrane vesicles as conveyors of immune responses, *Nat. Rev. Immunol.*, 9 (2009) 581.
- J. Palma, S. C. Yaddanapudi, L. Pigati, M. A. Havens, S. Jeong, G. A. Weiner, K. M. E. Weimer, B. Stern, M. L. Hastings, D. M. Duelli, MicroRNAs are exported from malignant cells in customized particles, *Nucleic Acids Res.*, 40 (2012) 9125-9138.
- S. El-Andaloussi, Y. Lee, S. Lakhali-Littleton, J. Li, Y. Seow, C. Gardiner, L. Alvarez-Erviti, I.L. Sargent, M.J. Wood, Exosome-mediated delivery of siRNA in vitro and in vivo, *Nat. Protoc.*, 7 (2012) 2112.
- C. Lässer, M. Eldh, J. Lötval, Isolation and characterization of RNA-containing exosomes, *Jove-J. Vis. Exp.*, (2012).
- M.M. Bradford, A rapid and sensitive method for the quantitation of microgram quantities of protein utilizing the principle of protein-dye binding, *Anal. Biochem.*, 72 (1976) 248-254.
- W. Li, D. Mu, F. Tian, Y. Hu, T. Jiang, Y. Han, J. Chen, G. Han, X. Li, Exosomes derived from Rab27a-overexpressing tumor cells elicit efficient induction of antitumor immunity, *Mol. Med. Rep.*, 8 (2013) 1876-1882.

13. M. Wysoczynski, M.Z. Ratajczak, Lung cancer secreted microvesicles: underappreciated modulators of microenvironment in expanding tumors, *Int. J. Cancer*, 125 (2009) 1595-1603.
14. M.A. Morse, J. Garst, T. Osada, S. Khan, A. Hobeika, T.M. Clay, N. Valente, R. Shreeniwas, M. A. Sutton, A. Delcayre, A phase I study of dexosome immunotherapy in patients with advanced non-small cell lung cancer, *J. Transl. Med.*, 3 (2005) 9.
15. Y.T. Tang, Y.-Y. Huang, L. Zheng, S.-H. Qin, X.P. Xu, T.X. An, Y. Xu, Y.S. Wu, X.M. Hu, B.H. Ping, Comparison of isolation methods of exosomes and exosomal RNA from cell culture medium and serum, *Int. J. Mol. Med.*, 40 (2017) 834-844.



Comparative Anatomical Survey on the species of *Iberis* L. (Brassicaceae) from Turkey

Türkiye'deki *Iberis* L. (Brassicaceae) Türlerinin Karşılaştırmalı Anatomisi

Emre Çilden¹, Golshan Zare²

¹Department of Biology, Faculty of Science, Hacettepe, University, Ankara, Turkey.

²Department of Pharmaceutical Botany, Faculty of Pharmacy, Hacettepe University, Ankara, Turkey.

ABSTRACT

Iberis taxa natively found in Turkey are represented by eight species and are annual and/or perennial herbs or subshrubs. In this study, we provide a detailed anatomical description of Turkish *Iberis* taxa for the first time and try to solve the complexity of taxonomical uncertainties of the genus. Root, stem and leaf anatomies are investigated and stomatal index of *Iberis* is indicated. Our results provided valuable evidence on the doubtful circumstance of species in this genus. *I. attica* is the only species that has winged stem structure and branched trichomes. *I. carica*, one of the endemics, is the only species with its continuous vascular cambium in stem that forms a vascular bundle circle. *I. sempervirens* is the only species without indumentum which has also a subshrub habit. *I. odorata* is the only annual species. There are two types of leaf anatomy as bilateral and isolateral. Turkish *Iberis* taxa show amphistomatic leaves. Myrosin cells that are the characteristic of the order Brassicales are observed in all examined species. Anatomical results support that *I. attica* and *I. spruneri* are two separate taxa instead of as combined *I. carnosa*.

Key Words

Iberis, Brassicaceae, anatomy, Turkey.

ÖZ

Türkiye'de doğal olarak yetişen *Iberis* cinsi ülkemizde 8 türle temsil edilmekte olup tek ve/veya çok yıllık otlar veya yarı çalılardan oluşmaktadır. Bu çalışmada, Türkiye'de yetişen *Iberis* taksonları anatomik olarak detaylı biçimde ilk defa çalışılmış ve bu sayede cinsle ilgili taksonomik belirsizlikler ve karmaşıklıklar çözülmeye çalışılmıştır. *Iberis* türlerinin kök, gövde, yaprak anatomileri çalışılmış ve stoma indeksi ortaya konmuştur. Bu çalışmada elde edilen sonuçlar, cinsin türleriyle ilgili şüpheli durumların çözümü için değerli kanıtlar sağlamaktadır. *I. attica* kanatlı gövde yapısına ve dallanmış tüylere sahip tek türdür. Endemik bir tür olan *I. carica*, gövde anatomisindeki devamlı vasküler kambiyum sayesinde iletim demeti halkası içeren tek türdür. *I. sempervirens* tüsüz ve yarı çalı formundaki tek türdür. *I. odorata* tek yıllıktır. Bilateral ve izolateral olmak üzere iki tip yaprak anatomisi görülmektedir. Türkiye'deki *Iberis* türleri amfistomatiktir. Brassicales ordosunun tipik özelliklerinden biri olan mirozin hücreleri incelenen tüm türlerde gözlenmiştir. Anatomik sonuçlar, *I. attica* ve *I. spruneri* türlerinin, *I. carnosa* olarak tek bir takson değil, ayrı türler olarak ele alınmasını desteklemektedir.

Anahtar Kelimeler

Iberis, Brassicaceae, anatomi, Türkiye.

Article History: Received: Feb 7, 2019; Revised: Jun 15, 2019; Accepted: Sep 7, 2019; Available Online: Nov 1, 2019.

DOI: <https://doi.org/10.15671/hjbc.585877>

Correspondence to: E. Çilden, Department of Biology, Faculty of Science, Hacettepe, University, Ankara, Turkey.

E-Mail: emrecilden@yahoo.com

INTRODUCTION

The genus *Iberis* L. (Brassicaceae) consists of about 28 species of annuals, perennials, and evergreen subshrubs worldwide [1,2]. *Iberis* is one of two genera of the tribe *Iberideae* Webb & Berthel. besides *Teesdalia* W.T.Aiton which is diagnosed by monosymmetric flower structure in *Brassicaceae* family, as in *Calepina* Adans. [3]. Therefore, zygomorphic symmetry is seen in *Iberis*, instead of bilateral symmetry. Flower colours are white, red, pinkish or purplish. Corymbose inflorescence, angustiseptate and two-seeded fruits are important diagnostic characters for identification of *Iberis* species [4]. It is currently represented by eight species in Turkey: *I. carica* (Bornm.) Prain, *I. carnosa* Willd., *I. halophila* Vural & H. Duman, *I. odorata* L., *I. saxatilis* L., *I. sempervirens* L., *I. simplex* DC. and *I. umbellata* L. [5-14].

Secretory cells containing myrosin as one of the diagnostic characters of the order Brassicales are widely distributed through the family Brassicaceae, but their frequency is partially controlled by nutritional and environmental factors. In this family member, the stomata are surrounded by three subsidiary cells of which one of them is usually much smaller than the other two, the so-called cruciferous type. Hairs are unicellular, but maybe simple, unbranched, Y-shaped, two-armed, pelate, or dendroid; rarely glandular [15].

A formal classification has been proposed by Dahlgren [16], bringing most of these families together in a single order, based on their shared production of glucosinolates, precursors of the mustard oils that give Brussel sprouts and capers their characteristic taste. Mustard oils (or isothiocyanates) are hydrolytic products of glucosinolates and had been shown to occur in some families on the order Brassicales, including Brassicaceae, Resedaceae, Capparaceae, etc. by the early 1990s [17]. The conversion of glucosinolates to mustard oils is provided by the enzyme myrosinase, which is normally found in myrosin cells. Isothiocyanates, thiocyanates or nitriles, generated by hydrolyses of glucosinolates function in defense mechanism of plant [17-19]. In addition, highly glycosylated flavonols in the non-flowering leafy shoots of *I. saxatilis* [20], antioxidant potential of *I. sempervirens* [21], and acylated pelargonidin glycosides occurrence in the red-purple flowers of *I. umbellata* [22] are reported. Plant defense mechanisms also include the production of secondary compounds that act as feeding deterrents or as toxins [23]. Also, it is stated that

I. amara (known as "bitter candytuft") is used as a remedy in homeopathy for some diseases such as asthma, bronchitis, dropsy, heart affections and is useful in the treatment of hypertrophy of the heart [24].

Although some studies have been carried out about the family Brassicaceae, the genus *Iberis* or some species of the genus [13, 14, 25-28], there are many points remain unresolved or doubtfully resulted.

In this study, we compile the limited information about anatomical properties of the *Iberis* species from literature and complement it with our new data. In addition, the aims of this study are to describe the anatomy of eight *Iberis* species from Turkey and evaluate the implementation and importance of anatomic structure on taxonomy of the genus.

MATERIALS and METHODS

Plant specimens used for this study were collected from different regions of Turkey. The data of all collected and examined plant specimens are listed in Table 1. Flora of Turkey and the East Aegean Islands [5] is used for identification of the species. *I. umbellata*, a cultivar species which is reported only from İstanbul, Turkey [12] has not been collected and evaluated.

The specimens are deposited in Hacettepe University Herbarium (HUB). Plant specimens were kept in 70% ethanol for anatomical investigations. Freehand sections were prepared using razor blades. In the anatomical analysis, paradermal sections and cross-sections were taken from the middle part of the leaves. Cross-sections of root were taken 1 cm above the base of the root and stem cross-sections from the lower part of the individuals. All sections are stained by double stain, containing astra blue and safranin in 9:1 ratio. Slides were observed with an Olympus CX41 microscope light microscope and photographed by DS-L1, DS-5M connected to Nikon Eclipse E600 camera. Data of all anatomical characters are based on the measurements of 30 sections of each taxon. Cluster analysis is carried out to determine the phenetic similarity between species. 18 qualitative and quantitative anatomical values are examined and listed in Table 2.

PAST (PAleontological STatistics) ver. 3.25 programme is used for the analysis [29]. Jaccard similarity index has been used to explain binary and multiple charac-

Table 1. Locality information of collected and/or examined taxa (*: endemic taxa).

Taxa	Voucher number	Locality
<i>I. attica</i>	E. Çilden 1807	İçel, between Gözne and Arslanköy, Yavca village, 100 m. after the exit of village, road side, calcereous soil, 36°1'6,74" N, 34°31'59,27 E, ca. 1200 m, 20.04.2018 (HUB).
<i>I. attica</i>	E. Çilden 1849	İzmir, Nif mountain, 38°23'9,59" N, 27°21'57,47 E, 1290 m, calcereous soil, 03.05.2018 (HUB).
<i>I. attica</i>	E. Çilden 1889b	Antalya, Alanya to Hadim village, 36°34'30" N, 32°22'4" E, 1330 m, 21.10.2018, leg. Ahmet Tıraş (HUB).
<i>I. attica</i>	E. Çilden 1841	Muğla, Köyceğiz, Hamitköy village, road side, 36°54'43,29" N, 28°37'12,8 E, 80 m, 02.05.2018 (HUB).
<i>I. attica</i>	E. Çilden 1759	Muğla, between Marmaris-Dağca, near Hisarönü village, road side, 36°47'29,05" N, 28°3'18,97" E, 33 m, 17.03.2018 (HUB).
<i>I. carica*</i>	E. Çilden 1829	Aydın, Söke, Güllübahçe village, ruins of Priene anthic city, in the screes, 37°39'39,16" N, 27°17'52,1" E, 160 m, 02.05.2018 (HUB) (type locality).
<i>I. halophila*</i>	E. Çilden 1766	Karaman, Eskil, near Tuz Gölü, salty soil, 38°26'33,762" N, 33°26'52,60 E, 930 m, 31.03.2018 (HUB).
<i>I. odorata</i>	H. Altınözlü 5877; A. Güner 8446	Mardin, Dargeçit, between Temelli and Kartalkaya villages, 37,753578 E 37,4161454 N, 739 m, steppe, 12.04.2008 (HUB); Hatay, Belen, calcereous fields, 700 m., 06.04.1991 (HUB).
<i>I. saxatilis ssp. saxatilis</i>	T. Dirmenci 2516a	Balıkesir, Kazdağ (İda), Nanekırı, limestone, 1500 m., 19.05.2004 (HUB).
<i>I. saxatilis ssp. magnesiana*</i>	D. Oskay 1376; E. Çilden 1895	Manisa, Soma district, Kocasıvri hill, 850 m, May 2011 (isotype); ibid 23.04.2019 (HUB).
<i>I. sempervirens</i>	E. Çilden 1891; B. Özüdoğru 4001	Muğla, Ula, Sandras mountain, in the screes, 37°2'11" N, 28°48'3" E, 1960 m, 21.10.2018, leg. Buse Topçuoğlu (HUB); Kahramanmaraş, between Göksun-Geben, Meryemçilbeli, 37,82231 N, 36,40699 E, ca. 1800 m, 30.04.2016 (HUB).
<i>I. simplex</i>	E. Çilden 1782; E. Çilden 1887	Niğde, Pozantı-Kamışlı road, Alpu village, 37°28'18,152" N, 34°52'30,46" E, 964 m, 19.05.2018 (HUB); Eskişehir, Alpu village, Kireçköy, gypseous soil, 30°96'58" N, 44°04'38,5" E, 25.05.2018, leg. H. Altınözlü (HUB).
<i>I. spruneri</i>	H. Yıldırım 3794; E. Çilden 1334	Denizli, Çameli district, Karabayır, marly soil, 36°55'59,5" N, 29°8'55,3" E, 1610 m, 30.04.2016 (HUB); Aydın, above Dağeymiri village, beyond Karlık tepesi, stony hills, 1515 m, 24.04.2010 (HUB).

ters. Cluster analysis has been carried out by SAHN (Sequential Agglomerative Hierarchical Nested Cluster Analysis) and UPGMA (Unweighted Pair Group Method with Arithmetic Average) method. Anatomical measurements are made using an ocular micrometer on stereoscopic binocular Leica Zoom 2000, with a standard ruler; and results are listed in Table 3-5.

RESULTS

The anatomy of the specimens is determined by examination of root, stem and leaf sections, trichome and stoma structures (Figures 1-5); and additionally, stoma-

tal index of the species is presented. In this study, *I. attica* Jordan and *I. spruneri* Jordan are treated as two separate species instead of *I. carnosa*.

Root anatomy

Annual and perennial root anatomy is present. Only *I. odorata* has an annual habit, whereas all other *Iberis* taxa are perennial. Periderm is generally scratched from cortex. Cortex is multi-layered (ca. 6 to 20 layer) and includes sclereids in *I. sempervirens*, *I. saxatilis*, *I. halophila*, *I. spruneri* and *I. simplex* at different frequencies. Cortex of *I. attica* has thicker and more vascular bundles rays compared to *I. spruneri*. Endodermis can-

Table 2. Characters used in cluster analysis.

1.	Life form: annual (0), perennial (1)
2.	Number of cortex layer: 0-10 (0), 11-20 (1)
3.	Sclereids in root cortex: absent (0), rarely present (1), present (2)
4.	Density of sclereids in root cortex: absent (0), lax (1), dense (2)
5.	Indumentum of stem: absent (0), Present (1)
6.	Indumentum type: absent (0), single (1), single and/or rarely branched (2)
7.	Density of indumentum: absent (0), lax (1), dense (2)
8.	Winged stem structure: absent (0), present (1)
9.	Sclereids in stem cortex: absent (0), rarely present (1), present (2)
10.	Density of sclereids in stem cortex: absent (0), moderately dense (1), dense (2)
11.	Intervascular bundles: parenchyma (0), sclerenchyma (1), cambium (2)
12.	Indumentum of leaves: absent (0), present (1)
13.	Density of indumentum: absent (0), lax (1), dense (2)
14.	Bulliform-like cells at midrib axis: absent (0), moderately dense (1), dense (2)
15.	Mesophyll type: bilateral (0), isolateral (1)
16.	Adaxial stoma cell dimension: < 20 (0), ≥ 20 (1)
17.	Abaxial stoma cell dimension: < 20 (0), ≥ 20 (1)
18.	Stoma index ratio: < 1 (0), ≥ 1 (1)

not be distinguished, and borders are not clear. Xylem is under phloem with secondary xylem and metaxylem regions, respectively (Figure 1). Measurements are listed in Table 3.

Stem anatomy

Single-layered epidermis is covered with a thin cuticula layer for all *Iberis* species (Figure 2). There are single cellular trichomes except for *I. attica*, which some

branched trichomes are detected on the epidermis (Figure 4b). *I. attica* is the only species that has a distinct winged stem structure (Figure 2a). Cortex is under epidermis, consisting of multi-layered parenchymatic cells and all studied taxa have sclereids in the cortex of the stem at different frequency of cells (Figure 2). Phloem, vascular cambium and xylem are located between cortex and pith, respectively. In some species cambium is continuous, but in *I. saxatilis*, sclerenchyma cells (Figure

Table 3. Anatomical measurement of the root characters of studied taxa.

	<i>I. attica</i>	<i>I. carica</i>	<i>I. halophila</i>	<i>I. odorata</i>	<i>I. saxatilis</i>	<i>I. sempervirens</i>	<i>I. simplex</i>	<i>I. spruneri</i>
Annual (a) / Perennial (p)	p	p	p	a	p	p	p	p
Cortex layer	8-11	9-10	10-15	5-10	10-16	9-10	15-20	10-12
Sclereids in cortex	rarely present	absent	present	absent	present	present	present	present
Density of sclereids	lax (if present)	-	dense	-	lax	dense	lax	lax
Number of rays	4-10	4-7	5-7	2-5	4-5	3-6	4-5	5-7

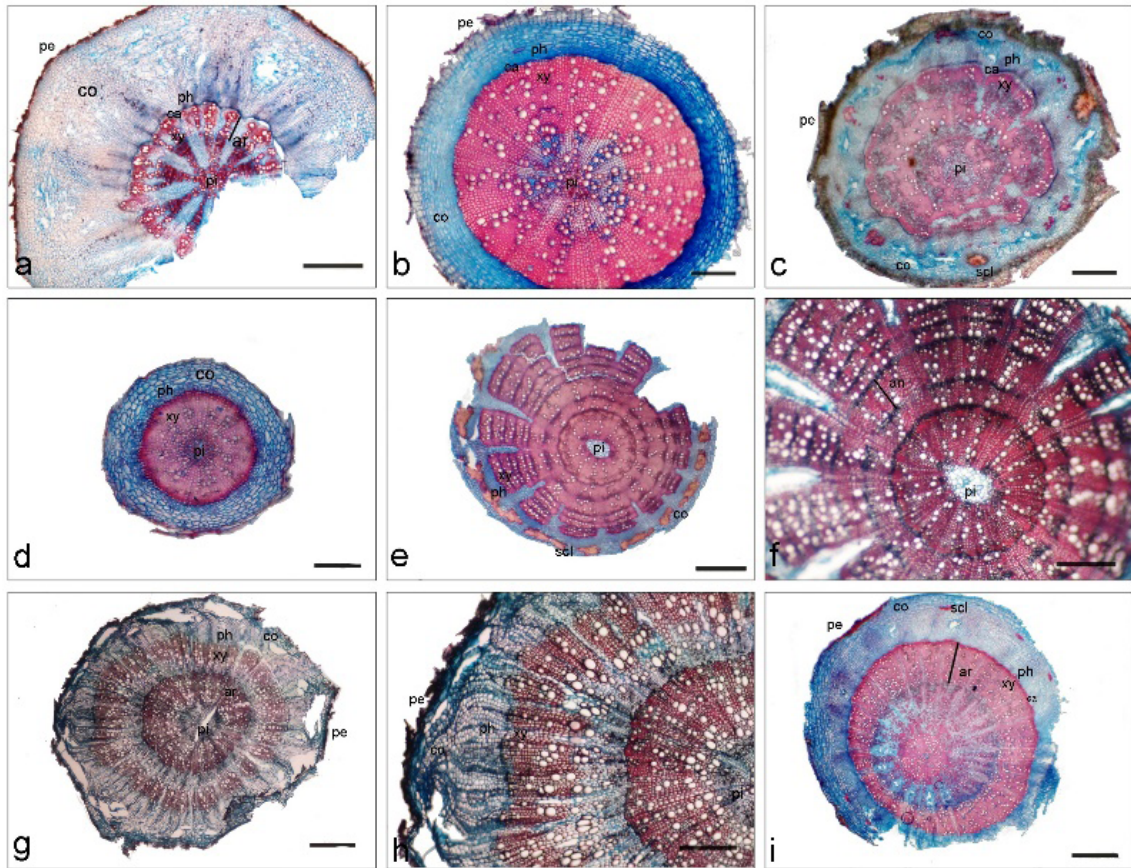


Figure 1. Transverse sections of *Iberis* root.

a. *I. attica* (EÇ 1807), b. *I. carica* (EÇ 1829), c. *I. halophila* (EÇ 1766), d. *I. odorata* (HA 5877), e.-f. *I. sempervirens* (EÇ 1891), g.-h. *I. simplex* (EÇ 1887) and i. *I. spruneri* (HY 3794). ar, annual ring; ca, cambium; co, cortex; pr, periderm; ph, phloem; pi, pith region; sc, sclerenchyma; xy, xylem. Scale bars: (a, b, c, e, g, i) 500 μ m, (f, h) 200 μ m.

2h) and in *I. odorata* parenchyma cells (Figure 2j) are located between vascular tissues, and cambium activity cannot be seen in these parts. When mature, pith begins to scatter (Figure 2h, m, n). Some parenchymatic pith cells of the stem are differentiated as myrosin cells, where glucosinolate metabolism occurs and those myrosin cells resemble the sieve-tube cells of phloem in shape but not in function (Figure 2f, i, m). They appear as an ordinary parenchyma cells but include myrosinase enzyme [30]. Measurements are listed in Table 4.

Leaf anatomy

Iberis taxa found in Turkey generally have equifacial/isolateral mesophyll structure, except *I. attica* and *I. sempervirens*; and are composed of multilayered palisade parenchyma cells. There is no sponge parenchyma, and stomatal cavities are small and narrow. This situation may be an adaptation to the arid habitat of these taxa. There is single-layered epidermis under cuticula

and also has bulliform-like cells in some parts, especially at the midrib axis. The bulliform cells mainly found in grasses are capable of rolling up in dry or bad conditions and reopening again under favourable conditions [30]. It is thought that these bulliform-like cells in the genus *Iberis* may also be used for the reflection of the excessive day light (Figure 3). Measurements are listed in Table 5.

There are single and some branched trichomes on both adaxial and abaxial faces of leaves (Figure 4). Anticlinal cell walls are straight and the shape of the epidermal cells are irregular. The stomata of the genus are surrounded by three subsidiary cells of which one is usually much smaller than the other two, and it is a typical "cruciferous" (anisocytic) type stomata [15, 30-32]. As the shapes of the stomata are not different on both adaxial and abaxial sides of the leaves, we prefer to show the best figure for each taxon in Figure 5. In Table 6, all

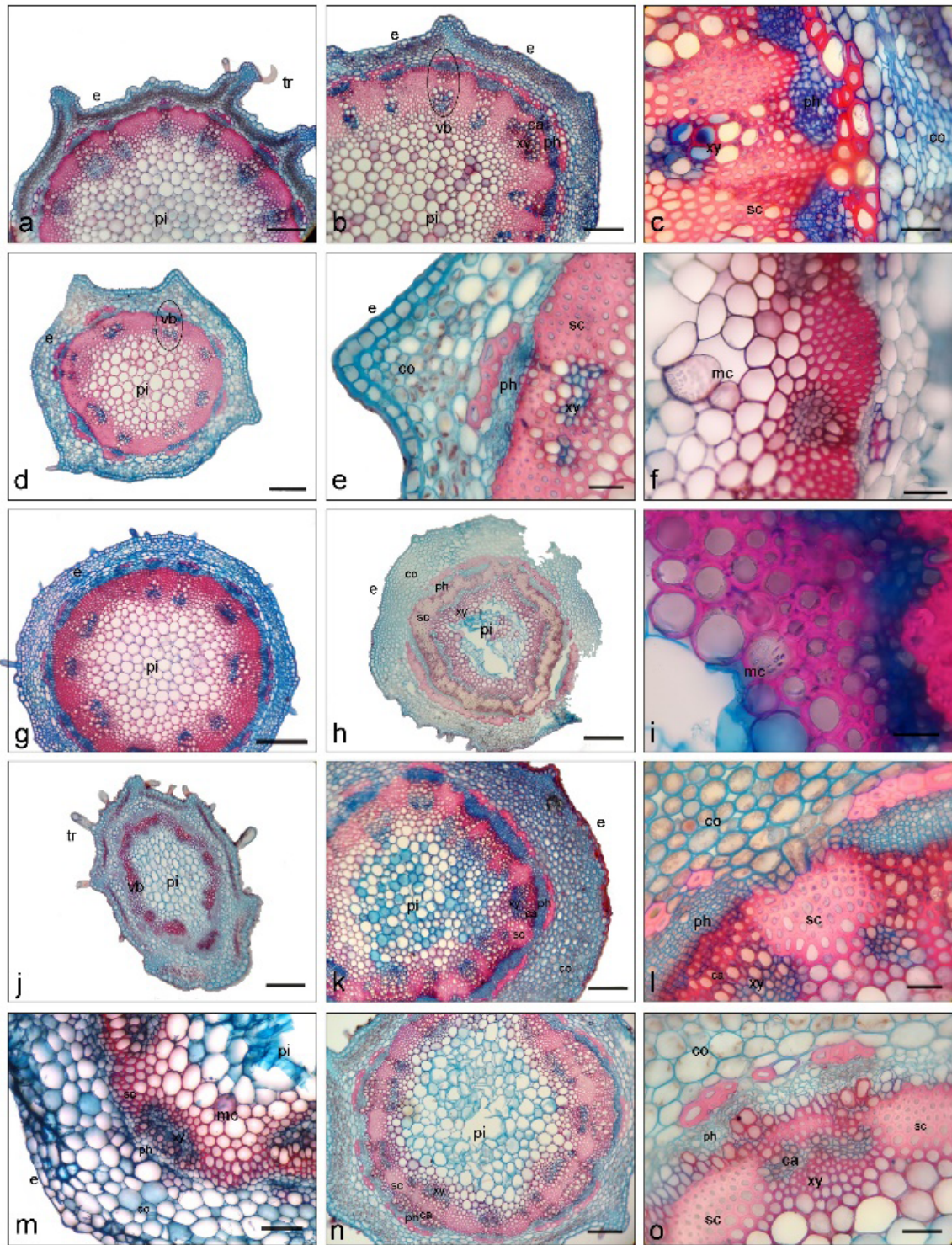
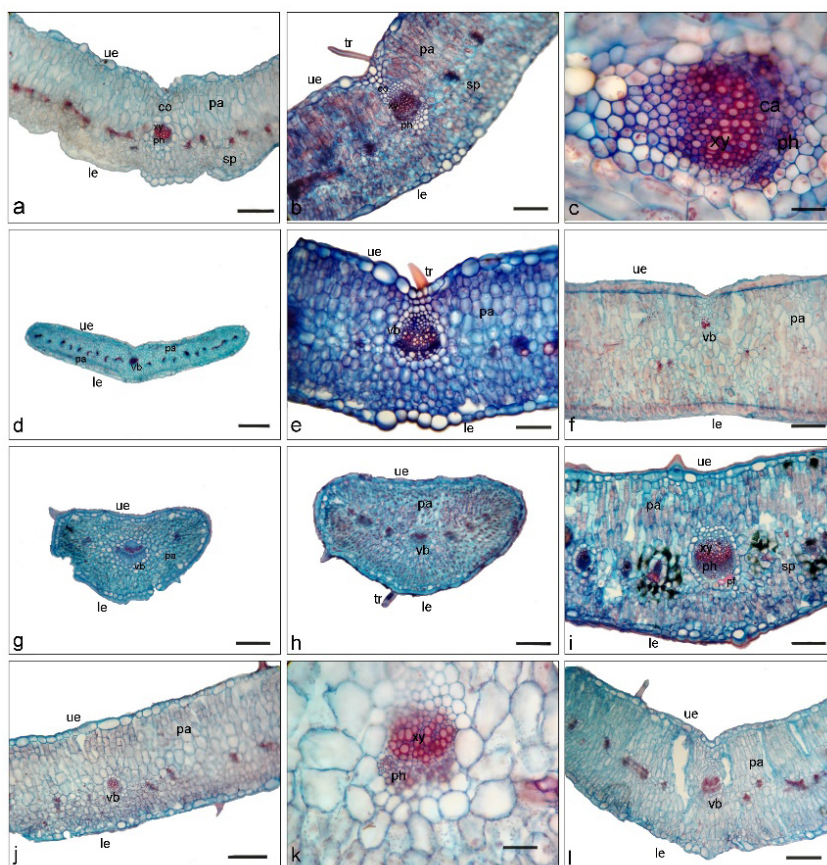


Figure 2. Transverse sections of *Iberis* stem.

a. *I. attica* (EÇ 1841), b-c. *I. attica* (EÇ 1889b), d, e and f. *I. halophila* (EÇ 1766), g. *I. carica* (EÇ 1829), h. *I. saxatilis* (TD 2516a), i. *I. saxatilis* - myrosin (DO 1376), j. *I. odorata* (HA 5877), k-l. *I. sempervirens* (EÇ 1891), m. *I. spruneri* (HY 3794), n-o. *I. simplex* (EÇ 1782). ca, cambium; co, cortex; ue, upper epidermis; le, lower epidermis; mc, myrosin cells; pa, palisade cell; sp, spongy parenchyma cell; ph, phloem; pi, pith region; sc, sclerenchyma; tr, trichome; xy, xylem. Scale bars: (d, h, j) 500 μ , (a, b, g, k, n) 200 μ , (c, e, f, i, l, m, o) 50 μ .

Table 4. Anatomical measurement of the stem characters of studied taxa.

	<i>I. attica</i>	<i>I. carica</i>	<i>I. halophila</i>	<i>I. odorata</i>	<i>I. saxatilis</i>	<i>I. sempervirens</i>	<i>I. simplex</i>	<i>I. spruneri</i>
Indumentum	present	present	present	present	present	absent	present	present
Indumentum type	single and/or rarely branched	single	single	single	single	-	single	single
Density of indumentum	dense	dense	lax	lax	lax; (dense in ssp. <i>magnesiana</i>)	-	dense	lax
Winged structure	present	absent	absent	absent	absent	absent	absent	absent
Number of cortex layer	5–10	8–15	8–10	6–8	11–15	10–13	10–13	6–13
Scleireids in cortex	present	present	present	absent	present	absent	present	rarely present
Density of scleireids	moderately dense	moderately dense	moderately dense	-	dense	-	moderately dense	very lax (if present)

**Figure 3.** Transverse sections of *Iberis* leaves.

a. *I. attica* (EÇ 1891), b-c. *I. attica* (EÇ 1889b), d-e. *I. carica* (EÇ 1829), f. *I. halophila* (EÇ 1766), g. *I. odorata* (HA 5877), h. *I. saxatilis* (TD 2516a), i. *I. sempervirens* (EÇ 1891), j. *I. simplex* (EÇ 1782), k. *I. simplex* (EÇ 1887), l. *I. spruneri* (HY 3794). ca, cambium; co, cortex; ue, upper epidermis; le, lower epidermis; pa, palisade parenchyma cell; sp, spongy parenchyma cell; ph, phloem; pi, pith region; sc, sclerenchyma; tr, trichome; vb, vascular bundle; xy, xylem. Scale bars: (d) 500 μm; (a, b, e, f, g, h, j, l) 200 μm; (c, k) 50 μm.

Table 5. Anatomical measurement of the leaf characters of studied taxa.

	<i>I. attica</i>	<i>I. carica</i>	<i>I. halophila</i>	<i>I. odorata</i>	<i>I. saxatilis</i>	<i>I. sempervirens</i>	<i>I. simplex</i>	<i>I. spruneri</i>
Indumentum	present	present	present	present	present	absent	present	present
Density of indumentum	dense	dense	lax	lax	lax; (dense in subsp. <i>magnesianae</i>)	-	dense	dense
Bulliform-like cells at midrib axis	present	present	absent	absent	absent	moderately present	moderately present	moderately present

Table 6. Stomatal index of examined *Iberis* taxa.

Taxa	Stoma cell			Guard cell			
	Adaxial (mm ²)	Abaxial (mm ²)	Stoma index ratio	Adaxial (μ)		Abaxial (μ)	
				Length	Width	Length	Width
<i>I. attica</i> (EÇ 1807)	20.61 ± 0.52	18.35 ± 0.75	1,12	29 ± 2.7	23 ± 1.3	29 ± 1.3	23 ± 2.2
<i>I. attica</i> (EÇ 1849)	21.11 ± 2.82	20.93 ± 0.78	1,01	28 ± 3.4	24 ± 1.8	31 ± 1.6	28 ± 1.2
<i>I. attica</i> (EÇ 1889b)	20.05 ± 0.80	23.46 ± 0.42	0,85	40 ± 2.1	31 ± 1.7	44 ± 2.2	31 ± 1.7
<i>I. attica</i> (EÇ 1841)	23.49 ± 1.33	22.66 ± 0.35	1,04	33 ± 2.0	27 ± 1.5	28 ± 2.7	23 ± 1.7
<i>I. attica</i> (EÇ 1759)	20.13 ± 0.69	18.27 ± 1.12	1.10	46 ± 3.3	34 ± 1.4	40 ± 1.9	30 ± 1.4
<i>I. carica</i> (EÇ 1829)	23.34 ± 1.11	23.58 ± 1.75	0,99	33 ± 2.9	29 ± 3.0	33 ± 2.4	26 ± 1.6
<i>I. halophila</i> (EÇ 1766)	22.48 ± 0.96	20.55 ± 1.03	1,09	35 ± 2.8	30 ± 1.2	32 ± 2.2	28 ± 1.9
<i>I. odorata</i> (HY 5877)	22.88 ± 0.41	23,95 ± 1.59	0,95	27 ± 1.6	24 ± 1.7	29 ± 1.7	25 ± 1.7
<i>I. saxatilis</i> (TD 2516a)	22.79 ± 3.06	21.80 ± 1.99	1,04	36 ± 1.4	31 ± 2.6	35 ± 1.7	30 ± 2.2
<i>I. sempervirens</i> (EÇ 1891)	16.53 ± 1.65	21.17 ± 0.99	0,78	30 ± 1.6	25 ± 1.0	27 ± 1.7	25 ± 0.9
<i>I. simplex</i> (EÇ 1782)	20.64 ± 0.62	23.30 ± 1.46	0,88	39 ± 2.4	30 ± 3.0	37 ± 3.0	29 ± 1.4
<i>I. simplex</i> (EÇ 1887)	18.93 ± 1.31	20.80 ± 1.53	0,91	37 ± 3.0	28 ± 1.2	47 ± 2.5	34 ± 1.8
<i>I. spruneri</i> (HY 3794)	18.50 ± 0.35	19.22 ± 0.27	0,96	33 ± 1.3	28 ± 1.4	29 ± 1.2	24 ± 2.2

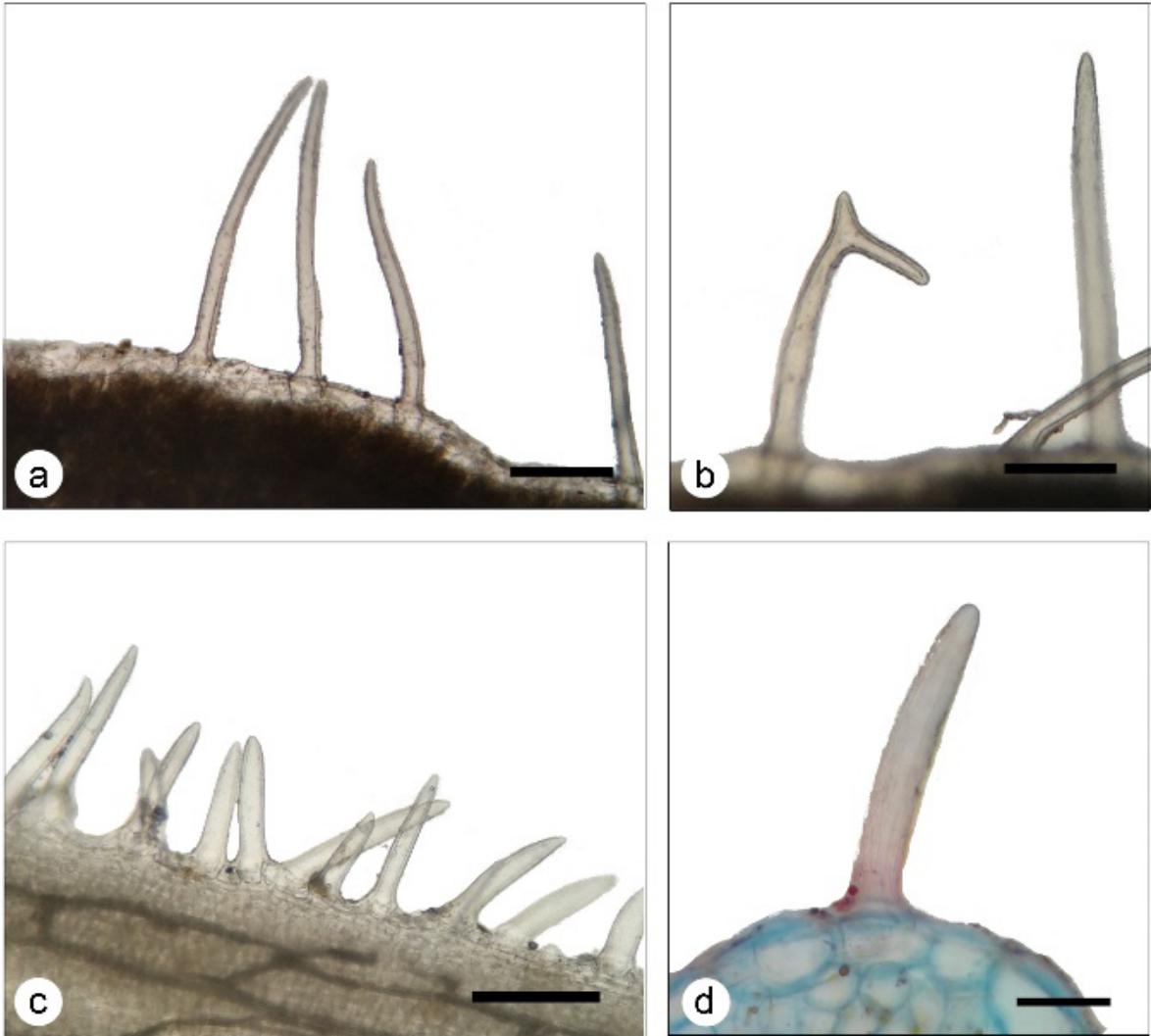


Figure 4. Trichomes.

a-b. *I. attica* (EÇ 1849); c, *I. spruneri* (HY 3794); d. *I. attica* (EÇ 1807). Scale bars: (a, b, c) 200 μ , (d) 50 μ .

measurements about the stomatal index of the taxa are indicated in detail. All studied taxa are amphistomatic and have stomata on both sides of the leaves (Figure 5).

DISCUSSION

The results of the current study suggest that anatomical features of *Iberis* taxa, which is natively found in Turkey help to improve the taxonomy of species and clarify the circumstance of the taxa.

The genus *Iberis* is evaluated anatomically for the first time in the present study. *I. sempervirens* is only species which subjected to the previous anatomical studies [15, 33]. Our results confirm that *I. sempervirens* is a peren-

nial subshrub (Figure 1e, f) and the only species without indumentum. This may also be verified by its lowest stomatal index values (Table 6). This species could be easily diagnosed with its evergreen habit, glabrous stem and leaves, and white flowers (Figure 2k, l). *I. sempervirens* is one of the two taxa in which bifacial/dorsiventral leaf anatomy is seen. There are multilayered and frequently aligned, quadrangular shaped palisade parenchyma cells in the adaxial side; and laxly aligned with air spaces, roundly shaped sponge parenchyma cells at the abaxial side of the leaf (Figure 3i).

According to mesophyll structure in studied taxa, some leaves lack a distinction of layers, and others have well-separated layers. While the mesophyll structure cannot

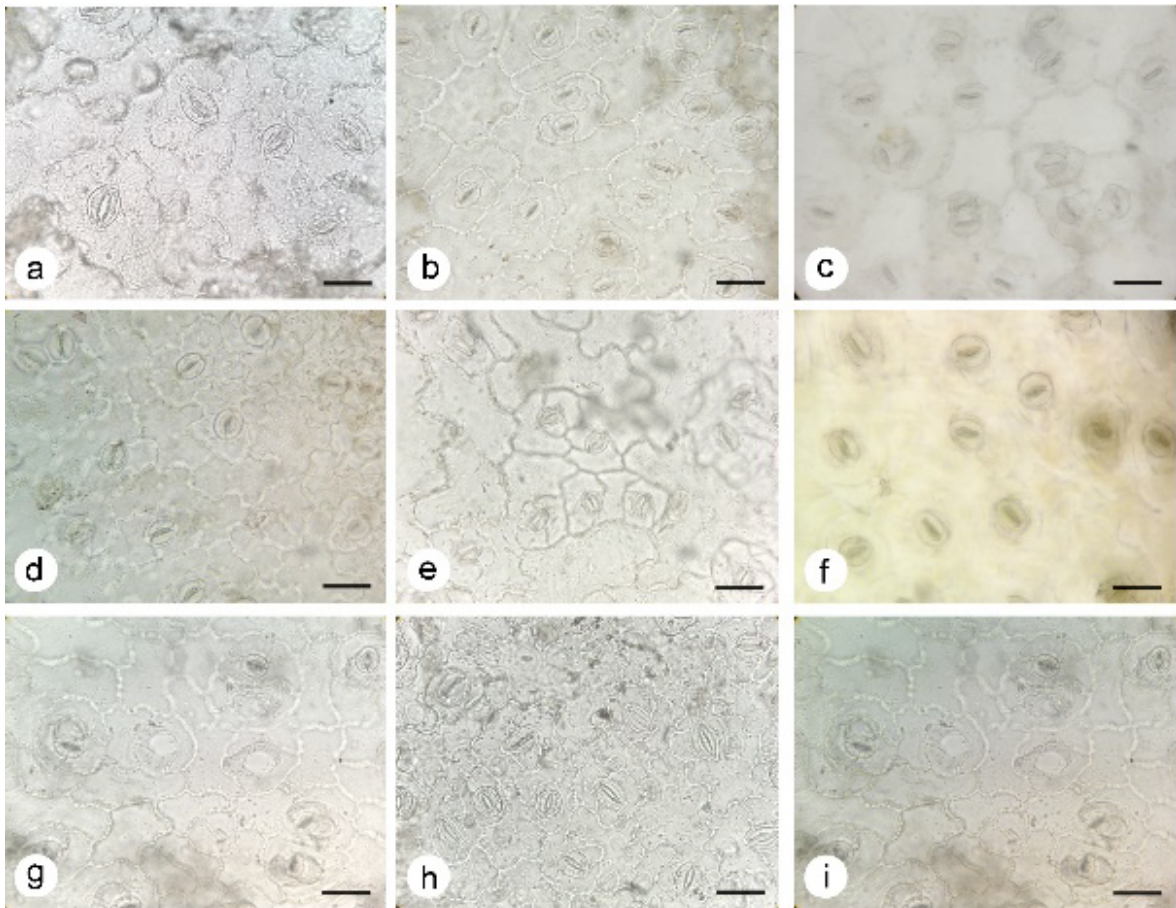


Figure 5. Stoma of *Iberis* taxa.

a. *I. attica*, le (EÇ 1759), b. *I. attica*, ue (EÇ 1807), c. *I. carica*, ue (EÇ 1829), d. *I. halophila*, ue (EÇ 1766), e. *I. odorata*, ue (HA 5877), f. *I. saxatilis*, ue (TD 2516a), g. *I. sempervirens*, ue (EÇ 1891), h. *I. simplex*, ue (EÇ 1887), i. *I. spruneri*, ue (HY 3794). Scale bars: 50 μ (le: lower epidermis, ue: upper epidermis)

often be used as a diagnostic character to evaluate the taxonomic position of a plant, it may provide useful information about some allied group of taxa. Cutler's suggestion [30] that the mesophyll could be used as an aid to identification of these taxa, considering that environmental variations will not alter arrangements that are rigidly controlled by the genome, supports our findings. In the present study *I. attica* and *I. spruneri* are taken into consideration separately instead of *I. carnosa* because of their anatomical differences, as well as their significant morphological and palynological distinctions (Çilden unpubl. data). *I. attica* is the only species of Turkish *Iberis* which has winged stem structure (Figure 2a, b), a valuable diagnostic character for stem anatomy (Table 4).

This species is distributed in the Mediterranean phyto-geographic region from İzmir to Hatay including some

parts of inner Anatolia, such as Karaman, Denizli, Burdur etc. and altitude from 30 to 1400 m. This character could be an adaptation of stem to increase the surface area for photosynthesis. *I. spruneri* is morphologically small-sized species up to 10 cm and generally grows at high altitudes near subalpine (in Aydın, Denizli) and alpine zone (in Bursa-Uludağ). *I. attica* has bifacial/dorsiventral leaf anatomy (Figure 3a, b, c), whereas *I. spruneri* has isolateral (Figure 3l). In addition, *I. attica* is the only species that has some branched trichomes on the epidermis besides unicellular simple hairs (Figure 4b). As a result, *I. attica* is considerably different from other Turkish *Iberis* taxa. Anatomical and palynological results from different *I. attica* populations shows that it is necessary to be examined in detail as a species complex. According to anatomical properties, *I. attica* and *I. spruneri* can be treated as two separate species.

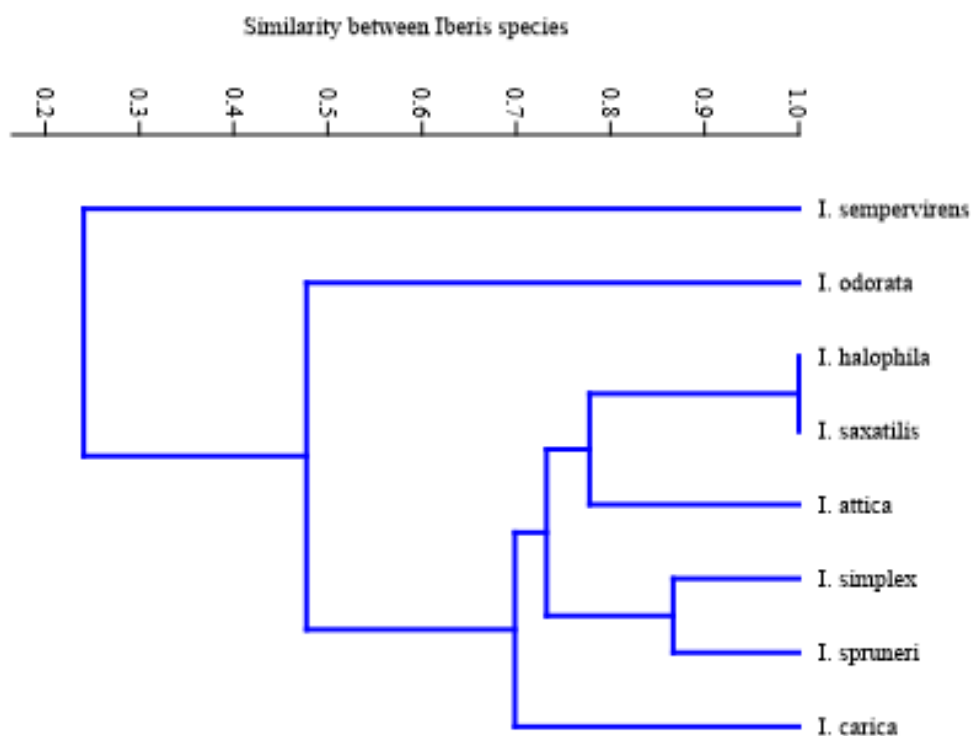


Figure 6. UPGMA phenogram about the relationship between *Iberis* species from Turkey.

I. carica is one of the three Turkish endemic taxa and unfortunately is the most misidentified *Iberis* species in Turkey. The common mistake made about the identification of *I. carica* is that the pre-admission of all *Iberis* species found in Aegean and/or Mediterranean regions of Turkey like İzmir, Aydın, Muğla and Antalya provinces as *I. carica*. But after the collection and examination of the type population (Aydın) in May 2018, we have found out that all other populations mentioned having been collected from Muğla, İzmir, Antalya and identified or doubtfully recorded as *I. carica* are *I. attica*. In addition to stomatal index values (Table 6), morphological and palynological results also verified the anatomical differences between *I. carica* collected from its type population and all *I. attica* populations, and with the other *Iberis* taxa (Çilden unpubl. data). In contrast with Flora of Turkey [5], *I. carica* has a perennial habit and isolateral leaf anatomy with locally placed bulliform-like epidermal cells. White flowers of this taxa are distinctly smaller than pinkish-purplish flowers of *I. attica*. Also, the cambium shows continuous structure between vascular bundles in *I. carica* and form an unbroken vascular circle in stem anatomy. However, *I. attica*, *I. halophila*, *I. saxatilis*, *I. simplex* and *I. spruneri* have sclerenchyma tissue between vascular bundles, whereas *I. odorata* and *I.*

sempervirens have parenchyma. We have not been able to find any evidence if there is a transition between parenchyma and sclerenchyma cells or not, but noticed that this is a remarkable difference between *Iberis* taxa, especially for Turkish endemic *I. carica*.

I. halophila is one of the endemic species in Turkey and found only in Tuzgölü region, Aksaray province [9]. Since it is grown in salty habitat, the morphology of leaves turns to be succulent compared with other taxa. Leaves are mostly glabrous and rarely have lax indumentum in the upper leaves with isolateral structure. Also some parts of the root cortex seem to be scattered and this could be an adaptation to the salty habitat.

I. saxatilis has been known as a European *Iberis* species when it was found in Kazdağı, Balıkesir, and published as a new record for Turkey in 2005 [7]. In 2017, a new subspecies, *I. saxatilis* subsp. *magnesiensis* Oskay was reported in Manisa province. Both taxa have a very restricted distribution area and *I. saxatilis* subsp. *magnesiensis* is considered as endemic; found only in Soma. So, the distribution area of these two taxa in Turkey are limited with Edremit (Balıkesir) and Soma (Manisa) districts for now, respectively. *I. saxatilis* subsp. *magnesiensis* can

be distinguished from *I. saxatilis* subsp. *saxatilis* by its retrorsely setulose stem and leave indumentum [13]. In the present study, we confirm the perennial habit and indumentum differences of these taxa. However, in *I. saxatilis* subsp. *saxatilis*, stem and leaves are not always glabrous and there is a sparsely distributed indumentum. The most important difference between *I. saxatilis* and the other *Iberis* taxa is the large amount of sclereids in the stem cortex of *I. saxatilis*, but the amount and density of sclereids are decreasing in root cortex. This could be the result of the calcareous and limestone structure of their habitats and of the semi-arid upper Mediterranean floristic region climate, they are found both in the upper part of the tree zone.

I. odorata is annual species and characterized with its 5-15 cm height of stem and the leaves with its short lobes [5]. Our results confirm its annual habit, and also we have found that there is no sclereids in the cortex of root and stem. There are parenchyma cells between the vascular bundles in stem, as seen also in *I. sempervirens* and the vascular cambium is not continuous. *I. odorata* has isolateral leaf anatomy as also seen in *I. simplex*, which has a broad distribution in Turkey. *I. simplex* is morphologically similar to *I. attica* with its whitish-purplish flowers, dense indumentum, but differs with its plant height, inflorescence, flower and fruit sizes and the distribution. As mentioned before, *I. simplex* has isolateral leaf anatomy whereas *I. attica* has bilateral. And in *I. simplex* there is no winged stem structure and branched trichomes can not be seen in the leaves.

Our cluster analysis based on anatomical characters is in partial agreement with Flora of Turkey [5] and indicates *I. attica* and *I. spruneri* have to be treated as separate species, in contrast with [12] and [28]. These contradictional results may come from different species conception of *I. carnosa* and/or mis-identification of some taxa (especially *I. carica*, *I. attica*, *I. simplex* and *I. spruneri*) (Figure 6).

As a conclusion, in this study we report a detailed study of anatomical properties of the genus *Iberis*, which is native to Turkey, for the first time. Root, stem and leaf anatomies are investigated and stomatal index of taxa is determined. The anatomical parameters provide useful characters to improve the taxonomy of taxa in the genus *Iberis*. In addition, it is necessary to combine the anatomical results with palynological, karyological, macro and micromorphological and the molecular data

as planned. Our results propose that *I. attica* and *I. spruneri* have to be considered as two separate taxa, not as synonyms of *I. carnosa*. And, endemic *I. carica* is perennial, not annual.

Acknowledgments:

We wish to thank Dr. Hasan Yıldırım, Dr. Ademi Fahri Pirhan, Dr. Barış Özüdoğru, İlgin Deniz Can, Yusuf Emre Özdemir, Şeyda Çilden and Şinasi Çilden for their help in field works in Turkey between 2014 and 2019; and also to Dr. Dilek Oskay, Haşim Altınözlü, Ahmet Tıraş and Buse Topçuoğlu for collecting and sending some *Iberis* specimens.

References

1. K. Marhold, Brassicaceae, in: Euro+Med Plantbase - the information resource for Euro-Mediterranean plant diversity. (2011). Available from: <http://www2.bgbm.org/EuroPlusMed/PTaxonDetail.asp?NameCache=Iberis&PTRefFk=7200000> (accessed 19 June 2019)
2. I.A. Al-Shehbaz, A generic and tribal synopsis of the Brassicaceae (Cruciferae), Taxon 61 (2012) 931-954.
3. A. Busch, S. Horn, A. Mühlhausen, K. Mummenhoff, S. Zachgo, Corolla Monosymmetry: Evolution of a Morphological Novelty in the Brassicaceae Family, Molecular Biology and Evolution 29 (2011) 1241-1254.
4. S.K. Gupta, Biology and Breeding of Crucifers, CRC Press, 2009.
5. C. Hedge, *Iberis* L. In: Davis PH (editor). Flora of Turkey and the East Aegean Islands Vol. 1. Edinburgh: Edinburg University Press, pp. 309-312, 1965.
6. Ş. Yıldırım, *Iberis* L. In: Güner A, Özhatay N, Ekim T & Başer KHC (editors), Flora of Turkey and the East Aegean Islands (Suppl.2), Vol 11, Edinburgh: Edinburg University Press, pp. 31, 2000.
7. T. Dirmenci, F. Satıl, G. Tümer, A new record for the Flora of Turkey: *Iberis saxatilis* L. (Brassicaceae), Turkish J. Bot. 29 (2005) 471-474.
8. I.A. Al-Shehbaz, B. Mutlu, A.A. Dönmez, The Brassicaceae (Cruciferae) of Turkey, Updated. Turkish J. Bot. 31 (2007) 327-336.
9. M. Vural, H. Duman, Z. Aytaç, N. Adigüzel, A new genus and three new species from Central Anatolia, Turkey, Turkish J. Bot. 36 (2012) 427-433.
10. Ş. Yıldırım, The Chorology of the Turkish species of Brassicaceae family, Ot Sist. Bot. Der. 8 (2001) 141-169.
11. N. Özhatay, Check-list of Additional Taxa to the Supplement Flora of Turkey IV, Turkish J. Bot. 33 (2009) 197.
12. B. Mutlu, *Iberis* L. In: Güner A, Aslan S, Ekim T, Vural M, Babaç MT (editors), Türkiye Bitkileri Listesi (Damarlı Bitkiler), N. Gökyiğit Botanik Bahçesi & Flora Araştırmaları Derneği Yayını, İstanbul, pp. 281-282, 2012.
13. D. Oskay, A new subspecies of *Iberis saxatilis* (Brassicaceae) from Turkey, Phytotaxa 306 (2017) 153-158.
14. B. Yılmaz Çitak, M.B. Crespo, Correct citation and lectotype designation for the name *Iberis carica* (Brassicaceae), Phytotaxa 405 (2019) 297-300.
15. C.R. Metcalfe, L. Chalk Anatomy of The Dicotyledons, Leaves, Stem and Wood in Relation to Taxonomy with Notes on Economical Uses, Vol 1, London: Oxford, The Clarendon Press, pp. 79-87, 1957.
16. R.M.T. Dahlgren, A system of classification of the angiosperms to be used to demonstrate the distribution of characters. Botaniska Notiser 128 (1975) 119-147.

17. M.F. Fay, M.J.M. Christenhusz, Brassicales-An order of plants characterised by shared chemistry, *Curtis's Botanical Magazine*, 27 (2010) 165-196.
18. APG III, An update of the Angiosperm Phylogeny Group classification for the orders and families of flowering plants: APG III, *Botanical Journal of the Linnean Society* 161 (2009) 105-121.
19. APG IV, An update o the Angiosperm Phylogeny Group classification for the orders and families of flowering plants: APG IV, *Botanical Journal of the Linnean Society* 181 (2016) 1-20.
20. T.A.K. Prescott, G.C. Kite, E.A Porter, N.C. Veitch, Highly glycosylated flavonols with an O-linked branched pentasaccharide from *Iberis saxatilis* (Brassicaceae), *Phytochemistry*, 88 (2013) 85-91.
21. M.F. Mahomoodally, S. Vlasisavljevic, S. Berezni, H.H. Abdallah, G. Zengin, A.G. Atasanov, A. Mollica, D. Lobine, A. Aktümsek, *Lotus aegaeus* (Gris.) Boiss. and *Iberis sempervirens* L.: Chemical fingerprints, antioxidant potential, and inhibition activities and docking on key enzymes linked to global health problems, *Indust. Crops & Prod.* 129 (2018) 271-278.
22. F. Tatsuzawa, Acylated pelargonidin glycosides from the red-purple flowers of *Iberis umbellata* L. and the red flowers of *Erysimum x cheiri* (L.) Crantz (Brassicaceae), 2019. *Phytochemistry*, 159: 108-118.
23. J.K. Nielsen, L.M. Larsen, H. Sorensen, Cucurbitacin E and I in *Iberis amara*: feeding inhibitors for *Phyllotreta nemorum*. *Phytochemistry*, 16 (1977) 1519-1522.
24. T.F. Allen, *The Encyclopedia of Pure Materia Medica* vol. 5. Boericke & Tafel, pp. 60-66, 1877.
25. I.A. Al-Shehbaz, M.A. Beilstein, E.A. Kellogg, Systematics and phylogeny of the Brassicaceae (Cruciferae): an overview, *Plant Syst. Evol.* 259 (2006) 89-120.
26. C.H. Huang, R. Sun, Y. Hu, L. Zeng, N. Zhang, L. cai, Q. Zhang, M.A. Koch, I.A. Shehbaz, P.P. Edger, J.C. Pires, D.-Y. Tan, Y. Zhong, H. Ma, Resolution of Brassicaceae phylogeny using nuclear genes uncovers nested radiations and supports convergent morphological evolution, *Mol. Bio. Evol.*, 33 (2015) 394-412.
27. A. Busch, S. Zachgo, Control of corolla monosymmetry in the Brassicaceae, *Iberis amara*. *Proceedings of the National Academy of Sciences*, 104 (2007) 16714-16719.
28. B. Yılmaz Çıtak, A palynological survey of the genus *Iberis* (Brassicaceae), known as candytufts, in Turkey, *Phytotaxa*, 397 (2019) 213-224.
29. Ø. Hammer, D.A.T. Harper, P.D. Ryan, PAST: Paleontological statistics software package for education and data analysis, *Palaeontologia Electronica*, 4 (2001) 9.
30. K. Esau, *Anatomy of Seed Plants*. Second second edition, John Wiley and Sons, Inc., 1977.
31. D.F. Cutler, T. Botha, D.W. Stevenson, *Plant Anatomy, An Applied Approach*, Blackwell Publishing, 2007.
32. S. Yentür, *Bitki Anatomisi*, İstanbul: İ. Ü. Fen Fakültesi, 2003.
33. F. Schweingruber, A. Börner, E.D. Schulze, *Atlas of Stem Anatomy in Herbs, Shrubs and Trees 1* Springer-Verlag Berlin Heidelberg, 2001.



Determination of Biochemical Profile of Bilecik Propolis

Bilecik Propolisinin Biyokimyasal Profilinin Belirlenmesi

Merve Keskin^{1*}, Şaban Keskin¹, Nazlı Mayda², Aslı Özkök³

¹Vocational School of Health Services, Bilecik Şeyh Edebali University, Bilecik, Turkey.

²Department of Biology, Hacettepe University, Ankara, Turkey.

³Hacettepe University, Bee and Bee Products Research and Application Center (HARUM), Ankara, Turkey.

ABSTRACT

Propolis, an important bee product, is used as a food supplement in apitherapy applications and daily life due to its antioxidant, antimicrobial, antitumoral and anti-inflammatory properties. The properties of propolis vary depending on the region in which it is obtained, the time and the form of collection. It is not possible to obtain propolis with the same characteristics from each hive or region. In this study, raw propolis samples were obtained from Bilecik province in Marmara Region and their biochemical properties were determined. Bilecik is rich in forestry covered with oak, beech, fir, linden and chestnut trees. Therefore, it has a rich flora. In order to determine the properties of propolis samples, ethanol extract of each sample was prepared separately by using 70% ethanol. The amount of balsam, wax, total phenolics and total flavonoid of each sample was determined. Chemical composition of each propolis sample was determined by using GC-MS. The amount of balsam which is an important quality parameter for propolis was found to vary between 13% and 52%. It was also found that total phenolic content ranged from 11 mg GAE / mL to 76 mg GAE / mL. It is determined that propolis samples were rich in aldehydes, aliphatic acid and esters, alcohols, hydrocarbons, carboxylic acid esters, ketones, terpenes, fatty acids and other components.

Key Words

Propolis, phenolic components, characterization, balsam..

Öz

Önemli bir arı ürünü olan propolis antioksidan, antimikrobiyal, antitumoral, antiinflamatuvar özellikleri nedeniyle apiterapi uygulamalarında ve günlük yaşamda gıda takviyesi olarak kullanılmaktadır. Propolisin özellikleri elde edildiği bölgeye, toplanma biçimine ve toplanma zamanına bağlı olarak değiştiğinden her kovandan veya bölgeden aynı özelliklere sahip propolis eldesi mümkün olmamaktadır. Yapılan bu çalışmayla Marmara Bölgesinde yer alan Bilecik ilinden temin edilen ham propolis örneklerinin biyokimyasal özellikleri belirlendi. Meşe, kayın, köknar, ıhlamur, kestane ağaçları ile çevrili olan Bilecik orman bakımından oldukça zengindir. Bu nedenle de zengin bir floraya sahiptir. Bu amaçla; %70'lik etil alkol çözeltisi kullanılarak ham propolislerden etanolik propolis özütleri hazırlandı. Hazırlanan propolis ekstraktlarının balsam miktarı, vaks miktarı, toplam polifenol miktarı ve toplam flavonoid miktarı belirlendi. GC/MS kullanılarak ham propolislerin içerdiği bileşenler tespit edildi. Propolis için önemli bir değer olan balsam miktarının %13 ile %52 arasında değiştiği; toplam polifenol miktarının ise 11 mg GAE/mL ile 76 mg GAE/mL arasında değiştiği belirlendi. Propolis örneklerinin aldehitler, alifatik asit ve esterler, alkoller, hidrokarbonlar, karboksilik asit esterleri, ketonlar, terpenler, yağ asitleri ve diğer bileşenler bakımından zengin olduğu belirlendi.

Anahtar Kelimeler

Propolis, fenolik bileşenler, karakterizasyon, balsam.

Article History: Received: Jul 18, 2019; Revised: Aug 2, 2019; Accepted: Aug 24, 2019; Available Online: Nov 1, 2019.

DOI: <https://doi.org/10.15671/hjbc.593940>

Correspondence to: M. Keskin, Vocational School of Health Services, Bilecik Şeyh Edebali University, Bilecik, Turkey.

E-Mail: merveozdemirkeskin@gmail.com

INTRODUCTION

Propolis is a resinous mixture which is collected by bees from leaves, buds and bark parts of plants and is a natural bee product that plays role in protecting hives against all kinds of danger. People have been used propolis in many areas from mummification to treatment of infectious diseases from ancient times to the present [1-3]. Propolis contains various essential oils, aldehydes, aliphatic acid and esters, alcohols, hydrocarbons, carboxylic acid esters, ketones, terpenes, fatty acids and other compounds. Because of these compounds propolis has high antioxidant, antimicrobial, anti-inflammatory and antitumoral activities. Today, propolis is mostly used as a supportive for general health and functional food.

The composition and production of raw propolis depends on many factors such as flora, harvesting season, collection style and bee strain [4,5]. Propolis has a highly complex chemical composition and varies qualitatively and quantitatively for each sample. Studies have focused on propolis extracts and around 300 different compounds found naturally in these extracts have been identified. Essential oils and polyphenolic substances are the major components of these compounds. Polyphenols with a high biologically active value are a large family and can be classified as phenolic acids, flavonoids, prenylated p-coumaric acid and acetogenone lignans, phenolic compounds, di and tri terpenes, sugars, sugar alcohols, hydrocarbons and mineral elements [6,7].

Bilecik Province is located in the southeast of the Marmara Region. It is located on the cutting points of Marmara, Black Sea, Central Anatolia and Aegean Regions. Bilecik has lots of forests with oak, larch, beech, pine, chestnut trees. Having such a diverse forest makes the region rich source of propolis.

In this study, biochemical properties of propolis samples collected from different regions of Bilecik in 2018 were investigated and the profile of Bilecik propolis was determined.

MATERIALS and METHODS

Materials

Propolis samples were supplied from local bee keepers in Bilecik city (Kurtkoy, Camiliyayla, Vezirhan, Poyra, Saraycik and Koyunkoy) Turkey in 2018. Camiliyayla is the

highest place and it has the least floral sources. The other places are covered with diverse forest. Methanol, Gallic acid, ethanol were purchased from sigma Aldrich, USA. All other reagents were analytical grade.

Methods

Preparation of Propolis Extracts

Extraction of propolis samples with ethanol (70% v/v) was carried out by simple maceration technique separately. 1:10 (g/v) ratio was used for the extraction. Frozen propolis sample was powdered by grinding and 2 g of this fine powder was mixed with 30 mL of 70% (v/v) ethanol solution. Extraction was carried out for 48 h on a magnetic stirrer under constant stirring at 150 rpm. Finally, mixtures were separately filtered and filtrates were stored at +4°C.

Determination of Balsam %

Balsam is usually defined as the alcohol soluble fraction of propolis. In order to determine the ratio of balsam, 2 mL of propolis extract was evaporated and the amount of resulted solid was quantified until reaching a constant weight. The amount of balsam of the extract was calculated and expressed as a percentage value [8].

Determination of Wax %

The amount of wax in raw propolis samples were determined as [9] method with minor revisions. Frozen propolis samples were powdered by grinding and 3 grams of samples mixed with 15 mL of methanol. The mixture was carried out for 2 h on a magnetic stirrer under constant stirring at 150 rpm and stored -18°C for 24 h. After the storing, the mixture was filtrated and the amount of wax was calculated.

Determination of Total Phenolic Content and Flavonoid Content

Total phenolic content of ethanol propolis extracts (EPE) was determined by using Folin–Ciocalteu method [10,11] Gallic acid as standard. Results were expressed as mg GAE/mL. Total flavonoid content of the samples was determined by using aluminum chloride method [12] quercetin as standard. Results were expressed as mg QE/mL.

GC-MS Analysis

Propolis extracts were passed through 45 µm pore filters and 2µl extract injected into the GC-MS. The analysis was performed using Agilent brand 5973N Selective Mass Detector, 6890N Network GC System (GCMS). DB

Table 1. . Obtained data for raw propolis samples.

Origin of Sample	Wax %	Balsam %	Total phenolic content mg GAE/mL	Total flavonoids mg QE/mL
Kurtköy	4.4±0.08	17.7±0.8	20.335±0.02	4.13±0.01
Camiliyayla	2.8±0.02	13.2±0.4	11.763±0.03	3.42±0.02
Vezirhan	5.1±0.06	52.3±0.6	75.765±0.08	16.47±0.02
Poyra	4.3±0.04	13.9±0.3	11.478±0.03	2.66±0.04
Saraycık	1.9±0.03	37.6±0.4	46.769±0.07	9.41±0.04

5MS column (30 m × 25 mm and 0.25 µm film thickness) was used. In the gas chromatography section, the temperature was maintained at 50°C for 1 minute then 10°C./min. It was raised to 150°C. by the rate of increase and maintained at this temperature for 2 minutes after this period. Finally, the injection temperature was increased to 280°C, and the time was adjusted to 49.5 minutes [13].

RESULTS and DISCUSSION

It was determined that wax amounts of raw propolis samples collected from 6 different regions of Bilecik ranged from 1.9% to 4%. Low wax and high balsam are important criteria for propolis quality [8,9]. In a research on ethanolic extracts of raw propolis samples collected from Brazil, China and Uruguay, no wax was found in Uruguay propolis extract, but it was stated that wax amount changed between 2.40% and 30.60% for other regions [14]. It was reported that wax amount of Anatolian propolis varies between 1.4% and 9.8% [15]. It is clear that wax value of Bilecik propolis is quite low. The amount of balsam determined in Bilecik propolis ranged between 13.9% and 52.3% (Table 1).

High amounts of balsam are reported to express high phenolic compounds and low waxes [8,16]. Indeed, Popova et al. (2017) stated that crude propolis contains between 40% and 60% balsam. It is reported that the amount of balsam in crude propolis samples collected from Spain varies between 52.5-76.2% and wax value is between 1.8 and 27.7% [17]. In different Portuguese propolis samples, it was reported that the amount of wax in raw propolis varies between 4.8% and 16.0% [18]. Since it is not possible to fully elucidate the phenolic contents of the plant extracts, the phenolic content is expressed in terms of total phenolic content. Total phenolic components are measured by spectrophotometric method based on color complex formation with

Folin-Ciocalteu reagent. The high amount of phenolic content refers to high antioxidant activity while at the same time high biological activity. It is seen that total phenolic content of ethanolic extracts of Bilecik propolis varies between 11.48- 75.77 mg GAE / mL (Table 1). The amount of the total flavonoid ranged between 2.66 mg QE / mL and 16.47 mg QE / mL. In a study, it was reported that total polyphenol content of crude propolis samples obtained from Brazil ranged between 8.8% and 13.7% and flavonoid content was minimum 0.35% and maximum 2.7% [19].

Total phenolic and flavonoid amounts of propolis samples collected from different regions of Bulgaria were determined in order to determine the chemical components of Bulgarian propolis and to make a simple standardization study. It was reported that total phenolic content ranged from 11.2% to 41.9% and total flavonoid amount ranged from 2.9% to 13.5% [20]. It was reported that total amount of phenolics in Anatolian propolis ranged between 10.6-178 mg GAE / g and the total amount of phenolics increased with increasing amount of balsam [15]. Aliyazıcıoğlu et. al. (2013) reported that total amount of phenolics ranged between 115 to 210 mg GAE/ g for different Turkish propolis samples [3]. It was reported that total phenolic content ranged between 1.2 to 15.6 mg/g for Turkish chestnut propolis [21]. It is clear that total phenolic content for propolis samples obtained from different regions of Turkey varies in wide range.

GC-MS analysis was performed to investigate the chemical composition of the propolis extracts (Table 2). As a result of GC-MS analysis, aldehydes, aliphatic acid and esters, alcohols, hydrocarbons, carboxylic acid esters, ketones, terpenes, fatty acids and other compounds were detected in propolis samples. It is clear that our results are consistent with the literature data [22-24].

Silici and Kutluca (2005) determined the chemical composition of some Anatolian propolis samples by using GC-MS. They reported that propolis samples were found to be rich in aliphatic acids, esters, flavonoids and other components [25]. Uzel et. al. (2005) determined the chemical composition of four different propolis

samples obtained from Anatolia using GC-MS. Their results showed that propolis samples were rich in aromatic acids, fatty acids, aromatic aldehydes, flavone and flavonones [26]. It is clear that our results are compatible with the literature data.

Table 2. GC-MS Analysis results of propolis samples.

Compounds	1	2	3	4	5	6	7
Aldehydes							
2,4-Dimethylbenzaldehyde	-	0.03	-	-	-	0.06	0.02
2-Methyl-2-pentenal	0.04	-	-	-	-	-	-
Benzaldehyde	-	0.03	-	-	-	0.41	-
Cinnamaldehyde	-	-	-	0.03	-	-	-
Lauric aldehyde	-	-	0.30	1.30	-	-	-
Phenylacetaldehyde	-	-	-	1.02	-	-	-
trans. trans-2,4-Hexadienal	-	0.04	-	-	-	-	-
Total	0.04	1.00	0.30	2.35	-	0.47	0.02
Aliphatic Acid and Esters							
Decanoic acid	-	0.05	-	-	-	-	-
Total	-	0.05	-	-	-	-	-
Alcohols							
1-Decanol	-	-	-	0.30	-	-	-
3-Octanol	-	-	-	-	0.17	-	0.16
3-Phenyl-1-propanol	-	-	-	0.46	0.15	-	-
alpha-Methylbenzylalcohol	-	-	-	-	0.51	-	-
Benzyl alcohol	14.46	0.08	1.31	1.23	1.10	0.32	11.36
Farnesol	0.45	3.28	0.33	-	6.65	0.47	-
Furfuryl alcohol	0.04	-	-	-	-	-	-
Geraniol	-	-	-	-	1.64	-	-
Lauryl alcohol	0.92	-	-	0.52	-	-	-
Phenethyl alcohol	4.41	0.16	1.63	2.14	1.16	0.90	2.26
Total	20.28	3.52	3.27	4.65	11.38	1.69	13.78
Hydrocarbons							
n-Tetracosane	-	2.20	-	-	-	0.59	-
Total	-	2.20	-	-	-	0.59	-
Carboxylic Acids and Esters							
Benzoic acid	1.32	-	0.93	-	1.08	-	0.05
Total	1.32	-	0.93	-	1.08	-	0.05
Ketones							
2-Nonanone	-	-	0.38	-	-	-	-
2-undecanone	-	-	-	0.56	-	-	-
4'-Methylacetophenone	-	-	-	-	0.19	0.53	-
6-Methyl-3,5-heptadien-2-one	-	0.12	-	-	-	-	-
Menthone	4.91	-	1.96	-	2.76	-	0.71
omega-Pentadecalactone	-	-	-	-	-	0.74	-
Total	4.91	0.12	2.34	0.56	2.95	1.27	0.71

Table 2. GC-MS Analysis results of propolis samples. Continued.

Compounds	1	2	3	4	5	6	7
Terpenes							
Isoborneol (isomer 1)	-	0.04	-	-	-	-	-
Limonene	-	-	-	-	-	0.84	-
Total	-	0.04	-	-	-	0.84	-
Fatty Acids							
Decyl acetate	-	-	-	-	0.58	-	-
Lauric acid	-	-	-	-	0.73	--	-
Myristic acid	-	-	0.34	-	0.14	-	-
Palmitic acid	0.53	0.76	-	0.45	-	0.48	-
Stearic acid	-	0.03	0.37	0.28	-	-	-
Total	0.53	0.79	0.76	0.73	1.45	0.48	-
Other Compounds							
2.3.5.6-Tetramethylpyrazine	-	-	-	0.12	-	-	2.83
3-Phenylpropionic acid	0.10	0.18	0.24	-	0.14	0.13	-
Acetanisole	0.03	-	-	-	0.71	-	3.97
alpha-Pinene	-	-	0.02	-	-	-	-
Benzyl acetate	0.17	-	-	-	-	-	-
Benzyl benzoate	0.12	-	-	-	0.13	-	0.12
Benzyl cinnamate	0.31	-	-	-	0.57	-	-
beta-Caryophyllene	-	-	-	-	-	-	0.39
beta-Damascone	-	-	0.63	-	-	-	-
beta-Ionone	-	1.08	0.73	-	0.60	-	-
Carvacrol	3.06	0.30	0.48	-	-	-	-
Cinnamil acetate	0.06	-	-	-	-	-	-
Citronellal	-	1.80	-	-	0.25	-	0.24
Delta-3-carene	-	0.06	-	-	-	-	-
Ethyl cinnamate	0.06	0.11	0.07	-	0.07	0.10	0.04
Ethyl laurate	-	0.08	-	-	-	-	-
Ethyl oleate	-	3.34	-	-	-	0.39	-
Ethyl palmitate	-	1.10	-	-	-	-	-
Ethyl-3-hydroxyhexenoate	-	0.10	-	-	-	-	-
Ethylphenyl acetate	-	-	-	-	-	0.88	-
Eucalyptol	-	-	0.11	-	-	-	-
Eugenol	0.46	-	0.22	-	-	-	-
Geranylacetone (Isomer 1)	-	-	-	-	-	0.57	-
Guaiacol	1.05	-	-	-	-	-	-
Indole	1.00	0.78	0.17	1.03	0.32	1.52	-
Linaloxide (cis. isomer B)	-	-	-	1.51	0.84	1.35	-
Linaloxide (trans. isomer A)	-	-	-	-	0.09	-	0.75
Linaloxide (trans. isomer B)	-	-	0.64	-	-	-	-
Linalyl formate	-	-	-	0.88	-	-	-
Methyl benzoate	-	-	-	-	-	-	0.05
Methyl octine carbonate	-	-	-	-	0.14	-	-
Methyl phenyl acetate	-	-	-	0.30	-	-	0.32

Table 2. GC-MS Analysis results of propolis samples. Continued. Continued.

Compounds	1	2	3	4	5	6	7
Methyl phenylethyl ether	0.25	-	-	-	-	-	0.07
Methyl-gamma-Ionone (isomer 1)	0.41	-	-	0.23	0.23	-	-
Methylvalerate	-	-	0.07	-	-	-	-
Neryl acetate	-	-	0.04	-	-	-	-
Nonyl acetate	0.22	-	-	-	-	-	-
p-Cresol	-	0.20	-	-	-	-	-
Phenethyl butyrate	-	-	0.02	-	-	-	-
Phenethylamine	-	-	0.02	-	-	-	-
Quinoline	0.76	0.24	0.44	0.75	0.41	0.75	-
Styrene	0.61	-	-	0.14	-	0.08	0.13
trans. trans-2.4-Heptadienal	-	-	0.18	-	-	-	0.42
Valencene	0.30	-	0.57	1.26	0.20	1.39	0.80
Vanillin	0.19	-	-	-	0.32	-	0.12
Total	9.26	11.72	4.65	6.22	4.52	7.16	10.25

Conclusion

In this study, physical and biochemical properties of propolis of Bilecik province were determined. It is clear that the amount of wax and balsam for Camiliyayla sample was found to be lower than the other samples. This shows that the amount of balsam is related to the flora of the region. Propolis samples with lower wax and higher balsam content seems to have more biologically active components.

References

- M.R., Ahn, S., Kumazawa, Y., Usui, J., Nakamura, M., Matsuka, F. Zhu, T. Nakayama, Antioxidant Activity and Constituents of Propolis Collected in Various Areas of China, *Food Chem.*, 101 (2007) 1383-1392.
- R., Aliyazicioglu, H., Sahin, O., Erturk, E., Ulusoy, S., Kolayli, Properties of phenolic composition and biological activity of propolis from Turkey, *Int. J. Food Prop.*, 16 (2013) 277-287.
- F., Li, S., Awale, Y., Tezuka, S., Kadota, Cytotoxic Constituents From Brazilian Red Propolis and Their Structure–Activity Relationship, *Bioorg., Med., Chem.*, 16 (2008) 5434–5440
- R.O., Silva, V.M., Andrade, E.S., Bulle Rego, G.A., Azevedo Doria, B., Santos Lima, F.A., Silva, A.A.S., Araújo, Acute and sub-acute oral toxicity of Brazilian red propolis in rats. *J. Ethnopharm.*, 170 (2015) 66-71.
- M.S.R., Neto, S.R., Tintino, A.R.P., da Silva, M.S., Costa, A.A., Boligon, E.F.F., Matias, V.Q., Balbino, R.A., Irwin Menezes, H.D.M. Coutinho, Seasonal variation of Brazilian red propolis: Antibacterial activity, synergistic effect and phytochemical screening. *Food Chem. Toxic.*, 107 (2017) 572-580.
- Ö., Saral, Determination of Antioxidant Activities of the Chestnut and Flower Honeys Collected from Eastern Black Sea Region in Turkey. *J. Apit. Nat.*, 1 (2018) 28-32.
- E., Talla, A., Tamfu, P., Biyanzi, P., Sakava, F., Asobo, J., Mbafor, N. F., Tchuenguem, R., Ndjouenkeu, Phytochemical Screening, Antioxidant Activity, Total Polyphenols and Flavonoids Content of Different Extracts of Propolis From Tekel (Ngaoundal, Adamawa Region, Cameroon), *J. Phytopharmac.*, 3 (2014) 321-329.
- M., Popova, E., Giannopoulou, K., Skalicka-Woźniak, K., Graikou, J., Widelski, V., Bankova, H., Kalofonos, G., Sivolapenko, K., Gawel, B., Eben, B., Antosiewicz, I., Chinou, Characterization and Biological Evaluation of Propolis from Poland, *Molecules*, 22 (2017) 1159.
- X., Feás, L., Pacheco, A., Iglesias, L.M., Estevinho, Use of Propolis in the Sanitization of Lettuce,, *Int. J. Mol. Sci.*, 15 (2014) 12243-12257.
- V. L. Singleton, J.A., Rossi Colorimetry of Total Phenolics with Phosphomolybdic–Phosphotungstic Acid Reagents, *American J. Eno. Vitic.*, 16 (1965) 144-158.
- V. L., Singleton, R.Orthofer, R.M., Lamuela-Raventos, Analysis of Total Phenols and Other Oxidation Substrates and Antioxidants by Means of Folin-Ciocalteu Reagent, *Methods in Enzy.*, 299 (1999) 152-178.
- L. R., Fukumoto, G., Mazza, Assessing antioxidant and prooxidant activities of phenolic compounds, *J. Agric. Food Chem.*, 48 (2000) 3597-3604.
- B., Trusheva, M., Popova, E. B., Koendhori, I., Tsvetkova, C., Naydenski, V., Bankova, Indonesian propolis: Chemical composition, biological activity and botanical origin, *Nat. Prod. Res.*, 25 (2011) 606–613.
- J.S., Bonvehi, F.V., Coll, R.E., Jorda, The Composition Active Components and Bacteriostatic Activity of Propolis in Dietetics, *JAACS*, 71 (1994) 18-25.
- M., Keskin, S., Kolaylı, Standardization of Propolis, is it Possible?, *Uludağ Arıcılık Dergisi – Uludag Bee Journal*, 18 (2018) 101-110.
- V., Bankova, S., De Castro, M., Marcucci, Propolis: recent advances in chemistry and plant origin, *Apidologie*, 31 (2000) 3-15.

17. J. S. Bonvehi, A. L. Gutierrez, Antioxidant Activity and Total Phenolics of Propolis from the Basque Country (Northeastern Spain), *Am. Oil Chem. Soc.*, 88 (2011) 1387-1395.
18. L.G., Dias, A.P., Pereira, L.M., Estevinho, Comparative Study of Different Portuguese Samples of Propolis: Pollinic, Sensorial, Physicochemical, Microbiological Characterization and Antibacterial Activity, *Food Chem. Toxic.*, 50 (2012) 4246-4253.
19. R. G., Woisky, A., Salatino,. Analysis of propolis: some parameters and procedures for chemical quality control, *J. Apic. Res.*, 37 (1998) 99-105.
20. V., Bankova, A., Dylgerov, S., Popov, N., Marekov, A GC/MS Study of the Propolis Phenolic Constituents, *Z. Naturforsch*, 42 (1987) 147-151.
21. A.O., Sarıkaya, E., Ulusoy., N., Öztürk, M., Tunçel, S., Kolaylı, Antioxidant Activity And Phenolic Acid constituents of Chestnut (*Castania Sativamill.*) Honey And Propolis, *J. Food Biochem.*, 33 (2009) 470-481.
22. N., Duran, M., Muz, G., Culha, G., Duran, B., Ozer, GC-MS analysis and antileishmanial activities of two Turkish propolis types, *Parasitol. Res.*, 108 (2011) 95-105.
23. M. Popova, S. Silici, O. Kaftanoglu, V. Bankova, Antibacterial activity of Turkish propolis and its qualitative and quantitative chemical composition, *Phytomedicine*, 12 (2005) 221-228.
24. H., Katircioglu, N., Mercan, Antimicrobial activity and chemical compositions of Turkish propolis from different regions, *African J. Biotech.*, 5 (2006) 1151-1153.
25. S., Silici, S., Kutluca, Chemical composition and antibacterial activity of propolis collected by three different races of honeybees in the same region, *J. Ethnopharmacology*, 99 (2005) 69-73.
26. A., Uzel, K., Sorkun, O., Onçağ, D., Çoğulu, O, Gencay, B., Salih, Chemical compositions and antimicrobial activities of four different Anatolian propolis samples, *Mic. Res.*, 160 (2005) 189-195.



The Effect of Interval Training Program on Nuclear Factor Erythroid-Derived 2-like 2 (NFE2L2/Nrf2) Gene Expression in Women

Aralıklı Antrenman Programının Kadınlarda NFE2L2/Nrf2 Gen İfadesine Etkisi

Neşe Akpınar Kocakulak¹

¹Department of Sport Science, İzmir Democracy University, İzmir, Turkey.

ABSTRACT

Purpose in this work, to investigate whether interval training program has an effect on Nuclear factor erythroid-derived 2-like 2 (NFE2L2/Nrf2) gene expression in women. The research was made on 12 women. Participants were given a medium-term interval training program for 8 weeks, 3 days a week. The blood samples of the participants were collected before and after the 8 weeks of training. RNA isolation was performed using TRIzol Reagent from peripheral blood mononuclear cells. NFE2L2 gene expression was determined by Biomark Real-Time PCR (RT-PCR). The participants was a significant increase in heart rate and maximal oxygen use capacity (VO₂ max) after the exercise (p <0.001). There was a significant decrease in the body weight and body mass index of women after the exercise (p <0.001). There was a decrease in NFE2L2 gene expressions after 8 weeks of the training program (p <0.05,). It shows that interval exercise reduces NFE2L2 gene expression in women.

Key Words

Exercise, gene expression, NFE2L2 gene, interval training.

Öz

Aralıklı antrenman programının bayanlarda Nuclear factor erythroid-derived 2-like 2 (NFE2L2/Nrf2) gen ekspresyonuna etkisinin olup olmadığını araştırmaktır. Araştırma 12 kadın üzerinde yapıldı. Katılımcılara, haftada 3 gün olmak üzere 8 hafta süreyle orta süreli interval antrenman programı uygulandı. 8 haftalık antrenmanlar öncesi ve sonrası kan örnekleri alındı. Periferik kan mononükleer hücrelerinden TRIzol Reaktif kullanılarak RNA izolasyonu yapıldı. NFE2L2 gen ekspresyonu Biomark Real-Time PCR (RT-PCR) ile belirlenmiştir. Çalışmaya katılan katılımcıların maksimal oksijen kullanma kapasitesinde (VO₂ Max) egzersiz sonrası önemli ölçüde artış bulundu (p<0.001). Kadınların vücut ağırlıkları ve vücut kitle indeksinde azalma olmuştur (p<0.001). NFE2L2 gen ifadelerinde 8 haftalık antrenman programı öncesine göre sonrasında azalma olmuştur (p<0.05,). Aralıklı yapılan egzersizin bayanlarda NFE2L2 gen ekspresyonunu azalttığını işaret etmektedir.

Anahtar Kelimeler

Egzersiz, gen ekspresyonu, NFE2L2, aralıklı antrenmanlar.

Article History: Received: Mar 29, 2017; Revised: Jul 20 2017; Accepted: Sep 15, 2019; Available Online: Nov 1, 2019.

DOI: <https://doi.org/10.15671/hjbc.546962>

Correspondence to: N. Akpınar Kocakulak, Department of Sport Science, İzmir Democracy University, İzmir, Turkey.

E-Mail: nese.kocakulak@idu.edu.tr

INTRODUCTION

According to many studies, it is reported that the increase in the physical activities of the people expands life-span by reducing the risk of death. Regular physical activity contributes to the treatment of various chronic diseases, especially lung, heart diseases, hypertension, metabolic disorders, especially type 2 diabetes and obesity, muscle, bone, joint injuries, cancer and neuropsychiatric disorders [1,2]. However, the type, intensity of exercise, competitions, traumas, and stress lead to both physiological and metabolic changes in the human body [3]. During the prolonged/intense exercise, the amount of consumed oxygen varies depending on the type and severity of the exercise varies, but generally by increasing in accordance with relaxation leads to the formation of free radicals (reactive oxygen species, ROS) that cause oxidative stress. ROSs are consistently built up in the body, but physical exercise leads to further increases in ROSs and cannot be removed sufficiently by the antioxidant defense system. They cause many damages by reacting with various molecules such as nucleic acids, proteins, membranes, cells and tissues [4,5]. Mitochondria, which participate dynamically in various muscle cell activities along with death, autophagy, differentiation, are generally accepted as the main source of reactive oxygen species (ROS) in skeletal muscles [6]. Some studies have emphasized that the ROSs, that emerged as a result of the reduction of oxygen in the normal metabolic stages, are not only the toxic. The significance of exercise in the process of adaptation, which is the most important impact on the human body, is specifically emphasized. In these studies, it is indicated that the increase in the levels of ROSs minimizes the damage by increasing the activity of the antioxidant enzymes during regular exercise, and emphasized that ROSs give more harm to the unprepared tissues [7,8]. Besides, ROSs play an important role in regulating the cell signaling and gene expression [9,10]. The transcription factor NFE2L2 is the main organizer of antioxidant defenses, regulating more than 200 cytoprotective genes as a response to oxidative stress. It is also reported that nuclear factor erythroid-derived 2-like 2 (NFE2L2), acute oxidative and nitrosative stress regulate antioxidant response and mitochondrial biogenesis. In addition, they also noted that NO and ROSs, that is produced through exercise, activated skeletal muscle NFE2L2 and required the NFE2L2 expression for normal mitochondrial biogenesis, acute exercise and antioxidant transcriptional response during regular training.

The studies reported that NFE2L2 activators protect mice against metabolic diseases and prolong the lifespan of *C. Elegans* and *M. Drosophila* [11]. The purpose of this study is to investigate the effect of interval training program on Nuclear factor erythroid-derived 2-like 2 (NFE2L2/Nrf2) gene expression in women.

MATERIALS and METHODS

Participants: The research was made on 12 women who have similar ages and physical characteristics that did not exercise regularly, active, non-smoker, did not take any of food supplement and did not have any health problem, average of age was 21.88 ± 2.44 years, average of height was 162.13 ± 5.83 cm, and the average of weight was 58.60 ± 2.04 kg. Our study protocol was approved by Erciyes University Ethics Committee. Our work was conducted under the direction of Declaration of Helsinki and local laws.

Experimental Design

Maximal Aerobic Capacity (VO₂ max): Maximal oxygen use capacities were determined proportionately (body weight / lean body mass / ml / kg / min) by applying the Bruce Test Protocol, which was performed before the training and at the end of the 8-week training.

Training Protocol: At the beginning of the study, participants were asked not to take any medication or nutritional supporters for 8 weeks, to avoid heavy physical activity 48 hours before the training and to be hungry at least 3 hours before the test time. Two days after the maximal oxygen use capacities were determined, 8-week training programs were started. Training Program: Participants were given a medium-duration interval training program in 3 days a week, for 8 weeks. The severity of the study was determined according to the volunteers' target heart rate (%90-95). Participants were received height, weight, systolic-diastolic blood pressure, heart rate and 10 ml peripheral blood samples with EDTA tubes before and after 8 weeks of exercise.

RNA Isolation and gene expression studies

2 ml venous blood samples were taken from the participants for the gene expression study. RNA samples were stored at the -80°C until analysis. Firstly, peripheral blood mononuclear cells were isolated using standard methods [12,13]. RNA isolation was performed using TRIzol Reactive (TRIzol, Roche, Almanya) from peripheral blo-

Table 1. Some of the physical and physiological characteristics of the participants.

Variables		BE.Avr±SD	AE.Avr±SD	t	P
Mass (kg)	(n=12)	58.60±2.04	56.24±1.65	4.2	0.001**
BMI (kg/m ²)	(n=12)	22.29±2.43	21.37±1.98	4.5	<0.001**
Heart Rate(pulse/min)	(n=12)	86.70±6.7	98.90±7.98	5.3	0.001**
Systolic H.P (mmHg)	(n=12)	114.90±19.9	107.70±12.17	1.2	0.269
Diastolic H.P (mmHg)	(n=12)	78.60±9.78	73.20±5.29	0.8	0.431
VO2 Max	(n=12)	35.74±2.5	46.16±3.25	5.1	0.001**

Paired Samples T Test / SD.: Standard Deviation / *p<0.05 **p<0.001

B.E.= Before Exercise A.E.= After Exercise B.M.I.= Body Mass Index

od mononuclear cells. The amount and quality of RNA samples were measured with a NanoDrop 2000 Spectrometer (Thermo Scientific, Waltham, MA). A reverse transcription polymerase chain reaction (RT-PCR) was used to detect the gene expressions through syntheses of the complementary DNA (cDNA) transcripts from the total RNA extracts. Complementary DNA (cDNA) was obtained from the RNA using RT2 HT First-Strand (Qiagen) kit. When complementary DNA was synthesized, it was left to incubate for 5 min at 95°C and for 15 min at 42°C. Nuclear factor erythroid-derived 2-like 2 (NFE2L2) gene expression was determined by Biomark Real-Time PCR (RT-PCR). Biomark Real-Time PCR (Qiagen) instrument was used for the expression study. The expression study was incubated at 95°C for 15 sec and 60°C for 60 sec through 95°C for 10 min and 40 cycles. Glyceraldehyde-3-phosphate dehydrogenase (GAPDH) was selected as the house keeping gene [14,15]. The data were collected with the Fluidigm Real-Time PCR analysis software and quantification cycle (Cq) values of 999. Cq values larger than 23 were removed since these readings were unreliable. The delta delta Ct (2- $\Delta\Delta$ Ct) method was applied for the relative quantification of the samples that normalized with Glyceraldehyde-3-phosphate dehydrogenase [12]. Genetic studies were carried out at Erciyes University Genomic and Stem Cell Center.

Statistical Analysis

The Comparisons were performed using two independent sample T-test, the Mann-Whitney U test, for quantitative data and calculated gene expression values. The statistical significance level was taken as p <0,05.

Results

Some of the physical and physiological characteristics and the blood samples of the 12 participants, who par-

ticipated in the study, were prepared and evaluated according to the methods mentioned in the related section. The average age of the participants was 21.88±2.44 years, and the average height was 162.13±5.83 cm (Table.1.).

There was no difference in systolic and diastolic blood pressures (mmHg) at the beginning and end of the 8-week training programs of participants attended the study (p>0.05 Table.1).

According to the statistical analysis results, there was a significant increase in heart rate and maximal oxygen use capacity (VO2 max) after exercise (p<0.001 Table.4.1). There was a significant reduction in body weight (p <0.001) and body mass index of women after the exercise (p<0.000).

The change in the Nuclear factor erythroid-derived 2-like 2 (NFE2L2) gene expression, performed in the analyses by the blood samples taken before and after the 8-week training program, is shown in the table below.

RESULTS and DISCUSSION

It is known that acute exercise systematically causes to oxidative, metabolic, mechanical and thermal stresses. It is reported that even a single exercise increases oxidative stress bioindicators in almost all tissues. ROSs contain one or more unpaired molecules with high energies. Normal cell metabolism converts about 1-2% oxygen molecules to ROSs.

This ROS is potentially toxic. Although there are significant contributions to the regulation of normal physical activities, such as ROS muscular contraction, the signifi-

Table 2. Female NFE2L2 gene expression change before and after the 8-week training program.

Gene	BE-W Median - IQR	8w.AE-W Median - IQR	P-value*
NFE2L2	15.807±2.986	12.11±1.087	<0.004

Mann Whitney U test / IQR: Interquartile range *p<0.05 **p<0.001

B.E.= Before Exercise A.E.= After Exercise W= Woman

There was a decrease in female NFE2L2 gene expressions after the 8-week training program than before (p<0.05, **p<0.001, Table-2).

cant increases in the concentrations of ROS may disrupt normal cell function and cause to oxidative damage of various biomolecules (protein, lipid) and cellular DNA [16-19]. Due to its role in the organ, tissue damage and the aetiopathogenesis of various diseases, ROS has been a growing area of interest in medicine recently. NFE2L2 or Nrf2 regulates basal antioxidant and antioxidant reactions against stress in various organisms from ferment to *Caenorhabditis elegans* and mammals. The cell culture studies using C2C12 skeletal muscle cells report that Nrf2 is activated by ROS. In a study of wild-type mice, it was emphasized that a single acute exercise increased Nrf2 proteins, Nrf2-bound phase II enzymes and Nrf2 gene expression in the skeletal muscle [20,21]. Horie et al. used an electrical impulse stimulation (EPS) to imitate acute exercise and emphasized that Nrf2 expression is related to both intensity and duration of the stimulus [22]. Similar to the cell culture studies, studies on some animals showed that increases in Nrf2 signalization depend on the duration of exercise. Less than one hour of running treadmill exercise was reported to have no effect on Nrf2 mRNA or protein expression [23,24,]. The data on the NFE2L2 signal related to exercise is still very limited in humans, but a recent study indicated that acute exercise increases Nrf2 proteins at all cellular levels measured in peripheral blood mononuclear cells (PBMCs) in young and old men. Again in the same study, nuclear accumulation of Nrf2 was observed only in the young group and emphasized that aging may be related to Nrf2 disruption. Similarly, in middle-aged women, who do regular exercise, Nrf2 mRNA increased significantly 2 hours after 30 minutes of moderate treadmill exercise, and sedentary women did not show any change in Nrf2 gene expression as a response to exercise [25]. This may suggest that sport may play a role in preserving the response of acute Nrf2 and aging. The impact of regular exercise training on the NFE2L2 response is investigated in the studies more extensively than the acute exercise. It is showed that medium-intensity or high-intensity interval training for 4-24 weeks activates Nrf2 signalization in several tissues, including skeletal muscle, kidney, brain, liver, testicle,

prostate and myocardium in rodents. It is stated that regular exercise in rats prevents the normal level of Nrf2 from falling due to the oxidative stress. At the same time, it is also emphasized that antioxidant supplement weakened the normal activation of NFE2L2 during the exercise [26].

Gomes et al. [27] had Sprague-Dawley rats instructed to exercise using a jumping protocol with a weighted vest as a resistance training. While no change in Nrf2 expression was observed in young animals, a decrease in Nrf2 was indicated in elderly animals subjected to the same training, and this difference was initially explained by highness in the Nrf2 expression in elderly animals. There are contradictory results about NFE2L2 gene expression in the studies. In some studies; increasing with exercise, a decrease, and no difference is detected. It is emphasized that these different results in the studies affected by the age of the subjects and periods of sampling after the exercise [28]. In our study, it was found that NFE2L2 gene expression in females decreased after the regular exercises compared to basic level. This make us consider that the reduction resulted from the time interval in blood sampling, the initially high level of NFE2L2 and the duration, intensity and severity of the exercise.

It is indicated that regular exercise reduces the Nuclear factor erythroid-derived 2-like 2 (NFE2L2) gene expression in women. Both animal studies and human studies are almost limited to male subjects only. We believe that different exercise protocols and taking samples at different time intervals may be important to a better explanation of this variation, activation of NFE2L2 and to catch different reaction times and general variation of NFE2L2 in females

Acknowledgments - This research was supported by Erciyes University Scientific Research Projects Units.

References

1. J.N. Stathopoulos , J. G.Tzanninis , A.A. Philippou, M. Koutsilieris, Epigenetic regulation on gene expression induced by physical exercise. *J. Musculoskelet. Neuronal Interact.*,13 (2013) 133-146.
2. P. Meier , M. Renga , H. Hoppeler, O. Baum, The impact of antioxidant supplements and endurance exercise on genes of the carbohydrate and lipid metabolism in skeletal muscle of mice, *Cell Biochem. Funct.*, 31 (2013) 5-159.
3. G. Bangi, M. Delfabbro, C. Maurş, M. Corsi, G.Melegati. Haematological parameters in elite rugby players during a competitive season. *Clin. Lab. Haem.*, 28 (2000) 183-188
4. Z. Rodak, J. Pucsek, S. Boros, L. Jofjai, A.W. Taylor, Changes in urine 8-hydroxydeoxyguanosine levels of super-marathon runners during a four-day race period, *Life Sci.*, 66 (2000) 1763-1767.
5. Z. Rodak, T. Kaneko, S. Tahara ,H. Nakamoto, H. Ohno, M. Sasvari, C. Nyakas, S. Goto, The effect of exercise training on oxidative damage of lipids, proteins, and DNA in rat skeletal muscle: evidence for beneficial outcomes, *Free Radic. Biol Med.*, 27 (1999) 69-74.
6. L. Packer, E. Cadenas, K.J.A. Davies, Free radicals and exercise: an introduction, *Free Radic. Biol. Med.*, 44 (2008) 123–125.
7. G. Gandhi, G. Gunjan, Exercise-Induced Genetic Damage: A Review, *Int. J. Hum. Genet.*, 9 (2009) 69-96
8. Z. Radak , Y.H. Chung , E. Koltai , A.W. Taylor, S. Goto, Exercise, oxidative stress and hormesis, *Ageing Res. Rev.*, 7 (2007) 9-170.
9. M.C. Gomez-Cabrera, E. Domenech. J. Vina, Moderate exercise is an antioxidant: upregulation of antioxidant genes by training, *Free Radic. Biol. Med.*, 44 (2008) 126-31.
10. C.L. Saw, Q. Wu, A.N. Kong, Anti-cancer and potential chemopreventive actions of ginseng by activating Nrf2 (NFE2L2) anti-oxidative stress/anti-inflammatory pathways, *Chinese Medicine*, 27(2010) 5-37
11. C. Nilsson, S. Aboud, K. Karlen, B. Hejdeman, W. Urassa, Optimal blood mononuclear cell isolation procedures for gamma interferon enzyme-linked immunospot testing of healthy Swedish and Tanzanian subjects, *Clin. Vaccine Immunol.*, 15 (2008) 585-589.
12. F. Bayram, H. Diri, E. F Sener, M. Dundar, Y. Simsek, Genetic expressions of thrombophilic factors in patients with Sheehan's syndrome, *Gynecol. Endocrinol.*, 32 (2016) 908-911
13. B. Jemiolo, S. Trappe, Single muscle fiber gene expression in human skeletal muscle: validation of internal contro lwith exercise, *Biochem. Biophys. Res. Commun.*, 320 (2004) 1043-1050.
14. M. Catoire, M. Mensink, W.V. Boekschoten, M.Müller, P. Schrauwen, S.Kersten, Pronounced effects of acute endurance exercise on gene expression in resting and exercising human skeletal muscle, *PLoS One* 7 (2012) e51066.
15. Z. Radak, S. Kumagai, A.W. Taylor, H. Hisashi, S. Goto, Effects of exercise on brain function: role of free radicals, *Appl. Physiol. Nutrition., Metabol.*, 32 (2007) 942-946.
16. T.L Merry, M. Ristow, Nuclear factor erythroid-derived 2-like 2 (NFE2L2, Nrf2) mediates exercise-induced mitochondrial biogenesis and the anti-oxidant response in mice, *J. Physiol.*, 594 (2016) 5195-5207
17. K. Nakatani, M. Komatsu, T. Kato, T. Yamanaka, H. Takekura, Habitual exercise induced resistance to oxidative stress, *Free Radical. Res.*, 39 (2005) 905-911,
18. H. Orhan, B. Van Holland, B. Krab, J. Moeken, N.P.Vermeulen, J.H. Meerman, Evaluation of a multiparameter biomarker set for oxidative damage in man: Increased urinary excretion of lipid, protein and DNA oxidation products after one hour of exercise, *Free Radical. Res.*, 38 (2004) 1269-1279.
19. R.J. Bloomer, A.H. Goldfarb, J.M. Mckenzie, Oxidative stress response to aerobic exercise: Comparison of antioxidant supplements, *Med. Sci. Sports Exerc.*, 38 (2006) 1099-1105
20. M. Horie, E. Warabi, S. Komine, S. Oh, J. Shoda, Cytoprotective role of Nrf2 in electrical pulse stimulated C2C12 myotube, *PLoS One.*, 10 (2015) e0144835.
21. P.C.G. Wang, Z. Li, D. Qi, S. Ding, Acute exercise stress promotes Ref/Nrf signaling and increases mitochondrial antioxidant activity in skeletal muscle, *Exp. Physiol.*, 101 (2015) 410-20.
22. A.J. Done, M.J. Gage, N.C. Nieto, T. Traustadottir, Exercise-induced Nrf2-signaling is impaired in aging, *Free Radic. Medic.*,96 (2016) 130-138.
23. M. Narasimhan, J. Hong, N. Atieno, V.R. Muthusamy, C.J. Davidson, N. Abu-Rmaleh, R. Richardson, A.V. Gomes, J.R. Hoidal, N.S. Rajasekaran, Nrf2 deficiency promotes apoptosis and impairs PAX7/MyoD expression in aging skeletal muscle cells, *Free Radic. Biol. Med.*,71 (2014) 402–414.
24. I. Bos, P. De Boever, L. Int Panis, S.Sarren, R. Meeusen, Negative effects of ultrafine particle exposure during forced exercise on the expression of Brain-Derived Neurotrophic Factor in the hippocampus of rats, *Neuroscience*, 223 (2012) 131–139.
25. T. Li, S. He, S.Liu, Z. Kong, J. Wang, Y. Zhang, Effects of different exercise durations on Keap1-Nrf2-ARE pathway activation in mouse skeletal muscle, *Free Radic. Res.*, 49 (2015) 1269-1274.
26. H.A. Scott, J.R. Latham, R. Callister, J.J. Pretto, K. Baines, N. Saltos, J.W. Upham, L.G. Wood, Acute exercise is associated with reduced exhaled nitric oxide in physically inactive adults with asthma, *Ann. Allergy Asthma Immunol.*, 114 (2015) 470-479.
27. F.C. Gomes, L.G. Chuffa, W.R. Scarano, P.F.F. Pinheiro, W.J.Favaro, R.F. Domeniconi, Nandrolone decanoate and resistance exercise training favor the occurrence of lesions and activate the inflammatory response in the ventral prostate, *Andrology*, 4 (2016) 473-480.
28. J. Done Aaron, T. Tinna, Nrf2 mediates redox adaptations to exercise, *Redox. Biol.*, 10 (2016) 191-199.



Facile Synthesis of Two Azete-Steroid Derivatives and Theoretical Evaluation of Its Interaction with the Aromatase Enzyme

İki Azete Steroid Türevinin Basit Sentezi ve Aromataz Enzimi ile Etkileşiminin Teorik Olarak Değerlendirilmesi

Figuroa-Valverde Lauro¹, Diaz-Cedillo Francisco², Rosas-Nexticapa Marcela³, Garcimarero-Espino E. Alejandra⁴, Mateu-Armand Virginia³, Hernandez-Vazquez Patricia³, Benitez-Coeto Laura³, Pool Gómez Eduardo¹, Lopez-Ramos Maria¹, Hau-Heredia-Lenin¹, Borges-Ballote Yaritza¹

¹Laboratory of Pharmaco-Chemistry at the Faculty of Chemical Biological Sciences of the University Autonomous of Campeche, Av. Agustín Melgar s/n, Col Buenavista C.P.24039 Campeche Cam., México.

²Escuela Nacional de Ciencias Biológicas del Instituto Politécnico Nacional. Prol. Carpio y Plan de Ayala s/n Col. Santo Tomas, México.

³Facultad de Nutrición, Universidad Veracruzana. Médicos y Odontólogos s/n, 91010, Xalapa, Veracruz. México.

⁴Facultad de Medicina, Universidad Veracruzana. Médicos y Odontólogos s/n, 91010, Xalapa, Veracruz. México.

ABSTRACT

Several aromatase inhibitors have used for the treatment of breast cancer; however, some of these drugs may produce some side effects such as endometrial cancer and bone loss. The aim of this study was to synthesize two new azete-steroid derivatives (compounds 9 or 10) to evaluate its theoretical interaction with an aromatase enzyme (2wd3) using anastrozole and exemestane as controls in a docking model. The preparation of 9 and 10 was carried out using a series of reactions which involves amination, etherification, nitration, and addition. Chemical structure of the compounds was confirmed using elemental analysis and NMR spectrum. The results showed that compounds 9 or 10 could bind to a different type of aminoacid residues involved in of 2wd3 protein surface compared anastrozole and exemestane; this phenomenon may exert changes in the biological activity of aromatase enzyme. All data suggest that compounds 9 or 10 could be an alternative for the treatment of breast cancer; therefore it could be a good candidate for the pharmaceutical industry.

Key Words

Azete, steroid, derivative, docking model.

Öz

Meme kanserinin tedavisi için birkaç aromataz inhibitörü kullanılmıştır; ancak, bu ilaçların bazıları endometrial kanser ve kemik kaybı gibi bazı yan etkiler yaratabilir. Bu çalışmanın amacı, bir yerleştirme modelinde kontroller olarak anastrozol ve exemestan kullanarak teorik etkileşimini bir aromataz enzimi (2wd3) ile teorik etkileşimini değerlendirmek için iki yeni azete-steroid türevini (bileşik 9 veya 10) sentezlemektir. 9 ve 10'un hazırlanması, aminasyon, eterleştirme, nitrasyon ve ekleme içeren bir dizi reaksiyon kullanılarak gerçekleştirildi. Bileşiklerin kimyasal yapısı element analizi ve NMR spektrumu kullanılarak doğrulandı. Sonuçlar, bileşikler 9 veya 10'un, anastrozol ve exemestan ile karşılaştırıldığında 2wd3 protein yüzeyinde yer alan farklı tipte bir amino asit tortusuna bağlanabileceğini gösterdi; bu fenomen, aromataz enziminin biyolojik aktivitesinde değişiklikler yapabilir. Tüm veriler, bileşik 9 veya 10'un, meme kanseri tedavisinde bir alternatif olabileceğini göstermektedir; bu nedenle ilaç endüstrisi için iyi bir aday olabilir.

Anahtar Kelimeler

Azete, steroid, türev, yerleştirme modeli.

Article History: Received: May 5, 2019; Revised: Jul 15, 2019; Accepted: Sep 10, 2019; Available Online: Nov 1, 2019.

DOI: <https://doi.org/10.15671/hjbc.602183>

Correspondence to: Figuroa-Valverde Lauro, Laboratory of Pharmacochemistry, University Autonomous of Campeche, Mexico.

E-Mail: lauro_1999@yahoo.com

INTRODUCTION

There are studies which indicate that breast cancer is one of the main health problems worldwide [1-4]. It is noteworthy that some drugs have been used to treatment of breast cancer such as tamoxifen (estrogen-receptor antagonist) [5], anastrozole, letrozole or exemestane (aromatase inhibitors) [6-8], fisetin or methyl paraben (17-hydroxy dehydrogenase type 1 inhibitors) [9, 10]; however, some of these drugs may produce some adverse effects such as secondary endometrial cancer [11] and bone loss [12]. In the search of new pharmacological treatment to breast cancer, some drugs have been developed; for example, the asymmetric synthesis of a piperidine derivative via an organocatalytic Michael-Henry reaction with biological activity against breast cancer in vitro [13]. In addition, a study showed the preparation of nimesulide from 2-Amino-5-nitro-phenol as a breast cancer inhibitor using SK-BR-3 cells [14]. Also, a series of dienone-derivatives were synthesized from oridonin which exerted effects against breast cancer in vitro [15]. Other study showed reaction of 4-(dimethyl-amino)benzaldehyde with N-(3-Acetyl-2-hydroxy-phenyl)-acetamide to form 8-Amino-4'-(dimethylamino)flavone and their biological activity against breast cancer on MCF-7 cells [16]. It is important to mention, that some theoretical models have been used to characterize the interaction of drugs with some biomolecules involved in breast cancer; for example, a theoretical analysis showed the interaction plumbagin-hydrazine (breast cancer inhibitor) with NF- κ B (nuclear factor kappa-light-chain-enhancer of activated B cells) using a Docking model [17]. Additionally, other report showed the interaction of tamoxifen, raloxifene, toremifene (breast cancer inhibitors) with estrogen receptor using the HEX-docking software [18]. Other data showed that some estrone derivatives can produce apoptosis of breast cancer cells via carbonic anhydrase IX inhibition using Autodock program [19]. All these data indicate that several drugs could exert effects on breast cancer; however, their interaction with several targets biological is confusing, this phenomenon could be due to the different chemical structures of each drug or to protocols used. Analyzing these data, the aim of this study was to synthesize two azete-steroid derivatives were prepared and their theoretical activity on aromatase enzyme was evaluated using a Docking-Server model.

MATERIALS and METHODS

2.1 General methods

The reagents involved in this investigation were purchased from Sigma-Aldrich Sigma-Aldrich Co., Ltd. The melting point for compounds was determinate using an Electrothermal (900 model). Infrared spectra (IR) were evaluated using i50 FT-IR Nicolet spectrometer.¹H and ¹³C NMR (nuclear magnetic resonance) spectra were determinate with a Varian VXR300/5 FT NMR spectrometer at 300 MHz (megahertz) in CDCl₃ (deuterated chloroform). EIMS (electron impact mass spectroscopy) spectra were evaluated using a Finnigan Trace Gas Chromatography Polaris Q-Spectrometer. Elementary analysis data were evaluated from a Perkin Elmer Ser. II CHNS/O2400 elemental analyzer.

Chemical Synthesis

Amination

In a round bottom flask (10ml), 2-nitroestrone or 2-nitroestradiol (0.50 mmol), 3-Ethynylaniline (60 μ l 0.53 mmol) and 5 ml of formaldehyde were stirred to reflux for 12h. The mixture was purified via a crystallization using the methanol:water (4:1) system.

4-[[3-Ethynyl-phenylamino)-methyl]-3-hydroxy-13-methyl-2-nitro-6,7,8,9,11,12,13,14,15,16-decahydro-cyclopenta[a]phenanthren-17-one (3)

yielding 44% of product; m.p. 43-45°C; IR (vmax, cm⁻¹) 3402, 3312, 2102, 1712 and 1352: ¹H NMR (300 MHz, Chloroform-d) δ_{H} : 0.93 (s, 3H), 1.20-1.90 (m, 7H), 2.12-2.50 (7H), 2.82 (s, 1H), 3.01 (m, 1H), 4.40 (m, 2H), 6.56-7.12 (m, 4H), 7.16 (m, 1H), 9.10 (broad, 2H) ppm. ¹³C NMR (300 Hz, CDCl₃) δ_{C} : 13.9, 21.6, 25.4, 27.4, 28.0, 30.8, 34.6, 37.2, 42.3, 47.9, 48.4, 50.4, 78.2, 84.0, 113.1, 122.5, 122.7, 123.5, 125.0, 125.0, 129.8, 134.3, 136.6, 145.4, 146.7, 147.1, 219.8 ppm. EI-MS m/z: 444.53. Anal. Calcd. for C₂₇H₂₈N₂O₄: C, 72.95; H, 6.35; N, 6.30; O, 14.40. Found: C, 72.90; H, 6.28.

4-[[3-Ethynyl-phenylamino)-methyl]-13-me- thyl-2-nitro-7,8,9,11,12,13,14,15,16,17-deca- hydro-6H-cyclopenta[a]phenanthrene-3,17-diol (4)

yielding 56% of product; m.p. 58-60°C; IR (vmax, cm⁻¹) 3400, 3310, 2102 and 1350: ¹H NMR (300 MHz, Chloroform-d) δ_{H} : 0.64 (s, 3H), 0.80-1.86 (m, 11H), 2.12-2.52 (m, 3H), 2.84 (s, 1H), 2.94-3.64 (m, 2H), 4.40 (m, 2H), 6.62-7.10 (m, 4H), 7.64 (m, 1H), 8.20 (broad, 3H) ppm. ¹³C NMR (300 Hz, CDCl₃) δ_{C} : 15.8, 24.2, 25.3, 27.7, 28.0,

32.7, 33.7, 37.2, 42.3, 44.4, 45.1, 50.7, 78.2, 82.4, 84.01, 113.1, 122.4, 122.7, 123.5, 125.0, 125.3, 129.8, 134.8, 136.6, 145.4, 147.0, 147.1 ppm. EI-MS m/z: 446.22. Anal. Calcd. for $C_{27}H_{30}N_2O_4$: C, 72.62; H, 6.77; N, 6.27; O, 14.33. Found: C, 72.58; H, 6.70.

Etherification

In a round bottom flask (10ml), compounds 3 or 4 (0.50 mmol), potassium carbonate (60 mg, 0.43) 5 ml of dimethyl sulfoxide were stirred to reflux for 6h. The solvent of mixture was reduced pressure and purified via a crystallization using the methanol:water (4:1) system.

4-[(3-Ethynyl-phenylamino)-methyl]-13-methyl-6,7,8,9,11,12,13,14,15,16-decahydro-20-oxa-cyclopropa[2,3]cyclopenta[a]phenanthren-17-one (5)

yielding 38% of product; m.p. 76-78°C; IR (vmax, cm^{-1}) 3310, 2104, 1712 and 1242: 1H NMR (300 MHz, Chloroform-d) δ_H : 0.90 (s, 3H), 1.20-1.92 (m, 7H), 2.12-2.54 (m, 8H), 2.88 (s, 1H), 4.48 (m, 2H), 4.73 (broad, 1H), 6.22 (m, 1H), 6.62-7.16 (m, 4H) ppm. 13.8, 21.7, 25.7, 27.4, 28.0, 31.3, 35.1, 37.5, 38.3, 47.4, 48.2, 50.5, 78.2, 84.0, 109.8, 113.1, 118.3, 122.5, 122.7, 125.0, 129.8, 131.9, 133.1, 143.6, 147.4, 148.5, 220.7 ppm. EI-MS m/z: 397.20. Anal. Calcd. for $C_{27}H_{27}NO_2$: C, 81.58; H, 6.85; N, 3.52; O, 8.05. Found: C, 81.50; H, 6.80.

4-[(3-Ethynyl-phenylamino)-methyl]-13-methyl-6,8,9,11,12,13,14,15,16,17-decahydro-7H-20-oxa-cyclopropa[2,3]cyclopenta[a]phenanthren-17-ol (6)

yielding 45% of product; m.p. 84-86°C; IR (vmax, cm^{-1}) 3400, 3312, 2102 and 1240: 1H NMR (300 MHz, Chloroform-d) δ_H : 0.76 (s, 3H), 0.82-1.88 (m, 11H), 2.12-2.54 (m, 4H), 2.88 (s, 1H), 3.64 (m, 1H), 4.48 (m, 2H), 5.58 (broad, 2H), 6.16 (m, 1H), 6.62-7.16 (m, 4H) ppm. 15.8, 24.2, 25.3, 27.7, 28.0, 32.7, 33.7, 37.2, 38.3, 44.4, 44.6, 50.7, 78.2, 82.4, 84.0, 110.2, 113.1, 118.3, 122.5, 122.7, 125.0, 129.8, 132.3, 133.5, 143.6, 147.4, 148.5 ppm. EI-MS m/z: 399.21. Anal. Calcd. for $C_{27}H_{29}NO_2$: C, 81.17; H, 7.32; N, 3.51; O, 8.01. Found: C, 81.12; H, 7.30.

Nitration

In a round bottom flask (10ml), compounds 5 or 6 (0.50 mmol), 5 ml of anhydride acetic and 1 ml of nitric acid were stirred to reflux for 6h. The solvent of mixture was reduced pressure and purified via a crystallization using the methanol:hexane:water (4:2:1) system.

4-[(3-Ethynyl-2,4,5,6-tetranitro-phenylamino)-methyl]-13-methyl-1-nitro-6,7,8,9,11,12,13,14,15,16-decahydro-20-oxa-cyclopropa[2,3]cyclopenta[a]phenanthren-17-one (7)

yielding 66% of product; m.p. 122-124°C; IR (vmax, cm^{-1}) 3312, 1244, 1712 and 1352: 1H NMR (300 MHz, Chloroform-d) δ_H : 0.92 (s, 3H), 1.20-1.91 (m, 7H), 2.12-3.00 (m, 15H), 3.90 (s, 1H), 4.84 (m, 2H), 9.92 (broad, 1H) ppm. ^{13}C NMR (300 Hz, $CDCl_3$) δ_C : 13.8, 21.7, 27.4, 28.1, 30.0, 31.3, 35.3, 37.7, 42.3, 45.2, 48.1, 50.2, 71.0, 79.7, 115.2, 125.1, 126.2, 128.5, 130.2, 132.5, 134.4, 135.1, 136.3, 136.5, 141.9, 142.3, 220.3 ppm. EI-MS m/z: 622.12. Anal. Calcd. for $C_{27}H_{22}N_6O_{12}$: C, 52.09; H, 3.56; N, 13.50; O, 30.84. Found: C, 52.00; H, 3.50.

4-[(3-Ethynyl-2,4,5,6-tetranitro-phenylamino)-methyl]-13-methyl-1-nitro-6,8,9,11,12,13,14,15,16,17-decahydro-7H-20-oxa-cyclopropa[2,3]cyclopenta[a]phenanthren-17-ol (8)

yielding 58% of product; m.p. 135-137°C; IR (vmax, cm^{-1}) 3400, 3312, 2102, 1350 and 1242: 1H NMR (300 MHz, Chloroform-d) δ_H : 0.78 (s, 3H), 0.80-1.86 (m, 9H), 2.22-3.64 (m, 7H), 3.92 (s, 1H), 4.82 (m, 2H), 8.12 (broad, 2H), 6.62-7.12 (m, 4H) ppm. ^{13}C NMR (300 Hz, $CDCl_3$) δ_C : 15.8, 24.2, 27.6, 27.7, 30.0, 32.8, 33.7, 37.6, 42.3, 44.3, 50.7, 71.0, 79.70, 82.4, 115.2, 125.1, 126.2, 129.0, 130.6, 132.5, 134.8, 135.12, 136.3, 136.5, 141.9, 142.3 ppm. EI-MS m/z: 624.14. Anal. Calcd. for $C_{27}H_{24}N_6O_{12}$: C, 51.93; H, 3.87; N, 13.46; O, 30.74. Found: C, 51.88; H, 3.80.

Synthesis of azete derivatives

In a round bottom flask (10ml), compounds 7 or 8 (0.50 mmol), 4-Nitrophenylacetone nitrile (85 mg, 0.52 mmol), CopperII chloride anhydrous (67 mg, 0.50 mmol) and 5 ml of methanol were stirred to room temperature for 48h. The solvent of mixture was reduced pressure and purified via a crystallization using the methanol:hexane:water (4:2:1) system;

13-Methyl-1-nitro-4-[(2,3,4,6-tetranitro-5-[2-(4-nitro-benzyl)-azet-3-yl]-phenylamino)-methyl]-6,7,8,9,11,12,13,14,15,16-decahydro-20-oxa-cyclopropa[2,3]cyclopenta[a]phenanthren-17-one (9)

yielding 72% of product; m.p. 156-158°C; IR (vmax, cm^{-1}) 3312, 1712, 1350 and 1154: 1H NMR (300 MHz, Chloroform-d) δ_H : 0.92 (s, 3H), 1.20-1.91 (m, 7H), 2.12-3.00 (m, 8H), 3.77 (m, 2H), 4.82 (broad, 1H), 5.70 (s, 1H),

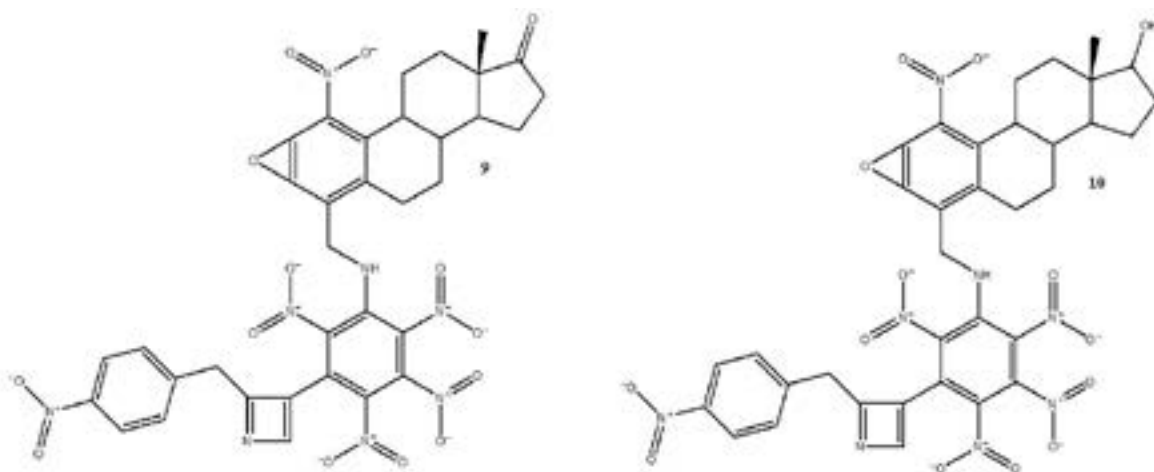


Figure 1. Chemical structure of two azete-steroid derivatives (9 and 10).

7.33-7.92 (m 4H), 9.32 (broad, 1H) ppm. ^{13}C NMR (300 Hz, CDCl_3) δ_c : 13.8, 21.7, 27.4, 28.1, 30.0, 31.3, 35.3, 37.7, 42.3, 44.5, 45.2, 48.1, 50.2, 78.2, 112.6, 114.4, 117.8, 124.1, 124.6, 125.7, 126.0, 128.1, 128.6, 130.2, 130.3, 133.7, 134.4, 135.7, 135.8, 136.3, 137.4, 138.3, 142.0, 146.6, 179.2, 220.3 ppm. EI-MS m/z : 784.17. Anal. Calcd. for $\text{C}_{35}\text{H}_{28}\text{N}_8\text{O}_{14}$: C, 53.58; H, 3.60; N, 14.28; O, 28.55. Found: C, 53.50; H, 3.54.

13-Methyl-1-nitro-4-((2,3,4,6-tetranitro-5-[2-(4-nitro-benzyl)-azet-3-yl]-phenylamino)-methyl)-6,8,9,11,12,13,14,15,16,17-decahydro-7H-20-oxa-cyclopropa[2,3]cyclopenta [a]phenanthren-17-ol (10) yielding 68% of product; m.p. 172-174°C; IR (ν_{max} , cm^{-1}) 3400, 3312, 1352 and 1154; ^1H NMR (300 MHz, Chloroform- d) δ_H : 0.78 (s, 3H), 0.80-1.86 (m, 9H), 2.20-3.62 (m, 7H), 3.77 (m, 2H), 4.82 (broad, 1H), 5.70 (s, 1H), 7.33 (m, 2H), 7.86 (broad, 2H), 7.92 (m 2H) ppm. ^{13}C NMR

(300 Hz, CDCl_3) δ_c : 15.8, 24.2, 27.7, 30.0, 32.7, 33.7, 37.7, 42.3, 42.3, 44.4, 44.5, 50.7, 82.4, 117.8, 124.1, 124.6, 125.7, 126.0, 128.1, 128.9, 130.2, 130.6, 133.7, 134.8, 135.7, 135.8, 136.3, 137.4, 138.3, 142.0, 146.6, 179.2 ppm. EI-MS m/z : 786.18. Anal. Calcd. for $\text{C}_{35}\text{H}_{30}\text{N}_8\text{O}_{14}$: C, 53.44; H, 3.84; N, 14.24; O, 28.47. Found: C, 53.38; H, 3.80.

2.3 Physicochemical parameters evaluation

Some electronic parameters such as HOMO (Highest Occupied Molecular Orbital), LUMO (Lowest Unoccupied Molecular Orbital) energy, orbital coefficients distribution, molecular dipole moment and HBD (hydrogen bond donor groups) and HBA (hydrogen bond acceptor groups) and PSA (polar surface area) were evaluated using the SPARTAN'06 software [20].

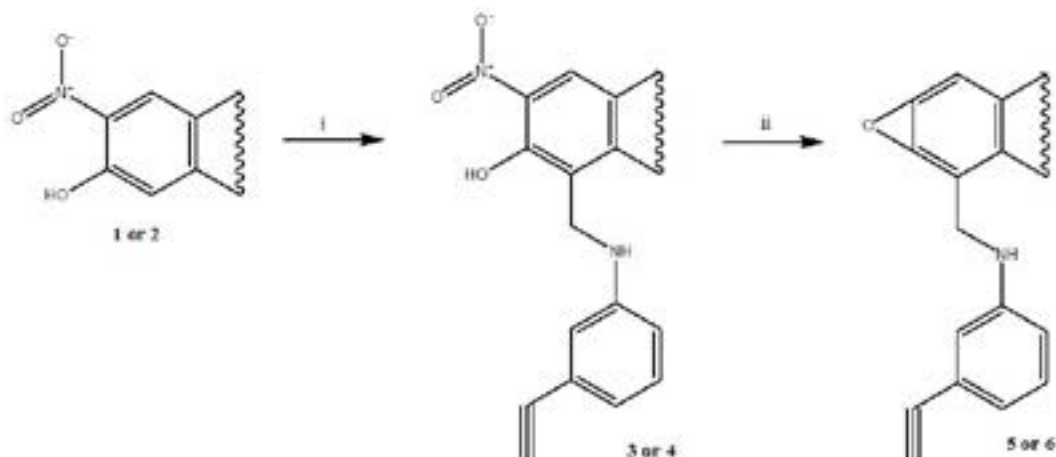


Figure 2. Synthesis of two ether-steroid derivatives (5 or 6). Reaction of 2-Nitroestrone (1) or 2-Nitroestradiol (2) with 3-Ethynylaniline (i) to form 4-[(3-Ethynyl-phenylamino)-steroid-17-one (3) or 4-[(3-Ethynyl-phenylamino)-steroid-3,17-diol (4). Then, the compound 5 or 6 were prepared via intramolecular displacement of nitrile group involved in the chemical structure from 3 or 4. ii = dimethyl sulfoxide.

Pharmacophore evaluation

The 3D pharmacophore model for the compounds 6 and 7 was determinate using LigandScout 4.08 software [21]

2.5 Theoretical evaluation of the interaction between compounds 9 or 10 and aromatase enzyme.

The interaction of compound 4 with aromatase enzyme (2wd3) [22] was carried out using a DockingServer [23].

RESULTS and DISCUSSION

In this study were prepared two azete-steroid derivatives (Figure 1) from 2-nitroestrone (compound 1) or 2-nitroestradiol (compound 2) using some chemical strategies.

The first stage was achieved for the synthesis of three amino steroids; it is important to mention that several methods have been used to synthesis some amino-steroid derivatives for example, the preparation of 17- α -amino steroids using a ω -transaminase enzyme from *Arthrobacter* sp [23]. Other studies showed the synthesis of amino-steroids through a nitro-steroids derivatives reduction [24]. Also, a report showed an amination of steroids using palladium as catalyst [25]. Other data showed the synthesis of some amino-steroid derivatives via Mannich reaction; it is noteworthy that structural chemistry of these compounds [26] involves an activated methyl group in ring A.

In this study, the reactivity of the hydrogen atom involved in ring A (C-4) of both compounds 1 or 2 was

evaluated using the Mannich reaction. Therefore, 1 or 2 reacted with 3-ethynyl-aniline in presence of formaldehyde (Figure 2) to form the amino-steroid derivatives (compounds 3 and 4). The results of ^1H NMR spectrum for 3 showed several signals at 0.93 ppm for methyl group bound to steroid nucleus; at 1.20-2.50, 3.01 and 7.16 ppm for steroid moiety; at 2.82 ppm for alkyne group; at 4.40 for methylene bound to both amino group and ring A; at 6.56-7.12 ppm for phenyl group; at 9.10 ppm for both hydroxyl and amino groups. The ^{13}C NMR showed several signals at 13.9 ppm for methyl group bound to steroid nucleus; at 21.6-37.2, 47.9-50.4, 123.5-125.0 and 134.3-146.7 ppm for steroid moiety; at 42.34 ppm for methylene group bound to both amino group and ring A; at 78.2-84.0 ppm for alkyne group; at 113.1-122.7, 125.0-129.8 and 147.1 ppm for phenyl group; at 219.8 ppm for ketone group. Finally, the mass spectrum from 3 showed a molecular ion (m/z) 444.53.

Other results showed several signals involved in the ^1H NMR spectrum for 4 at 0.64 ppm for methyl group; at 0.80-2.52, 2.94-3.64 and 7.64 ppm for steroid moiety; at 2.84 ppm for alkyne group; at 4.40 ppm for methylene bound to amino group and ring A; at 6.62-7.10 for phenyl group; at 8.20 ppm for both hydroxyl and amino groups. The ^{13}C NMR showed several signals at 13.8 ppm for methyl bound to steroid nucleus; at 24.2-37.2, 44.2-50.7, 86.4, 123.5, 125.3, 134.8-145.4 and 147.1 ppm for steroid moiety; at 42.3 ppm for methylene bound to amino group and ring A; at 78.2-84.0 ppm for alkyne group; at 113.1-122.7, 125.00, 129.8 and 147.0 ppm for phenyl group; at 220.3 ppm for ketone group.

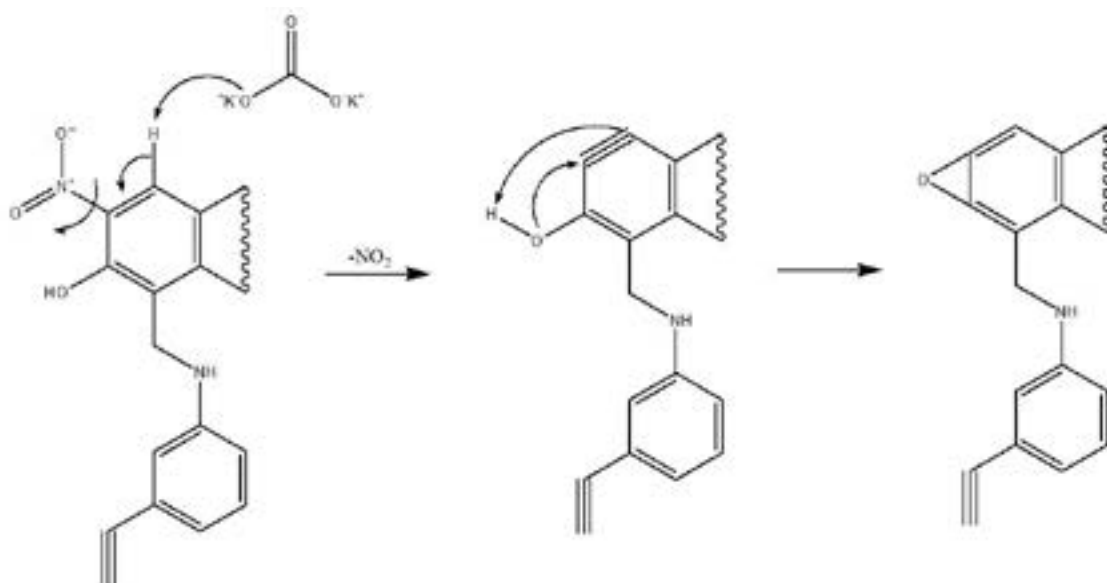


Figure 3. Reaction mechanism of synthesis of compounds 5 or 6.

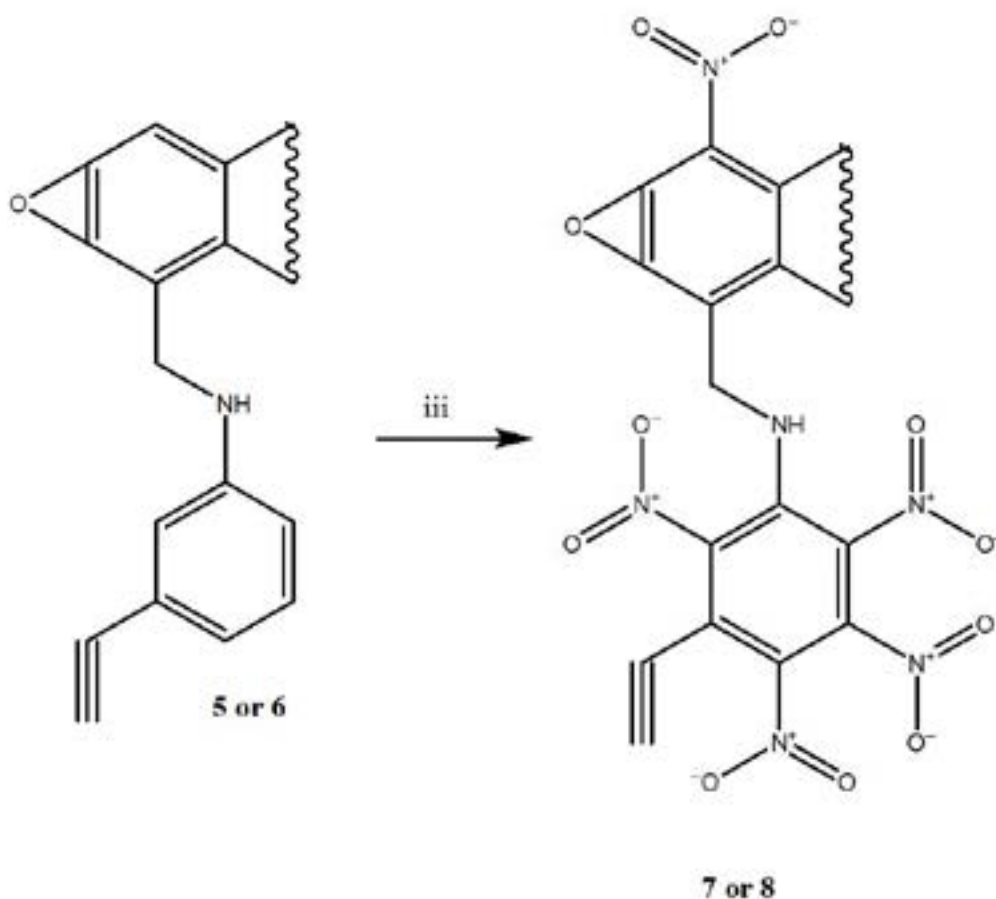


Figure 4. Synthesis of two tetranitro-phenylamino-1-nitro-steroid derivatives (7 or 8). Nitration of two ether-steroid derivatives (5 or 6) with HNO₃/(CH₃CO)₂O (iii) to form 7 or 8.

In addition, the mass spectrum from 4 showed a molecular ion (*m/z*) 446.22.

Etherification of 3 or 4

Several studies showed the preparation of ether groups using some reagents such as (E)-alk-2-en-ol [27], CuCl [28], Cu(AcO)₂ [29], PhCOOH [30]. In addition, there are some methods to the synthesis of ether groups, via displacement of nitro groups using dipolar aprotic solvents [31]. Analyzing these data, in this study, two ether-steroid derivatives (compound 5 or 6) were prepared using a previously method reported via intramolecular displacement of the nitro group from compounds 3 and 4 in the presence of dimethyl sulfoxide (Figure 2). In addition, the formation of 5 or 6 involves an cyclohexa-1,3-dien-5-yne as intermediary (Figure 3).

The results of ¹H NMR spectrum for 5 showed several signals at 0.90 ppm for methyl group bound to steroid nucleus; at 1.20-2.54 and 6.22 ppm for steroid moiety; at 4.48

ppm for methylene group bound to both amino and A-ring of steroid; at 2.88 ppm for alkyne group; at 4.73 ppm for amino group; at 6.62-7.16 ppm for phenyl group. The ¹³C NMR displayed several signals at 13.8 ppm for methyl group bound to steroid nucleus; at 21.7-35.7, 47.4-50.5, 109.8, 118.3 and 131.9-147.4 ppm for steroid moiety; at 38.44 ppm for methylene bound to both amino and A-ring; at 78.2-84.0 ppm for alkyne group; at 113.1, 122.5-129.8 and 148.5 ppm for phenyl group; at 220.70 for ketone group. Finally, the mass spectrum from 5 showed a molecular ion (*m/z*) 397.20.

Other results showed several signals involved in the ¹H NMR spectrum for 6 at 0.76 ppm for methyl group bound to steroid nucleus; at 0.82-2.54, 3.64 and 6.16 ppm for steroid moiety; at 2.88 ppm for alkyne group; at 4.48 ppm for methylene bound to both amino and A-ring; at 5.58 ppm for both hydroxyl and amino groups; at 6.62-7.16 ppm for phenyl group. The ¹³C NMR showed several signals at 15.82 ppm for methyl group bound to steroid nucleus; at

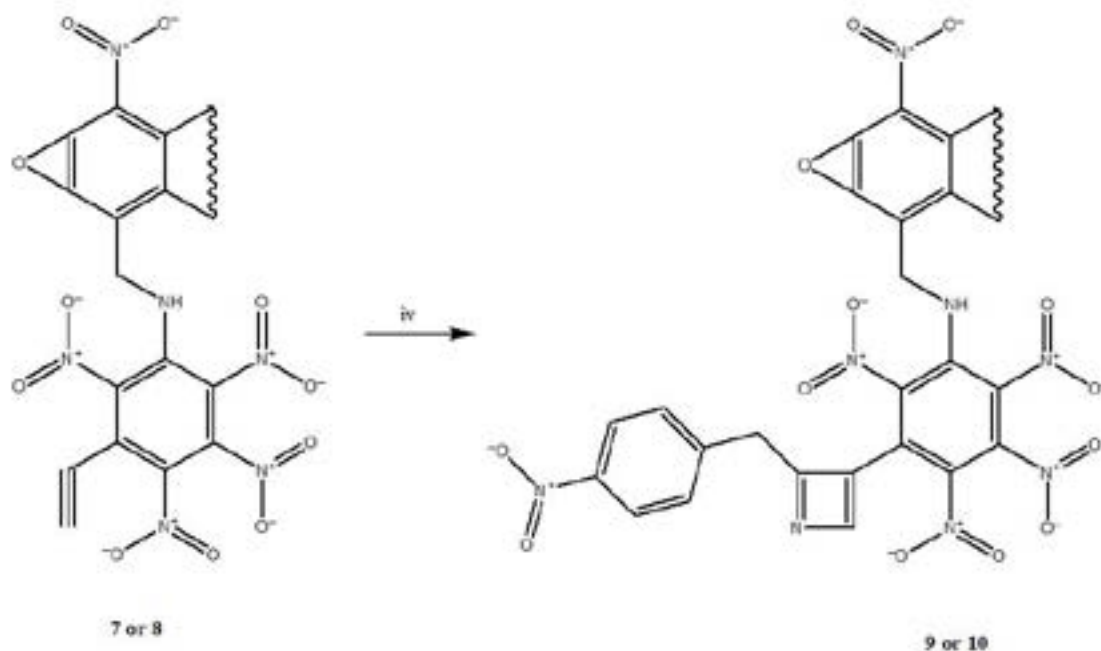


Figure 5. Preparation of two azete-steroid derivatives (9 or 10). Reaction of 7 or 8 with 4-Nitrophenylacetonitrile to form 9 or 10 using CopperII (iv) as catalyst.

24.2-37.2, 44.4-50.7, 82.4, 110.2, 118.3 and 132.3-147.4 ppm for steroid moiety; at 38.4 ppm for methylene bound to both amino group and A-ring; at 78.21 and 84.00 for alkyne group; at 113.14, 122.5-129.8 and 148.5 ppm for phenyl group. Additionally, the mass spectrum from 6 showed a molecular ion (m/z) 399.21.

Nitration of 5 or 6

There are several reports in the literature for preparation of nitro derivatives using some reagents such as WO_3/ZrO_2 [32], NO_2 [33], $\text{HNO}_3/\text{montmorillonite}$ [34], NH_4NO_3 and $(\text{CF}_3\text{CO})_2\text{O}$ [35], BF_3 [36], $\text{HNO}_3/\text{H}_2\text{SO}_4$ [37] and others. In this study, compounds 7 or 8 (Figure 4) were prepared through nitration of phenyl groups involved in the chemical structure of 5 or 6 with $\text{HNO}_3/(\text{CH}_3\text{CO})_2\text{O}$. The ^1H NMR spectrum for 7 showed several signals at 0.92 ppm for methyl group bound to steroid nucleus; at 1.20-3.00 ppm for steroid moiety; at 3.90 ppm for alkyne group; at 4.84 ppm for methylene bound to both amino and phenyl groups; at 9.92 ppm for amino group. The ^{13}C NMR displayed several signals at 13.8 ppm for methyl group bound to steroid nucleus; at 21.7-37.7, 45.2-50.2, 126.2-130.2, 134.4, 136.3 and 141.9 ppm for steroid moiety; at 42.3 ppm for methylene bound to both amino and phenyl groups; at 71.0-79.7 ppm for alkyne group; at 115.2-125.1, 132.5, 135.1, 136.5 and 142.3 ppm for phenyl group; at 220.30 ppm for ketone group. Finally, the mass spectrum from 7 showed a molecular ion (m/z) 622.12.

Other results showed several signals involved in the ^1H NMR spectrum for 8 at 0.78 ppm for methyl group bound to steroid nucleus; at 0.80-3.64 ppm for steroid moiety; at 3.92 ppm for alkyne group; at 4.82 ppm for methylene bound to both amino and phenyl groups; at 8.12 ppm for both hydroxyl and amino groups. The ^{13}C NMR showed several signals at 15.8 ppm for methyl group; at 24.2-37.6, 44.3-50.7, 82.4, 126.2-130.6, 134.8, 136.3 and 141.9 ppm for steroid moiety; at 42.3 ppm for methylene bound to both amino and phenyl groups; at 71.0-79.7 ppm for alkyne group; at 115.2-125.2, 132.5, 135.1, 136.5 and 142.3 ppm for phenyl groups. Additionally, the mass spectrum from 8 showed a molecular ion (m/z) 624.14.

Formation of Azete Derivatives (compound 9 or 10)

Several oxazete-derivatives have been synthesized using some reagents such as mesitronitrile oxide [38], α,α -bis(alkylthio) oxime [39], acylisothiocyanate [40] and others. In this investigation, two azete derivatives were prepared via reaction 2 + 2 addition of compounds 7 or 8 and 1-Nitro-4-prop-2-ynyl-benzene using CopperII chloride as catalyst (Figures 5 and 6).

The ^1H NMR spectrum for 9 (Figure 7) at 0.92 ppm for methyl group bound to steroid nucleus; at 1.20-3.00 ppm for steroid moiety; at 3.77 ppm for methylene bound to both phenyl group and azete ring; at 4.82 ppm for methylene

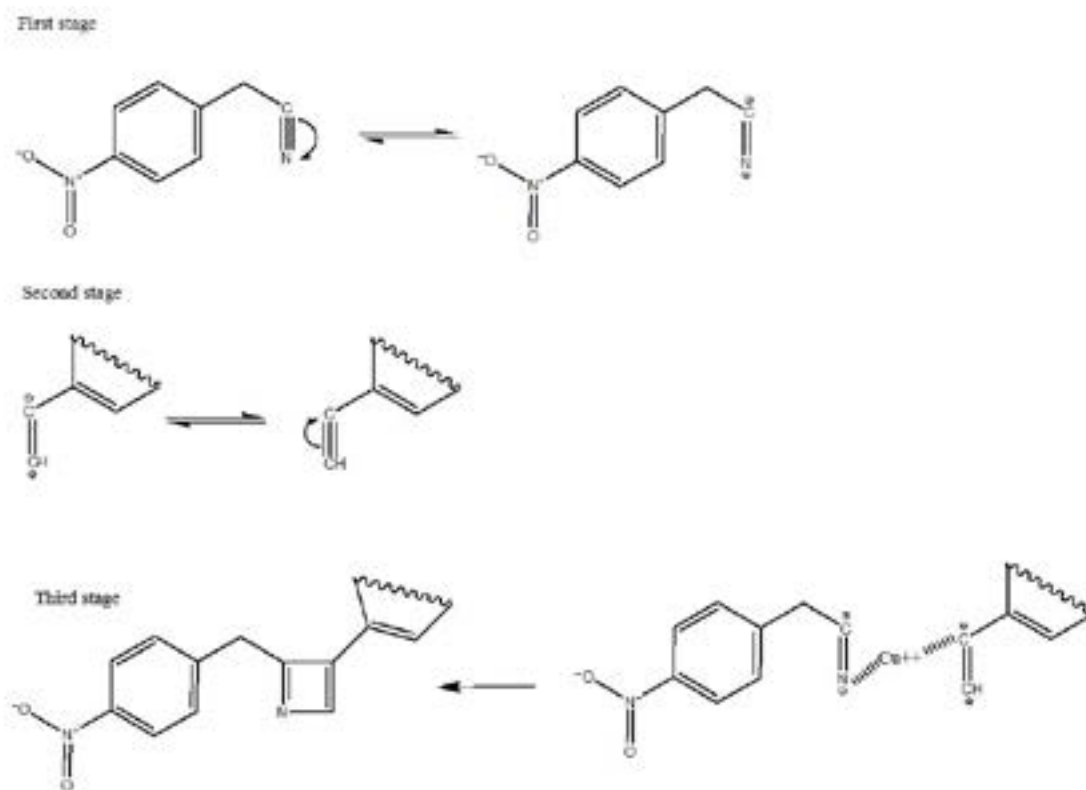


Figure 6. Reaction mechanism of synthesis of compounds 9 or 10.

bound to both amino and phenyl group; at 5.70 ppm for azete ring; at 7.33-7.92 ppm for phenyl group; at 9.32 for amino group.

The ^{13}C NMR displayed several signals at 13.8 ppm for methyl group; at 21.7-37.7, 45.2-50.2, 124.1, 128.6, 130.3, 134.4, 136.3 and 142.0 ppm for steroid moiety; at 42.3 ppm for methylene bound to both phenyl and amino groups; at 44.5 ppm for methylene bound to phenyl group and azete ring; at 117.8, 138.3 and 179.2 ppm for azete ring; at 124.6-128.1, 130.2, 133.7, 135.7-135.8, 137.4 and 146.6 ppm for phenyl groups; at 220.30 for ketone group. Additionally, the mass spectrum from 9 showed a molecular ion (m/z) 784.17.

Finally, the ^1H NMR spectrum for 10 (Figure 8) showed several signals at 0.78 ppm for methyl group bound to steroid nucleus; at 0.80-3.62 ppm for steroid moiety; at 3.77 ppm for methylene bound to both phenyl group and azete ring; at 4.82 ppm for methylene bound to both amino and phenyl groups; at 5.70 ppm for azete ring; at 7.36 and 7.92 ppm for phenyl group; at 7.86 ppm for both hydroxyl and amino groups.

The ^{13}C NMR showed several signals at 15.8 ppm for methyl group; at 24.2-37.7, 42.3-44.4, 50.7-82.4, 128.9, 130.6, 134.8, 136.3 and 142.0 ppm for steroid moiety; at 42.3 ppm for methylene bound to both amino and phenyl groups; at 44.5 ppm for methylene bound to both phenyl group and azete ring; at 117.8, 138.32 and 179.2 ppm for azete ring; at 124.1-128.1, 130.2, 133.7, 135.8, 137.4 and 146.6 ppm for phenyl groups. Additionally, the mass spectrum from 10 showed a molecular ion (m/z) 786.18.

Electronic Parameters

There are some studies which indicate that molecular orbitals and frontier electron density are used to predict the most reactive position in some electron system on several types of reactions [41, 42]. These studies suggest that values of highest occupied molecular orbital (HOMO), lowest unoccupied molecular orbital (LUMO) and their energy gap reflect the chemical activity of a molecule [43].

Here, it is important to mention, that, some methods have been developed to evaluate the relation between HOMO and LUMO with biological activity of some

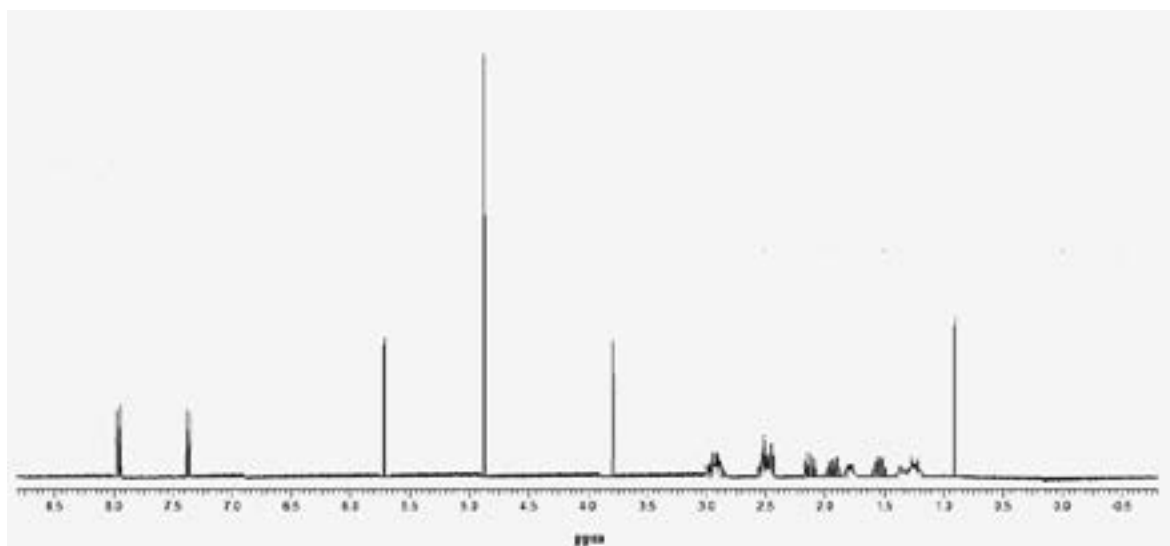


Figure 7. The scheme showed ^1H NMR spectrum from compound 9. The spectrum was analyzed with a Varian VXR300/5 FT NMR apparatus at 300 MHz in CDCl_3 . Axis abscissa (ppm). ppm = parts per million.

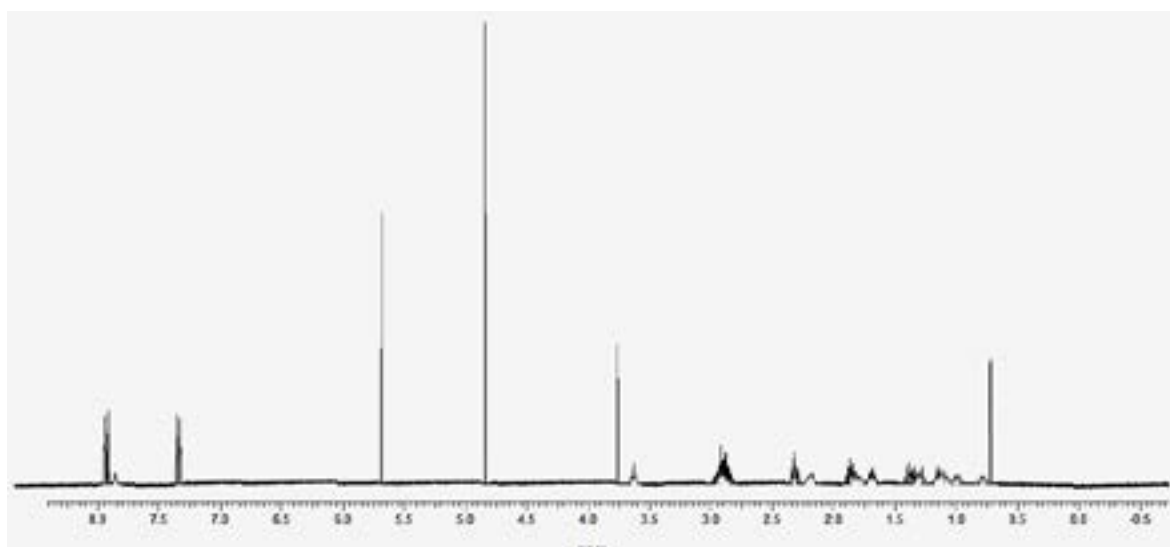


Figure 8. The scheme showed ^1H NMR spectrum from compound 10. The spectrum was analyzed with a Varian VXR300/5 FT NMR apparatus at 300 MHz in CDCl_3 . Axis abscissa (ppm). ppm = parts per million.

Table 1. Physicochemical parameters involve in the structure of compounds 9 and 10.

Parameters	C-9	C-10
Polarizability (cm^3)	93.12	93.52
PSA \AA^2	240.23	244.82
LogP	-1.38	-1.87
Energy (au)	-2605.54	-2606.72
HBD	1	2
HBA	19	19
HOMO (eV)	-8.46	-8.49
LUMO (eV)	-1.68	-1.66

HBD (hydrogen bond donors); HBA (hydrogen bond acceptors); PSA (polar surface area).

compounds; for example, there are some data which showed the evaluation of the frontier molecular orbitals (HOMO-LUMO gap) from some steroid using MIINDO and ZINDO models [44, 45]. In this study, the Hartree-Fock method (method of approximation for the determination of the wave function and the energy of a quantum many-body system in a stationary state) was used to determine both HOMO and LUMO orbitals (Figure 9 and Table 1) in Spartan'06 V112 program [46].

The results showed changes in both HOMO and LUMO values for the compound 9 compared with 10; this phenomenon could be conditioned by the difference in π orbitals density that is located in chemical structure 9 and 10.

Pharmacophore Ligand Model

For several years, some chemical models have been used to determine the three-dimensional orientation adopted by the functional groups of a molecule to predict its interaction with several biomolecules [46]; for example, the use of a pharmacophore model which can furnish a new insight to design novel molecules that can

enhance or inhibit the function of a biological target which can be useful in new drug discovery. Analyzing this premise in this study, the LigandScout software [47] was used to develop a pharmacophore model for compounds 9 and 10 (Figure 10).

The results showed that functional groups involved in the compounds 9 and 10 could interact via hydrophobic contacts or as hydrogen bond acceptors or as hydrogen bond donor with some biomolecules.

Interaction Theoretical (Protein-Ligand)

Analyzing the hypothesis mentioned above and some reports which suggest that the formation of binary complexes between some compounds that act as ligands with several target biomolecules could induce changes in many activities of some biological systems [48-53]; Therefore, in this study, was carried out a theoretical analysis on the interaction of both compound 9 or 10 with Dwd3 protein using exemestane and anastrozole (aromatase inhibitors) [54] as a control in a Doc-

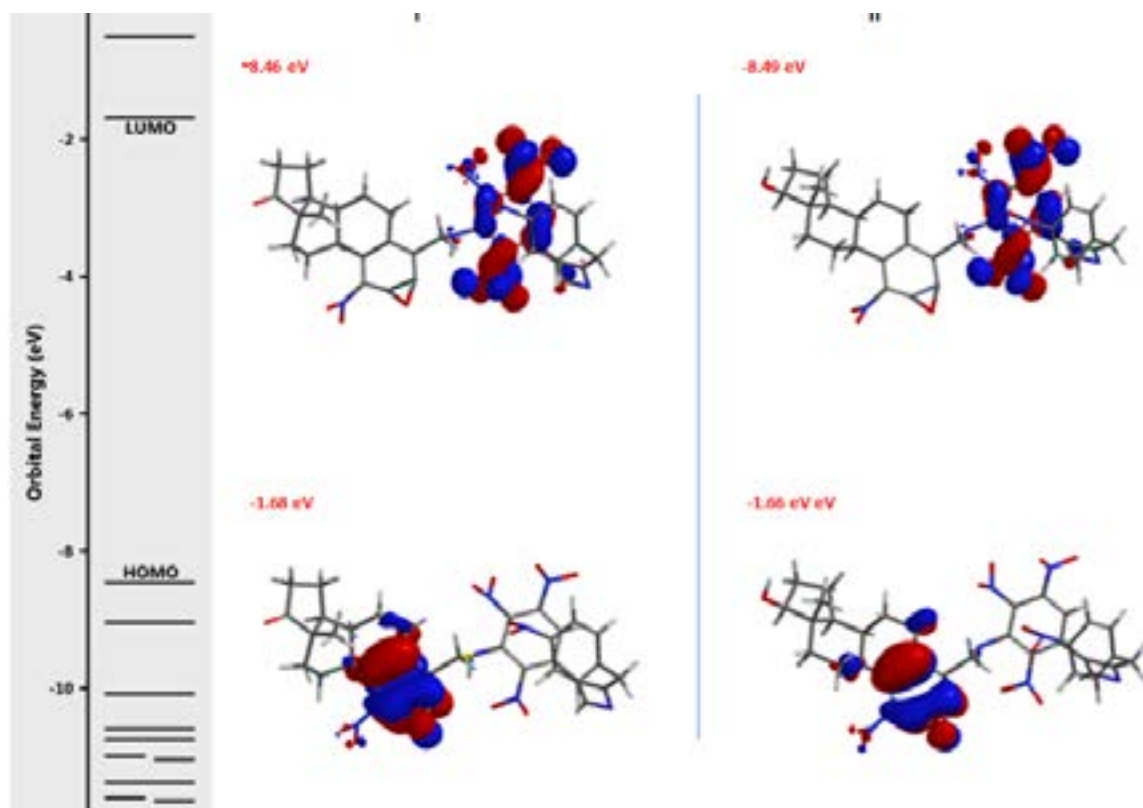


Figure 9. Molecular orbitals (HOMO and LUMO) involved in the compounds 9 (I) and 10 (II). Visualized with SPARTAN'06 software

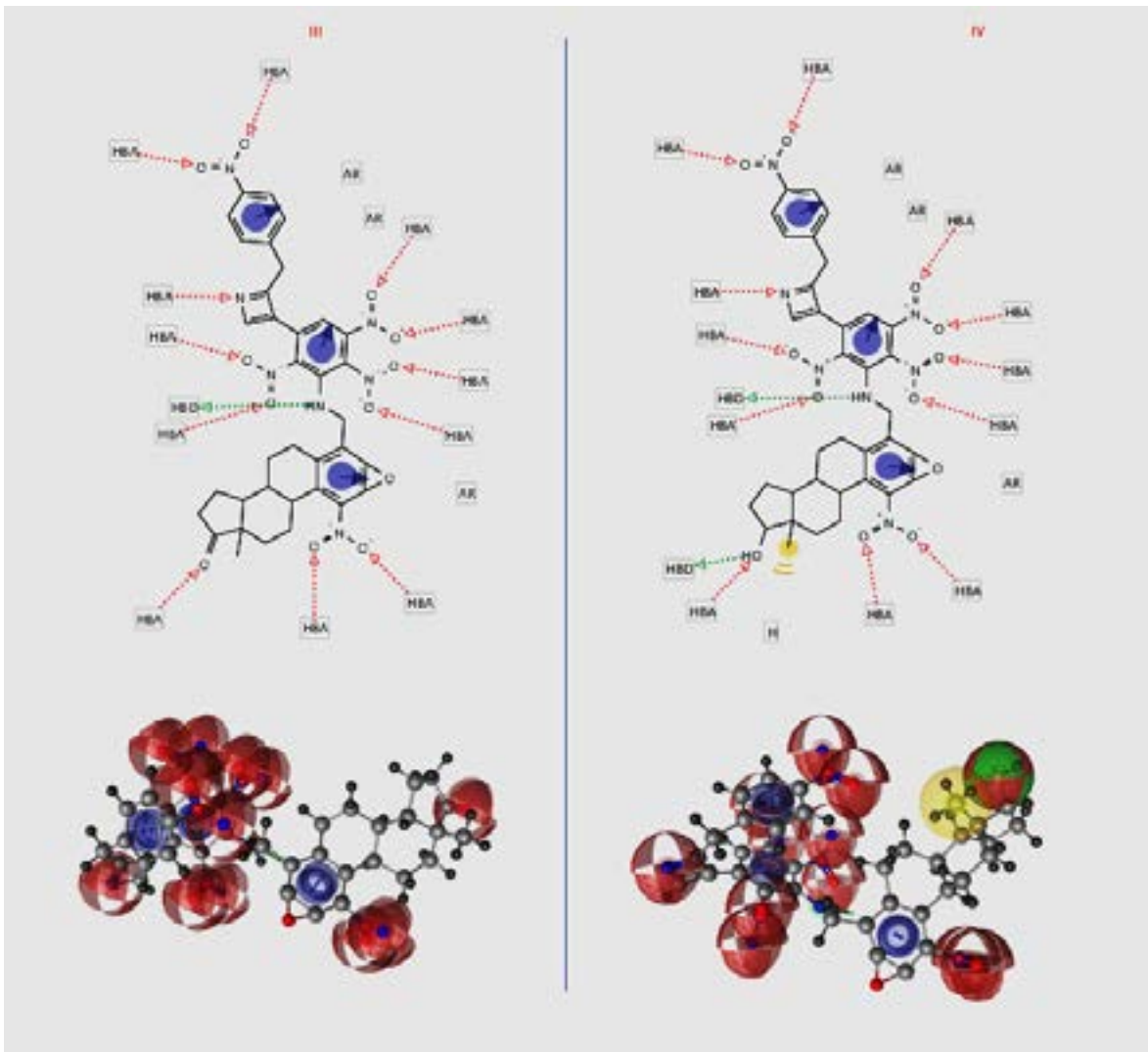


Figure 10. Theoretical pharmacophore from both compounds 9 (III) and 10 (IV) using the LigandScout software. The model involves a methyl group (yellow) hydrogen bond acceptors (HBA, red) and hydrogen bond donor (HBD, green).

kingServer [23]; here, it is important to mention that Dockingserver was used because we believe that it is one of the most complete to analyze the protein-drug interaction.

The data (Table 2) showed differences in the interaction of both compounds 9 and 10 with some aminoacid residues involved in 2wd3 protein surface. In addition, other data suggest that there is another type of aminoacid residues in the interaction of both exemestane and anastrozole with 2Wd3. This phenomenon could be conditioned by the different conformations adopted by both compound 9 and 10 or the length of bound between the steroid-derivatives and the aminoacid residues involved in 2Wd3 protein surface. However, it is impor-

tant to mention that some reports suggest that other thermodynamic factors such as free energy of binding, electrostatic energy, total intermolecular energy and Van der Waals (vdW) + hydrogen bond (Hbond) + desolvation energy can be involved in the interaction of several compounds with the proteins or enzymes [25, 26].

Thermodynamic Parameters

Analyzing the hypothesis above mentioned, in this study, some thermodynamic parameters were determinate using DockigServer [23]. Theoretical data (Table 3) indicates that there are differences in the thermodynamic parameters of exametane and anastrozole compared with both compounds 9 and 10. However, the theoretical results showed that inhibition constant (Ki)

involved in the interaction of both compounds 9 and 10 with 2WD3 protein surface was lower compared with exametane and anastrozole.

All these results suggest that both compounds 9 and 10 could exert a higher interaction with the 2Wd3 protein surface of, which can be translated as a decrease in aromatase activity.

CONCLUSIONS

In this study, is reported a facile synthesis of two steroid derivatives using several chemical strategies. In addition, the theoretical interaction of steroid derivatives (9 or 10) with the aromatase enzyme indicate that both compounds 9 and 10 could act as aromatase enzyme inhibitors which can be translated as good candidates for their evaluation in some cancer model; Nevertheless, possibly the compound 10 could have higher activity against aromatase enzyme. However, to demonstrate

Table 2. Aminoacids residues involved in the interaction of anastrozole, exametane and compounds 9 (C-9) and 10 (C-10) with 2WD3 protein surface.

Anastrozole	Exametane	C-9	C-10
Gln ₉₂	Trp ₅	Trp ₅	Trp ₅
His ₉₄	His ₆₄	Leu ₆₀	Asn ₆₂
Val ₁₂₁	Ala ₆₅	Asn ₆₂	Asn ₆₇
Phe ₁₃₀	His ₉₄	His ₆₄	Glu ₆₉
Val ₁₃₄	His ₁₁₉	Glu ₆₉	Ile ₉₁
Leu ₁₄₀	Val ₁₂₁	His ₉₄	Gln ₉₂
Leu ₁₉₇	Val ₁₄₂	Phe ₁₃₀	His ₉₄
Thr ₁₉₉	Leu ₁₉₇	Thr ₁₉₉	Val ₁₂₁
Pro ₂₀₁	Thr ₁₉₈	Pro ₂₀₁	Phe ₁₃₀
	Thr ₁₉₉		Pro ₂₀₁
	Val ₂₀₆		
	Trp ₂₀₈		

Gln (glutamine); His (histidine); Val (valine); Leu (leucine); Thr (threonine);

Pro (proline); Ala (alanine); Trp (tryptophan); Asn (aspartic acid); Glu (glutamine);

Phe (phenylalanine); Ile (isoleucine).

Table 3. Thermodynamic parameters involved in the interaction of anastrozole, exametane and compounds 9 (C-9) and 10 (C-10) with 2WD3 protein surface.

Compound	Est. Free Energy of Binding (Kcal/mol)	Est. Inhi-bition Constant, Ki (μM)	cdW + Hbond + desolv Energy
Anastrozole	-5.11	180.06	-6.92
Exametane	-8.39	710.67	-8.36
C-9	-7.08	6.42	-7.11

Table 4. Thermodynamic factors involved in the interaction of anastrozole, exametane and compounds 9 (C_9) and 10 (C-10) with 2WD3 protein surface.

Compound	Electrost. Energy	Total Inter-molec. Energy	Interact. Surface
Anastrozole	-0.01	-6.92	666.43
Exametane	-0.03	-8.39	648.45
C-9	-0.01	-7.11	828.06
C-10	0.02	-8.83	927.79

this, experimental analyzes would have to be done in some biological model.

ACKNOWLEDGEMENTS

The authors extend their sincere thanks to Dr. Cindy Rossina Saravia, Rector of the Autonomous University of Campeche for their support in carrying out this study.

CONFLICT OF INTEREST

On behalf of all authors, the corresponding author states that there is no conflict of interest.

References

- M.D. Pegram, G.E. Konecny, C. O'Callaghan, M. Beryt, R. Pietras, D.J. Slamon, Rational combinations of trastuzumab with chemotherapeutic drugs used in the treatment of breast cancer, *J. Natl. Cancer Inst.*, 96 (2004) 739-749.
- K.C. Chu, C.A. Lamar, H.P. Freeman, Racial disparities in breast carcinoma survival rates: separating factors that affect diagnosis from factors that affect treatment, *Cancer*, 97 (2003) 2853-2860.
- B.N. Polite, O.I. Olopade, Breast cancer and race: a rising tide does not lift all boats equally, *Perspect Biol Med.*, 48 (2005) 166-175.
- R.T. Chlebowski, Z. Chen, G.L. Anderson, T. Rohan, A. Aragaki, D. Lane, L.L. Adams, Ethnicity and breast cancer: factors influencing differences in incidence and outcome, *J. Natl. Cancer Inst.*, 97 (2005) 439-448.
- L.J. Pierce, L.F. Hutchins, S.R. Green, D.L. Lew, J.R. Gralow, R.B. Livingston, K.S. Albain, Sequencing of tamoxifen and radiotherapy after breast-conserving surgery in early-stage breast cancer, *J. Clin. Oncol.*, 23 (2005) 24-29.
- B. Gerber, A. Krause, T. Reimer, I. Mylonas, J. Makovitzky, W. Janni, Anastrozole versus tamoxifen treatment in postmenopausal women with endocrine-responsive breast cancer and tamoxifen-induced endometrial pathology, *Clin. Cancer Res.*, 12 (2006) 1245-1250.
- M. Colleoni, W. Luo, P. Karlsson, J. Chirgwin, S. Aebi, G. Jerusalem, C. Kamby, Extended adjuvant intermittent letrozole versus continuous letrozole in postmenopausal women with breast cancer (SOLE): a multicentre, open-label, randomised, phase 3 trial, *Lancet Oncol.*, 19 (2018) 127-138.
- S. De Placido, C. Gallo, M. De Laurentiis, G. Bisagni, G. Arpino, M.G. Sarobba, F. Cognetti, Adjuvant anastrozole versus exemestane versus letrozole, upfront or after 2 years of tamoxifen, in endocrine-sensitive breast cancer (FATA-GIM3): a randomised, phase 3 trial, *Lancet Oncol.*, 19 (2018) 474-485.
- P. Brožič, P. Kocbek, M. Sova, J. Kristl, S. Martens, J. Adamski, T.L. Rižner, Flavonoids and cinnamic acid derivatives as inhibitors of 17 β -hydroxysteroid dehydrogenase type 1, *Mol. Cell Endocrinol.*, 301 (2009) 229-234.
- M. Salah, A.S. Abdelsamie, M. Frotscher, Inhibitors of 17 β -hydroxysteroid dehydrogenase type 1, 2 and 14: Structures, biological activities and future challenges, *Mol. Cell Endocrinol.*, 18 (2018) 0303-7207.
- G. Yang, S. Nowsheen, K. Aziz, A.G. Georgakilas, Toxicity and adverse effects of Tamoxifen and other anti-estrogen drugs, *Pharmacol. Therapeut.*, 139 (2013) 392-404.
- J.E. Lester, D. Dodwell, O.P. Purohit, S.A. Gutcher, S.P. Ellis, R. Thorpe, R.E. Coleman, Prevention of anastrozole-induced bone loss with monthly oral ibandronate during adjuvant aromatase inhibitor therapy for breast cancer, *Clin. Cancer Res.*, 14 (2008) 6336-6342.
- M.C. Yang, C. Peng, H. Huang, L. Yang, X.H. He, W. Huang, H. Cui, B. Han, Organocatalytic Asymmetric Synthesis of Spiro-oxindole Piperidine Derivatives That Reduce Cancer Cell Proliferation by Inhibiting MDM2-p53 Interaction, *Org. Lett.*, 19 (2017) 6752-6755.
- B. Su, S. Landini, D.D. Davis, R.W. Brueggemeier, Synthesis and biological evaluation of selective aromatase expression regulators in breast cancer cells, *J. Med. Chem.*, 50 (2007) 1635-1644.
- C. Ding, Y. Zhang, H. Chen, Z. Yang, C. Wild, N. Ye, C. Ester, A. Xiong, M. White, Q. Sheng, J. Zhou, Oridonin ring A-based diverse constructions of enone functionality: identification of novel dienone analogues effective for highly aggressive breast cancer by inducing apoptosis, *J. Med. Chem.*, 56 (2013) 1-31.
- T. Akama, Y. Shida, T. Sugaya, H. Ishida, K. Gomi, M. Kasai, Novel 5-aminoflavone derivatives as specific antitumor agents in breast cancer, *J. Med. Chem.*, 39 (1996) 3461-3469.
- P. Dandawate, E. Khan, S. Padhye, H. Gaba, S. Sinha, J. Deshpande, S. Venkateswara, M. Khetmalas, A. Ahmad, F. Sarkar, Synthesis, characterization, molecular docking and cytotoxic activity of novel plumbagin hydrazones against breast cancer cells, *Bioorg. Med. Chem. Lett.*, 22 (2012) 3104-3108.
- G. Macindoe, L. Mavridis, V. Venkatraman, M. Devignes, D. Ritchie, HexServer: an FFT-based protein docking server powered by graphics processors, *Nucleic acids Res.*, 38 (2010) W445-W449.
- Stander, F. Joubert, A. Joubert, Docking, synthesis, and in vitro evaluation of antimetabolic estrone analogs, *Chem. Biol. Drug Des.*, 77 (2011) 173-181.
- N. Nishimura, K. Kobayashi, Self-Assembly of a Cavitand-Based Capsule by Dynamic Boronic Ester Formation, *Ang. Chem. Int. Ed.*, 47 (2008) 6255-6258.
- V. Temml, T. Kaserer, Z. Kutil, P. Landa, T. Vanek, D. Schuster, Pharmacophore modeling for COX-1 and -2 inhibitors with LigandScout in comparison to Discovery Studio, *Future Med. Chem.*, 6 (2014) 1869-1881.
- L. Woo, T. Jackson, A. Putey, G. Cozier, P. Leonard, K. Acharya, B. Potter, Highly potent first examples of dual aromatase-steroid sulfatase inhibitors based on a biphenyl template, *J. Med. Chem.*, 53 (2010) 2155-2170.
- E. Hazai, S. Kovács, L. Demkó, Z. Bikádi, DockingServer: molecular docking calculations online, *Acta Pharm. Hung.*, 79 (2009) 17-21.
- N. Richter, R. Simon, W. Kroutil, J. Ward, H. Hailes, Synthesis of pharmaceutically relevant 17- α -amino steroids using an ω -transaminase, *Chem. Commun.*, 50 (2014) 6098-6100.
- T. Curran, G. Flynn, D. Rudisill, P. Weintraub, A novel route to a 4-amino steroid: MDL 19687, *Tetrahedron Lett.*, 36 (1995) 4761-4764.
- A. Averin, E. Ranyuk, N. Lukashev, S. Golub, A. Buryak, I. Beletskaya, Palladium-catalyzed amination in the synthesis of macrocycles comprising cholane, polyamine and pyridine units, *Tetrahedron Lett.*, 49 (2008) 1188-1191.
- L. Figueroa, F. Díaz, M. Rosas, E. García, E. Pool, A. Camacho, M. López, R. García, A facile synthesis and theoretical analysis of a steroid-cyclophano, *Lett. Org. Chem.*, 12 (2015) 614-621.

28. R.S. Lankalapalli, J.T. Eckelkamp, D. Sircar, D.A. Ford, P.V. Subbaiah, R. Bittman, Synthesis and antioxidant properties of an unnatural plasmalogen analogue bearing a trans O-vinyl ether linkage, *Org. Lett.*, 11 (2009) 2784-2787.
29. E. Buck, Z.J. Song, D. Tschäen, P.G. Dormer, R.P. Volante, P.J. Reider, Ullmann diaryl ether synthesis: Rate acceleration by 2, 2, 6, 6-tetramethylheptane-3, 5-dione, *Org. Lett.*, 4 (2002) 1623-1626.
30. T.D. Quach, R.A. Batey, Copper (II)-catalyzed ether synthesis from aliphatic alcohols and potassium organotrifluoroborate salts, *Org. Lett.*, 5 (2003) 1381-1384.
31. K.L. Zheng, M.Q. You, W.M. Shu, Y.D. Wu, A.X. Wu, Acid-Mediated Intermolecular [3+ 2] Cycloaddition toward Pyrrolo [2, 1-a] isoquinolines: Total Synthesis of the Lamellarin Core and Lamellarin G Trimethyl Ether, *Org. Lett.*, 19 (2017) 2262-2265.
32. L. Figueroa, F. Diaz, M. Rosas, G. Maldonado, E. García, E. Pool, Design and synthesis of some carbamazepine derivatives using several strategies, *Lett. Org. Chem.*, 12 (2015) 394-401.
33. V.V. Brei, S.V. Prudius, O.V. Melezhyk, Vapour-phase nitration of benzene over superacid WO_3/ZrO_2 catalysts, *Appl. Catal. A.*, 239 (2003) 11-16.
34. H. Sato, K. Hirose, Vapor-phase nitration of benzene over solid acid catalysts (1): Nitration with nitric oxide (NO_2), *Appl. Catal. A.*, 174 (1998) 77-81.
35. H. Sato, K. Hirose, K. Nagai, H. Yoshioka, Y. Nagaoka, Vapor phase nitration of benzene over solid acid catalysts: II. Nitration with nitric acid (1); montmorillonite and mixed metal oxide catalysts, *Appl. Catal. A.*, 175 (1998) 201-207.
36. J.V. Crivello, Nitrations and oxidations with inorganic nitrate salts in trifluoroacetic anhydride, *J. Org. Chem.*, 46 (1981) 3056-3060.
37. G.A. Olah, H.C. Lin, Aromatic substitution. XXXV. Boron trifluoride catalyzed nitration of benzene, alkylbenzenes, and halobenzenes with methyl nitrate in nitromethane solution, *J. Am. Chem. Soc.*, 96 (1974) 2892-2898.
38. M.A. Paul, Ortho-para directive effects for aromatic nitration in acetic anhydride, *J. Am. Chem. Soc.*, 80 (1958) 5332-5333.
39. T. Matsumoto, N. Tokitoh, R. Okazaki, First oxazagermete: synthesis, structure and thermal cycloreversion into a germanone, *Chem. Commun.*, 16 (1997) 1553-1554.
40. H.L. Corkins, L. Storace, E.R. Osgood, A new route to the 4H-1, 2-oxazete ring system by the stereospecific oxidation of (Z)-3, 3-dimethyl-1, 1-bis (methylthio)-2-butanone oxime, *Tetrahedron Lett.*, 21 (1980) 2025-2028.
41. W. Walter, W. Ruback, 2,2,4-Trisubstituted 2H-1, 3-Oxazetes-A New Type of Heterocycles-A Reinvestigation, *Liebigs Ann. Chem.*, 2 (1982) 231-239.
42. K.N. Houk, Frontier molecular orbital theory of cycloaddition reactions, *Acc. Chem. Res.*, 8 (1975) 361-369.
43. D.H. Ess, K.N. Houk, Theory of 1, 3-dipolar cycloadditions: distortion/interaction and frontier molecular orbital models, *J. Am. Chem. Soc.*, 130 (2008) 10187-10198.
44. Y.R. Prasa, P.R. Kumar, D.J. Smiles, P.A. Babub, QSAR studies on chalcone derivatives as antibacterial agents against *Bacillus pumilis*, *Arxivok.*, 11 (2008) 266-276.
45. J.N. Latosińska, J. Kasprzak, Z. Kazimierczuk, Effects of chlorination and deoxyribose substitution on electron density distribution in indazole molecule studied by ^{35}Cl NQR spectroscopy and ab initio calculations, *J. Mol. Struct. THEOCHEM.*, 530 (2000) 217-222.
46. L. Figueroa, F. Díaz, E. Garcia, Synthesis of Two steroids derivatives and its relationship with some physicochemical parameters, *J. Chem.*, 9 (2012) 27-34.
47. N. Obi-Egbedi, I. Obot, M. El-Khaiary, S. Umoren, E. Ebenso, Computational Simulation and Statistical Analysis on the Relationship Between Corrosion Inhibition Efficiency and Molecular Structure of Some Phenanthroline Derivatives on Mild Steel Surface, *Int. J. Electrochem. Sci.*, 6 (2011) 5649-5675.
48. D. Seeliger, B.L. de Groot, Ligand docking and binding site analysis with PyMOL and Autodock/Vina, *J. Computer-Aided Mol. Des.*, 24 (2010) 417-422.
49. M.L. Verdonk, V. Berdini, M.J. Hartshorn, W.T. Mooij, C.W. Murray, R.D. Taylor, P. Watson, Virtual screening using protein- ligand docking: avoiding artificial enrichment, *J. Chem. Inf. Comp. Sci.*, 44 (2004) 793-806.
50. S.Y. Huang, X. Zou, Advances and challenges in protein-ligand dockin, *Int. J. Mol. Sci.*, 11 (2010) 3016-3034.
51. M. Shalbafan, G. Rezaei Behbehani, H. Ghasemzadeh, Study of interaction of human serum albumin with doxorubicin (anti-cancer drug) by docking simulation, *Chem. Methodol.*, 3 (2019) 348-353.
52. R.K. Bommeraa, R. Merugu, L. Eppakayala, A Facile Synthesis and Docking Studies of N-(3-(4-Chlorophenoxy) benzyl)-2-methyl-7H-pyrrolo [2, 3-d] pyrimidin-4-amine, *Chem. Methodol.*, 3 (2019) 354-361.
53. J. Jays, S. Mohan, J. Saravanan, Molecular docking studies of novel aminopyrimidines as potent antifungal agents, *Chem. Methodol.*, 3 (2019) 442-450.
54. S. Chumsri, T. Howes, T. Bao, G. Sabnis, A. Brodie, Aromatase, aromatase inhibitors, and breast cancer, *J. Steroid Biochem. Mol. Biol.*, 125 (2011) 13-22.



Chemical Taxonomy Applications of Some Water Mite Species (Acari, Hydrachnidia) Using Fourier Transform Infrared Spectroscopy (FTIR) Methods

Fourier Dönüşümü Kızılötesi Spektroskopisi (FTIR) Yöntemlerini Kullanarak Bazı Su Akar Türlerinin (Acari, Hydrachnidia) Kimyasal Taksonomisi Uygulamaları

Ferruh Aşçı¹, Gülderen Uysal Akkuş², Nazife Alpaslan¹, Gamze Kübra Çetin¹

¹Department of Molecular Biology and Genetics, Afyon Kocatepe University, Afyonkarahisar, Turkey.

²Department of Chemistry, Afyon Kocatepe University, Afyonkarahisar, Turkey.

ABSTRACT

This study employed water mite (Acari, Hydrachnidia) species collected from a natural lake water environment. These species included *Hydrodroma despiciens*, *Eylais infundibulifera*, *Hydryphantes flexiosus*, *Georgella helvetica*, *Hygrobates nigromacutlatus*, *Hydryphantes thoni* ve *Torrenticola bevirostris*. Chemical analyses of these species were conducted using the Fourier infrared spectrophotometer (FTIR) technique. Solid phase IR spectra were made individually for each species. The data obtained for all species were examined graphically and were identified in four different spectral regions. Finally, the spectrum frequency ranges of these species were determined. The functional groups OH, C-H, C=O, C-O, and C-N were observed. The vibrational frequencies of each species studied were determined. When evaluating the results of the spectroscopic analysis, the range of the spectrum of these species was shown to be similar to one another; however, peak intervals were different for each species.

Key Words

Water mites, acari, Hydrachnidia, infrared spectroscopy, chemical taxonomy.

Öz

Bu çalışmada, doğal göl suyu ortamından toplanan su kenesi (Acari, Hydrachnidia) türleri kullanılmıştır. Bu türler *Hydrodroma despiciens*, *Eylais infundibulifera*, *Hydryphantes flexiosus*, *Georgella helvetica*, *Hygrobates nigromacutlatus*, *Hydryphantes thoni* ve *Torrenticola bevirostris*'dir. Bu türlerin kimyasal analizleri, Fourier kızılötesi spektrofotometre (FTIR) tekniği kullanılarak yapıldı. Katı faz IR spektrumları her tür için ayrı ayrı yapıldı. Tüm türler için elde edilen veriler grafiksel olarak incelendi ve dört farklı spektral bölgede tanımlandı. Son olarak, bu türlerin spektrum frekans aralıkları belirlendi. Fonksiyonel gruplar OH, C = H, C = O, C = O ve C = N gözlemlendi. Çalışılan her türün titreşim frekansları belirlendi. Spektroskopik analiz sonuçları değerlendirilirken, bu türlerin spektrum aralığının birbirine benzer olduğu ancak, en yüksek aralıkların her tür için farklı olduğu gösterilmiştir.

Anahtar Kelimeler

Su keneleri, acari, Hydrachnidia, infraraed spektroskopisi, kimyasal taksonomi

Article History: Received: Dec 26, 2018; Revised: Jul 5, 2019; Accepted: Oct 2, 2019; Available Online: Nov 1, 2019.

DOI: <https://doi.org/10.15671/hjbc.646737>

Correspondence to: F. Aşçı, Department of Molecular Biology and Genetics, Afyon Kocatepe University, Afyonkarahisar, Turkey.

E-Mail: f_asci@aku.edu.tr

INTRODUCTION

A large number of studies have been conducted on water mites that are commonly found in marine and inland waters. Water mite species (Acari: Hydrachnidia) belong to 57 families, 400 genera and approximately 6000 species [1-6]. Water mites are important ecologically as bioindicator organisms. Molecular and chemical studies have been conducted on this group [7-14]. In terms of solving systemic problems and the level of understanding of the phylogenetic relationships encountered between water mites, chemical techniques have recently been employed [7, 8, 10, 11]. The data obtained by this method serve as a significant contribution for systematizers and taxonomists. Considering the continuing systematic discussion of some water mite species, it is important to note that the molecular and chemical methods currently being employed by researchers indicate certain and clear results.

The FTIR technique used in this study provides determination of functional groups' (OH, C-H, C=O, C-O, C-N, etc.) structure by measuring the vibrational energy of molecules within the structure. This method is generally used to determine the structure of chemical compounds, particularly organic compounds, alongside other spectrophotometric methods (NMR, Mass, UV, etc.) [15-16].

Infrared spectroscopy is a spectroscopy-based technique that absorbs the infrared rays of the material under study. All molecules, except for homo-nuclear (N_2 , O_2 , Cl_2) molecules, have a unique infrared spectrum. The IR spectrum is generally divided into four regions: 3700-2700 cm^{-1} (X-H); 2700-1850 cm^{-1} (triple bonds); 1950-1550 cm^{-1} (double bonds) and 1550-600 cm^{-1} (except for X-H, single bonds).

- The 3700-2700 cm^{-1} region: absorption peaks in this region generally result from hydrogen vibrations.

- O-H and N-H stretching vibration frequency absorptions are seen at 3700-3000 cm^{-1} .
- The 1950-1550 cm^{-1} region: this region is called the carbonyl (C=O) double bond region.
- The 1500-700 cm^{-1} region: This region is called the fingerprint region. Most of the single bond absorption peaks are collected in this region. Esters (C-O-C) ethers (R-O-R) inorganic phosphates, inorganic sulfates, inorganic carbonates, and inorganic nitrates are observed in this region (Figure 1) [4].

IR (infrared spectroscopy) has recently become one of the molecular methods used in invertebrate animals for taxonomic purposes. This study is the first to identify functional groups in water mite species using IR. The infrared technique was used for the first time in Acariidae in 1989 by Leal et al. In this study, Leal and colleagues isolated rosefuran and perylene derivatives from *Tyrophagus neiswanderi* (Acariformes, Acaridae) species. The study described these natural compounds using IR and other spectroscopic techniques and compared them with synthetic ones [17].

Another study by Leal et al. (1989) isolated a novel monoterpene 2(E)-(4-methyl-3-pentenyl) butanediol (α -acari dial) from another Acari species, *Tyrophagus perniciosus*, and determined the structure of this compound by spectroscopic methods (GS-FTIR, MS). Subsequently, a series of reactions on the part of this compound was carried out to obtain the E and Z isomers of this α -acari dial compound. The study also compared the spectroscopic results of these natural monoterpene derivatives with that of synthetic ones [17]. A similar study by Hiraoka and colleagues (2001) obtained a mixture of two monoterpenes from *Histiogaster* sp. A096

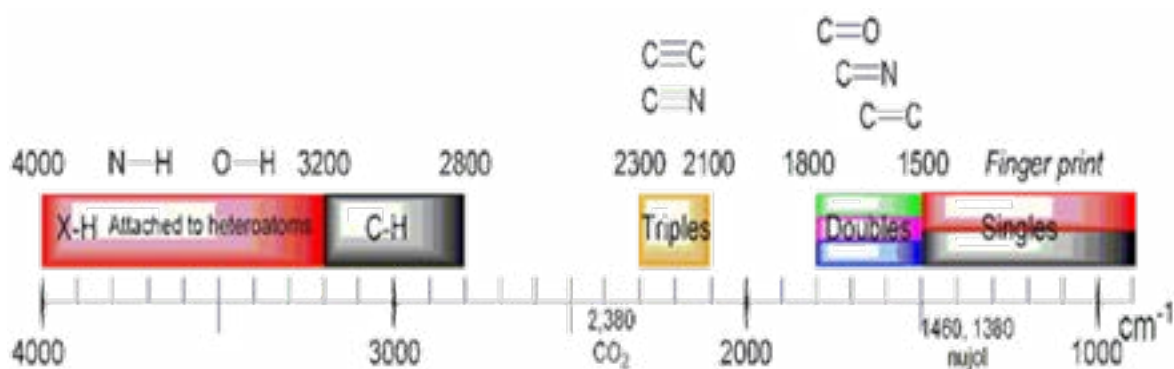


Figure 1. Functional group regions [4].

(Acari: Acaridae). They then elucidated their structure by GC/MS, GC/FTIR, UV and ^1H NMR spectroscopy ((2E, 4E) - and (2Z, 4E)-3,7-dimethyl-2,4,6-octatrienals) [18]. In a study conducted by Sato et al. (1993) researchers extracted a new salicylaldehyde derivative with a yield of 37% by extracting *Dermatophagoides pteronyssinus*, a type of mite, with hexane [19]. In another study, a new monoterpene lactone was obtained from *Tyrophagus putrescentiae*, a type of mold fungus by Morino and coworkers (1997). The researchers noted the chemical name of this lactone as (E)-2-(4'-methyl-3'-pentenylidene)-4-butanol and assigned it the β -acarolide trivial name [20]. There is no information in the literature about the use of this method in relation to water mites. In the present study, the similarities or differences between species belonging to different families were evaluated using a systematic approach.

MATERIALS and METHODS

The water mites used in the study were collected from Karamık Lake (Afyonkarahisar-Turkey) from May-August 2015. Samples were identified in the laboratory under a microscope. The samples were washed with pure water and dried in sterile petri dishes at room temperature;

100 mg of anhydrous KBr (potassium bromide) was added to roughly 5 mg of water mite species (*Hydrodroma despiciens*, *Eylais infundibulifera*, *Hydryphantes flexiosus*, *Georgella helvatica*, *Hygrobates nigromacutlatus*, *Hydryphantes thoni*, *Torrenticola bevirostris*) by weighing each species with a precision scale. The mixture of water mites and potassium bromide was placed into a mortar and thoroughly crushed for homogenization. This mixture was pressed into thin transparent discs and then analyzed by FTIR (Perkin Elmer Spectrum BX). The results of the analysis were graphically evaluated.

RESULTS

When the results obtained from samples of seven water mite species were examined, four functional groups in the spectrum were observed. These functional groups were: (1) functional group (OH, NH) in the range of $3600\text{-}3200\text{ cm}^{-1}$; (2) functional group (C-H) in the range of $2900\text{-}2850\text{ cm}^{-1}$; (3) functional group (C-C, C=O, C=N) in the range of $1780\text{-}1650\text{ cm}^{-1}$; (4) functional group (C-O, C-N, C-S) in the range of $1200\text{-}400\text{ cm}^{-1}$ (Figure 1). All of these functional groups were observed in all species.

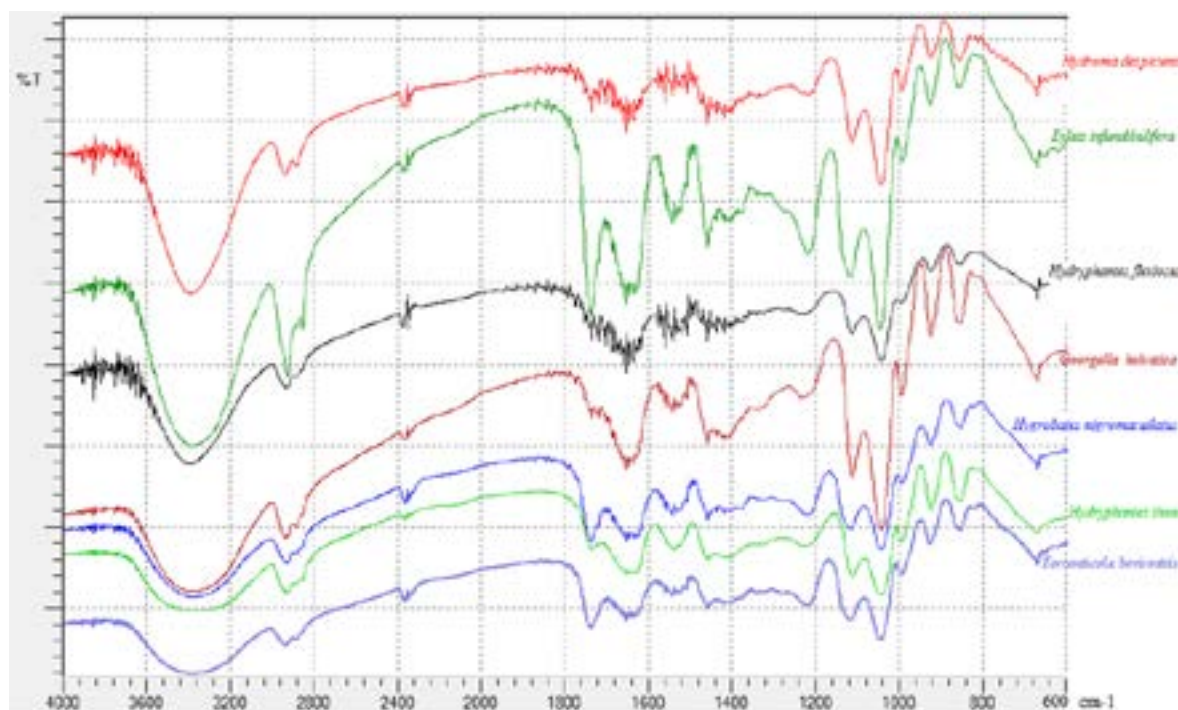


Figure 2. FTIR analysis of water mites species *Hydrodroma despiciens* (1), *Eylais infundibulifera* (2), *Hydryphantes flexiosus* (3), *Georgella helvatica* (4), *Hygrobates nigromacutlatus* (5), *Hydryphantes thoni* (6) and *Torrenticola bevirostris* (7).

The first functional group is the OH and NH range. It is observed that the similarity rate among the six species studied for this region is very high. This result is also expected. Because it is the carbohydrates and proteins that make up the structure in living things. OH, group is the basis of carbohydrates and NH group is the basis of proteins. When the % T values are examined; bands in the range of 3600-3200 cm^{-1} it is seen that *Eylais infundibulifera* and *Hydrodroma despicdens* are more similar to each other. On the other hand, it is understood that *Georgella helvetica*, *Hygrobates nigromacutlatus*, *Hydryphantes thoni*, and *Torrenticola bevirostris* are more similar to each other in these functional groups in the same region. This situation does not support the taxonomic order based on structural features at the genus and family level [21-22].

The second functional group is the stretching vibration region of aliphatic and aromatic C-H bonds. This band in the range of 2900-2850 cm^{-1} is observed in almost all organic compounds. In the studied species, the graphical analysis values of this region were observed very close to each other.

The second functional group region is the double bond at C-C, C-O or C-N in the range of 1780-1650 cm^{-1} . These functional groups are found in the amino acids that form the basis of proteins. Therefore, it can be said that the third functional group belongs to proteins. When the studied species are considered in terms of these groups, it is seen that at least one of these functional groups is found in all. Although the similarity between species is very high in this region, *Eylais infundibulifera* is different from others in this range. It is known that this species has a different morphological structure in the family of Eylaidae than all other species of Eylais. Because this species of chitinization is different from the others [21, 24, 25]. Though there is more chitinization in the species of *Torrenticola bevirostris*, the same difference is not seen in the graph. The fourth functional group is in the region of 1200-400 cm^{-1} . This region is also known as the fingerprint region. The frequencies of C-O, C-N functional groups are in this range. These bonds form the basis of both carbohydrates and proteins. Within this functional group, the frequency of *Hydryphantes flexus* differs. But it seems that the others are more similar to each other in terms of their general qualities.

DISCUSSION

When all these data are examined in whole, it seems that it is not possible to use the results in a systematic comparison in different species of water mites. But it can be considered that this method may be useful for future studies in terms of determining the chemical structures of the species and determining the compositions of the basic organic compounds (carbohydrate, protein, lipid, etc.).

When comparing this study with previous studies, the difference is that previous studies have been directed toward the identification of individual alkaloids. In these previous studies, the structures of alkaloid derivatives have been elucidated and separated into their isomers by different reactions. Furthermore, new compounds were obtained from these and trivial names were given and the results were compared with synthetic market products. The purpose of this study is; Analyzing the whole as a living thing and making a comparison between species of the same group in terms of chemical structures. Another difference is; Previous studies were done with CS-FTIR technique, solid phase FT IR technique was used in this study. When these two techniques are compared, the samples to be analyzed are taken as gas in the CS-FTIR method, while the samples are taken as potassium bromide discs in the solid FTIR method. However, there is no difference in terms of the obtained spectrum values.

CONCLUSION

In this study water mites (Acari, Hydrachnidia) species (*Hydrodroma despicdens*, *Eylais infundibulifera*, *Hydryphantes flexiosus*, *Georgella helvetica*, *Hygrobates nigromacutlatus*, *Hydryphantes thoni*, and *Torrenticola bevirostris*) were used. The chemical analyses of these species were carried out by the Fourier transform infrared spectrophotometer (FTIR). The results of the analysis for all species were evaluated graphically and four spectral regions belonging to these species have been identified. The vibrational frequencies of each species studied were determined. When evaluating the results of FTIR analysis, the range of the spectrum of these species was shown to be similar to each other (Figure 2).

Acknowledgments

This study was supported by a project of the Afyon Kocatepe University Research Foundation, Project No. BAP.16.FENED.02, 2017.

References

1. A. Di Sabatino, H. Smit, R. Gerecke, T. Goldschmidt, N. Matsumoto, B. Cicolani, Global diversity of water mites (Acari, Hydrachnidia; Arachnida) in freshwater, *Hydrobiol.*, 595 (2008) 303-315.
2. I.M. Smit, D.R. Cook, Water mites. In J.H. Thorp and A.P. Covich, eds., *Ecology and classification of North American freshwater invertebrates*, Academic, San Diego, CA, USA. (1991) 523-592.
3. E. Meyer. Der Entwick lungs zyklus von *Hydrodroma despiciens* (O.F. Müller, 1776) (Acari, Hydrodromidae), *Arch. Hydrobiol. Suppl.*, 66 (1985) 321-453.
4. D.A. Skoog, D.M. West, *Principles of instrumental analysis* (Vol. 158). Philadelphia: Saunders College pp.
5. H. Smit, 2015. The water mite family Hygrobatidae Koch in Australia. The genera *Aspidiobatella* Cook, *Australorivacarus* Viets, *Gondwanabates* Imamura and *Rhynchaustrobates* Cook (Acari: Hydrachnidia), *Zootaxa.*, 4033 (1980) 567-583.
6. P.V. Tuzovskij, K.A. Semenchenko, Morphology and taxonomy of deutonymphs of the genus *Unionicola* Haldeman, 1842 (Acari, Hydrachnidia, Unionicolidae) in Russia, *Zootaxa.*, 69 (2015) 3994.
7. Y.Ö. Boyacı, P.Gülle, New records of the water mite family Hydryphantidae (Acari: Hydrachnidia) from Turkey, with the description of a new species. *Syst. Appl. Acarol.*, 19 (2014) 160-165.
8. F. Aşçı, G.U. Akkuş, İ. Yaman, Determination of the ecological impact levels on *Hydrodroma despiciens* (Müller 1776) (Acari, Hydrachnidia) which is a common water mite in terms of heavy metal applications, *Pak. J. Zool.*, 48 (2016) 345-348.
9. F. Aşçı, M. Bahadır, G.U. Akkuş, Study on the Impact of Elements in Water on the Diversity of Water Mites (Acari, Hydrachnidia) Species, *Adv. Biosci. Biotechnol.*, 6 (2015) 259-264.
10. S.T. Onrat, F. Aşçı, M. Özkan, A cytogenetic study of *Hydrodroma despiciens* (Müller, 1776) (Acari, Hydrachnellae, Hydrodromidae), *Genet. Mol. Res.*, 5 (2006) 342-349.
11. P. Martin, M. Koester, L. Schynawa, R. Gergs, First detection of prey DNA in *Hygrobatas fluviatilis* (Hydrachnidia, Acari): A new approach for determining predator-prey relationships in water mites, *Exp. Appl. Acarol.*, 67 (2015) 373-380.
12. B.A. Dorda, A.G. Valdecasas, Traditional water mite fixatives and their compatibility with later DNA studies, *Exp. Appl. Acarol.*, 34 (2002) 59-65.
13. A.J. Bohonak, B.P. Smith, M. Thornton, Distributional, morphological and genetic consequences of dispersal for temporary pond water mites, *Freshw. Biol.*, 49 (2004) 170-180.
14. B.R. Ernsting, D.D. Edwards, M.F. Vidrine, K.S. Myers, C.M. Harmon, Phylogenetic relationships among species of the *Subgenus parasitax* (Acari: Unionicolidae: Unionicola) based on DNA sequence of the mitochondrial cytochrome oxidase I gene, *Int. J. Acarol.*, 32 (2006) 195-202.
15. M. Więcek, P. Martin, A. Lipinski, Water mites as potential long-term bioindicators in formerly drained and rewetted raised bogs, *Ecol. Indic.*, 34 (2013) 332-335.
16. S.W. Sharpe, T.J. Johnson, R.L. Sams, P.M. Chu, G.C. Rhoderick, P.A. Johnson, Gas-phase databases for quantitative infrared spectroscopy, *Appl. Spectrosc.*, 58 (2004) 1452-1461.
17. J. Chen, B. Gu, E.J. LeBoeuf, H. Pan, S. Dai, Spectroscopic characterization of the structural and functional properties of natural organic matter fractions, *Chemosphere.*, 48 (2002) 59-68.
18. W.S. Leal, Y. Kuwahara, Y. Nakano, H. Nakao, T. Suzuki, 2 (E)-(4-Methyl-3-pentenyl)-butenedial, α -Acaridial, a Novel Monoterpene from the Acarid Mite *Tyrophagus perniciosus* (Acarina, Acaridae), *Agric. Biol. Chem.*, 53 (1989) 1193-1196.
19. M. Sato, Y. Kuwahara, S. Matsuyama, T. Suzuki, 2-Formyl-3-hydroxybenzyl formate (rhizoglyphinyl formate), a novel salicylaldehyde analog from the house dust mite *Dermatophagoides pteronyssinus* [Astigmata, Pyroglyphidae], *Biosci. Biotech. Biochem.*, 57 (1993) 1299-1301.
20. H. Hiraoka, N. Mori, R. Nishida, Y. Kuwahara, (4E)-Dehydrocitrals [(2E, 4E)-and (2Z, 4E)-3, 7-dimethyl-2, 4, 6-octatrienals] from Acarid Mite *Histiogaster* sp. A096 (Acari: Acaridae), *Biosci. Biotechnol. Biochem.*, 65 (2001) 2749-2754.
21. A. Morino, Y. Kuwahara, S. Matsuyama, T. Suzuki, (E)-2-(4'-Methyl-3'-pentenylidene)-4-butanolide, Named β -Acariolide: A New Monoterpene Lactone from the Mold Mite, *Tyrophagus putrescentiae* (Acarina: Acaridae), *Biosci. Biotechnol. Biochem.*, 61 (1997) 1906-1908.
22. M. Özkan, Doğu Anadolu Su Akarları (Acari, Hydrachnellae) Üzerine Sistematik Araştırmalar-II. Atatürk Üniversitesi, Fen Fak. Derg. 1 (1982) 145-163.
23. C. Bader, H. Sepasgozarian, Wassermilben (Acari, Prostigmata) aus dem Iran - 5. Mitteilung. *Hydrovolzia persica* nov. spec. *Acarologia*, 21 (1979) 70-83.
24. K. Viets, VII: Wassermilben oder Hydracarina (Hydrachnellae und Halacaridae). Die Tierwelt Deutschlands und der angrenzenden Meeresteile nach ihren Merkmalen und nach ihrer Lebensweise (Tl. 31, 32) Show all parts in this series, 1936.
25. L. Szalay, Vízitkákat Hydracarina fauna Hungariae, *Akadémiai Kiadó, Budapest*, 380, (1964) Google Scholar.



Practical Synthesis of Pyrido [1,2-A] Benzimidazoles Via Multicomponent Reactions

Çok Bileşenli Tepkimeler Yoluyla Pirido [1,2-A] Benzimidazolların Pratik Sentezi

Akın Sağırılı

Department of Chemistry, MS 14018, Bolu Abant İzzet Baysal University, Bolu, Turkey.

ABSTRACT

A facile and efficient synthesis of 1-amino-3-(4-substituted)-4-nitro-3,5-dihydrobenzo[4,5]imidazo[1,2-a]pyridine-2-carbonitriles was conducted via one-pot multicomponent reaction of 2-(nitromethylene)-2,3-dihydro-1H-benzo[d]imidazole with malononitrile and aromatic aldehydes. Besides, no tedious work-up procedure was necessary for the isolation of desired products which were precipitated out of reaction medium in pure state. Ten new title compounds were characterized by the means of physical and spectroscopic methods (m.p., IR, NMR and TOF-MS analyses).

Key Words

Heterocyclic ketene aminal, enamine, multicomponent, benzimidazole, pyrido[1,2-a]benzimidazole.

Öz

Tek basamakta siklik enamın (2-(nitrometilen)-2,3-dihidro-1H-benzo[d]imidazol), malononitril ve aromatik aldehit ile çoklu bileşenli tepkime üzerinden 1-amino-3-(4-substitue)-4-nitro-3,5-dihidrobenzo[4,5]imidazo[1,2-a]piridin-2-karbonitril lerin kolay ve etkili bir biçimde sentezi açığa çıkarıldı. Ayrıca, istenilen ürünlerin eldesinde herhangi bir saflaştırma prosedürü gerektirmedi. Bütün ürünler saf olarak tepkime ortamında çöktüldü. On yeni yapı fiziksel ve spektroskopik yöntemler kullanılarak karakterize edildi (e.n., IR, NMR ve TOF-MS analizleri).

Anahtar Kelimeler

Heterosiklik keten aminal, enamın, çok-bileşenli, benzimidazol, pirido[1,2-a]benzimidazol.

Article History: Received: Apr 8, 2019; Revised: Jul 15, 2019; Accepted: Sep 12, 2019; Available Online: Nov 1, 2019.

DOI: <https://doi.org/10.15671/hjbc.550890>

Correspondence to: A. Sağırılı, Department of Chemistry, Bolu Abant İzzet Baysal University, Bolu, Turkey.

E-Mail: sagirli_a@ibu.edu.tr

INTRODUCTION

Benzimidazole as an important heterocycle represents key structure of many biologically active compounds [1]. Molecules containing this core have taken great attention in the field of medicinal chemistry during last decades. Especially, the pyrido[1,2-a]benzimidazoles exhibited various bioactivities such as anticancer [2], antimalarial [3], antiproliferative [4], antifungal [5], antiviral and antipyretic agents [3]. Moreover, this heterocyclic unit can also be found as embedded in a commercially available antibiotic drug, Rifaximin [6] (Figure 1).

Due to aforementioned biological properties and medicinal applications, development of efficient and atom economic strategies through the synthesis of pyrido[1,2-a]benzimidazoles has attracted considerable interest [7]. Up to now, many methods have been utilized for the synthesis of these heterocycles by transition metal-catalyzed nucleophilic substitution of 2-aminopyridines with *o*-dihaloarenes (1) [8], C-N coupling of 2-haloanilines with 2-halopyridines, intramolecular cyclization of *N*-aryl-2-aminopyridines (2) [9], metal-free annulation of arenes with 2-aminopyridine derivatives (3) [10] and cyclocondensation of benzimidazoles with bifunctional reagents (4) (Figure 2) [11].

Although the synthetic methods in recent literature are convenient for the construction of pyrido[1,2-a]benzi-

midazoles, many of them may require expensive transition-metal catalysts, elevated reaction temperatures, extensive reaction times and tedious work-up procedures [7]. The difficulties in the preparation of this heterocycles prompted us to investigate simple and work-up free synthetic methodology. In this context, we herein report one-pot synthetic method by the multicomponent reaction of 2-(nitromethylene)-2,3-dihydro-1H-benzo[d]imidazoles with an active methylene compound, malononitrile, and aromatic aldehydes in a single-step without further purification.

MATERIALS and METHODS

General

Infrared spectra were recorded on a SHIMADZU FTIR-8400S instrument using KBr pellets. HRMS were run on a Waters Lct Premier XE oa-TOF Mass Spectrometer. ¹H-NMR and ¹³C-NMR spectra were recorded on JEOL-ECS400 Delta2 NMR spectrometer (400 MHz for proton and 100 MHz for carbon) at ambient temperature. All chemical shifts were reported in ppm downfield from TMS. Coupling constants (*J*) are reported in Hz. Melting points were determined on a MELTEMP apparatus and uncorrected. TLC was performed using precoated plates with fluorescent indicator (Merck 5735). The stain solutions of permanganate were used for visualization of the TLC spots. Cyclic enamines, 2-(nitromethylene)-2,3-dihydro-1H-benzo[d]imidazole and ((*E*)-5-methyl-2-

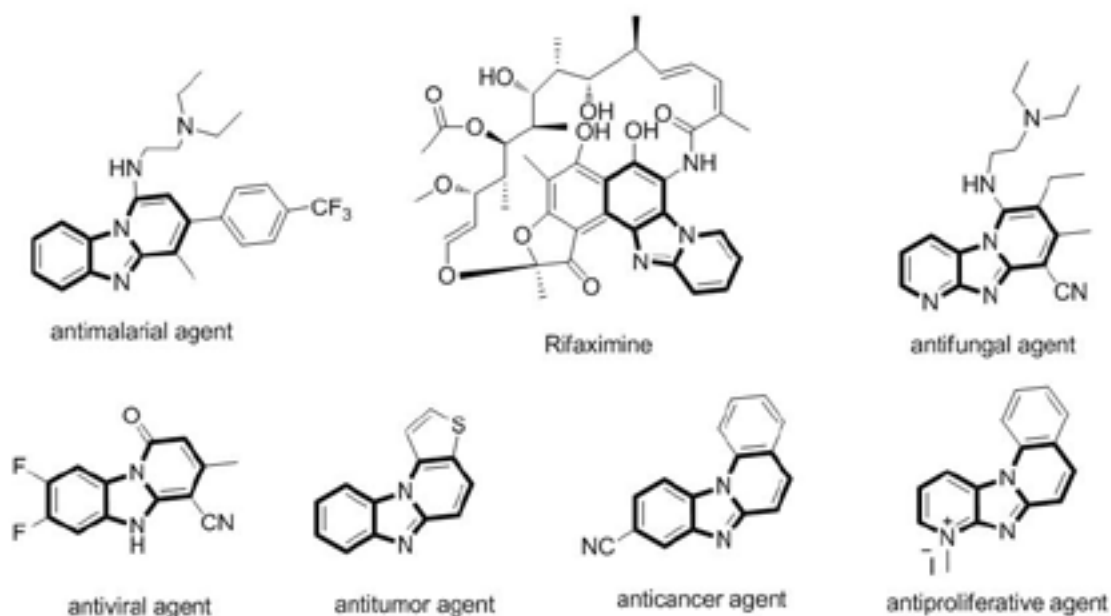


Figure 1. Some biologically important pyrido[1,2-a]benzimidazole derivatives.

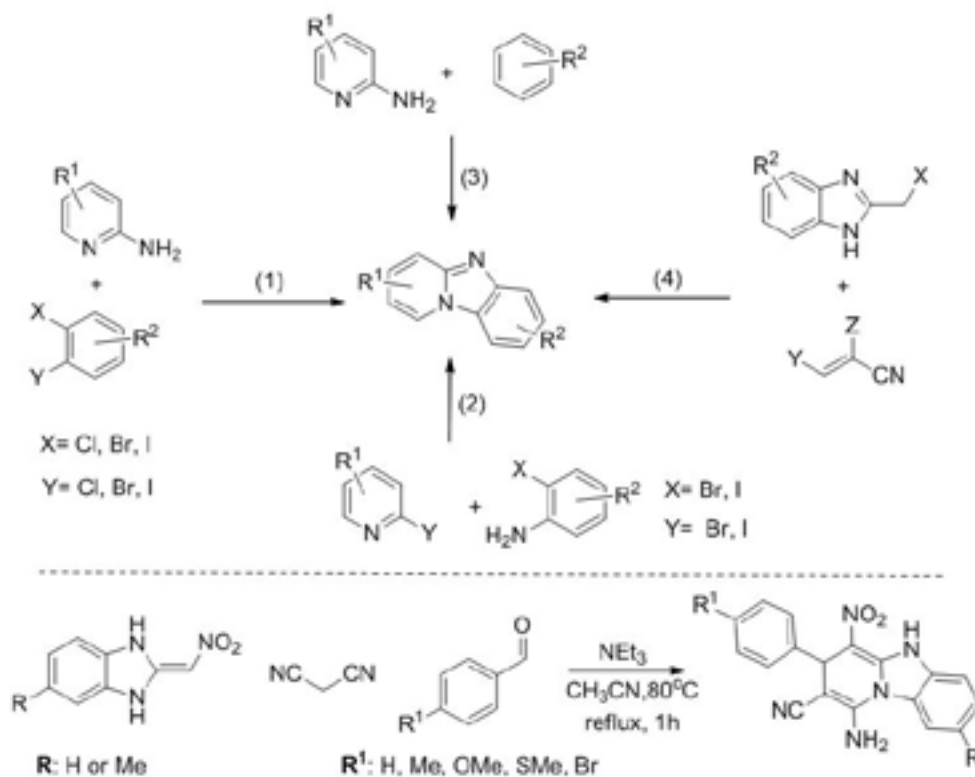


Figure 2. Methods for the synthesis of pyrido[1,2-a]benzimidazoles.

(nitromethylene)-2,3-dihydro-1H-benzo[d]imidazole), were prepared according to the literature method [12].

General Procedure for the Preparation of Pomppound 4a-l

Aromatic aldehyde (1 mmol), heterocyclic enamines (1 mmol) and malononitrile (1 mmol) were mixed in acetonitrile (15 mL) in a round-bottomed flask, and the reaction mixture was stirred at 60°C for 15 min. Triethylamine (0.5 mmol) was added and the reaction mixture was heated under reflux for 1 h (Table 1). After completion of the reaction, the precipitated solid was filtered, and washed with Et₂O (25 mL) to give the pure products with data given below.

1-amino-4-nitro-3-phenyl-3,5-dihydrobenzo[4,5]imidazo[1,2-a]pyridine-2-carbonitrile (4a): Yellow solid. Yield: 78% m.p. 245°C (decomp.). IR (KBr): $\nu = 3456$ (NH₂), 2202 (CN), 1670, 1624, 1477, 1388, 1300, 1091, 1049, 748 cm⁻¹; ¹H NMR (400 MHz, DMSO) δ 12.96 (s, 1H, NH), 7.89 (d, *J* = 8.2 Hz, 1H), 7.59 (d, *J* = 7.7 Hz, 1H), 7.45 – 7.21 (m, 4H), 7.18 (d, *J* = 7.1 Hz, 3H), 6.46 (s, 2H, NH₂), 4.95 (s, 1H); ¹³C NMR (101 MHz, DMSO) δ 148.21, 144.73, 143.49, 132.48, 129.05, 128.60, 127.55,

127.29, 125.60, 124.25, 119.51, 115.21, 113.45, 70.20, 41.59, 31.11; HRMS (-ESI-TOF) calcd for C₁₈H₁₃N₅O₂ [M-H]⁻ 331.1069, found 331.1066.

1-amino-4-nitro-3-(p-tolyl)-3,5-dihydrobenzo[4,5]imidazo[1,2-a]pyridine-2-carbonitrile (4b): Yellow solid. Yield: 82% m.p. 245°C (decomp.). IR (KBr): $\nu = 3462$, 3416 (NH₂), 2200 (CN), 1670, 1622, 1479, 1398, 1301, 1089, 1045, 734 cm⁻¹; ¹H NMR (400 MHz, DMSO) δ 13.11 (s, 1H, NH), 7.87 (d, *J* = 8.0 Hz, 2H), 7.57 (d, *J* = 7.5 Hz, 2H), 7.38 – 7.23 (m, 4H), 6.55 (s, 2H, NH₂), 4.87 (s, 1H), 2.19 (s, 3H, CH₃); ¹³C NMR (101 MHz, DMSO) δ 148.12, 144.57, 140.53, 136.75, 132.40, 129.60, 128.56, 127.23, 125.61, 124.29, 119.65, 115.31, 113.42, 105.71, 70.16, 41.15, 21.13; HRMS (-ESI-TOF) calcd for C₁₉H₁₅N₅O₂ [M-H]⁻ 345.1226, found 345.1209.

1-amino-3-(4-methoxyphenyl)-4-nitro-3,5-dihydrobenzo [4,5]imidazo[1,2-a]pyridine-2-carbonitrile (4c): Yellow solid. Yield: 85% m.p. 242°C (decomp.). IR (KBr): $\nu = 3448$, 3244 (NH₂), 2200 (CN), 1670, 1618, 1514, 1394, 1301, 1093, 1045, 736 cm⁻¹; ¹H NMR (400 MHz, DMSO) δ 13.13 (s, 1H, NH), 7.88 (d, *J* = 8.1 Hz, 1H), 7.57 (d, *J* =

7.6 Hz, 1H), 7.39 – 7.23 (m, 2H), 7.08 (d, J = 8.6 Hz, 2H), 6.79 (d, J = 6.9 Hz, 2H), 6.55 (s, 2H, NH₂), 4.86 (s, 1H), 3.65 (s, 3H, OCH₃); ¹³C NMR (101 MHz, DMSO) δ 158.85, 148.07, 144.48, 135.57, 132.40, 128.57, 128.47, 125.61, 124.27, 119.69, 115.31, 114.41, 113.41, 105.91, 70.31, 55.57, 40.74; HRMS (-ESI-TOF) calcd for C₁₉H₁₅N₅O₃ [M-H]⁻ 360.1097, found 360.1141.

1-amino-3-(4-(methylthio)phenyl)-4-nitro-3,5-dihydrobenzo [4,5]imidazo[1,2-a]pyridine-2-carbonitrile (4d): Yellow solid. Yield: 80% m.p. 247°C (decomp.). IR (KBr): ν = 3458, 3246 (NH₂), 2200 (CN), 1670, 1620, 1477, 1394, 1301, 1091, 1045, 736 cm⁻¹; ¹H NMR (400 MHz, DMSO) δ 13.00 (s, 1H, NH), 7.89 (d, J = 6.5 Hz, 1H), 7.58 (d, J = 5.5 Hz, 1H), 7.34 – 7.26 (m, 3H), 7.22 – 7.05 (m, 3H), 6.46 (s, 2H, NH₂), 4.91 (s, 1H), 2.38 (s, 3H, SCH₃); ¹³C NMR (101 MHz, DMSO) δ 148.21, 144.64, 140.33, 137.25, 132.46, 128.60, 127.99, 127.02, 125.60, 124.26, 119.47, 115.20, 113.45, 105.59, 70.09, 41.13, 15.52; HRMS (-ESI-TOF) calcd for C₁₉H₁₅N₅O₂S [M-H]⁻ 376.0868, found 376.0871.

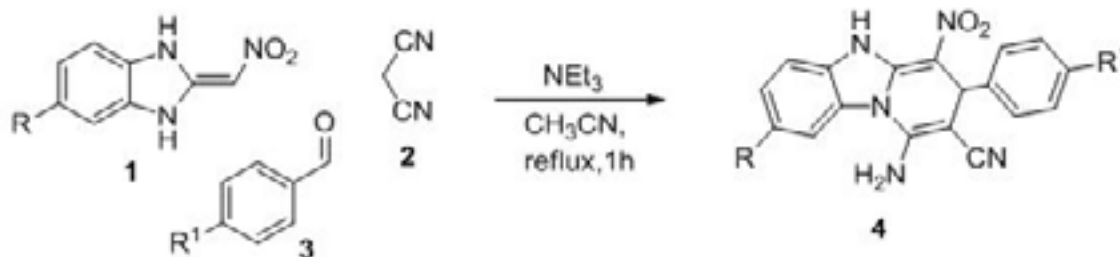
1-amino-3-(4-bromophenyl)-4-nitro-3,5-dihydrobenzo[4,5] imidazo[1,2-a]pyridine-2-carbonitrile (4e): Yellow solid. Yield: 87% m.p. 247°C (decomp.). IR (KBr): ν = 3460, 3248 (NH₂), 2198(CN), 1670, 1620, 1477, 1394, 1300, 1091, 1045, 736 cm⁻¹; ¹H NMR (400 MHz, DMSO)

δ 13.13 (s, 1H, NH), 7.88 (d, J = 7.8 Hz, 1H), 7.58 (d, J = 7.7 Hz, 1H), 7.42 (d, J = 5.5 Hz, 2H), 7.38 – 7.07 (m, 4H), 6.50 (s, 2H, NH₂), 4.94 (s, 1H); ¹³C NMR (101 MHz, DMSO) δ 148.33, 144.53, 142.87, 132.43, 131.90, 129.77, 128.57, 125.63, 124.31, 120.61, 119.49, 115.31, 113.46, 105.33, 69.37, 41.23; HRMS (-ESI-TOF) calcd for C₁₈H₁₂BrN₅O₂ [M-H]⁻ 408.0096, found 408.0098.

1-amino-8-methyl-4-nitro-3-phenyl-3,5-dihydrobenzo[4,5] imidazo[1,2-a]pyridine-2-carbonitrile (4f): Yellow solid. Yield: 75% m.p. 246°C (decomp.). IR (KBr): ν = 3397, 3253 (NH₂), 2191 (CN), 1657, 1629, 1433, 1365, 1284, 1093, 1040, 708 cm⁻¹; ¹H NMR (400 MHz, DMSO) δ 12.92 (s, 1H, NH), 7.74 (d, J = 7.3 Hz, 1H), 7.46 (d, J = 8.2 Hz, 1H), 7.23 (d, J = 7.0 Hz, 2H), 7.16 (d, J = 7.8 Hz, 4H), 6.48 (s, 2H, NH₂), 4.93 (s, 1H), 2.39 (s, 3H, CH₃); ¹³C NMR (101 MHz, DMSO) δ 148.24, 144.68, 143.53, 135.44, 133.98, 129.04, 127.53, 127.25, 126.45, 125.15, 119.62, 115.38, 113.09, 105.54, 69.76, 41.53, 21.76; HRMS (-ESI-TOF) calcd for C₁₉H₁₅N₅O₂ [M-H]⁻ 344.1147, found 344.1140.

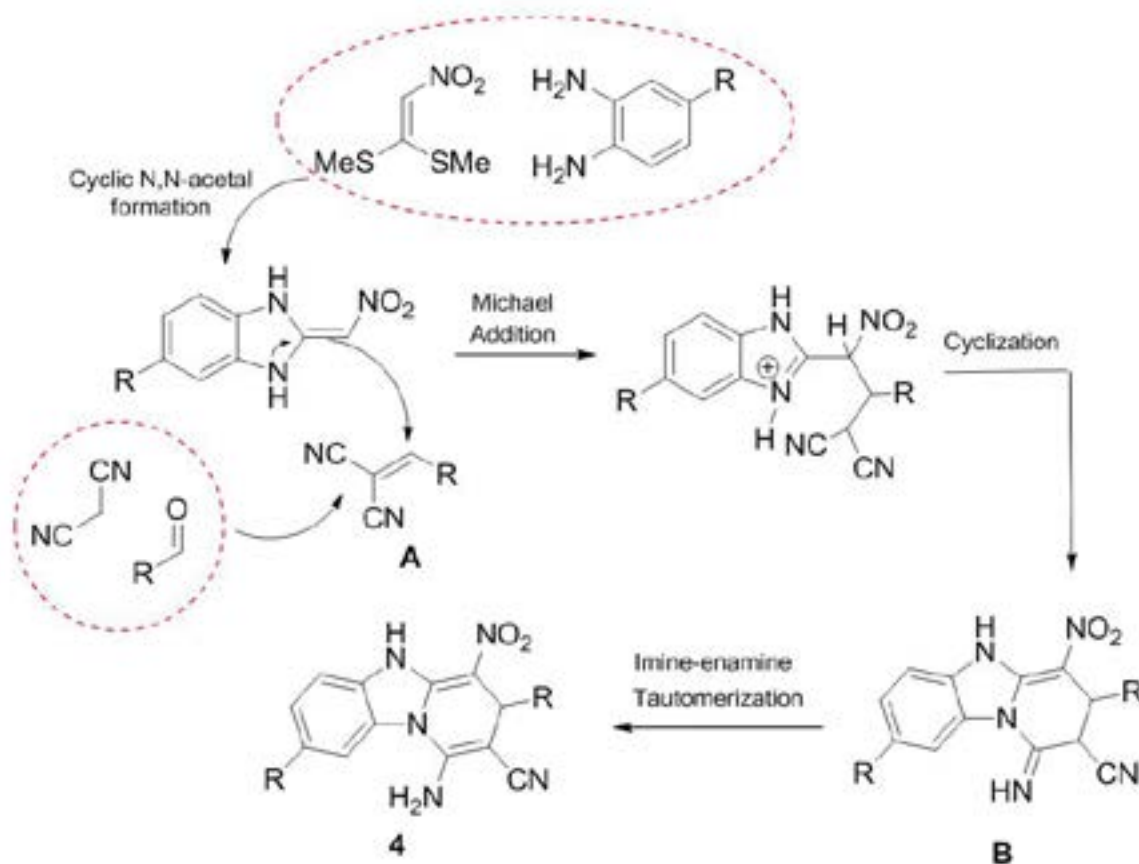
1-amino-8-methyl-4-nitro-3-(p-tolyl)-3,5-dihydrobenzo[4,5] imidazo[1,2-a]pyridine-2-carbonitrile (4g): Yellow solid. Yield: 84% m.p. 244°C (decomp.). IR (KBr): ν = 3408, 3302 (NH₂), 2202 (CN), 1670, 1624, 1458, 1396,

Table 1. Reactions of 2-(nitromethylene)-2,3-dihydro-1H-benzo[d]imidazoles with malononitrile and aromatic aldehydes.



Entry	Compound	R	R ¹	Yield(%) ^a
1	4a	H	H	78
2	4b	H	Me	82
3	4c	H	OMe	85
4	4d	H	SMe	80
5	4e	H	Br	87
6	4f	Me	H	75
7	4g	Me	Me	84
8	4h	Me	OMe	82
9	4i	Me	SMe	78
10	4l	Me	Br	85

^a Yields after purification.



Scheme 1. Possible reaction mechanism for formation of compound 4.

1282, 1093, 1043, 788 cm⁻¹; ¹H NMR (400 MHz, DMSO) δ 12.92 (s, 1H, NH), 7.75 (d, J = 8.5 Hz, 1H), 7.38 (s, 1H), 7.09 (d, J = 8.3 Hz, 1H), 7.04 (s, 4H), 6.41 (s, 2H, NH₂), 4.89 (s, 1H), 2.37 (s, 3H, CH₃), 2.20 (s, 3H, CH₃); ¹³C NMR (101 MHz, DMSO) δ 148.06, 144.64, 140.59, 136.71, 135.42, 132.63, 129.57, 127.15, 126.59, 125.13, 119.58, 114.79, 113.41, 105.65, 70.04, 41.17, 21.45, 21.08; HRMS (-ESI-TOF) calcd for C₂₀H₁₇N₅O₂ [M-H]⁻ 358.1304, found 358.1328.

1-amino-3-(4-methoxyphenyl)-8-methyl-4-nitro-3,5-dihydrobenzo[4,5]imidazo[1,2-a]pyridine-2-carbonitrile (4h): Yellow solid. Yield: 82% m.p. 240°C (decomp.). IR (KBr): ν = 3456, 3253 (NH₂), 2199 (CN), 1670, 1622, 1458, 1396, 1282, 1093, 1043, 788 cm⁻¹; ¹H NMR (400 MHz, DMSO) δ 12.88 (s, 1H, NH), 7.75 (d, J = 8.5 Hz, 1H), 7.37 (s, 1H), 7.08 (t, J = 8.3 Hz, 3H), 6.79 (d, J = 8.5 Hz, 2H), 6.40 (s, 2H, NH₂), 4.88 (s, 1H), 3.66 (s, 3H, OCH₃), 2.37 (s, 3H, CH₃); ¹³C NMR (101 MHz, DMSO) δ 158.93, 148.02, 144.60, 135.68, 135.38, 132.75, 128.38, 126.62, 125.09, 119.62, 114.79, 114.50, 113.43, 105.83, 70.15, 55.63, 40.81, 21.45; HRMS (-ESI-TOF) calcd for C₂₀H₁₇N₅O₃ [M-H]⁻ 374.1253, found 374.1286.

1-amino-8-methyl-3-(4-(methylthio)phenyl)-4-nitro-3,5-dihydrobenzo[4,5]imidazo[1,2-a]pyridine-2-carbonitrile (4i): Yellow solid. Yield: 78% m.p. 246°C (decomp.). IR (KBr): ν = 3456, 3298 (NH₂), 2200 (CN), 1670, 1622, 1456, 1392, 1284, 1095, 1043, 788 cm⁻¹; ¹H NMR (400 MHz, DMSO) δ 12.92 (s, 1H, NH), 7.75 (d, J = 8.5 Hz, 2H), 7.38 (d, J = 8.1 Hz, 1H), 7.12 (d, J = 6.1 Hz, 4H), 6.46 (s, 2H, NH₂), 4.90 (s, 1H), 2.38 (s, 3H, SCH₃), 2.37 (s, 3H, CH₃); ¹³C NMR (101 MHz, DMSO) δ 148.16, 144.62, 140.39, 137.22, 135.43, 132.69, 127.94, 127.02, 126.60, 125.14, 119.53, 114.79, 113.44, 105.51, 69.69, 41.12, 21.45, 15.53; HRMS (-ESI-TOF) calcd for C₂₀H₁₇N₅O₂S [M-H]⁻ 390.1025, found 390.1001

1-amino-3-(4-bromophenyl)-8-methyl-4-nitro-3,5-dihydrobenzo[4,5]imidazo[1,2-a]pyridine-2-carbonitrile (4l): Yellow solid. Yield: 85% m.p. 247°C (decomp.). IR (KBr): ν = 3460, 3278 (NH₂), 2200 (CN), 1670, 1624, 1456, 1394, 1249, 1095, 1043, 788 cm⁻¹; ¹H NMR (400 MHz, DMSO) δ 12.96 (s, 1H, NH), 7.76 (d, J = 8.4 Hz, 1H), 7.42 (d, J = 7.7 Hz, 3H), 7.15 (d, J = 7.6 Hz, 2H), 7.09 (d, J = 8.1 Hz, 1H), 6.50 (s, 2H, NH₂), 4.93 (s, 1H), 2.37 (s, 3H, CH₃);

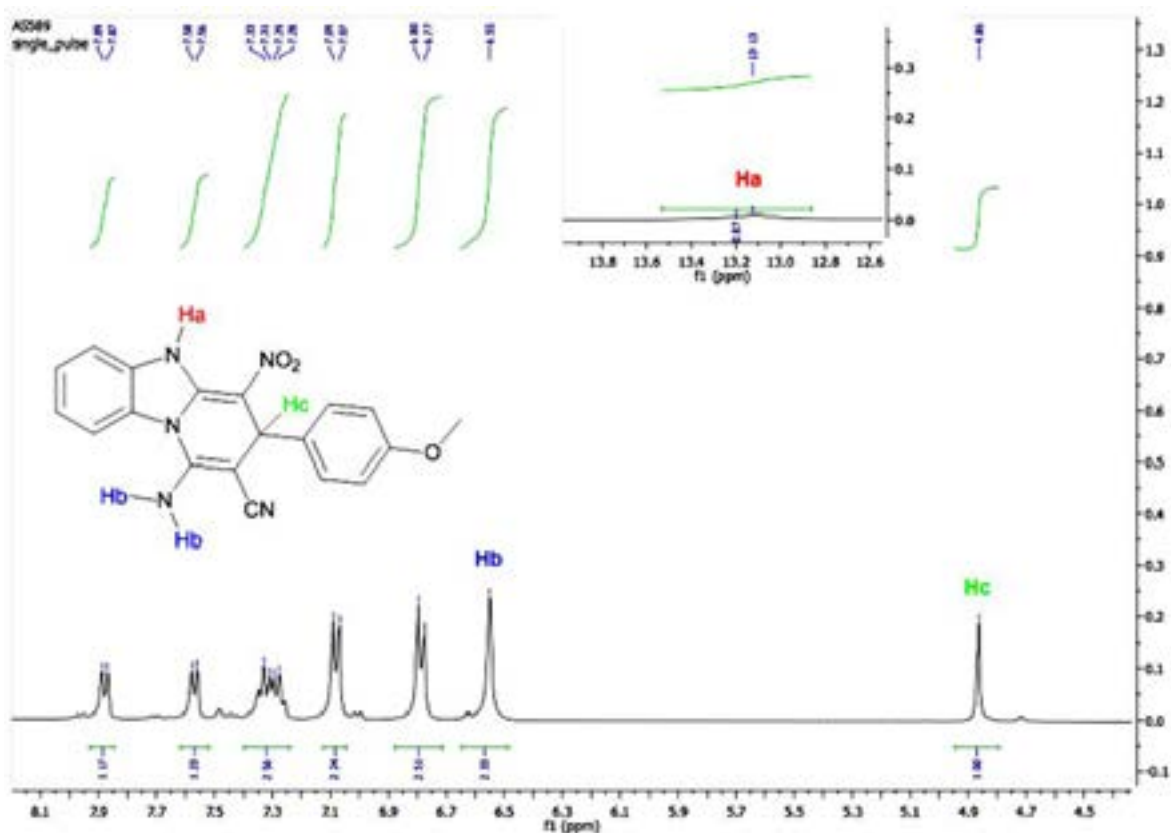


Figure 3. Expanded ^1H NMR spectrum of compound 4c.

^{13}C NMR (101 MHz, DMSO) δ 148.27, 144.58, 142.92, 135.47, 132.64, 131.89, 129.67, 126.59, 125.18, 120.58, 119.41, 114.80, 113.45, 105.25, 69.24, 41.26, 21.45; HRMS (-ESI-TOF) calcd for $\text{C}_{19}\text{H}_{14}\text{BrN}_5\text{O}_2$ [M-H] $^-$ 422.0225, found 422.0253.

RESULTS and DISCUSSION

Heterocyclic ketene enaminals (HKAs) have been widely used as valuable intermediates in multicomponent reactions due to their bisnucleophilic property that allow reaction with various substrates such as unsaturated carbonyl compounds [13], iminium ions [14], diazonium salts [12] and olefins bearing electron-withdrawing group (CN, SO_2Ph , CO_2Ph) [15].

Our initial efforts to synthesize cyclic enamine containing benzimidazole scaffold that was derived from the condensation reaction between substituted o-phenylenediamine and 1,1-bis(methylthio)-2-nitroethylene, and characterized by IR, ^1H NMR and physical data such as melting point. To the best of our knowledge, there has been only one exam-

ple mentioned in literature regarding multicomponent reaction of o-phenylenediamine, 1,1-bis(methylthio)-2-nitroethylene, malononitrile and salicylaldehyde [16]. However, no other aromatic aldehydes were used for this reaction.

Therefore, after preparation of cyclic enamines, we decided to perform multicomponent reaction by introducing related cyclic enamines 1 with malononitrile 2 and aromatic aldehydes 3 in CH_3CN at reflux temperature. After 1 hour, consumption of cyclic enamine was controlled by TLC to understand the completion of reaction. The reaction afforded the desired pyrido[1,2-a]benzimidazoles 4 in high yield (75-87%) without any purification step. The reaction condition and scope of reaction (in Table 1) clearly indicates that the reaction proceeded efficiently and smoothly with a variety of aromatic aldehydes.

The plausible reaction mechanism was proposed for the formation of corresponding pyrido[1,2-a]benzimidazoles. Presumably, the reaction begins by the addition of cyclic enamines 3 to in situ formed arylidinemalononitrile (A) which was early derived from the Knoevenagel condensation of the aldehyde 3 with malononitrile 2, and then sec-

ondary amine group of enamine attacks to nitrile carbon and cyclization affords intermediate B. This is followed by imine-enamine tautomerization of B to give desired product 4.

The structures of pyrido[1,2-a]benzimidazoles 4a-l were identified by means of IR, NMR and HRMS data. In IR spectra for compounds 4a-l, most indicative vibrational bands of NH, NH₂ and CN group appeared at around 3420, 3314-3250 and 2200 cm⁻¹, respectively. In the ¹H- and ¹³C-NMR spectra of products 4a-l, the most confirmative proton signal was the methinic CH (Hc) of the formed dihydropyrimidine ring and it resonated as singlet in a range of 4.86-4.95 ppm. Whereas another confirmative proton NMR signals belonging to NH₂ (Hb) resonated at ca. 6.40-6.55 ppm. The NH (Ha) proton of benzimidazole ring resonated at around 12.90 ppm as broad singlet and in some cases they were not easily detected (Figure 3). As for ¹³C-NMR shifts of the compound 4a-l, the resonance of the only one aliphatic carbon attached to substituted phenyl ring appeared at around 41 ppm, and the double bond carbon bearing CN group did at around 67 ppm. This indicative carbon signals are in accord with previous report where only o-hydroxyphenyl substituted of compound 4 has been exploited [16]. Also, HRMS measurements revealed that M-H values accurately coincide with the molecular formulas of the proposed structures.

Conclusion

In summary, we described a facile and efficient method for the construction of new pyrido[1,2-a]benzimidazoles via multicomponent reaction of heterocyclic enamines (1) without using tedious purification steps and identified the pyrido[1,2-a]benzimidazoles products (4) by means of spectroscopic methods successfully.

Acknowledgments

Bolu Abant İzzet Baysal University, Directorate of Research Projects Commission (BAP grant no 2018.03.03.1348) are gratefully acknowledged for financial support.

References

1. Y. Bansal, O. Silakari, The therapeutic journey of benzimidazoles: A review, *Bioorg. Med. Chem.*, 20 (2012) 6208-6236.
2. E. Badawey, T. Kappe, Benzimidazole condensed ring system. IX. Potential antineoplastics. New synthesis of some pyrido[1,2-a]benzimidazoles and related derivative, *Eur. J. Med. Chem.*, 30 (1995) 327-332.
3. J. Ndakala, R.K. Gessner, P.W. Gitari, N. October, K.L. White, A. Hudson, F. Fakorede, D.M. Shackelford, M. Kaiser, C. Yeates, S.A. Charman, K. Chibale, Antimalarial pyrido[1,2-a]benzimidazoles, *J. Med. Chem.*, 54 (2011) 4581-4589.
4. M. Hranjec, I. Piantanida, M. Kralj, L. Suman, K. Pavelic, G. Karminski-Zamola, Novel amidino-substituted thienyl- and furylvinylbenzimidazole: derivatives and their photochemical conversion into corresponding diazacyclopenta[c]fluorenes. synthesis, interactions with DNA and RNA, and antitumor evaluation. 4., *J. Med. Chem.*, 51 (2008) 4899-4910.
5. H. Takeshita, J. Watanabe, Y. Kimura, K. Kawakami, H. Takahashi, M. Takemura, A. Kitamura, K. Someya, R. Nakajima, Novel pyridobenzimidazole derivatives exhibiting antifungal activity by the inhibition of beta-1,6-glucan synthesis, *Bioorg. Med. Chem. Lett.*, 20 (2010) 3893-3896.
6. H.L. Koo, H.L. Dupont, Rifaximin: a unique gastrointestinal-selective antibiotic for enteric diseases, *Curr. Opin. Gastroenterol.*, 26 (2010) 17-25.
7. H.J. Knölker, R. Boese, R. Hitzemann, Imidazole derivatives, III. Regiospecific synthesis, structure, and fluorescence properties of highly substituted imidazo[1,2-a]pyridines and pyrido[1,2-a]benzimidazoles, *Chem. Ber.*, 123 (1990) 327-339.
8. S. Ohta, T. Yuasa, Y. Narita, I. Kawasaki, E. Minamii, M. Yamashita, Synthesis and application of imidazole derivatives. Synthesis of pyrido[1,2-a]benzimidazolone derivatives, *Heterocycles*, 32 (1991) 1923-1931.
9. H. Schaefer, M. Gruner, G. Grossmann, K. Gewald, On the synthesis and structure of 8-nitro-imidazo[1,2-a]pyridines, *Monatsh. Chem.*, 122 (1991) 959-966.
10. D.B. Zhao, J.Y. Hu, N.J. Wu, X.L. Huang, X.R. Qin, J.B. Lan, J.S. You, Regiospecific synthesis of 1,2-disubstituted (hetero) aryl fused imidazoles with tunable fluorescent emission, *Org. Lett.*, 13 (2011) 6516-6519.
11. T. Iwaki, A. Yasuhara, T. Sakamoto, Novel synthetic strategy of carbolines via palladium-catalyzed amination and arylation reaction, *J. Chem. Soc., Perkin Trans.*, 1 (1999) 1505-1510.
12. Z. Wu, Q. Huang, X. Zhou, L. Yu, Z. Li, D. Wu, Synthesis of pyrido[1,2-a]benzimidazoles through a copper-catalyzed cascade C-N coupling process, *Eur. J. Org. Chem.*, 2011 (2011) 5242-5245.
13. H. Wang, Y. Wang, C. Peng, J. Zhang, Q. Zhu, A direct intramolecular C-H amination reaction cocatalyzed by copper(II) and iron(III) as part of an efficient route for the synthesis of pyrido[1,2-a]benzimidazoles from N-aryl-2-aminopyridines, *J. Am. Chem. Soc.*, 132 (2010) 13217-13219.
14. K.S. Masters, T.R.M. Rauws, A.K. Yadav, W.A. Herrebout, B. Van der Veken, B. U.W. Maes, On the importance of an acid additive in the synthesis of pyrido[1,2-a]benzimidazoles by direct copper-catalyzed amination, *Chem. Eur. J.*, 17 (2011) 6315-6330.

15. D. Liang, Y. He, L. Liu, Q. Zhu, A metal-free tandem demethylenation/C(sp²)-H cycloamination process of N-benzyl-2-aminopyridines via C-C and C-N bond cleavage, *Org. Lett.*, 15 (2013) 3476-3479.
16. S.M. Barolo, Y. Wang, R.A. Rossi, G.D. Cuny, Synthesis of pyrido [1, 2-a] benzimidazoles by photo-stimulated C-N bond formation via S_{RN}1 reactions, *Tetrahedron*, 69 (2013) 5487-5494.
17. Y. He, J. Huang, D. Liang, Q. Zhu, C-H cycloamination of N-aryl-2-aminopyridines and N-arylamidines catalyzed by an in situ generated hypervalent iodine(III) reagent, *Chem. Commun.*, 49 (2013) 7352-7354.
18. D. Rao, S. Rasheed, R. Vishwakarma, P. Das, Hypervalent iodine(III) catalyzed oxidative C-N bond formation in water: synthesis of benzimidazole-fused heterocycles, *RSC Adv.*, 4 (2014) 25600-25604.
19. G. Qian, B. Liu, Q. Tan, S. Zhang, B. Xu, Hypervalent iodine(III) promoted direct synthesis of imidazo[1,2-a]pyrimidines, *Eur. J. Org. Chem.*, 2014 (2014) 4837-4843.
20. N. Kutsumura, S. Kunimatsu, K. Kagawa, T. Otani, T. Saito, Synthesis of benzimidazole-fused heterocycles by intramolecular oxidative C-N bond formation using hypervalent iodine reagents, *Synthesis*, 43 (2011) 3235-3240.
21. S. Manna, K. Matcha, A.P. Antonchick, Metal-free annulation of arenes with 2-aminopyridine derivatives: The methyl group as a traceless non-chelating directing group, *Angew. Chem. Int. Ed.*, 53 (2014) 8163-8166.
22. H. Foks, D. Pancechowska-Ksepko, M. Janowiec, Z. Zwolska, E. Augustynowicz-Kopeć, Synthesis and tuberculostatic activity of some 1,1-bis-methylthio-2-nitro-ethene derivatives, *Phosphorus Sulfur*, 180 (2005) 2291-2297.
23. M. Yildırım, D. Celikel, N. Evis, D.W. Knight, B.M. Kariuki, Base-promoted new C-C bond formation: an expedient route for the preparation of thiazolo-and imidazolo-pyridinones via Michael addition, *Tetrahedron*, 70 (2014) 5674-5681.
24. M. Yildırım, D. Celikel, Y. Dürüst, D.W. Knight, B.M. Kariuki, A rapid and efficient protocol for the synthesis of novel nitrothiazolo [3, 2-c] pyrimidines via microwave-mediated Mannich cyclisation, *Tetrahedron*, 70 (2014) 2122-2128.
25. C. Altug, A.K. Burnett, E. Caner, Y. Dürüst, M.C. Elliott, R.P. Glanville, A.D. Westwell, An efficient one-pot multicomponent approach to 5-amino-7-aryl-8-nitrothiazolo [3,2-a] pyridines, *Tetrahedron*, 67 (2011) 9522-9528.
26. D. Elumalai, R. Gnanasekaran, S. Leelakrishnan, G. Nachimuthu, T. Kannan, T.P. Paramasivam, K. Jayabal, InCl₃-assisted eco-friendly approach for N-fused 1,4-dihydropyridine scaffolds via ring opening michael addition of cyclic nitroketene and iminocoumarin: Synthesis and DFT studies, *Chem. Select*, 3 (2018) 2070-2079.



Practical Synthesis of Pyrido [1,2-A] Benzimidazoles Via Multicomponent Reactions

Çok Bileşenli Tepkimeler Yoluyla Pirido [1,2-A] Benzimidazolların Pratik Sentezi

Akın Sağırılı

Department of Chemistry, MS 14018, Bolu Abant İzzet Baysal University, Bolu, Turkey.

ABSTRACT

A facile and efficient synthesis of 1-amino-3-(4-substitued)-4-nitro-3,5-dihydrobenzo[4,5]imidazo[1,2-a]pyridine-2-carbonitriles was conducted via one-pot multicomponent reaction of 2-(nitromethylene)-2,3-dihydro-1H-benzo[d]imidazole with malononitrile and aromatic aldehydes. Besides, no tedious work-up procedure was necessary for the isolation of desired products which were precipitated out of reaction medium in pure state. Ten new title compounds were characterized by the means of physical and spectroscopic methods (m.p., IR, NMR and TOF-MS analyses).

Key Words

Heterocyclic ketene aminal, enamine, multicomponent, benzimidazole, pyrido[1,2-a]benzimidazole.

Öz

Tek basamakta siklik enamın (2-(nitrometilen)-2,3-dihidro-1H-benzo[d]imidazol), malononitril ve aromatik aldehit ile çoklu bileşenli tepkime üzerinden 1-amino-3-(4-substitue)-4-nitro-3,5-dihidrobenzo[4,5]imidazo[1,2-a]piridin-2-karbonitril lerin kolay ve etkili bir biçimde sentezi açığa çıkarıldı. Ayrıca, istenilen ürünlerin eldesinde herhangi bir saflaştırma prosedürü gerektirmedi. Bütün ürünler saf olarak tepkime ortamında çöktüldü. On yeni yapı fiziksel ve spektroskopik yöntemler kullanılarak karakterize edildi (e.n., IR, NMR ve TOF-MS analizleri).

Anahtar Kelimeler

Heterosiklik keten aminal, enamın, çok-bileşenli, benzimidazol, pirido[1,2-a]benzimidazol.

Article History: Received: Apr 8, 2019; Revised: Jul 15, 2019; Accepted: Sep 12, 2019; Available Online: Nov 1, 2019.

DOI: <https://doi.org/10.15671/hjbc.550890>

Correspondence to: A. Sağırılı, Department of Chemistry, Bolu Abant İzzet Baysal University, Bolu, Turkey.

E-Mail: sagirli_a@ibu.edu.tr

INTRODUCTION

Benzimidazole as an important heterocycle represents key structure of many biologically active compounds [1]. Molecules containing this core have taken great attention in the field of medicinal chemistry during last decades. Especially, the pyrido[1,2-a]benzimidazoles exhibited various bioactivities such as anticancer [2], antimalarial [3], antiproliferative [4], antifungal [5], antiviral and antipyretic agents [3]. Moreover, this heterocyclic unit can also be found as embedded in a commercially available antibiotic drug, Rifaximin [6] (Figure 1).

Due to aforementioned biological properties and medicinal applications, development of efficient and atom economic strategies through the synthesis of pyrido[1,2-a]benzimidazoles has attracted considerable interest [7]. Up to now, many methods have been utilized for the synthesis of these heterocycles by transition metal-catalyzed nucleophilic substitution of 2-aminopyridines with *o*-dihaloarenes (1) [8], C-N coupling of 2-haloanilines with 2-halopyridines, intramolecular cyclization of *N*-aryl-2-aminopyridines (2) [9], metal-free annulation of arenes with 2-aminopyridine derivatives (3) [10] and cyclocondensation of benzimidazoles with bifunctional reagents (4) (Figure 2) [11].

Although the synthetic methods in recent literature are convenient for the construction of pyrido[1,2-a]benzi-

midazoles, many of them may require expensive transition-metal catalysts, elevated reaction temperatures, extensive reaction times and tedious work-up procedures [7]. The difficulties in the preparation of this heterocycles prompted us to investigate simple and work-up free synthetic methodology. In this context, we herein report one-pot synthetic method by the multicomponent reaction of 2-(nitromethylene)-2,3-dihydro-1H-benzo[d]imidazoles with an active methylene compound, malononitrile, and aromatic aldehydes in a single-step without further purification.

MATERIALS and METHODS

General

Infrared spectra were recorded on a SHIMADZU FTIR-8400S instrument using KBr pellets. HRMS were run on a Waters Lct Premier XE oa-TOF Mass Spectrometer. ¹H-NMR and ¹³C-NMR spectra were recorded on JEOL-ECS400 Delta2 NMR spectrometer (400 MHz for proton and 100 MHz for carbon) at ambient temperature. All chemical shifts were reported in ppm downfield from TMS. Coupling constants (*J*) are reported in Hz. Melting points were determined on a MELTEMP apparatus and uncorrected. TLC was performed using precoated plates with fluorescent indicator (Merck 5735). The stain solutions of permanganate were used for visualization of the TLC spots. Cyclic enamines, (2-(nitromethylene)-2,3-dihydro-1H-benzo[d]imidazole and ((*E*)-5-methyl-2-

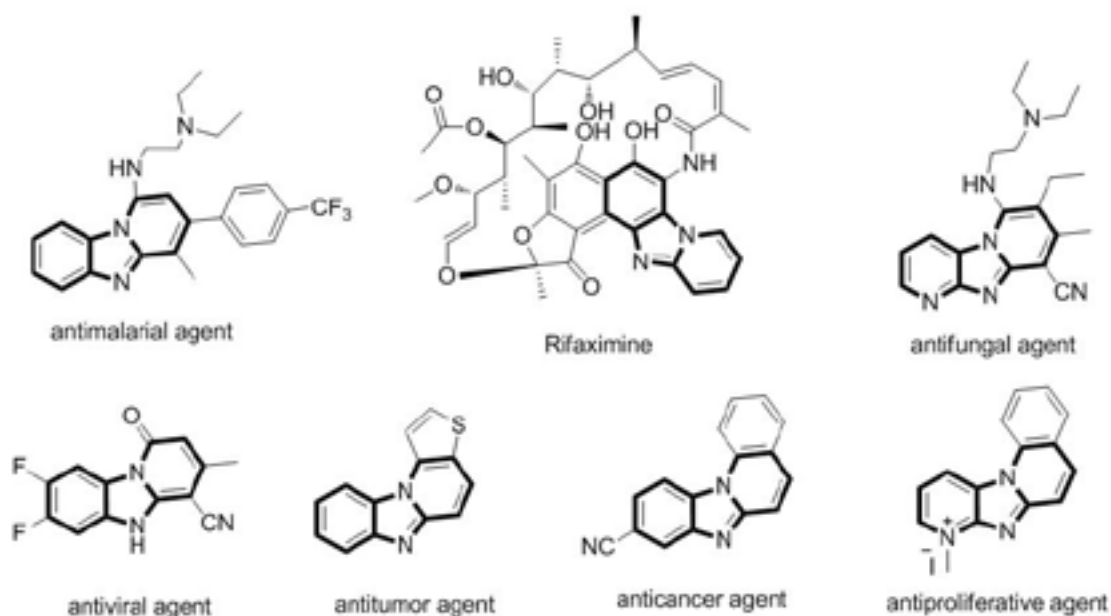


Figure 1. Some biologically important pyrido[1,2-a]benzimidazole derivatives.

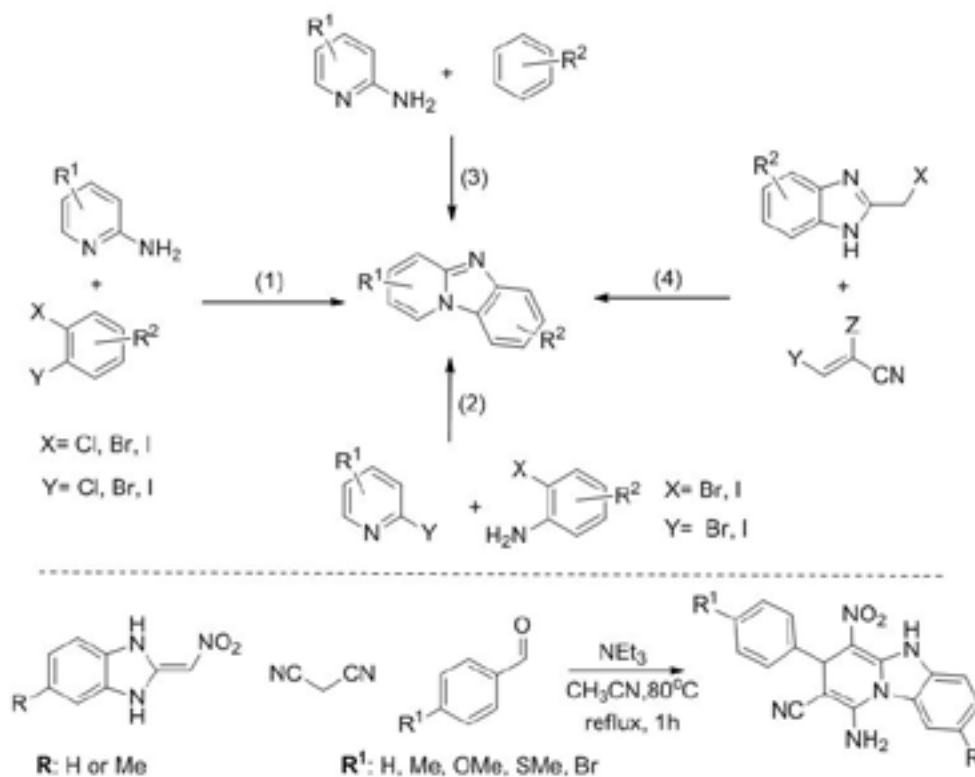


Figure 2. Methods for the synthesis of pyrido[1,2-a]benzimidazoles.

(nitromethylene)-2,3-dihydro-1H-benzo[d]imidazole), were prepared according to the literature method [12].

General Procedure for the Preparation of Pomppound 4a-l

Aromatic aldehyde (1 mmol), heterocyclic enamines (1 mmol) and malononitrile (1 mmol) were mixed in acetonitrile (15 mL) in a round-bottomed flask, and the reaction mixture was stirred at 60°C for 15 min. Triethylamine (0.5 mmol) was added and the reaction mixture was heated under reflux for 1 h (Table 1). After completion of the reaction, the precipitated solid was filtered, and washed with Et₂O (25 mL) to give the pure products with data given below.

1-amino-4-nitro-3-phenyl-3,5-dihydrobenzo[4,5]imidazo[1,2-a]pyridine-2-carbonitrile (4a): Yellow solid. Yield: 78% m.p. 245°C (decomp.). IR (KBr): $\nu = 3456$ (NH₂), 2202 (CN), 1670, 1624, 1477, 1388, 1300, 1091, 1049, 748 cm⁻¹; ¹H NMR (400 MHz, DMSO) δ 12.96 (s, 1H, NH), 7.89 (d, *J* = 8.2 Hz, 1H), 7.59 (d, *J* = 7.7 Hz, 1H), 7.45 – 7.21 (m, 4H), 7.18 (d, *J* = 7.1 Hz, 3H), 6.46 (s, 2H, NH₂), 4.95 (s, 1H); ¹³C NMR (101 MHz, DMSO) δ 148.21, 144.73, 143.49, 132.48, 129.05, 128.60, 127.55,

127.29, 125.60, 124.25, 119.51, 115.21, 113.45, 70.20, 41.59, 31.11; HRMS (-ESI-TOF) calcd for C₁₈H₁₃N₅O₂ [M-H]⁻ 331.1069, found 331.1066.

1-amino-4-nitro-3-(*p*-tolyl)-3,5-dihydrobenzo[4,5]imidazo[1,2-a]pyridine-2-carbonitrile (4b): Yellow solid. Yield: 82% m.p. 245°C (decomp.). IR (KBr): $\nu = 3462$, 3416 (NH₂), 2200 (CN), 1670, 1622, 1479, 1398, 1301, 1089, 1045, 734 cm⁻¹; ¹H NMR (400 MHz, DMSO) δ 13.11 (s, 1H, NH), 7.87 (d, *J* = 8.0 Hz, 2H), 7.57 (d, *J* = 7.5 Hz, 2H), 7.38 – 7.23 (m, 4H), 6.55 (s, 2H, NH₂), 4.87 (s, 1H), 2.19 (s, 3H, CH₃); ¹³C NMR (101 MHz, DMSO) δ 148.12, 144.57, 140.53, 136.75, 132.40, 129.60, 128.56, 127.23, 125.61, 124.29, 119.65, 115.31, 113.42, 105.71, 70.16, 41.15, 21.13; HRMS (-ESI-TOF) calcd for C₁₉H₁₅N₅O₂ [M-H]⁻ 345.1226, found 345.1209.

1-amino-3-(4-methoxyphenyl)-4-nitro-3,5-dihydrobenzo [4,5]imidazo[1,2-a]pyridine-2-carbonitrile (4c): Yellow solid. Yield: 85% m.p. 242°C (decomp.). IR (KBr): $\nu = 3448$, 3244 (NH₂), 2200 (CN), 1670, 1618, 1514, 1394, 1301, 1093, 1045, 736 cm⁻¹; ¹H NMR (400 MHz, DMSO) δ 13.13 (s, 1H, NH), 7.88 (d, *J* = 8.1 Hz, 1H), 7.57 (d, *J* =

7.6 Hz, 1H), 7.39 – 7.23 (m, 2H), 7.08 (d, $J = 8.6$ Hz, 2H), 6.79 (d, $J = 6.9$ Hz, 2H), 6.55 (s, 2H, NH_2), 4.86 (s, 1H), 3.65 (s, 3H, OCH_3); ^{13}C NMR (101 MHz, DMSO) δ 158.85, 148.07, 144.48, 135.57, 132.40, 128.57, 128.47, 125.61, 124.27, 119.69, 115.31, 114.41, 113.41, 105.91, 70.31, 55.57, 40.74; HRMS (-ESI-TOF) calcd for $\text{C}_{19}\text{H}_{15}\text{N}_5\text{O}_3$ [$\text{M}-\text{H}$] 360.1097, found 360.1141.

1-amino-3-(4-(methylthio)phenyl)-4-nitro-3,5-dihydrobenzo [4,5]imidazo[1,2-a]pyridine-2-carbonitrile (4d): Yellow solid. Yield: 80% m.p. 247°C (decomp.). IR (KBr): $\nu = 3458, 3246$ (NH_2), 2200 (CN), 1670, 1620, 1477, 1394, 1301, 1091, 1045, 736 cm^{-1} ; ^1H NMR (400 MHz, DMSO) δ 13.00 (s, 1H, NH), 7.89 (d, $J = 6.5$ Hz, 1H), 7.58 (d, $J = 5.5$ Hz, 1H), 7.34 – 7.26 (m, 3H), 7.22 – 7.05 (m, 3H), 6.46 (s, 2H, NH_2), 4.91 (s, 1H), 2.38 (s, 3H, SCH_3); ^{13}C NMR (101 MHz, DMSO) δ 148.21, 144.64, 140.33, 137.25, 132.46, 128.60, 127.99, 127.02, 125.60, 124.26, 119.47, 115.20, 113.45, 105.59, 70.09, 41.13, 15.52; HRMS (-ESI-TOF) calcd for $\text{C}_{19}\text{H}_{15}\text{N}_5\text{O}_2\text{S}$ [$\text{M}-\text{H}$] 376.0868, found 376.0871.

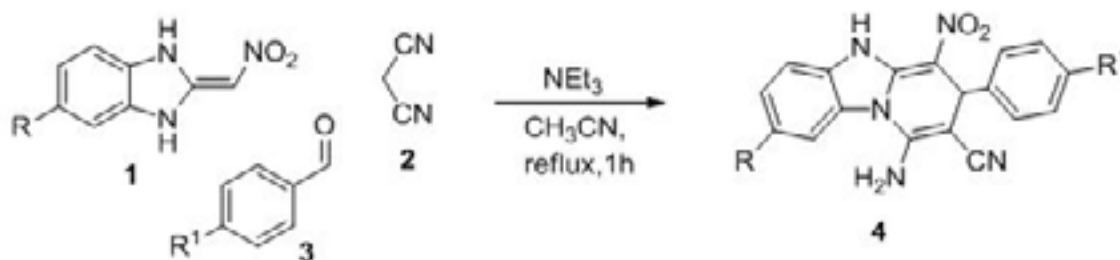
1-amino-3-(4-bromophenyl)-4-nitro-3,5-dihydrobenzo[4,5] imidazo[1,2-a]pyridine-2-carbonitrile (4e): Yellow solid. Yield: 87% m.p. 247°C (decomp.). IR (KBr): $\nu = 3460, 3248$ (NH_2), 2198 (CN), 1670, 1620, 1477, 1394, 1300, 1091, 1045, 736 cm^{-1} ; ^1H NMR (400 MHz, DMSO)

δ 13.13 (s, 1H, NH), 7.88 (d, $J = 7.8$ Hz, 1H), 7.58 (d, $J = 7.7$ Hz, 1H), 7.42 (d, $J = 5.5$ Hz, 2H), 7.38 – 7.07 (m, 4H), 6.50 (s, 2H, NH_2), 4.94 (s, 1H); ^{13}C NMR (101 MHz, DMSO) δ 148.33, 144.53, 142.87, 132.43, 131.90, 129.77, 128.57, 125.63, 124.31, 120.61, 119.49, 115.31, 113.46, 105.33, 69.37, 41.23; HRMS (-ESI-TOF) calcd for $\text{C}_{18}\text{H}_{12}\text{BrN}_5\text{O}_2$ [$\text{M}-\text{H}$] 408.0096, found 408.0098.

1-amino-8-methyl-4-nitro-3-phenyl-3,5-dihydrobenzo[4,5] imidazo[1,2-a]pyridine-2-carbonitrile (4f): Yellow solid. Yield: 75% m.p. 246°C (decomp.). IR (KBr): $\nu = 3397, 3253$ (NH_2), 2191 (CN), 1657, 1629, 1433, 1365, 1284, 1093, 1040, 708 cm^{-1} ; ^1H NMR (400 MHz, DMSO) δ 12.92 (s, 1H, NH), 7.74 (d, $J = 7.3$ Hz, 1H), 7.46 (d, $J = 8.2$ Hz, 1H), 7.23 (d, $J = 7.0$ Hz, 2H), 7.16 (d, $J = 7.8$ Hz, 4H), 6.48 (s, 2H, NH_2), 4.93 (s, 1H), 2.39 (s, 3H, CH_3); ^{13}C NMR (101 MHz, DMSO) δ 148.24, 144.68, 143.53, 135.44, 133.98, 129.04, 127.53, 127.25, 126.45, 125.15, 119.62, 115.38, 113.09, 105.54, 69.76, 41.53, 21.76; HRMS (-ESI-TOF) calcd for $\text{C}_{19}\text{H}_{15}\text{N}_5\text{O}_2$ [$\text{M}-\text{H}$] 344.1147, found 344.1140.

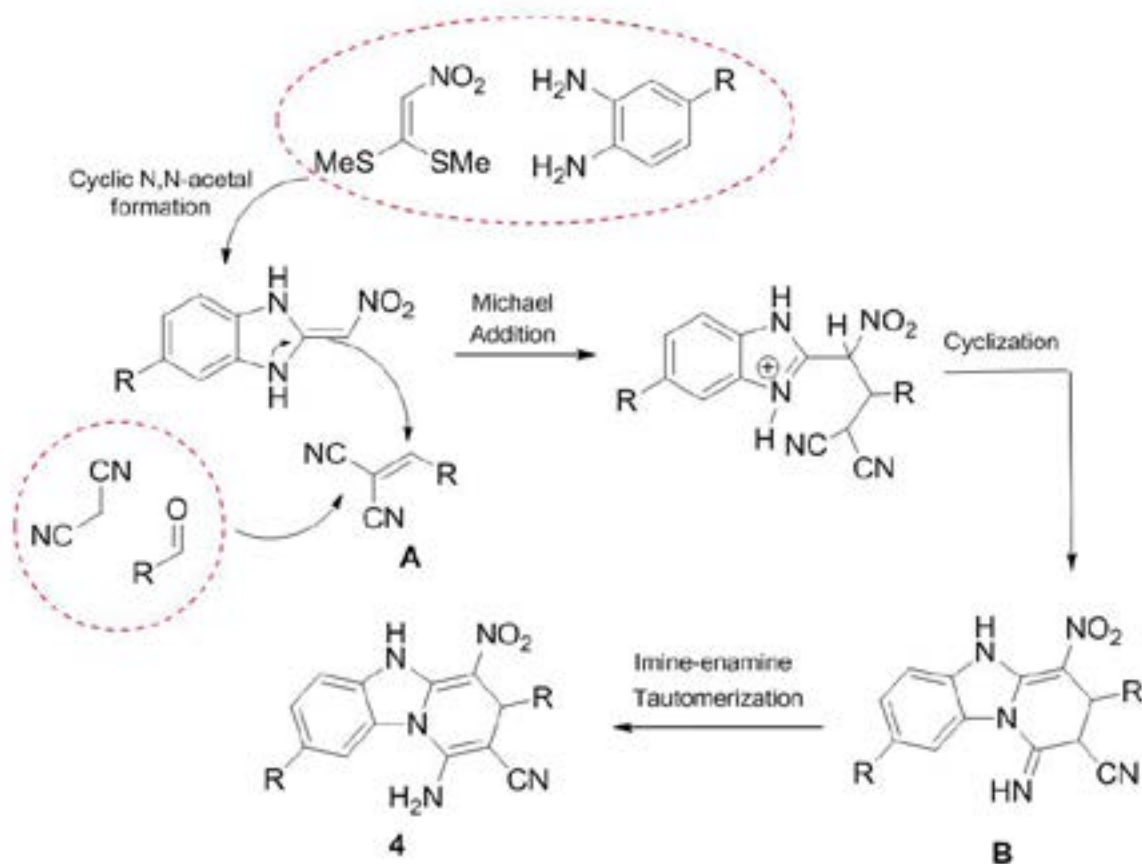
1-amino-8-methyl-4-nitro-3-(p-tolyl)-3,5-dihydrobenzo[4,5] imidazo[1,2-a]pyridine-2-carbonitrile (4g): Yellow solid. Yield: 84% m.p. 244°C (decomp.). IR (KBr): $\nu = 3408, 3302$ (NH_2), 2202 (CN), 1670, 1624, 1458, 1396,

Table 1. Reactions of 2-(nitromethylene)-2,3-dihydro-1H-benzo[d]imidazoles with malononitrile and aromatic aldehydes.



Entry	Compound	R	R ¹	Yield(%) ^a
1	4a	H	H	78
2	4b	H	Me	82
3	4c	H	OMe	85
4	4d	H	SMe	80
5	4e	H	Br	87
6	4f	Me	H	75
7	4g	Me	Me	84
8	4h	Me	OMe	82
9	4i	Me	SMe	78
10	4l	Me	Br	85

^a Yields after purification.



Scheme 1. Possible reaction mechanism for formation of compound 4.

1282, 1093, 1043, 788 cm⁻¹; ¹H NMR (400 MHz, DMSO) δ 12.92 (s, 1H, NH), 7.75 (d, J = 8.5 Hz, 1H), 7.38 (s, 1H), 7.09 (d, J = 8.3 Hz, 1H), 7.04 (s, 4H), 6.41 (s, 2H, NH₂), 4.89 (s, 1H), 2.37 (s, 3H, CH₃), 2.20 (s, 3H, CH₃); ¹³C NMR (101 MHz, DMSO) δ 148.06, 144.64, 140.59, 136.71, 135.42, 132.63, 129.57, 127.15, 126.59, 125.13, 119.58, 114.79, 113.41, 105.65, 70.04, 41.17, 21.45, 21.08; HRMS (-ESI-TOF) calcd for C₂₀H₁₇N₅O₂ [M-H]⁻ 358.1304, found 358.1328.

1-amino-3-(4-methoxyphenyl)-8-methyl-4-nitro-3,5-dihydrobenzo[4,5]imidazo[1,2-a]pyridine-2-carbonitrile (4h): Yellow solid. Yield: 82% m.p. 240°C (decomp.). IR (KBr): ν = 3456, 3253 (NH₂), 2199 (CN), 1670, 1622, 1458, 1396, 1282, 1093, 1043, 788 cm⁻¹; ¹H NMR (400 MHz, DMSO) δ 12.88 (s, 1H, NH), 7.75 (d, J = 8.5 Hz, 1H), 7.37 (s, 1H), 7.08 (t, J = 8.3 Hz, 3H), 6.79 (d, J = 8.5 Hz, 2H), 6.40 (s, 2H, NH₂), 4.88 (s, 1H), 3.66 (s, 3H, OCH₃), 2.37 (s, 3H, CH₃); ¹³C NMR (101 MHz, DMSO) δ 158.93, 148.02, 144.60, 135.68, 135.38, 132.75, 128.38, 126.62, 125.09, 119.62, 114.79, 114.50, 113.43, 105.83, 70.15, 55.63, 40.81, 21.45; HRMS (-ESI-TOF) calcd for C₂₀H₁₇N₅O₃ [M-H]⁻ 374.1253, found 374.1286.

1-amino-8-methyl-3-(4-(methylthio)phenyl)-4-nitro-3,5-dihydrobenzo[4,5]imidazo[1,2-a]pyridine-2-carbonitrile (4i): Yellow solid. Yield: 78% m.p. 246°C (decomp.). IR (KBr): ν = 3456, 3298 (NH₂), 2200 (CN), 1670, 1622, 1456, 1392, 1284, 1095, 1043, 788 cm⁻¹; ¹H NMR (400 MHz, DMSO) δ 12.92 (s, 1H, NH), 7.75 (d, J = 8.5 Hz, 2H), 7.38 (d, J = 8.1 Hz, 1H), 7.12 (d, J = 6.1 Hz, 4H), 6.46 (s, 2H, NH₂), 4.90 (s, 1H), 2.38 (s, 3H, SCH₃), 2.37 (s, 3H, CH₃); ¹³C NMR (101 MHz, DMSO) δ 148.16, 144.62, 140.39, 137.22, 135.43, 132.69, 127.94, 127.02, 126.60, 125.14, 119.53, 114.79, 113.44, 105.51, 69.69, 41.12, 21.45, 15.53; HRMS (-ESI-TOF) calcd for C₂₀H₁₇N₅O₂S [M-H]⁻ 390.1025, found 390.1001

1-amino-3-(4-bromophenyl)-8-methyl-4-nitro-3,5-dihydrobenzo[4,5]imidazo[1,2-a]pyridine-2-carbonitrile (4l): Yellow solid. Yield: 85% m.p. 247°C (decomp.). IR (KBr): ν = 3460, 3278 (NH₂), 2200 (CN), 1670, 1624, 1456, 1394, 1249, 1095, 1043, 788 cm⁻¹; ¹H NMR (400 MHz, DMSO) δ 12.96 (s, 1H, NH), 7.76 (d, J = 8.4 Hz, 1H), 7.42 (d, J = 7.7 Hz, 3H), 7.15 (d, J = 7.6 Hz, 2H), 7.09 (d, J = 8.1 Hz, 1H), 6.50 (s, 2H, NH₂), 4.93 (s, 1H), 2.37 (s, 3H, CH₃);

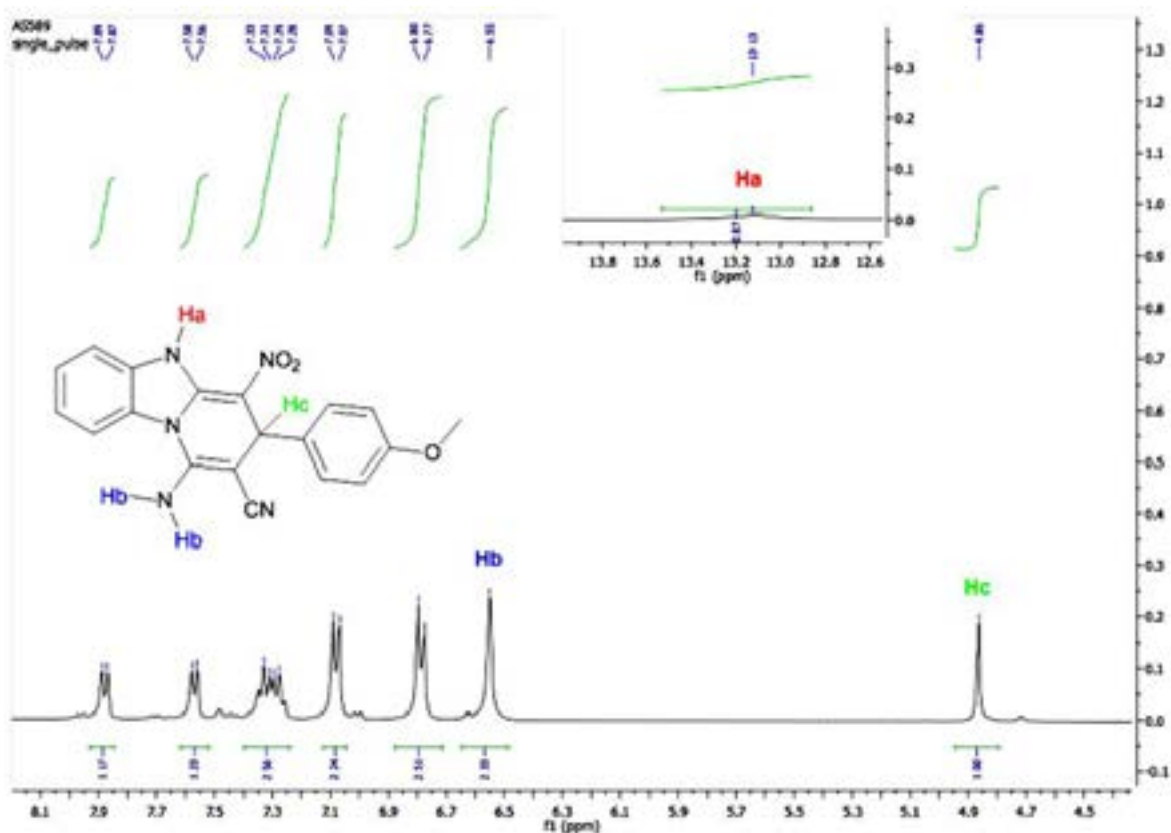


Figure 3. Expanded ^1H NMR spectrum of compound 4c.

^{13}C NMR (101 MHz, DMSO) δ 148.27, 144.58, 142.92, 135.47, 132.64, 131.89, 129.67, 126.59, 125.18, 120.58, 119.41, 114.80, 113.45, 105.25, 69.24, 41.26, 21.45; HRMS (-ESI-TOF) calcd for $\text{C}_{19}\text{H}_{14}\text{BrN}_5\text{O}_2$ [M-H] $^-$ 422.0225, found 422.0253.

RESULTS and DISCUSSION

Heterocyclic ketene enaminals (HKAs) have been widely used as valuable intermediates in multicomponent reactions due to their bisnucleophilic property that allow reaction with various substrates such as unsaturated carbonyl compounds [13], iminium ions [14], diazonium salts [12] and olefins bearing electron-withdrawing group (CN, SO_2Ph , CO_2Ph) [15].

Our initial efforts to synthesize cyclic enamine containing benzimidazole scaffold that was derived from the condensation reaction between substituted o-phenylenediamine and 1,1-bis(methylthio)-2-nitroethylene, and characterized by IR, ^1H NMR and physical data such as melting point. To the best of our knowledge, there has been only one exam-

ple mentioned in literature regarding multicomponent reaction of o-phenylenediamine, 1,1-bis(methylthio)-2-nitroethylene, malononitrile and salicylaldehyde [16]. However, no other aromatic aldehydes were used for this reaction.

Therefore, after preparation of cyclic enamines, we decided to perform multicomponent reaction by introducing related cyclic enamines 1 with malononitrile 2 and aromatic aldehydes 3 in CH_3CN at reflux temperature. After 1 hour, consumption of cyclic enamine was controlled by TLC to understand the completion of reaction. The reaction afforded the desired pyrido[1,2-a]benzimidazoles 4 in high yield (75-87%) without any purification step. The reaction condition and scope of reaction (in Table 1) clearly indicates that the reaction proceeded efficiently and smoothly with a variety of aromatic aldehydes.

The plausible reaction mechanism was proposed for the formation of corresponding pyrido[1,2-a]benzimidazoles. Presumably, the reaction begins by the addition of cyclic enamines 3 to in situ formed arylidinemalononitrile (A) which was early derived from the Knoevenagel condensation of the aldehyde 3 with malononitrile 2, and then sec-

ondary amine group of enamine attacks to nitrile carbon and cyclization affords intermediate B. This is followed by imine-enamine tautomerization of B to give desired product 4.

The structures of pyrido[1,2-a]benzimidazoles 4a-l were identified by means of IR, NMR and HRMS data. In IR spectra for compounds 4a-l, most indicative vibrational bands of NH, NH₂ and CN group appeared at around 3420, 3314-3250 and 2200 cm⁻¹, respectively. In the ¹H- and ¹³C-NMR spectra of products 4a-l, the most confirmative proton signal was the methinic CH (Hc) of the formed dihydropyrimidine ring and it resonated as singlet in a range of 4.86-4.95 ppm. Whereas another confirmative proton NMR signals belonging to NH₂ (Hb) resonated at ca. 6.40-6.55 ppm. The NH (Ha) proton of benzimidazole ring resonated at around 12.90 ppm as broad singlet and in some cases they were not easily detected (Figure 3). As for ¹³C-NMR shifts of the compound 4a-l, the resonance of the only one aliphatic carbon attached to substituted phenyl ring appeared at around 41 ppm, and the double bond carbon bearing CN group did at around 67 ppm. This indicative carbon signals are in accord with previous report where only o-hydroxyphenyl substituted of compound 4 has been exploited [16]. Also, HRMS measurements revealed that M-H values accurately coincide with the molecular formulas of the proposed structures.

Conclusion

In summary, we described a facile and efficient method for the construction of new pyrido[1,2-a]benzimidazoles via multicomponent reaction of heterocyclic enamines (1) without using tedious purification steps and identified the pyrido[1,2-a]benzimidazoles products (4) by means of spectroscopic methods successfully.

Acknowledgments

Bolu Abant İzzet Baysal University, Directorate of Research Projects Commission (BAP grant no 2018.03.03.1348) are gratefully acknowledged for financial support.

References

1. Y. Bansal, O. Silakari, The therapeutic journey of benzimidazoles: A review, *Bioorg. Med. Chem.*, 20 (2012) 6208-6236.
2. E. Badawey, T. Kappe, Benzimidazole condensed ring system. IX. Potential antineoplastics. New synthesis of some pyrido[1,2-a]benzimidazoles and related derivative, *Eur. J. Med. Chem.*, 30 (1995) 327-332.
3. J. Ndakala, R.K. Gessner, P.W. Gitari, N. October, K.L. White, A. Hudson, F. Fakorede, D.M. Shackelford, M. Kaiser, C. Yeates, S.A. Charman, K. Chibale, Antimalarial pyrido[1,2-a]benzimidazoles, *J. Med. Chem.*, 54 (2011) 4581-4589.
4. M. Hranjec, I. Piantanida, M. Kralj, L. Suman, K. Pavelic, G. Karminski-Zamola, Novel amidino-substituted thienyl- and furylvinylbenzimidazole: derivatives and their photochemical conversion into corresponding diazacyclopenta[c]fluorenes. synthesis, interactions with DNA and RNA, and antitumor evaluation. 4., *J. Med. Chem.*, 51 (2008) 4899-4910.
5. H. Takeshita, J. Watanabe, Y. Kimura, K. Kawakami, H. Takahashi, M. Takemura, A. Kitamura, K. Someya, R. Nakajima, Novel pyridobenzimidazole derivatives exhibiting antifungal activity by the inhibition of beta-1,6-glucan synthesis, *Bioorg. Med. Chem. Lett.*, 20 (2010) 3893-3896.
6. H.L. Koo, H.L. Dupont, Rifaximin: a unique gastrointestinal-selective antibiotic for enteric diseases, *Curr. Opin. Gastroenterol.*, 26 (2010) 17-25.
7. H.J. Knölker, R. Boese, R. Hitzemann, Imidazole derivatives, III. Regiospecific synthesis, structure, and fluorescence properties of highly substituted imidazo[1,2-a]pyridines and pyrido[1,2-a]benzimidazoles, *Chem. Ber.*, 123 (1990) 327-339.
8. S. Ohta, T. Yuasa, Y. Narita, I. Kawasaki, E. Minamii, M. Yamashita, Synthesis and application of imidazole derivatives. Synthesis of pyrido[1,2-a]benzimidazolone derivatives, *Heterocycles*, 32 (1991) 1923-1931.
9. H. Schaefer, M. Gruner, G. Grossmann, K. Gewald, On the synthesis and structure of 8-nitro-imidazo[1,2-a]pyridines, *Monatsh. Chem.*, 122 (1991) 959-966.
10. D.B. Zhao, J.Y. Hu, N.J. Wu, X.L. Huang, X.R. Qin, J.B. Lan, J.S. You, Regiospecific synthesis of 1,2-disubstituted (hetero) aryl fused imidazoles with tunable fluorescent emission, *Org. Lett.*, 13 (2011) 6516-6519.
11. T. Iwaki, A. Yasuhara, T. Sakamoto, Novel synthetic strategy of carbolines via palladium-catalyzed amination and arylation reaction, *J. Chem. Soc., Perkin Trans.*, 1 (1999) 1505-1510.
12. Z. Wu, Q. Huang, X. Zhou, L. Yu, Z. Li, D. Wu, Synthesis of pyrido[1,2-a]benzimidazoles through a copper-catalyzed cascade C-N coupling process, *Eur. J. Org. Chem.*, 2011 (2011) 5242-5245.
13. H. Wang, Y. Wang, C. Peng, J. Zhang, Q. Zhu, A direct intramolecular C-H amination reaction cocatalyzed by copper(II) and iron(III) as part of an efficient route for the synthesis of pyrido[1,2-a]benzimidazoles from N-aryl-2-aminopyridines, *J. Am. Chem. Soc.*, 132 (2010) 13217-13219.
14. K.S. Masters, T.R.M. Rauws, A.K. Yadav, W.A. Herrebout, B. Van der Veken, B. U.W. Maes, On the importance of an acid additive in the synthesis of pyrido[1,2-a]benzimidazoles by direct copper-catalyzed amination, *Chem. Eur. J.*, 17 (2011) 6315-6330.

15. D. Liang, Y. He, L. Liu, Q. Zhu, A metal-free tandem demethylenation/C(sp²)-H cycloamination process of N-benzyl-2-aminopyridines via C-C and C-N bond cleavage, *Org. Lett.*, 15 (2013) 3476-3479.
16. S.M. Barolo, Y. Wang, R.A. Rossi, G.D. Cuny, Synthesis of pyrido [1, 2-a] benzimidazoles by photo-stimulated C-N bond formation via S_{RN}1 reactions, *Tetrahedron*, 69 (2013) 5487-5494.
17. Y. He, J. Huang, D. Liang, Q. Zhu, C-H cycloamination of N-aryl-2-aminopyridines and N-arylamidines catalyzed by an in situ generated hypervalent iodine(III) reagent, *Chem. Commun.*, 49 (2013) 7352-7354.
18. D. Rao, S. Rasheed, R. Vishwakarma, P. Das, Hypervalent iodine(III) catalyzed oxidative C-N bond formation in water: synthesis of benzimidazole-fused heterocycles, *RSC Adv.*, 4 (2014) 25600-25604.
19. G. Qian, B. Liu, Q. Tan, S. Zhang, B. Xu, Hypervalent iodine(III) promoted direct synthesis of imidazo[1,2-a]pyrimidines, *Eur. J. Org. Chem.*, 2014 (2014) 4837-4843.
20. N. Kutsumura, S. Kunimatsu, K. Kagawa, T. Otani, T. Saito, Synthesis of benzimidazole-fused heterocycles by intramolecular oxidative C-N bond formation using hypervalent iodine reagents, *Synthesis*, 43 (2011) 3235-3240.
21. S. Manna, K. Matcha, A.P. Antonchick, Metal-free annulation of arenes with 2-aminopyridine derivatives: The methyl group as a traceless non-chelating directing group, *Angew. Chem. Int. Ed.*, 53 (2014) 8163-8166.
22. H. Foks, D. Pancechowska-Ksepko, M. Janowiec, Z. Zwolska, E. Augustynowicz-Kopeć, Synthesis and tuberculostatic activity of some 1,1-bis-methylthio-2-nitro-ethene derivatives, *Phosphorus Sulfur*, 180 (2005) 2291-2297.
23. M. Yildırım, D. Celikel, N. Evis, D.W. Knight, B.M. Kariuki, Base-promoted new C-C bond formation: an expedient route for the preparation of thiazolo-and imidazolo-pyridinones via Michael addition, *Tetrahedron*, 70 (2014) 5674-5681.
24. M. Yildırım, D. Celikel, Y. Dürüst, D.W. Knight, B.M. Kariuki, A rapid and efficient protocol for the synthesis of novel nitrothiazolo [3, 2-c] pyrimidines via microwave-mediated Mannich cyclisation, *Tetrahedron*, 70 (2014) 2122-2128.
25. C. Altug, A.K. Burnett, E. Caner, Y. Dürüst, M.C. Elliott, R.P. Glanville, A.D. Westwell, An efficient one-pot multicomponent approach to 5-amino-7-aryl-8-nitrothiazolo [3,2-a] pyridines, *Tetrahedron*, 67 (2011) 9522-9528.
26. D. Elumalai, R. Gnanasekaran, S. Leelakrishnan, G. Nachimuthu, T. Kannan, T.P. Paramasivam, K. Jayabal, InCl₃-assisted eco-friendly approach for N-fused 1,4-dihydropyridine scaffolds via ring opening michael addition of cyclic nitroketene and iminocoumarin: Synthesis and DFT studies, *Chem. Select*, 3 (2018) 2070-2079.



Modified Graphite Surfaces Prepared for Electrochemical Biomolecular Interaction Detection Studies

Elektrokimyasal Biyomoleküler Etkileşim Tespit Çalışmaları İçin Modifiye Grafit Yüzeyler

Filiz Kuralay[✉]

Department of Chemistry, Faculty of Science, Hacettepe University, Ankara, Turkey.

ABSTRACT

This paper demonstrates the fabrication of electroactive polymer modified electrode materials for monitoring biomolecular interactions between double-stranded DNA (dsDNA) and Mitomycin C (MMC) which is an important and commonly used anticancer drug. The modified electrode materials were constructed by the electropolymerization of *o*-phenylenediamine (*o*PD) monomer in a solution containing nanomaterial as well. The nanomaterial used as the dopant molecule was graphene (GN) and the electropolymerization technique was cyclic voltammetry (CV). Subsequently immobilization of dsDNA was achieved onto poly(*o*-phenylenediamine) (PoPD) polymer modified surfaces. So-formed dsDNA immobilized nanomaterial incorporated polymer modified electrodes were used as the biosensing platforms for the detection of dsDNA-MMC interaction. Different MMC interaction times were studied in order to identify biomolecular interactions.

Key Words

Modified electrodes, electropolymerization, dsDNA, Mitomycin C.

Öz

Bu çalışma, çift sarmal DNA (dsDNA) ile önemli ve sık kullanılan bir antikanser ilacı olan Mitomisin C (MMC) arasındaki biyomoleküler etkileşimin görüntülenmesi için elektroaktif polimer modifiye elektrot malzemelerinin hazırlanmasını göstermektedir. Modifiye elektrot malzemeleri, *o*-fenilendiamin (*o*PD) monomerinin nanomalzeme içeren bir çözeltide elektropolimerizasyonu ile oluşturulmuştur. Katkı maddesi (dopant) molekül olarak kullanılan nanomalzeme grafen (GN)'dir ve elektropolimerizasyon tekniği dönüşümlü voltametri (CV)'dir. Sonrasında poli(*o*-fenilendiamin) polimer modifiye yüzeylere dsDNA immobilizasyonu gerçekleştirilmiştir. Oluşturulan nanomalzeme katılmış bu polimer modifiye elektrotlar, dsDNA-MMC etkileşiminin tespitinde biyotayin platformları olarak kullanılmışlardır. Biyomoleküler etkileşimlerini aydınlatmak için farklı MMC etkileşim süreleri çalışılmıştır.

Anahtar Kelimeler

Modifiye elektrotlar, elektropolimerizasyon, dsDNA, Mitomisin C.

Article History: Received: Nov 26, 2019; Revised: Dec 5, 2019; Accepted: Dec 5, 2019; Available Online: Dec 20, 2019.

DOI: <https://doi.org/10.15671/hjbc.676957>

Correspondence to: F. Kuralay, Department of Chemistry, Faculty of Science, Hacettepe University, Ankara, Turkey.

E-Mail: filizkur@hacettepe.edu.tr

INTRODUCTION

Deoxyribonucleic acid (DNA) is among the fundamental molecules of life since it is the hereditary material that carries genetic instructions for humans and many other organisms. This important biomolecule consists of two strands that form a double helix structure. Each strand has a backbone made of deoxyribose and phosphate groups and attached to these sugars, four DNA bases exist. These DNA bases combine each strand together. The genetic information coded in DNA exists in four DNA bases called guanine (G), adenine (A), cytosine (C) and thymine (T). Thus, any damage on these bases has severe effects on transcription and DNA replication process. It is well-known that DNA is one of the major target for anticancer drugs due to their ability to interfere with cell growth and division [1-5]. For these reasons, investigation of the interaction between DNA and anticancer drugs is one of the key topics for drug discovery and drug dose determination studies [6-9]. With this aim in mind, in this paper, investigation of double-stranded DNA (dsDNA) with Mitomycin C (MMC) using electroactive polymer coated electrodes was demonstrated and detailed. MMC is a chemotherapeutic agent known with its antitumour activity and effectively used in gastro-intestinal cancers, anal cancers and breast cancers [7]. There have been various studies based on the investigation of DNA molecule and anticancer drugs. For example, Gürsoy et al. have synthesized polyglycine on graphite electrodes in order to identify the interaction between dsDNA and Mitomycin C [7]. Multi-walled carbon nanotubes (MWCNTs) added polyglycine has been used for the electrode modification. Erdem and her colleagues have used single-walled carbon nanotubes (SWCNTs) modified graphite electrodes for dsDNA and anticancer drug, daunorubicin (DNR) [8]. Differential pulse voltammetry (DPV) and electrochemical impedance spectroscopy (EIS) have been used in order to investigate the interaction. Interaction has been followed by the changes in the oxidation signal of guanine base of dsDNA. Bruzaca et al. have studied electrochemical oxidation of Mitomycin C and its interaction with DNA on an electrochemical biosensor platform using cyclic voltammetry, square wave voltammetry (SWV) and differential pulse voltammetry at carbon paste electrode [9].

Polymers are materials that are made of long and repeating chains of different molecules. Differentiation of the polymers can be done according to the types of

molecules and bonds. Among many polymers, electroactive polymers have attracted significant attention due to their certain and important characteristics [10-12]. Electroactive polymers can be fabricated onto electrode materials in a polymerization medium containing their monomers, dopant molecules and convenient solvents. So-formed polymeric layers not only have good electrochemical properties but also have robust, stable and uniform structures. They exhibit similar responses to biological systems and they are permeable to electroactive species. Furthermore, most of them have porous structures that increase their active surface areas. Unique surface chemistry of these materials has facilitated their interactions with biological molecules. Hence, these polymer modified surfaces found various important applications including biosensing with their good electrical, structural and mechanical properties [13-15]. In the literature one of the preferred ways to improve the characteristics of electroactive polymers is the formation of their composites with nanomaterials. Graphene, carbon nanotubes or nanoparticles have been widely used for this purpose since they have excellent chemical, electrical, mechanical, thermal and optical features [16-18]. In the present work, graphene (GN) was used as the dopant material of the polymeric structure, poly(*o*-phenyldiamine) (PoPD) which realized in a fast, simple and one-step electropolymerization. Graphene is among the most attractive nanomaterials that takes place in different application fields such as biosensor studies, electrochromic devices and supercapacitors. It is a two-dimensional structure (2D) of sp^2 -bonded monolayer carbon atoms having high electrical conductivity, good electrocatalytic activity and high surface area. Nanocomposites of graphene with electroactive polymers are commonly used in the literature since graphene improved the electrochemical properties of these polymers [19-23].

In the current study, *o*-phenylenediamine monomer was electropolymerized in the presence of graphene in a single step polymerization onto disposable pencil graphite electrodes (PGEs) in order to investigate dsDNA-MMC interaction. Cyclic voltammetry (CV) technique was used for the formation of graphene incorporated poly(*o*-phenylenediamine) layer onto PGE using various cyclic scans. Modified electrodes were characterized electrochemically by cyclic voltammetry. The surface characteristics of the modified surfaces were identified via scanning electron microscopy (SEM). Afterwards, biomolecular interactions were monitored

by a biosensing platform constructed by the immobilization of dsDNA on the graphene doped electroactive polymeric layer. The interaction was evaluated based on the changes in the electrooxidation of electroactive DNA bases, guanine and adenine. There were decreases in the oxidation of these bases after MMC interaction of the dsDNA immobilized polymer modified electrode. Poly(*o*-phenylenediamine) is one of the attractive electroactive polymers that plays an important role in electrochemical biosensor researches due to its inhibitory effect on electroactive interferences. Thus, it is chosen as the polymeric structure to host biomolecule in this study. It has been used in effective electrochemical biosensor platforms with its simple and low-cost preparation yielding high sensitivity, and selectivity [21,24,25]. Graphene doped poly(*o*-phenylenediamine) modification improved the electrochemical properties of the bare electrode material and also served as a convenient immobilization layer for dsDNA with its high electroactive surface area. Besides these advantages the nanomaterials doped polymeric layer showed good

electrocatalytic activity for the oxidation of DNA bases, guanine and adenine. This work is the first example of the use of dsDNA immobilized graphene incorporated poly(*o*-phenylenediamine) modified electrodes for dsDNA-MMC interaction detection. The fabricated electrode presented promising results that could be used for different DNA-anticancer drug studies. So-formed nanobiosensing platform will definitely have interesting applications in the field of DNA-based studies.

MATERIALS and METHODS

Instrumentation

Electrochemical studies including electrode material preparation and characterization of the fabricated electrode materials were conducted by an AUTOLAB-PGSTAT 204 analysis system supported with a NOVA software package (Metrohm, The Netherlands). Three electrode system was used in the electrochemical experiments. These are pencil graphite working electrode,

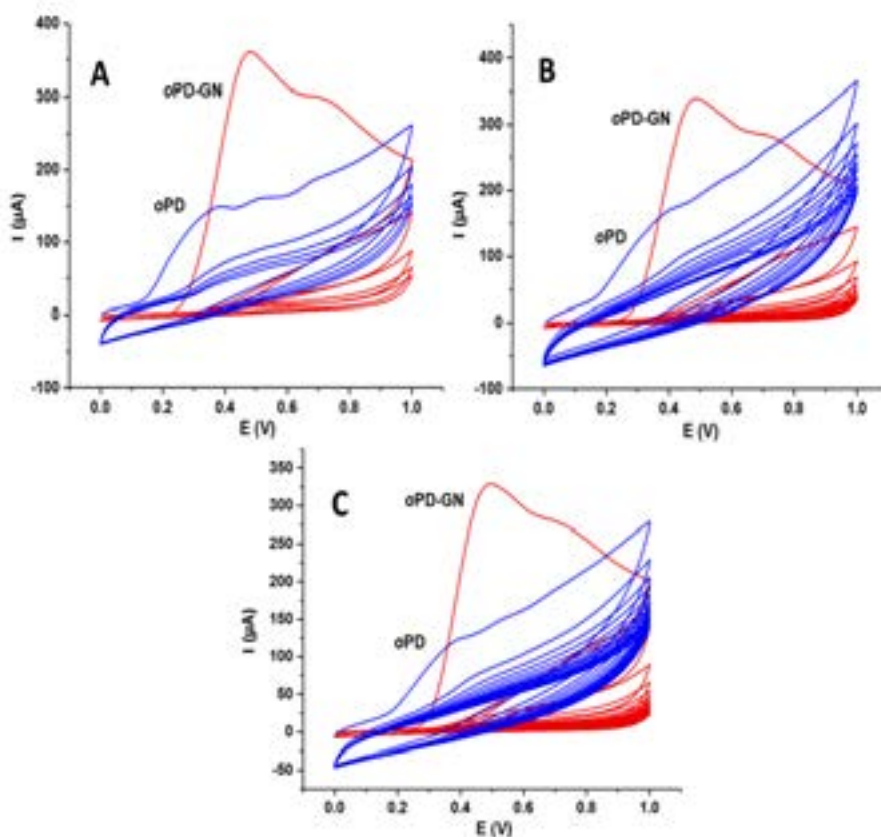


Figure 1. Electropolymerization curves obtained using cyclic voltammetry for oPD-GN (red line) and oPD (blue line): A) 5 cycles, B) 10 cycles and C) 15 cycles (scan rate: 100 mV s^{-1}).

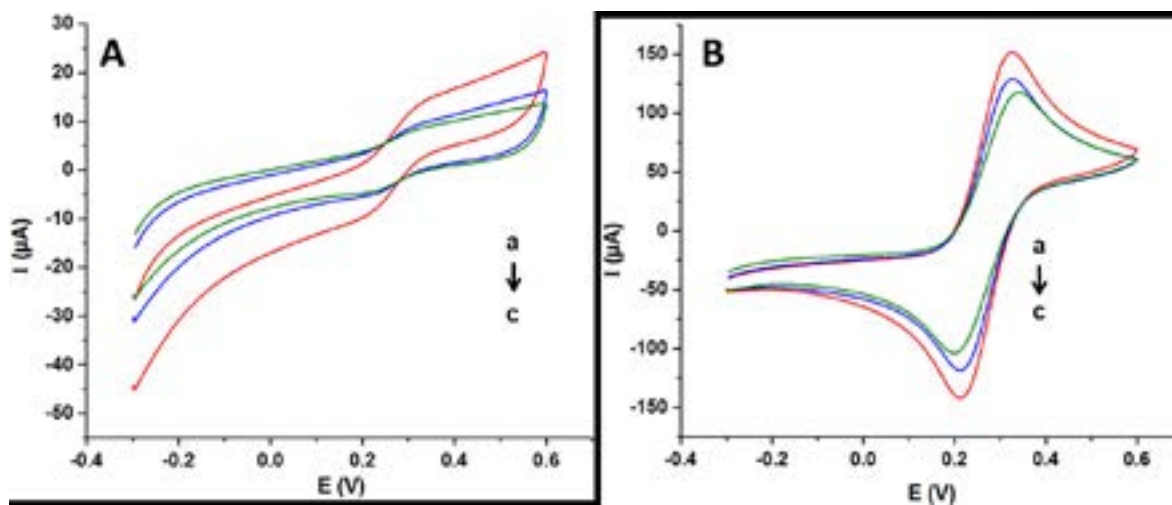


Figure 2. Electrochemical responses of the modified electrode materials: A) PoPD/PGEs, B) PoPD-GN/PGEs a) 5 cycles, b) 10 cycles, c) 15 cycles of electropolymerization in 5 mM $\text{Fe}(\text{CN})_6^{3-/4-}$ redox probe containing 0.1 M (scan rate: 100 mV s^{-1})

Ag/AgCl reference electrode (BASi, USA) and Pt wire counter electrode (BASi, USA). 0.5 mm HB Tombow tip was used and the connector was a Tombow pencil. For surface characterization studies, Hitachi SU 1510 (Hitachi, Japan) was used. Experiments were carried out at room temperature.

Chemicals and Preparation of Solutions

o-Phenylenediamine, graphene (powder), Mitomycin C (from Streptomyces), lithium perchlorate, potassium ferri-cyanide and potassium ferrocyanide were purchased from Sigma-Aldrich. *o*-Phenylenediamine was distilled before used. dsDNA was obtained from Serva. Other chemicals used in the studies were in analytical reagent grade and purchased from Sigma-Aldrich.

Preparation of solutions: Electropolymerization solution was prepared in the presence of 10 mM *o*-phenylenediamine, 50 mM lithium perchlorate and graphene (2.0 mg mL^{-1}) in 50 mM pH 7.4 phosphate buffer [21]. Electropolymerization solution was sonicated for 10 min and then saturated with nitrogen gas (N_2) (BOS, Turkey) before the experiments. For the comparison experiments, monomer solution containing lithium perchlorate was prepared. dsDNA solution was prepared with 50 mM pH 4.8 acetate buffer containing 20 mM NaCl. Stock solutions of MMC (250 mg L^{-1}) were prepared in ultra-pure distilled water. Diluted solutions of MMC were prepared with 50 mM pH 7.4 phosphate buffer containing 20 mM NaCl.

Preparation of the Modified Electrode Materials

Fabrication of the polymer modified electrodes in the presence of graphene onto pencil graphite electrodes was carried out with cyclic voltammetry at a potential range of +0.0 V and +1.0 V using cyclic scans of 5, 10 and 15 (scan rate of 100 mV s^{-1}). Electrochemical characterization of these modified electrode surfaces was done in a solution of 0.1 M KCl containing 5 mM $\text{Fe}(\text{CN})_6^{3-/4-}$ at a potential range of -0.30 V and +0.60 V (scan rate of 100 mV s^{-1}). In addition, these experiments were compared with only poly(*o*-phenylenediamine) modified electrodes.

dsDNA Immobilization on Graphene Incorporated Poly(*o*-phenylenediamine) Modified Electrode Materials

For the immobilization of dsDNA onto the graphene incorporated poly(*o*-phenylenediamine) modified electrode materials, modified electrodes were held at +0.0 V in a solution of 100 mg mL^{-1} dsDNA solution for 360 s. In this process dsDNA was accumulated onto the modified electrodes. These electrodes were denoted as dsDNA/PoPD-GN/PGEs in the rest of the study.

Interaction Studies Performed Between dsDNA/PoPD-GN/PGEs and MMC

For the interaction studies, dsDNA/PoPD-GN/PGEs were incubated in 50 mg L^{-1} MMC solutions for 5, 10 and 30 min. The interaction of the modified surfaces with MMC was monitored with differential pulse vol-

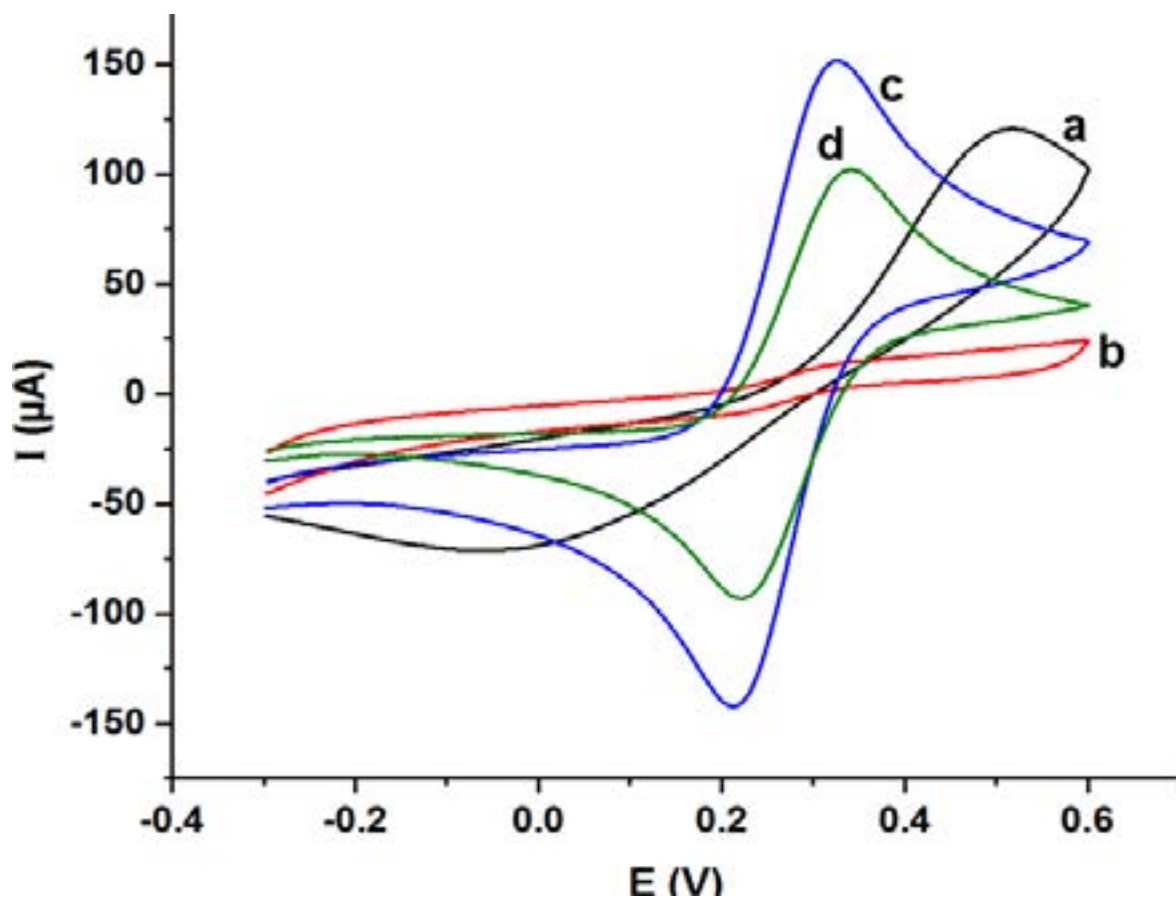


Figure 3. Electrochemical responses of the modified electrode materials: a) bare PGE, b) PoPD/PGE, c) PoPD-GN/PGE, d) GN/PGE in 5 mM $\text{Fe}(\text{CN})_6^{3-/4-}$ redox probe containing 0.1 M (scan rate: 100 mV s^{-1}).

tammometry technique using +0.70 V and +1.50 V in 50 mM pH 4.8 acetate buffer (at a step potential of 50 mV and at a scan rate of 10 mV s^{-1}).

RESULTS and DISCUSSION

The main purpose of this paper was to develop a poly(*o*-phenylenediamine) modified disposable pencil graphite electrode for the examination and identification of dsDNA and MMC which held an important topic in terms of drug discovery and drug dose regulation studies. The electroactive surface on the electrode was accomplished by the cyclic voltammetry using 5, 10 and 15 polymerization cycles. Figure 1A to C present the cyclic voltammograms related to these electropolymerization experiments, respectively. In each case, comparison of the only *o*PD electropolymerization was also added into the figures in order to illustrate the advantage of incorporation of graphene into the polymeric structure. It is seen that with the presence of graphene, electropolymerization was achieved with higher efficiency re-

sulting in higher currents. And, there was a resistance in the polymerization of *o*PD in the aqueous media onto PGE. In the first cycles of both polymerizations, the oxidation of the monomer existed and then in the other cycles, polymerization behavior was obtained [21].

After the electropolymerization process, characterization of the modified surfaces was performed in a redox probe containing solution. Figure 2A presents the cyclic voltammograms of the modified electrodes as a result of *o*PD electropolymerization (Figure 2A-a to c for 5, 10 and 15 cycles of polymerization, respectively). As seen from these electrochemical characterization studies, electrochemical behaviors of the PoPD modified electrodes did not have good responses. The reversibilities of the polymeric surfaces and the peak currents achieved were poor. However, as illustrated in Figure 2B, there were very good improvements with the addition of graphene into the polymeric structure. The reversibilities of the polymeric surfaces and the peak currents achieved were highly enhanced which signifi-

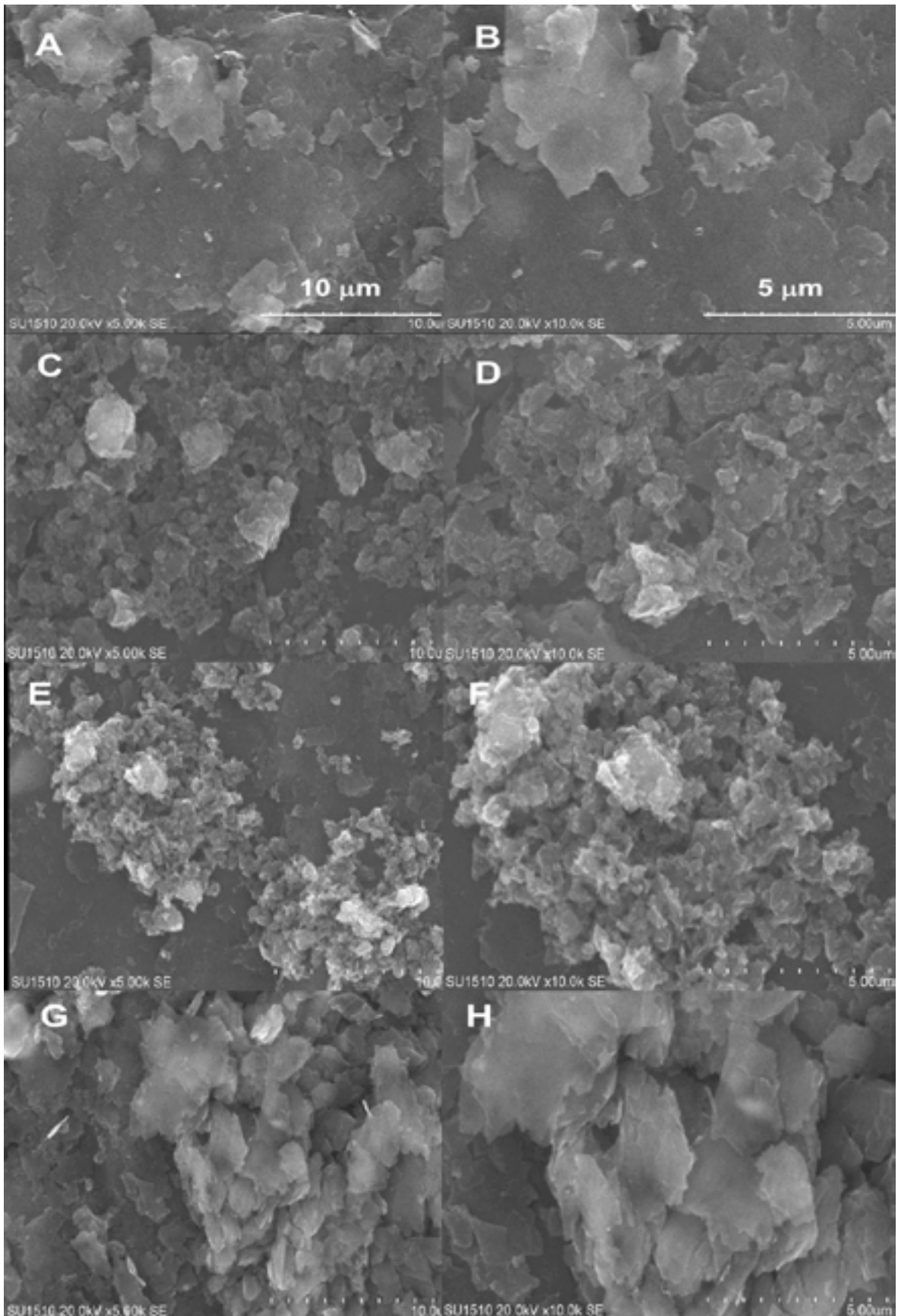


Figure 4. SEM images of (A,B) bare PGE, (C,D) PoPD/PGE, (E,F) PoPD-GN/PGE, (E,F) GN/PGE.

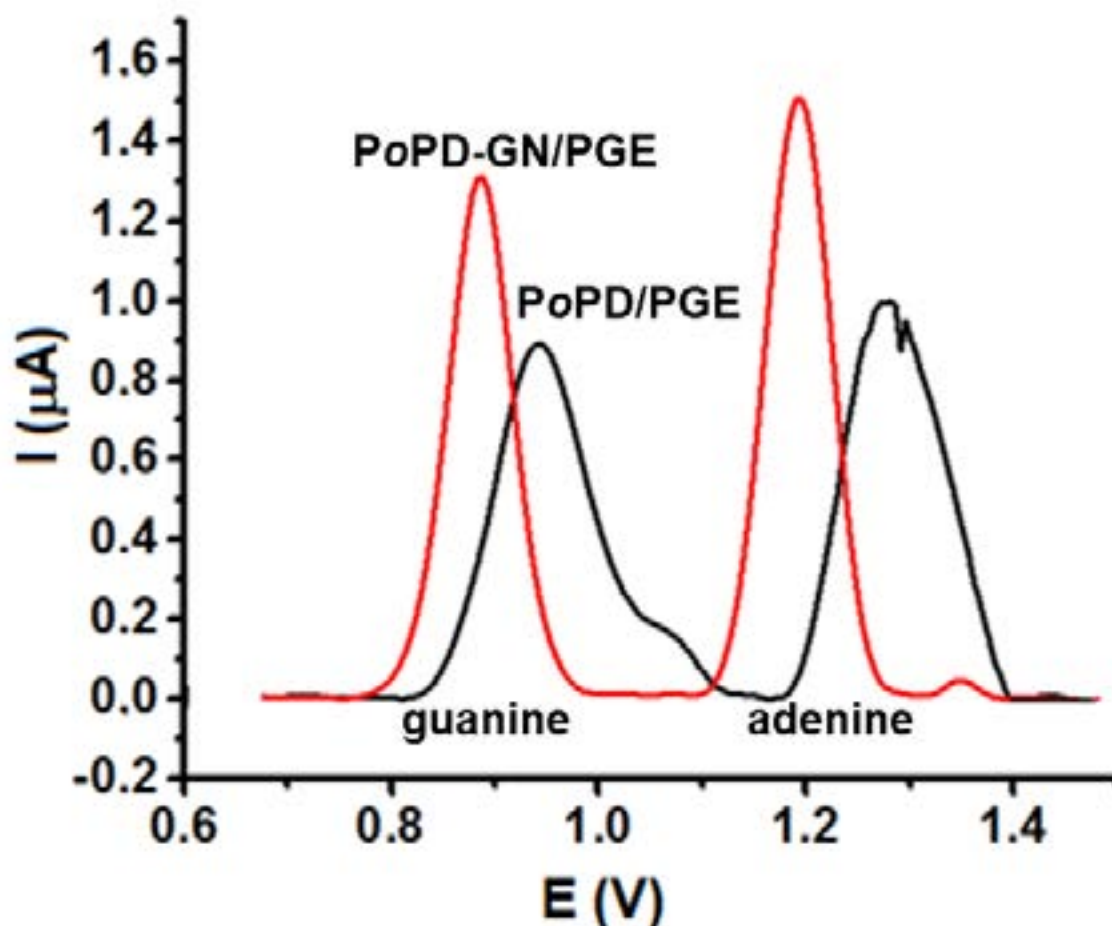


Figure 5. Differential pulse voltammograms of PoPD-GN/PGE (red line) and PoPD/PGE (black line) in pH 4.8 50 mM acetate buffer after dsDNA immobilization (dsDNA concentration: 100 mg L^{-1} , step potential: 50 mV, scan rate: 10 mV s^{-1}).

ed the advantage of using graphene incorporated PoPD (Figure 2B-a to c for 5, 10 and 15 cycles of polymerization, respectively). The results showed that the effect of nanomaterials addition and revealed the advantage of in-situ and one-step electropolymerization. The resulted electrode materials had improved and good characteristics. Therefore, practical and efficient electrode materials modifications were accomplished.

In Figure 3, cyclic voltammetric behaviors of the modified electrode materials and bare electrode material were compared. It is clearly seen from these comparisons that the bare electrode had also poor electrochemical activity. The comparison of only graphene modification onto the pencil graphite electrode was also performed. This modification was achieved by using 2.0 mg mL^{-1} graphene prepared in dimethylformamide (DMF) by dipping the bare electrode into this solution. GN modified electrode exhibited a worse response than the

PoPD-GN/PGE proving the use of electrochemical modification. The peak currents achieved with the nanocomposite modified electrode was higher. The reversibilities based on the electrooxidation and electroreduction of the redox probe was almost the same with GN/PGE and PoPD-GN/PGE.

After the electrochemical characterization of these modified electrode materials, surface morphologies of them were investigated with scanning electron microscopy (SEM). SEM images for the bare PGE at different magnifications were given as Figure 4A and Figure 4B. These images revealed the smooth graphite layers of the pencil graphite electrode [7]. SEM images of PoPD modified PGE at different magnitudes were given as Figure 4C and Figure 4D. As seen from these images, pencil graphite electrode surface was modified with the polymeric film. Figure 4E and Figure 4F present the SEM images of graphene incorporated PoPD. In these figu-

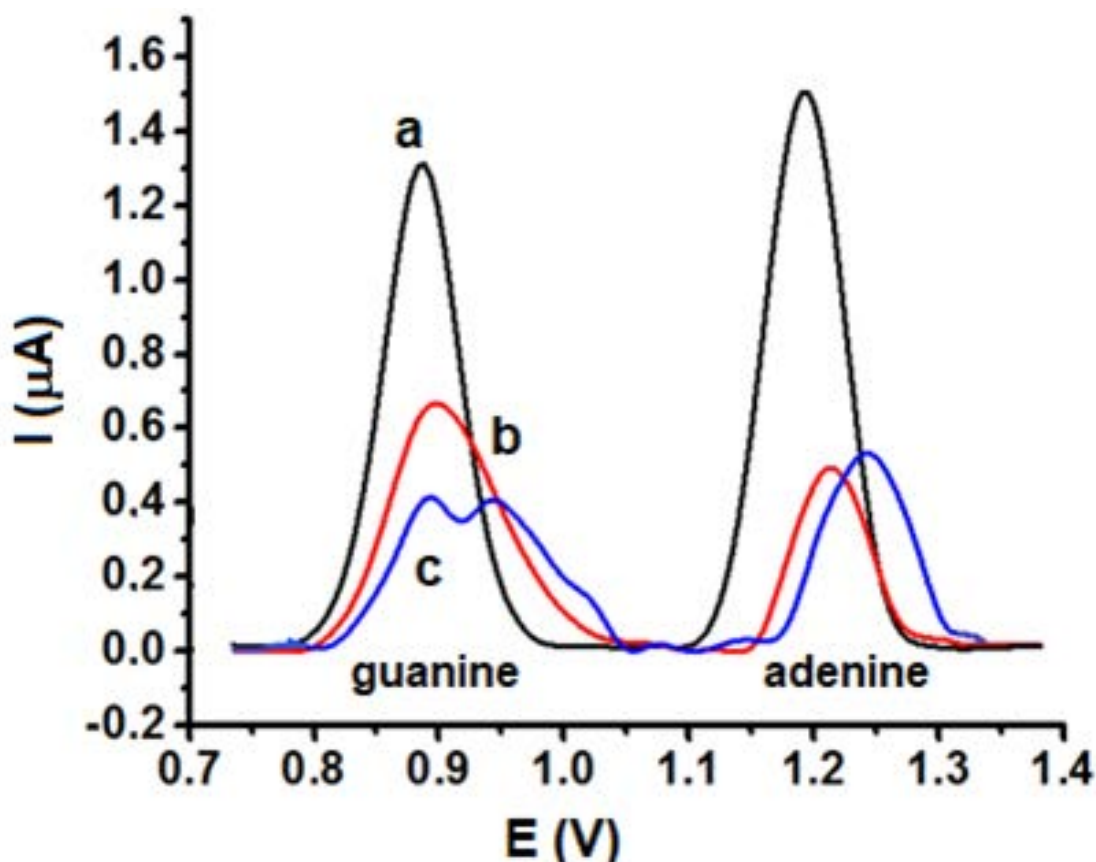


Figure 6. Differential pulse voltammograms of dsDNA/PoPD-GN/PGE in pH 4.8 50 mM acetate buffer after interaction with MMC a) 0 min, b) 5 min, c) 10 min (MMC concentration: 50 mg L⁻¹, step potential: 50 mV, scan rate: 10 mV s⁻¹).

res, it is obvious that the polymerization of *o*PD became more dominant with the addition of graphene. Graphene facilitated the electropolymerization of *o*PD. In the end, the comparison with GN modified electrode was made. Figures 4G and Figure 4H illustrate the related images at different magnitudes. Graphene layers on the pencil graphite electrode revealed clearly indicating the rough surface formed. SEM images identified different modifications on the graphite electrode in a clear vision.

dsDNA-MMC interaction studies were then carried out as the application of the graphene incorporated PoPD modified electrode material. For the evaluation of this interaction first dsDNA was immobilized onto the modified electrode prepared with 5 cycles of polymerization since this electrode gave the best electrochemical behavior and features. Immobilization of dsDNA was performed by holding the modified electrode material at +0.0 V for 360 s. dsDNA concentration was 100 mg L⁻¹ for the experiments. Modification of dsDNA onto bare PGE was also carried out in order to compare the electrochemical behaviors of electroactive DNA bases,

guanine and adenine. Electrochemical oxidation peaks for these two DNA bases were obtained in a higher sensitivity with the modified electrode compared to the bare electrode as expected. Differential pulse voltammetry was used in these experiments. There were also electrocatalytic effects observed with the graphene incorporated PoPD modified graphite electrode material [7,21]. This result can be concluded as the nanocomposite electrode facilitated the oxidations of guanine and adenine. Peak separation with the modified electrode was well-defined having a value of 0.31 V. Guanine oxidation was observed at about +0.88 V and adenine oxidation was observed at about 1.19 V.

Interaction of MMC with dsDNA immobilized PoPD-GN/PGE was conducted at various interaction times: 5, 10 and 30 min. These interaction studies were presented as Figure 6. These studies pointed out that after the incubation of the modified electrode materials with MMC, the oxidation of DNA bases became difficult. Thus, decreases in the oxidation peaks of both guanine and adenine were obtained and the findings were parallel to the

literature [7,26]. By increasing the interaction time, the quantity of the reduction increased. At 30 min of interaction, the oxidation peaks for guanine and adenine were almost absent (not shown). The reduction in the oxidation peak of guanine was 47.7% and it was 65.7% for adenine at 5 min of interaction. The reduction in the oxidation peak of guanine was 69.6% and it was 72.3% for adenine at 10 min of interaction. The tendency in the oxidation peak current reduction was more visible and meaningful by considering the guanine oxidation peak compared to the adenine oxidation peak by using this electrode material at the given working interaction times. It can be concluded that the modified electrode presented a fast, reliable and convenient sensing platform for the investigation of dsDNA-MMC interaction. The repeatability of the modified electrodes was also tested using the oxidation peak for guanine at 5 min of interaction with five modified electrodes. The relative standard deviation was calculated and found as 4.4% (n=5).

Conclusions

As a summary, in the present study an electroactive polymer depended polymeric surface having good electrochemical properties was prepared using cyclic voltammetry technique in the presence of an attractive nanomaterial, graphene. The presence of graphene highly improved the electrochemical characteristics and the responses of the polymer modified electrode material and also bare electrode material. The use of electroactive polymer, PoPD, with graphene together presented that a very good synergistic effect occurred. One-step fabrication of the electrode material resulted with a cost-effective, rapid and reproducible process. The prepared electrodes were characterized by cyclic voltammetry and their surface morphologies were identified with scanning electron microscopy. The changes in the surface morphologies on the graphite electrodes were monitored obviously. As the application of the effective electrode material obtained, dsDNA-MMC interaction was evaluated in the study. Immobilization of dsDNA was accomplished efficiently and the biomolecular interactions between dsDNA and the anticancer drug were probed in a high sensitivity. PoPD-GN modified surfaces serve as potential candidates for various DNA-biomolecule interactions.

Acknowledgments

F. Kuralay acknowledges Turkish Academy of Sciences (TÜBA) as an associate member and TÜBA-GEBİP program for financial support. F. Kuralay also acknowledges Yaşar Bayramlı for his technical support.

References

1. J. Wang, Nanoparticle-based electrochemical DNA detection, *Anal. Chim. Acta*, 500 (2003) 247-257.
2. E.M. Boon, J.K. Barton, DNA electrochemistry as a probe of base pair stacking in A-, B-, and Z-form DNA, *Bioconjugate Chem.*, 14 (2003) 1140-1147.
3. J. Wang, G. Liu, A. Merkoçi, Electrochemical coding technology for simultaneous detection of multiple DNA targets, *J. Am. Chem. Soc.*, 125 (2003) 3214-3215.
4. Q. Gong, Y. Wang, H. Yang, A sensitive impedimetric DNA biosensor for the determination of the HIV gene based on graphene-Nafion composite film, *Biosens. Bioelectron.*, 89 (2017) 565-569.
5. F. Kuralay, N. Dükar, Y. Bayramlı, Poly-L-lysine coated surfaces for ultrasensitive nucleic acid detection, *Electroanal.*, 30 (2018) 1556-1565.
6. A. Erdem, Nanomaterial-based electrochemical DNA sensing strategies, *Talanta*, 74 (2007) 318-325.
7. S. Gürsoy, N. Dükar, Y.T. Yaman, S. Abacı, F. Kuralay, Electroactive polyglycine coatings for nanobiosensing applications: Label-free DNA hybridization, DNA-antitumor agent interaction and antitumor agent determination, *Anal. Chim. Acta*, 1072 (2019) 15-24.
8. A. Erdem, H. Karadeniz, A. Caliskan, Single-walled carbon nanotubes modified graphite electrodes for electrochemical monitoring of nucleic acids and biomolecular interactions, *Electroanal.*, 21 (2009) 464-471.
9. E.E.S. Bruzaca, I.C. Lopes, E.H.C. Silva, P.A.V. Carvalho, A.A. Tanaka, Electrochemical oxidation of the antitumor antibiotic mitomycin C and in situ evaluation of its interaction with DNA using a DNA-electrochemical sensor, *Microchem. J.*, 133 (2017) 81-89.
10. G.G. Wallace, M. Smyth, H. Zhao, Conducting electroactive polymer-based biosensors, *TrAC Trends in Anal. Chem.*, 18 (1999) 245-251.
11. O.E. Fayemi, A.S. Adekunle, B.E. Swamy, E.E. Ebenso, Electrochemical sensor for the detection of dopamine in real samples using polyaniline/NiO, ZnO, and Fe₃O₄ nanocomposites on glassy carbon electrode, *J. Electroanal. Chem.* 818 (2018) 236-249.
12. F. Kuralay, H. Özyörük, A. Yıldız, Potentiometric enzyme electrode for urea determination using immobilized urease in poly(vinylferrocenium) film, *Sens. Actuat. B: Chem.*, 109 (2005) 194-199.
13. S. Cosnier, Biomolecule immobilization on electrode surfaces by entrapment or attachment to electrochemically polymerized films. A review, *Biosens. Bioelectron.*, 14 (1999) 443-456.
14. X. Liu, L. Zhang, S. Wei, S. Chen, X. Ou, Q. Lu, Overoxidized polyimidazole/graphene oxide copolymer modified electrode for the simultaneous determination of ascorbic acid, dopamine, uric acid, guanine and adenine, *Biosens. Bioelectron.*, 57 (2014) 232-238.

15. M.D. Zavolskova, V.N. Nikitina, E.D. Maksimova, E.E. Karyakiba, Constant potential amperometric flow-injection analysis of ions and neutral molecules transduced by electroactive (conductive) polymers, *Anal. Chem.*, 91 (2019) 7495-7499.
16. D.A.C. Brownson, C.E. Banks, Graphene electrochemistry: an overview of potential applications, *Analyst*, 135 (2010) 2768-2778.
17. M. Pumera, Graphene-based nanomaterials and their electrochemistry, *Chem. Soc. Rev.*, 39 (2010) 4146-4157.
18. A. Ambrosi, M. Pumera, Electrochemically exfoliated graphene and graphene oxide for energy storage and electrochemistry applications, *Chem. European J.*, 22 (2016) 153-159.
19. A. Halder, M. Zhang, Q. Chi, Electroactive and biocompatible functionalization of graphene for the development of biosensing platforms, *Biosens. Bioelectron.*, 87 (2017) 764-771.
20. O. Tovide, N. Jahed, C.E. Sunday, K. Kokpas, R.F. Ajayi, H.R. Makelane, K.M. Molapoi S.V. John, P.G. Baker, E.I. Iwuoha, Electro-oxidation of anthracene on polyanilino-graphene composite electrode, *Sens. Actuat. B: Chem.*, 205 (2014) 184-192.
21. N. Dükar, S. Tuñç, K. Öztürk, S. Demirci, M. Dumangöz, M. Sönmez çelebi, F. Kuralay, Highly sensitive and selective dopamine sensing in biological fluids with one-pot prepared graphene/poly(*o*-phenylenediamine) modified electrodes, *Mater. Chem. Phys.*, 228 (2019) 357-362.
22. X. Feng, H. Cheng, Y. Pan, H. Zheng, Development of glucose biosensors based on nanostructured graphene-conducting polyaniline composite, *Biosens. Bioelectron.*, 70 (2015) 411-417.
23. E. Muthusankar, V.K. Ponnusamy, D. Ragupathy, Electrochemically sandwiched poly(diphenylamine)/phosphotungstic acid/graphene nanohybrid as highly sensitive and selective urea biosensor, *Synt. Metals*, 254 (2019) 134-140.
24. X. Liu, H. Zhu, X. Yang, An electrochemical sensor for dopamine based on poly(*o*-phenylenediamine) functionalized with electrochemically reduced graphene oxide, *RSC Adv.* 4 (2014) 3706-3712.
25. X. Wang, D. Sun, Y. Tong, Y. Zhong, Z. Chen, A voltammetric aptamer-based thrombin biosensor exploiting signal amplification via synergetic catalysis by DNAzyme and enzyme decorated AuPd nanoparticles on a poly(*o*-phenylenediamine) support, *Microchim. Acta*, 184 (2017) 1791-1799.
26. F. Kuralay, A. Erdem, Gold nanoparticle/polymer nanocomposite for highly sensitive drug-DNA interaction, *Analyst*, 140 (2015) 2876-2880.